

VOLTAGE PROGRAMMABLE MATERIALS

by

Uwe Bauer

Diplom Ingenieur Nanostrukturtechnik, University of Würzburg (2009)

Submitted to the Department of Materials Science and Engineering
in partial fulfilment of the requirements for the degree of

Doctor of Philosophy in Materials Science and Engineering

at the

MASSACHUSETTS INSTITUTE OF TECHNOLOGY

February 2015

© Massachusetts Institute of Technology 2014. All rights reserved.

Author
Department of Materials Science and Engineering
September 12, 2014

Certified by.....
Geoffrey S. D. Beach
Class of '58 Associate Professor of Materials Science and Engineering
Thesis Supervisor

Accepted by.....
Gerbrand Ceder
Chairman, Department Committee on Graduate Students

To my mother who nurtured and always supported my interest in science and my father who taught me that if I am going to do something then I should take the time and do it right

VOLTAGE PROGRAMMABLE MATERIALS

by

Uwe Bauer

Submitted to the Department of Materials Science and Engineering
on September 12, 2014, in Partial Fulfillment of the
Requirements for the Degree of
Doctor of Philosophy in Materials Science and Engineering

ABSTRACT

The physical and chemical properties of nanoscale materials derive largely from structure and composition at interfaces. The possibility to electrically modify these interfacial characteristics would provide a powerful means to control material properties. Of particular recent scientific and technological interest are metal/metal-oxide bilayers, in which properties as varied as catalytic activity, charge and spin transport, ionic exchange, mechanical behavior, thermal conductivity, and magnetism all depend sensitively on oxygen stoichiometry and defect structure at the metal/metal-oxide interface. The possibility to dynamically control interface characteristics through electric-field-induced oxygen transport and electrochemical interface reactions paves the way towards voltage control of these properties in solid-state devices.

Here, we focus on ferromagnetic metal/metal-oxide bilayers that exhibit strong perpendicular magnetic anisotropy derived from interfacial oxygen hybridization. In these materials, we directly observe, *in situ* voltage-driven oxygen migration at room temperature and show that electrical switching of the interfacial oxidation state allows for voltage control of magnetic properties to an extent never before achieved through conventional magneto-electric coupling mechanisms. By engineering the electrode and metal-oxide layers for efficient ionic exchange and transport, we improve the response time by six orders of magnitude and switch perpendicular magnetic anisotropy at the millisecond timescale. Based on this magneto-ionic coupling mechanism we demonstrate a printer-like system to reversibly pattern magnetic properties and realize a prototype nonvolatile memory device in which voltage-controlled domain wall traps facilitate electrical bit selection in a magnetic nanowire register. Moreover, we report on voltage control over electronic transport properties in the same bilayer structures and show that solid-state switching of interface oxygen chemistry provides a path towards voltage-gating the wide range of phenomena governed by metal/oxide interfaces.

Thesis supervisor: Geoffrey S. D. Beach

Title: Class of '58 Associate Professor of Materials Science and Engineering

ACKNOWLEDGEMENTS

"It is good to have an end to journey toward; but it is the journey that matters, in the end."

Ernest Hemingway

Now that I am approaching the end of my Ph.D., I have the pleasure to look back with a smile on my face and a tear in my eyes, what a journey indeed! Here, I would like to take the opportunity to show my gratitude to the many that contributed to this thesis and made my Ph.D. into such a rewarding experience.

First and foremost, I would like to show my gratitude to my advisor Prof. Geoffrey Beach. Geoff, you have been the best advisor I could have wished for. Thank you for your guidance and trust, your help and support, and your contagious enthusiasm about my work. I believe this thesis was shaped by our first meeting. I proposed a collaboration with the Max Planck Institute of Microstructure Physics and you supported it whole heartedly. In many ways that made all the difference, and I am deeply grateful for having had the freedom and support to pursue this collaboration and the many others that followed. Geoff, thanks for being open to new ideas, for always having your students' interest at heart, and for giving me more credit than I deserve.

I would also like to express my gratitude to the other members of my thesis committee, Prof. Caroline Ross and Prof. Harry Tuller. Thank you for your guidance, feedback, and advice throughout my Ph.D.. This thesis wouldn't be what it is without your invaluable input. I would especially like to thank Prof. Tuller for giving me the opportunity to perform impedance measurements in his lab, for sharing his sputter targets, and for patiently explaining to me all things ionic.

Many of the experiments presented in this thesis would not have been possible without the help of David Bono and his ability to build and repair anything with a power switch. David, thank you for your generosity with your time, knowledge, and resources. I have benefitted greatly from working with you. Thank you for always going above and beyond.

During my thesis I have heavily relied on the DMSE machine shops and other shared facilities at MIT. I am indebted to Mike Tarkanian for his training, his teaching, his expert advice on many projects, and the many conversations inside and outside of the shop. I am also grateful to Ike Feitler, Franklin Hobbs, Matt Humbert and Chris Di Perna for their help in the LEM and all the good times had in the basement. I would also like to thank Jim Daley at the NanoStructures Laboratory, Mark Mondol at the Scanning Electron Beam facility at the RLE, and Libby Shaw at the Center for Materials Science and Engineering. My thanks also extend to the DMSE administrative office staff, especially Angelita Mireles and Elissa Haverty.

I would also like to express my gratitude to Jagadeesh Moodera for his advice and generosity. Thank you for always having an open door. I benefitted greatly from our discussions on physics and life in general. I am also grateful to Prof. Polina Anikeeva. Teaching 3.024 was a great experience and an integral part of my Ph.D.

I have been very lucky to be a member of the Beach group. The faces may have changed over the years, but the Beach group has remained the incredibly joyful and productive place that it always has been. To Parnika Agrawal, Sungmin Ahn, Lucas Caretta, Tristan Delaney, Satoru Emori, Max Mann, Dan Montana, Elie Nadal, Minae Ouk, Liz Rapoport, Sarah Schlotter, Greg Steinbrecher, Aik Jun Tan, CK Umachi, Nicholas Whiteway and Seonghoon Woo, thank you for your help and support; you have become my friends and family at MIT. For their contributions to the content of this thesis, I would like to especially thank: Liz and Satoru for training me on all the equipment in the Beach group; Liz for her help with machining essential parts and her advice on figures and writing; Satoru for teaching me all about DW measurements, for essential software to analyze DW motion, for our collaboration on DW traps, and for developing the MOKE anisotropy measurement technique; Lucas, Max and Parnika for helping build the goniometer stage necessary for MOKE anisotropy measurements; Parnika for the crucial AFM and VSM measurements; AJ for growing essential samples and for many MOKE and XPS measurements. Thanks also to Lucas Caretta, Satoru Emori and Liz Rapoport for proofreading my thesis.

This thesis, its topic, key insights and breadth are the result of much collaboration with outstanding research groups from all over the world.

I am very grateful to Prof. Jürgen Kirschner and Prof. Marek Przybylski for giving me the opportunity to work at the Max Planck Institute of Microstructure Physics. Thank you for welcoming me back with open arms even after I had decided to do my Ph.D. at MIT. The support, discussions, and work done in Halle were instrumental to the success of this thesis. Marek, thank you for your continued help and support, inside the lab and out. I am truly grateful. My work in Halle would have been impossible without the excellent technical support from Wolfgang Greie, Günter Kroder, Heike Menge and Frank Weiss. Thank you for always being available for questions and for always going the extra mile. I am also indebted to Oussama Moutanabbir without whose generous help and advice I might not have made it to MIT in the first place. Special thanks goes to Maciek Dabrowski for his friendship and the many long hours we worked together in the Big Lab. I am also grateful to, Rantej Bali, Kuntala Bhattacharjee, Pavel Buczek, Pratyush Das Kanungo, Pedro Gastelois, Piotr Kuswik, Sujit Mana, Somendra Parihar, Parul Parihar, Thiago Peixoto, Nitin Shigne, Christian Tusche, Ionela Vrejoiu, Fikret Yildiz and Khalil Zakeri. You made every visit to Halle a special one.

There wouldn't be a chapter on voltage control of electrical properties without Prof. Henrique Gomes at the Universidade do Algarve. Thank you for hosting me on such short notice and for going out of your way to make my visit possible. I greatly benefitted from our discussions on electrical measurement techniques and resistive switching. Special thanks to Paulo Rocha for taking the time during his thesis writing to help with my experiments. I am also grateful to Joana Canudo, Asal Kiazaded, Ana Mestre and Romina Rega for making my time in Faro so memorable.

I would like to thank Prof. Sebastiaan van Dijken and Lide Yao at Aalto University for a truly remarkable collaboration. Sometimes one conversation at a conference can indeed change everything. It was the TEM and EELS measurements that really allowed me to prove the concept of magneto-ionics and to understand its wider applications in voltage programmable materials.

I am also grateful to Prof. Martin Veis at Charles University of Prague for performing initial magneto-optic spectroscopy measurements on my samples, for Prof. Sean Bishop at Kyushu University for instilling in me the importance of the triple phase boundary, and to Raoul Ouedraogo, Eric Phelps and Andy Vidan from MIT Lincoln Labs for the insightful discussions on applications of voltage programmable materials.

This list would not be complete without my friends and family. Graduate school can be a trying experience, but I have been privileged to share that experience with great friends, not only in the Beach group, but also at MIT and around the world. Thanks to Aziz Abdellahi, Nicolas Aimon, , Jordan Chesin, Jean Anne Currivan, Nilma Dominique, Megan Freeman, Ying Gao, William Herbert, Yu-Ting Huang, Jason Hummelt, Samuel Humphry-Baker, Jae Jin Kim, Mabel Lew, Benjamin Mailly Giacchetti, SiSi Ni, Siamrut Patanavanich, John Rogosic, Brian Spatocco, Lara Triputen and Stian Ueland for making my experience at MIT such a great one. Special thanks to Ahmed Al-Obeidi, Satoru Emori, Jean-Philippe Peraud and Liz Rapoport for being my best friends at MIT, for the lunches, dinners, walks home, movie nights, meat extravaganzas, MADMEC and so much more. To Ying Gao, thanks for making the thesis writing so much better than it could have been. I am also grateful to Johannes Kern and Tobias Umbach for making the long distance friendship work and for keeping me connected to back home. I am truly indebted to Isabel Morgado. In so many ways I could not have done this without you. Thank you for everything. Above all, I am grateful to my family. Thank you for your love and support, I owe everything to you.

This work would have been impossible without financial support by the Nicholas J. Grant Fellowship, the National Science Foundation under NSF-ECCS -1128439, the MRSEC Program under DMR-0819792, the Samsung Global MRAM Innovation program, the Max Planck Institute of Microstructure Physics, the MIT Science and Technology Initiative, the MIT Portugal Program and the MIT Energy Initiative.

Thank you to Kayla Friedman and Malcolm Morgan of the Centre for Sustainable Development, University of Cambridge, UK for producing the Microsoft Word thesis template that I adapted to produce this document.

CONTENTS

1 INTRODUCTION	23
1.1 VOLTAGE PROGRAMMABLE MATERIALS.....	24
1.2 THESIS OUTLINE	27
2 BACKGROUND	31
2.1 PERPENDICULAR MAGNETIC ANISOTROPY.....	32
2.2 MAGNETIC HYSTERESIS LOOPS	39
2.3 THERMALLY ACTIVATED DOMAIN WALL MOTION	43
2.4 THE MAGNETO-ELECTRIC EFFECT IN METAL FERROMAGNETS.....	50
2.5 NANOIONICS AND MEMRISTIVE SWITCHING IN METAL/OXIDE/METAL DEVICES.....	58
2.6 MOTIVATION: A FIRST EXPERIMENT WITH UNEXPECTED RESULTS	67
3 EXPERIMENTAL METHODS.....	73
3.1 SAMPLE FABRICATION.....	74
3.1.1 Sputter Deposition.....	74
3.1.2 Shadow mask lithography.....	77
3.1.3 Electron beam lithography and lift off.....	81
3.1.4 Sample structure and layout.....	83
3.2 SAMPLE CHARACTERIZATION	88
3.2.1 Magneto-optic Kerr Effect	88
3.2.2 Time-Resolved Scanning Magneto-optic Kerr Effect System.....	91
3.2.3 Domain Wall Dynamics in Magnetic Thin Films Measured via MOKE	95
3.2.4 Local Probing of Magnetic Anisotropy via Polar MOKE	97
3.2.5 Vibrating Sample Magnetometry	100
4 VOLTAGE CONTROL OF DOMAIN WALL MOTION	103

4.1 EXPERIMENTAL METHODS:.....	105
4.2 ELECTRIC FIELD CONTROL OF DOMAIN WALL PROPAGATION	106
4.3 ELECTRIC FIELD CONTROL OF DOMAIN WALL VELOCITY	110
4.4 SUMMARY AND CONCLUSION	117
5 VOLTAGE-CONTROLLED DOMAIN WALL TRAPS.....	119
5.1 EXPERIMENTAL METHODS.....	121
5.2 TWO REGIMES OF VOLTAGE RESPONSE.....	123
5.3 THE ROLE OF THE ELECTRODE EDGE	127
5.4 VOLTAGE CONTROLLED DOMAIN WALL TRAPS IN MAGNETIC THIN FILMS	131
5.5 VOLTAGE CONTROLLED DOMAIN WALL TRAPS IN MAGNETIC NANOWIRES	138
5.6 PROTOTYPE NANOWIRE REGISTER.....	142
5.7 SUMMARY AND CONCLUSION	145
6 MAGNETO-IONIC CONTROL OF INTERFACIAL MAGNETISM.....	147
6.1 EXPERIMENTAL METHODS.....	149
6.2 <i>IN SITU</i> TRACKING OF THE OXIDATION FRONT	152
6.3 THERMALLY ACTIVATED ANISOTROPY MODIFICATIONS.....	154
6.4 MAGNETIC ANISOTROPY AND THE POSITION OF THE OXIDATION FRONT	159
6.5 LASER DEFINED ANISOTROPY PATTERNS AND DOMAIN WALL CONDUITS.....	167
6.6 SUMMARY AND CONCLUSION	172
7 FAST SWITCHING OF MAGNETIC PROPERTIES.....	173
7.1 EXPERIMENTAL METHODS.....	175
7.2 ENGINEERING MAGNETO-IONIC DEVICES FOR FAST SWITCHING	176
7.3 MICROSECOND SWITCHING OF MAGNETIC ANISOTROPY.....	180
7.4 SUMMARY AND CONCLUSIONS	184

8 VOLTAGE CONTROL OF ELECTRICAL RESISTANCE	185
8.1 EXPERIMENTAL METHODS.....	187
8.2 VOLTAGE CONTROL OF VERTICAL RESISTANCE.....	189
8.3 VOLTAGE CONTROL OF LATERAL RESISTANCE IN NANOWIRE DEVICES	196
8.4 SUMMARY AND CONCLUSION	200
9 SUMMARY AND OUTLOOK	201
9.1 SUMMARY.....	201
9.2 OUTLOOK	206
9.2.1 <i>A Magnetic Window into Memristive Switching</i>	206
9.2.2 <i>Nanosecond Magneto-Ionic Switching</i>	207
9.2.3 <i>Voltage Programmable Materials: Beyond Magnetism and Memristors</i>	208
10 REFERENCES.....	211

LIST OF FIGURES

FIGURE 2-1: SPIN REORIENTATION TRANSITION IN Co/Pt MULTILAYERS.	33
FIGURE 2-2: PERPENDICULAR MAGNETIC ANISOTROPY IN Co/AlOx FILMS.	37
FIGURE 2-3: MAGNETIC HYSTERESIS LOOPS: STONER WOHLFARTH MODEL VERSUS REALITY	40
FIGURE 2-4: NÉEL AND BLOCH DOMAIN WALLS.....	43
FIGURE 2-5: DOMAIN WALL PINNING SITES ARISING FROM LOCAL ANISOTROPY MODIFICATIONS.....	46
FIGURE 2-6: REGIMES OF DOMAIN WALL MOTION.....	47
FIGURE 2-7: MAGNETO-ELECTRIC CONTROL OF MAGNETIC PROPERTIES.	51
FIGURE 2-8: MAGNETO-ELECTRIC COUPLING AT FERROMAGNETIC METAL/DIELECTRIC INTERFACE.	52
FIGURE 2-9: ELECTRIC FIELD EFFECTS IN Fe/MGO FROM FIRST PRINCIPLES.	53
FIGURE 2-10: ELECTRIC FIELD EFFECTS ON THE BAND STRUCTURE OF Fe.	55
FIGURE 2-11: MEMRISTIVE SWITCHING IN METAL/OXIDE/METAL MEMRISTOR.....	59
FIGURE 2-12: DRIVING FORCES FOR OXYGEN MIGRATION IN METAL/OXIDE/METAL MEMRISTORS.....	60
FIGURE 2-13: ELECTROFORMING IN Pt/TiO ₂ /Pt MEMRISTORS.	62
FIGURE 2-14: OXYGEN GAS EVOLUTION DURING ELECTROFORMING OF Pt/TiO ₂ /Pt MEMRISTORS.	63
FIGURE 2-15: COMPARISON BETWEEN MEMRISTIVE AND MAGNETO-ELECTRIC DEVICES.....	65
FIGURE 2-16: VOLTAGE EFFECTS ON THE SPIN REORIENTATION TRANSITION.	68
FIGURE 2-17: DEVICE CAPACITANCE AND MAGNETIC ANISOTROPY.....	70
FIGURE 3-1: INTERIOR OF THE HIGH-VACUUM MAGNETRON SPUTTER SYSTEM.	75
FIGURE 3-2: SHADOW MASK FABRICATION.....	78
FIGURE 3-3: SHADOW MASK POSITIONER FOR SINGLE CRYSTAL METAL SUBSTRATES.....	79
FIGURE 3-4: SHADOW MASK LITHOGRAPHY.....	81
FIGURE 3-5: ELECTRON BEAM LITHOGRAPHY AND LIFT-OFF.....	82
FIGURE 3-6: PROCEDURE TO CONTACT THE BOTTOM ELECTRODE IN THIN FILM CAPACITORS.....	85

FIGURE 3-7: IMPROVED PROCEDURE TO CONTACT THE BOTTOM ELECTRODE IN THIN FILM CAPACITORS....	87
FIGURE 3-8: THE MAGNETO-OPTIC KERR EFFECT.....	90
FIGURE 3-9: SCANNING MAGNETO-OPTIC KERR EFFECT SYSTEM.....	92
FIGURE 3-10: SCANNING MOKE MAP.....	94
FIGURE 3-11: DOMAIN WALL VELOCITY MEASUREMENTS IN MAGNETIC THIN FILMS.	96
FIGURE 3-12: TIME AND SPACE RESOLVED MAGNETIZATION MAPS.....	97
FIGURE 3-13: LOCAL PROBING OF MAGNETIC ANISOTROPY BY POLAR MOKE.....	99
FIGURE 4-1: DOMAIN WALL PROPAGATION FIELD MEASUREMENTS.	106
FIGURE 4-2: VOLTAGE DEPENDENCE OF SWITCHING FIELD.	108
FIGURE 4-3: DOMAIN WALL VELOCITY MEASUREMENTS.....	110
FIGURE 4-4: DOMAIN EXPANSION UNDER BIAS VOLTAGE.....	112
FIGURE 4-5: TEMPERATURE, FIELD AND VOLTAGE DEPENDENCE OF DOMAIN WALL VELOCITY.....	113
FIGURE 4-6: EFFICIENCY OF VOLTAGE CONTROL OF DOMAIN WALL MOTION.....	115
FIGURE 5-1: DIFFERENT REGIMES OF VOLTAGE MODIFICATION OF MAGNETIC PROPERTIES.....	124
FIGURE 5-2: NONVOLATILE SWITCHING OF THE MAGNETIC STATE.....	125
FIGURE 5-3: ANISOTROPY MODIFICATION AND PHYSICAL ELECTRODE DEGRADATION AT HIGH VOLTAGE..	128
FIGURE 5-4: EXPERIMENT SCHEMATICS AND MAGNETIC HYSTERESIS LOOPS.....	132
FIGURE 5-5: DOMAIN WALL PROPAGATION.....	133
FIGURE 5-6: SPACE AND TIME RESOLVED DOMAIN EXPANSION.	135
FIGURE 5-7: DOMAIN WALL VELOCITY INSIDE AND OUTSIDE OF ELECTRODE.....	136
FIGURE 5-8: NANOWIRE CONDUIT WITH INTEGRATED DOMAIN WALL TRAP.....	138
FIGURE 5-9: CONTROL OF DOMAIN WALL PROPAGATION IN MAGNETIC NANOWIRE CONDUITS.....	139
FIGURE 5-10: PROPERTIES OF DOMAIN WALL TRAPS IN NANOWIRE CONDUITS.....	140
FIGURE 5-11: TRAPPING HIGH VELOCITY DOMAIN WALLS.....	141

FIGURE 5-12: DOMAIN WALL TRAP BASED 3-BIT REGISTER.....	143
FIGURE 6-1 VIBRATING SAMPLE MAGNETOMETRY.....	149
FIGURE 6-2: CROSS-SECTIONAL TEM AND EELS ANALYSIS.....	153
FIGURE 6-3: DEVICE SCHEMATICS AND VOLTAGE CONTROL OF MAGNETIC ANISOTROPY.....	155
FIGURE 6-4: LACK OF ANNEALING AT 100 °C.....	156
FIGURE 6-5: VOLTAGE-INDUCED PROPAGATION OF OXIDATION FRONT.....	159
FIGURE 6-6: ANISOTROPY TRANSITION IN Pt/Co/Gd/GdOx FILMS.....	160
FIGURE 6-7: NONMONOTONIC VOLTAGE RESPONSE OF MAGNETIC ANISOTROPY.....	162
FIGURE 6-8: VOLTAGE RESPONSE AT CENTER AND EDGE OF AU ELECTRODES.....	165
FIGURE 6-9: LASER-DEFINED DOMAIN WALL NUCLEATION SITE.....	167
FIGURE 6-10: EFFECTS OF COMBINED GATE VOLTAGE AND LASER ILLUMINATION.....	168
FIGURE 6-11: EFFECTS OF VOLTAGE AND LASER ILLUMINATION ON MAGNETIC ANISOTROPY.....	169
FIGURE 6-12: LASER-DEFINED ANISOTROPY PATTERNS AND DOMAIN WALL CONDUITS.....	171
FIGURE 7-1: IMAGING SHADOW MASKED AU ELECTRODES.....	176
FIGURE 7-2: EFFECT OF ELECTRODE POROSITY ON MAGNETIC PROPERTIES.....	178
FIGURE 7-3: ANISOTROPY SWITCHING VIA SHORT VOLTAGE PULSES AT ELEVATED TEMPERATURE.....	180
FIGURE 7-4: FAST ANISOTROPY SWITCHING BY ENGINEERING ELECTRODE AND OXIDE.....	182
FIGURE 8-1: ELECTRICAL CHARACTERIZATION OF VIRGIN DEVICE STATE.....	190
FIGURE 8-2: ELECTROFORMING VIA CONSTANT CURRENT STRESS.....	191
FIGURE 8-3: MEMRISTIVE SWITCHING IN Pt/Co/GdOx/Gd/AU DEVICES.....	192
FIGURE 8-4: SCHEMATICS OF MEMRISTIVE SWITCHING MECHANISM.....	194
FIGURE 8-5: LATERAL RESISTIVE SWITCHING IN NANOWIRE DEVICES.....	197
FIGURE 8-6: LATERAL RESISTIVE SWITCHING AND MAGNETIC PROPERTY MODIFICATIONS.....	198

FIGURE 9-1: ILLUSTRATION OF SOLID-STATE SWITCHING OF INTERFACE OXYGEN CHEMISTRY FOR VOLTAGE CONTROL OF MATERIAL PROPERTIES202

FIGURE 9-2: VOLTAGE CONTROL OF MATERIAL PROPERTIES.....205

FIGURE 9-3: MATERIAL PROPERTIES GOVERNED BY METAL/METAL-OXIDE INTERFACES.....209

LIST OF FREQUENTLY USED ABBREVIATIONS AND ACRONYMS

AFM	Atomic force microscopy
BD	Dielectric breakdown
BE	Bottom electrode
BeCu	Beryllium Copper
CCS	Constant current stress
DW	Domain wall
EELS	Electron energy loss spectroscopy
FM	Ferromagnetic
GdO _x	Gadolinium oxide
HRTEM	High resolution transmission electron microscopy
MAE	Magnetic anisotropy energy
ML	Monolayer
MOKE	Magneto-optic Kerr effect
MTJ	Magnetic tunnel junction
NM	Nonmagnetic
PEEK	Polyether ether ketone
PMA	Perpendicular magnetic anisotropy
PMMA	Poly(methyl methacrylate)
RT	Room temperature
SRT	Spin reorientation transition
STEM	Scanning transmission electron microscopy
TEM	Transmission electron microscopy
TMR	Tunneling magneto resistance
UHV	Ultra-high vacuum
VSM	Vibrating sample magnetometry

LIST OF FREQUENTLY USED SYMBOLS

ϵ_0	Permittivity of free space
ϵ_r	Dielectric constant
A	Exchange stiffness
C	Capacitance
D	Diffusion constant
d_{Co}	Thickness of Co film
d_{Fe}	Thickness of Fe film
d_{Gd}	Thickness of Gd film
d_{GdOx}	Thickness of gadolinium oxide film
d_{SRT}	Spin reorientation transition thickness
\mathcal{E}	Electric field
E_a	Activation energy
E_F	Fermi level
F	Electrode area
H	Magnetic field
H_c	Coercive field
H_{crit}	Characteristic domain wall depinning field
H_x	Magnetic field in film plane
H_z	Magnetic field perpendicular to film plane
I	Leakage current
I_L	Laterally flowing electrical current
I_V	Vertically flowing electrical current
J	Kerr intensity
k	Boltzmann constant
K_s	Surface magnetic anisotropy constant
K_u	Uniaxial magnetic anisotropy constant
M	Magnetization

M_r	Remanence
M_r/M_s	Remanence to saturation magnetization ratio
M_s	Saturation magnetization
M_z	Magnetization component perpendicular to film plane
P	Optical power of MOKE laser
R_L	Lateral electrical resistance
R_V	Vertical electrical resistance
s	Distance between MOKE laser probe and artificial nucleation site
t	Time
T	Temperature
$t_{1/2}$	Mean magnetization reversal time
v	Domain wall velocity
v_{drift}	Ionic drift velocity
V_g	Gate voltage
α	Magneto-electric Coefficient
ε_{el}	Domain wall elastic energy density
ε_{el}	Domain wall elastic energy density
Φ'	Kerr rotation
Φ''	Kerr ellipticity
δ	Domain wall width

1 INTRODUCTION

One of the basic tenants of materials science is that the properties of materials are defined during synthesis and processing and cannot be altered once they have been put into use.

But what if that wasn't the whole story? What if the properties of materials could be altered at any time? What if they could be modified dynamically to adapt to environmental changes, to new applications or simply to our needs?

And what if that wouldn't require anything more than a line of code? In a nutshell that is my vision of voltage programmable materials.

1.1 Voltage Programmable Materials

The physical and chemical properties of nanoscale materials derive largely from structure and composition at interfaces. The possibility to electrically modify these interfacial characteristics would provide a powerful means to control material properties dynamically. Of particular recent scientific and technological interest are metal/metal-oxide bilayers,¹⁻¹⁵ in which properties as varied as catalytic activity,^{1,2} charge and spin transport,³⁻⁶ ionic exchange,^{12,13} mechanical behavior,^{14,15} thermal conductivity^{10,11} and magnetism⁶⁻⁹ all depend sensitively on oxygen stoichiometry and defect structure at the metal/metal-oxide interface. Voltage-induced ion transport and electrochemical interface reactions could provide the necessary means to effectively control interface structure and composition and make the rich chemical, electronic, and magnetic properties that emerge at the metal/metal-oxide interface amenable to solid-state electrical control.

At the macroscale, electric-field-driven ion transport has long been exploited in a wide range of electrochemical devices, from oxygen gas sensors^{16,17} to solid oxide fuel cells^{18,19}. At the nanoscale, voltage-induced O²⁻ migration has been demonstrated as a mechanism for resistive switching in anionic metal/oxide/metal memristors^{3,4}. However, the much broader application of voltage-driven oxygen transport to control interfacial properties and phenomena in metal/metal-oxide structures is only beginning to be explored.

For example, ferromagnetic metal/metal-oxide bilayers such as Co/AlO_x and CoFe/MgO exhibit strong perpendicular magnetic anisotropy derived from interfacial oxygen hybridization.^{8,9,20} These material systems and their magnetic properties are of crucial importance in the field of spintronics,^{6,21,22} which aims to exploit the electron charge and spin degree of freedom for novel, ultra-low power device application.²³⁻²⁶ One of the most promising spintronic devices is the magnetic tunnel junction, which is the fundamental building block of magnetic random access memory (MRAM), a promising candidate for next generation nonvolatile memory.^{27,28} Like many other spintronic devices, the power consumption in magnetic tunnel junctions is largely determined by the energy

required to switch the magnetization state.²⁷ Much work has focused on using spin-polarized electric currents to switch the magnetization via spin-transfer torques.^{29,30} While significantly more efficient than conventional magnetic fields, this mechanism remains dissipative and often requires inhibitive high current densities.

The ability to toggle magnetic anisotropy with a gate voltage would dramatically reduce switching energies of spintronic devices, and could enable new device architectures exploiting local gating of magnetic properties.^{23,26,31-35} Voltage-gated control of magnetic anisotropy is most often achieved by using complex materials such as multiferroic oxides,^{33,34} magnetic semiconductors,³⁵⁻³⁸ or strain-coupled magnetostrictive/piezoelectric composites.^{33,34,39} However, these materials are often limited to low operating temperature and pose challenges to integration with semiconductor processing technology.

Only recently it has been shown that in ferromagnetic metal/metal-oxide bilayers interface anisotropy can be modulated by a gate voltage at room temperature and using materials which are amenable to semiconductor processing.^{31,41-43} This anisotropy modification has been attributed to voltage-induced charge accumulation and band shifting in the ferromagnetic metal layer, which can alter its magnetic properties.⁴⁴⁻⁴⁶ Unfortunately, in metals the charge density can be varied only slightly, which fundamentally limits the achievable changes in magnetic anisotropy energy.

Here we introduce an entirely different approach to voltage control of magnetic anisotropy that occurs at room temperature in similar metal/metal-oxide bilayers, but which produces orders of magnitude larger effects. Since perpendicular magnetic anisotropy in ferromagnetic metal/metal-oxide bilayers derives from interfacial oxygen hybridization,^{20,47} we propose that by using a gate oxide with high oxygen mobility, one can electrically displace O^{2-} at the interface and thereby not only tune the anisotropy, but remove and reintroduce its very source. Based on this idea, we report on direct *in situ* observation of voltage-driven O^{2-} migration in metal/metal-oxide bilayers at room temperature, and show that solid-state electro-chemical switching of the interfacial

oxidation state can indeed be used to generate unprecedentedly strong modifications of perpendicular magnetic anisotropy in thin ferromagnetic metal films.

Moreover, through local activation of ionic migration, we introduce a general method to reversibly imprint material properties, which we use to locally pattern magnetic anisotropy and create domain wall conduits in continuous magnetic films. Since the magneto-ionic coupling effect does not rely on maintaining an electrical charge, these voltage-induced changes to magnetic properties persist at zero bias, enabling nonvolatile switching and state retention in the power-off state. These results establish magneto-ionic coupling as a powerful mechanism for voltage control of magnetism.

Finally, based on this new magneto-ionic coupling effect we generate unprecedentedly-strong voltage-controlled domain wall traps that function as nonvolatile, electrically programmable and switchable pinning sites. By integrating these domain wall traps into magnetic nanowire devices we demonstrate a prototype nonvolatile memory device in which voltage-controlled domain wall traps facilitate electrical bit selection in a magnetic nanowire register.

Although this work largely focuses on magnetic properties, we also report on voltage-induced modifications of electronic transport properties in the same bilayer structures, demonstrating that reversible voltage-gated control of oxygen stoichiometry in metal/metal-oxide bilayers can make a wide range of materials properties amenable to solid-state electrical control. These results thus provide a path towards voltage-programmable materials based on solid-state switching of interface oxygen chemistry.

1.2 Thesis Outline

The future of ultra-low power electronics, multifunctional devices, and intelligent materials, hinges on the availability of energy efficient means to electrically control material properties at the nanoscale. Since physical and chemical properties of nanoscale materials derive largely from structure and composition at interfaces, the aim of this thesis is to demonstrate that voltage-gated control of interfacial oxygen stoichiometry makes the wide range of material properties that emerge at metal/metal-oxide interfaces amenable to solid-state electrical control. In the following chapters we demonstrate the efficacy of this ionic effect by voltage-gating magnetic and electrical properties at ferromagnetic metal/metal-oxide interfaces and show that solid-state switching of interface oxygen chemistry indeed provides a path towards programming material properties at the nanoscale.

This thesis is separated into several chapters. Chapter 1 provides a short introduction to voltage programmable materials and motivates the research presented in this thesis.

Chapter 2, lays the theoretical foundation and provides an overview of the major physical concepts required to understand the results discussed in this thesis. Specifically, it covers voltage-induced effects in metal/oxide/metal devices and their impact on material properties. Based on this information, Chapter 2 also describes an initial experiment on voltage control of magnetic properties whose unexpected results motivated the majority of the work presented in the following chapters.

Chapter 3 reviews the main experimental methods employed in this thesis. It provides an overview of the fabrication techniques used to prepare the ferromagnetic metal/metal-oxide bilayers and describes the characterization techniques utilized to analyze their magnetic properties. The chapter also introduces the Pt/Co/gadolinium oxide material system, which is used in the majority of the experiments presented here.

In Chapters 4 and 5 we investigate voltage-induced effects on the magnetic properties of Pt/Co/gadolinium oxide films and identify two distinct regimes. At low voltage, the

effects are relatively weak and directly follow the gate voltage, consistent with electric-field-induced charge accumulation in the ferromagnetic layer. At high voltage, however, much stronger and nonvolatile voltage effects are observed. In Chapter 4, we characterize the low voltage regime and demonstrate for the first time, electric field control of domain wall motion in a ferromagnetic metal film. A thorough investigation of this effect, however, reveals that it is suitable to control only domain wall motion in the relatively slow, thermally activated regime.

In order to effectively control domain walls moving at device relevant velocities, larger voltage effects are required. Thus, in Chapter 5, we study the high voltage regime in more detail and based on our results propose the concept of magneto-ionics, a new magneto-electric coupling mechanism that relies on voltage driven oxygen migration to modulate the interfacial chemistry that determines magnetic properties. By optimizing device geometry for more efficient ion transport, we extend to lower voltages the regime corresponding to strong nonvolatile anisotropy modifications, allowing us to create unprecedentedly strong voltage-controlled domain wall traps that are nonvolatile, programmable, and switchable. These domain wall traps allow efficient control over domain walls moving at device relevant velocities. We exploit this to demonstrate a prototype nonvolatile memory device in which domain wall traps facilitate bit selection in a nanowire register

In Chapter 6, the fundamental origin of the magneto-ionic effect is verified experimentally. We observe for the first time *in situ* voltage-driven O^{2-} migration in a Co/metal-oxide bilayer at room temperature, and show that electrical switching of the interfacial oxidation state allows for voltage control of magnetic properties to an extent never before achieved through conventional magneto-electric coupling mechanisms. We also introduce a general method to reversibly imprint material properties through local activation of ionic migration, which we use to locally pattern magnetic anisotropy and create domain wall conduits in continuous magnetic films.

Chapter 7 takes the concept of magneto-ionics a significant step further and shows that the timescale of magneto-ionic switching can be improved by 6 orders of magnitude by employing design principles that are already well-established in solid-state ionics and memristive switching devices. This allows us to demonstrate magneto-ionic control of magnetic anisotropy at the microsecond timescale.

Chapter 8 shows that voltage-gated control of oxygen stoichiometry does not only allow control over the magnetic properties but can also be used to switch the vertical and lateral electrical resistance in ferromagnetic-metal/metal-oxide bilayers. These results demonstrate the broad applicability of solid-state switching of interface oxygen chemistry to control material properties.

Chapter 9 summarizes the results presented in this thesis and provides a short outlook on future experiments and potential applications of voltage programmable materials.

2 BACKGROUND

The aim of this chapter is to provide an overview of the major physical concepts relevant to the results presented in this thesis. Section 2.1 describes the origin of magnetic anisotropy in magnetic thin films. In particular, the emergence of perpendicular magnetic anisotropy at metal/metal and metal/oxide interfaces will be discussed. Based on the Stoner Wohlfarth model, Section 2.2 explains the origin of magnetic hysteresis and its dependence on magnetic anisotropy. While the Stoner Wohlfarth model provides a qualitative description of magnetic hysteresis loops, it does not account for domain nucleation and growth, which dominates magnetization reversal in the films studied here. Thus, in Section 2.3, thermally activated domain wall motion and particularly its dependence on magnetic anisotropy are discussed. Section 2.4 describes the current understanding of the magneto-electric effect in metal ferromagnets. It is argued that in ferromagnetic metal/oxide/metal devices, voltage modification of electron density allows control over interfacial anisotropy. Very similar metal/oxide/metal devices are used in nanoionics and memristive switching, which is why Section 2.5 gives an introduction to memristors and the voltage-driven processes occurring in them. Finally in Section 2.6, we describe a first experiment on voltage control of magnetic anisotropy whose unexpected results represented the starting point for the work presented in this thesis.

2.1 Perpendicular Magnetic Anisotropy

Material properties are said to be anisotropic if they exhibit directional dependence. In many magnetic materials, the energy required to magnetize the material depends on the direction in which the magnetic field is applied.⁴⁸ This behavior is referred to as magnetic anisotropy and manifests itself in a preference of the magnetization vector to align with the minimum energy axis, the so called easy magnetization axis. Magnetic anisotropy is one of the most important properties of magnetic materials. It determines the shape of magnetic hysteresis loops (Section 2.2), affects magnetic domain wall motion (Section 2.3), and is exploited in nearly all applications of magnetic materials.⁴⁹ There are several techniques available to characterize magnetic anisotropy; in this work we rely on the magneto-optic Kerr effect (Section 3.2.4) and vibrating sample magnetometry (Section 3.2.5) to quantify the anisotropy strength. Depending on the type of application, materials with low or high anisotropy are required, and the ability to precisely engineer and dynamically control magnetic anisotropy (Section 2.4) could open entirely new applications for magnetic materials.

Here, we focus our discussion on thin films of transition metal ferromagnets, which are of great technological interest, particularly for information storage applications. Magnetic anisotropy in thin films is markedly different from bulk materials. Not only can the strength of magnetic anisotropy vary greatly, but also the orientation of the easy magnetization axis can change.⁴⁹ This difference originates from the presence of symmetry breaking elements such as the planar surfaces and interfaces characteristic of thin film and multilayer geometries.⁴⁹ Due to the sensitivity to surfaces and interfaces, magnetic anisotropy in thin films can be tuned by changing film thicknesses and interface materials.⁴⁹ The most astonishing manifestation of this effect is perpendicular magnetic anisotropy (PMA), which refers to the change of easy magnetization axis from the typical orientation in the film plane to perpendicular to the film plane. The existence of such interface anisotropies was first predicted by Néel in 1954⁵⁰ and later confirmed experimentally in thin films⁵¹ and Co/Pt⁵² and Co/Pd⁵³ multilayers with (111) crystal orientation. The studies showed an

easy axis perpendicular to the film plane with an anisotropy strength proportional to the inverse film thickness. These results can be phenomenologically described by separating the magnetic anisotropy K_u into a volume K_V and interface contribution K_S that approximately follows the relation:^{50,51}

$$K_u = K_V + K_S/d \quad (2.1)$$

This expression is nothing but the weighted average of the magnetic anisotropy energy (MAE) stemming from the interface and the volume of a magnetic thin film of thickness d .⁴⁹ Here, we use the convention that positive K_u corresponds to an easy axis perpendicular to the film plane and K_S corresponds to the combined effect of the top and bottom interface of the film.

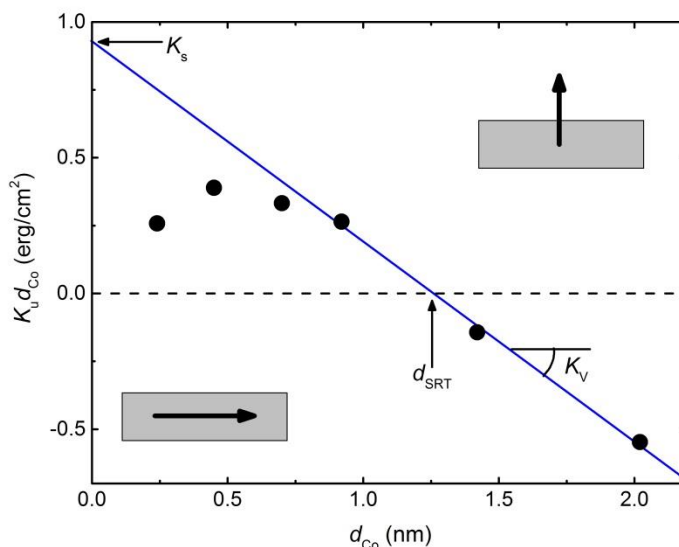


Figure 2-1: Spin reorientation transition in Co/Pt multilayers. Plot of magnetic anisotropy energy K_u times the Co film thickness d_{Co} as a function of d_{Co} . The blue line is a fit with the model described in Equation (2.1). The intercept with the vertical axis gives the interface anisotropy K_S whereas the slope yields the volume anisotropy K_V . The deviation from the model at low d_{Co} is a result of discontinuity in the Co film. The insets indicate that perpendicular magnetization is favored for positive $K_u d_{Co}$ where in-plane magnetization is preferred for negative $K_u d_{Co}$. Data taken from Reference [54].

As we will discuss in detail below, K_v typically prefers an orientation of the magnetization vector in the film plane and is therefore negative. If at the same time K_s is positive, then the system undergoes a so called spin reorientation transition. That is; below a certain film thickness d_{SRT} , the interface contribution dominates over the volume contribution to the MAE and the easy axis reorients from in-plane to perpendicular to the film plane. The values of K_v , K_s and the transition thickness d_{SRT} can then be obtained from a plot of $K_v d$ versus d , which is shown schematically in Figure 2-1.⁴⁹ In very thin films of only a few atomic layers, the assumption that magnetic anisotropy can be separated into surface and volume contributions, becomes questionable.⁵⁵ But even in this case the phenomenological model works surprisingly well, which is why it has become such an invaluable tool to evaluate and engineer magnetic anisotropy in thin films and multilayers.

So far our discussion focused on a phenomenological description of PMA, leaving open the question of its microscopic origin. At the microscopic level, the two main effects that give rise to magnetic anisotropy are dipolar and spin-orbit interaction.⁴⁹

With its long range, dipolar interaction can sense the boundaries of the sample and its contribution to magnetic anisotropy typically depends on the shape of the sample.⁴⁹ In the absence of strain, this so called shape anisotropy is the main contribution to K_v in Equation (2.1) and largely responsible for the preference for in-plane magnetization commonly observed in magnetic thin films. Using a continuum approach, the shape effect resulting from dipolar interaction can be described by introducing the demagnetization field H_d . In an ellipsoidal ferromagnetic sample, the demagnetization field is given by $\vec{H}_d = -N_d \vec{M}$, where \vec{M} is the magnetization vector, and N_d is the shape-dependent demagnetization tensor.⁴⁹ An ideal thin film extends infinitely in two dimensions but is constrained in the third dimension. Therefore, with the exception of the direction perpendicular to the film plane, all elements of the demagnetization tensor are zero.⁴⁹ The magnetostatic energy resulting from the demagnetization field can then result in an anisotropy energy per unit volume of the film of:^{49,56}

$$E_d = -\frac{1}{8\pi V} \int \vec{M} \vec{H}_d dv = 2\pi M_s^2 \cos^2 \theta \quad (2.2)$$

Here, θ is the angle between \vec{M} and the film normal, M_s is the saturation magnetization, dv is a volume element and the integration extends over all space. As expected, E_d is at a minimum when the magnetization is in the film plane, which gives rise to the negative slope in Figure 2-1 and explains the preference for in-plane magnetization commonly observed in magnetic thin films.

While the dipolar interaction gives rise to shape anisotropy, the spin-orbit interaction is largely responsible for the so called magnetocrystalline anisotropy.⁴⁹ In a magnetic material, spin-orbit interaction describes the coupling between the spin and orbital moments of each electron. Since the orbital moments are strongly coupled to the crystal lattice, spin-orbit interaction effectively results in a coupling between the spin and the crystal lattice. As a result, the total energy of the magnetic system depends on the orientation of the magnetization vector with respect to the crystal axes. This directional dependence is referred to as magnetocrystalline anisotropy.⁴⁹

In the bulk of cubic transition metal ferromagnets, the orbital moments are almost entirely quenched, which results in a very weak magnetocrystalline anisotropy.⁵⁷ At interfaces of thin films however, the reduced symmetry can strongly modify the magnetocrystalline anisotropy and yield a much stronger so called interface anisotropy.⁵⁰ This interface anisotropy was first predicted by Néel⁵⁰ and is largely responsible for K_s in Equation (2.1). Although Néel's pair interaction model contributed tremendously to the understanding of magnetic anisotropy in thin films, it is fundamentally incorrect, often predicts the wrong sign for K_s , and does not consider the interfacing material.⁴⁹

In order to get a quantitative and complete description of interface anisotropy, it is necessary to perform *ab-initio* band structure calculations that include spin-orbit interaction.^{58,59} Unfortunately, these calculations are often complex and not very intuitive.

However, considering their key results and functional dependencies can illuminate which factors give rise to strong interface anisotropy and result in PMA.

Band structure calculations show that interface anisotropy is very sensitive to the details of the electronic band structure near the Fermi surface and particularly the band filling of crystal field split d -bands in the vicinity of the Fermi level.⁵⁸⁻⁶⁰ Partial occupation of the split bands gives rise to a net orbital moment, which is larger perpendicular to the film plane than in the film plane.⁵⁸⁻⁶⁰ Due to this anisotropy in the orbital moment, spin-orbit coupling results in an interface anisotropy that prefers perpendicular magnetization. This interface anisotropy is at a maximum when the Fermi level is right in between the two split bands, such that they are half filled.⁵⁹ Changing the relative position of the Fermi level and the split bands can alter the anisotropy dramatically.⁵⁸ The degree of band splitting and the position of the split $3d$ -bands are determined by the crystal field, which arises from symmetry breaking and hybridization at the film interface.⁵⁸⁻⁶¹ Whereas the position of the Fermi level depends on the filling of the valence band, which is determined by the ferromagnetic material and interface hybridization.^{58-60,62}

In Co thin films and Co/metal bilayers with (111) crystal orientation, it was shown that the sign and strength of the interface anisotropy can be controlled by tuning the filling of the Co valence band.^{58,59} One way to control the band filling is hybridization between the Co $3d$ -orbitals and the orbitals of an adjacent nonmagnetic metal layer, such as Pd, Pt, Cu, Au or Ag.^{60,62} Strong interface anisotropy favoring perpendicular magnetization has been observed for Co/Pt, Co/Pd, and Co/Au. In the Co/Pt case it was shown that this is due to hybridization between Co $3d$ and Pt $5d$ orbitals.⁶⁰⁻⁶² The role of the adjacent metal layer however goes beyond controlling band filling, the large spin-orbit interaction in Pt, Pd and Au also provides the strong coupling between the spin and orbital moments that drives PMA.^{59,61}

In addition to the well-known Co(Fe)/metal systems, strong PMA has recently been observed in Co(Fe)/metal-oxide films.^{63,64} The investigated metal-oxides include aluminum oxide (AlO_x), magnesium oxide (MgO) and tantalum oxide (TaO_x).^{47,64} In these

Co(Fe)/metal-oxide systems, hybridization between the Co 3d and oxygen 2p orbitals splits the Co *d*-bands and positions the Fermi level such that even the relatively weak spin-orbit interaction of O is sufficient to drive strong PMA.^{9,20,47}

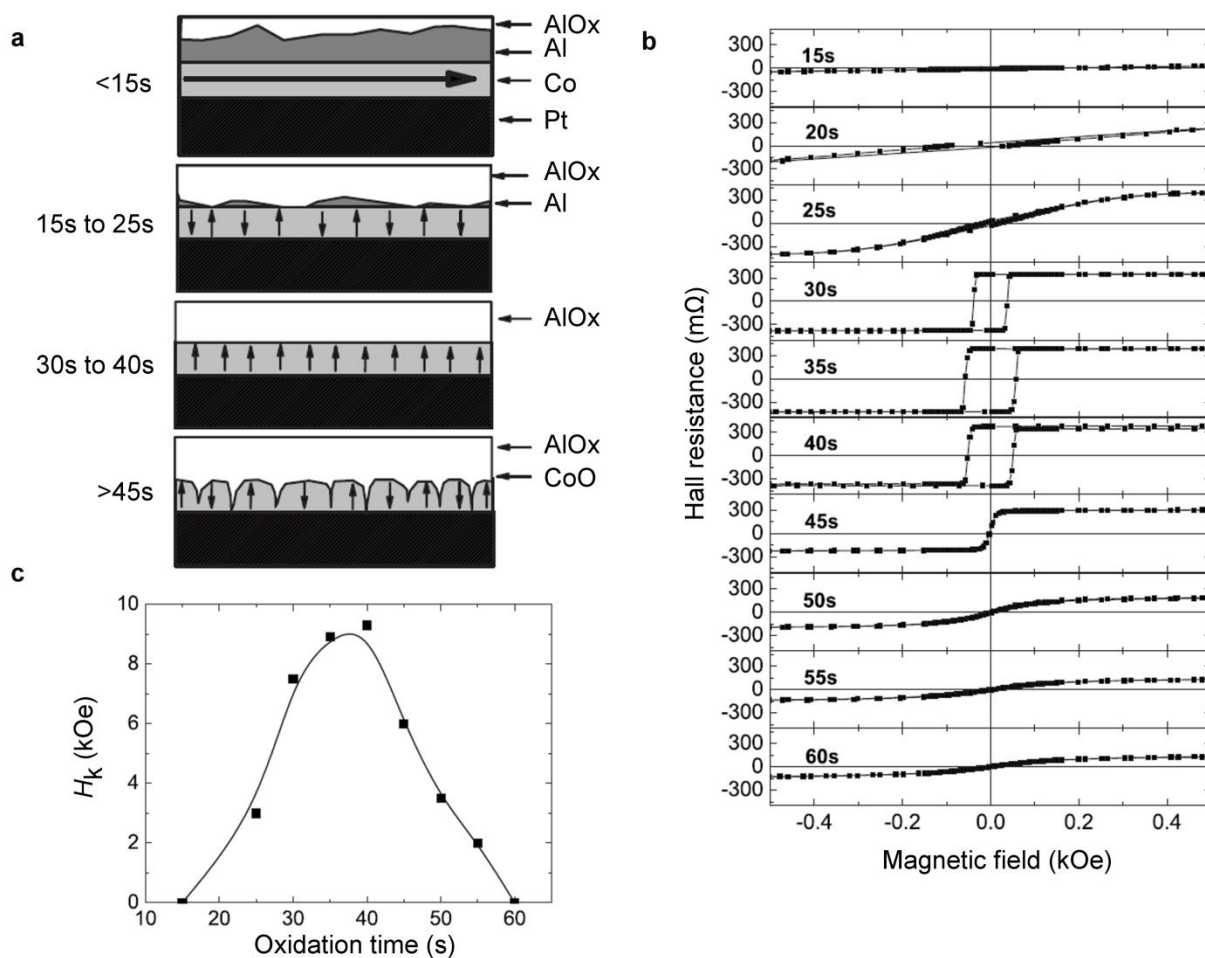


Figure 2-2: Perpendicular magnetic anisotropy in Co/AlOx films. (a) Schematics of the Pt/Co/Al structure, showing the influence of plasma oxidation on magnetic properties at various oxidation times. (b) Out-of-plane hysteresis loops measured for the same samples with increasing oxidation times. (c) Out-of-plane anisotropy field H_k measured via the extraordinary Hall effect as a function of oxidation time. Reprinted with permission from Manchon, A. *et al.* Analysis of oxygen induced anisotropy crossover in Pt/Co/MOx trilayers. *J. Appl. Phys.* 104, 043914. Copyright 2008, AIP Publishing LLC.

Manchon *et al.*^{8,9,47} investigated the evolution of PMA in Co/AlOx as a function of the density of Co-O bonds at the interface (see Figure 2-2). They showed that the density of Co-

O bonds at the interface can be tuned experimentally by controlling the plasma oxidation time of Co/Al layers. The longer the oxidation time, the closer the oxidation front to the Co interface (Figure 2-2(a)) and the higher the density of Co-O bonds. For short oxidation times (see Figure 2-2(a-c)), only a fraction of the Al layer is oxidized and the interface is largely made up of Co-Al bonds. As a result, the Co film favors magnetization in the film plane. For intermediate oxidation times (see Figure 2-2(a-c)), the Al layer has been mostly oxidized and a significant number of O atoms has reached the Co interface. In this phase, the interface is mostly made up of Co-O bonds, the Co film favors perpendicular magnetization and PMA reaches its maximum. For longer oxidation times (see Figure 2-2(a-c)), the Co layer itself is oxidized and PMA weakens again. PMA in Co/metal-oxide layers is thus very sensitive to the oxidation state at the Co interface (Figure 2-2(c)). Consistent with recent *ab-initio* calculations for the Fe/MgO system,²⁰ strong PMA is only observed for the optimally oxidized interface and underoxidation or overoxidation weakens PMA dramatically.^{8,9,47} Control over the interface oxidation state thus provides a powerful means to control PMA in ferromagnetic metal thin films.

From this discussion we can conclude that interfacial anisotropy, sufficiently strong to overcome the shape anisotropy, occurs only in the special case where the crystal field produces the correct band splitting and the Fermi level is positioned just right.⁶¹ The critical role of the crystal field and band filling provides a very intriguing means to engineer and control PMA and explains why it is only observed in a very limited number of material combinations.

2.2 Magnetic Hysteresis Loops

Magnetic hysteresis loops are sometimes referred to as the “universal currency” in magnetism.⁶⁵ Simply by studying the hysteresis loops of a material it is possible to determine a wide range of its magnetic properties. In a hysteresis loop, the magnetization M is measured along the direction of the applied field H , while the applied field is swept for a full magnetization reversal cycle. There exist a wide range of experimental techniques to acquire magnetic hysteresis loops, but in this thesis we rely on the magneto-optic Kerr effect (Section 3.2.1) and vibrating sample magnetometry (Section 3.2.5) to acquire hysteresis loops.

Due to magnetic anisotropy, the magnetic field required to magnetize a material depends on the direction in which the field is applied (see Section 2.1). The shape of magnetic hysteresis loops is therefore strongly dependent on magnetic anisotropy and varies greatly when the field is applied along different directions. In this thesis we focus on magnetic thin films with PMA. PMA is characterized by a single easy axis perpendicular to the film plane, which is why it is also referred to as uniaxial magnetic anisotropy. With the easy axis perpendicular to the film, the film plane itself is a hard plane, meaning that it is energetically least favorable to align the magnetization with the film plane. As we will see below, the strength of PMA can be derived from hysteresis loops measured along an axis in the hard plane, i.e., a hard axis.

The Stoner Wohlfarth model is the simplest model that is adequate to describe the magnetization of single domain ferromagnet.^{66,67} It correctly describes magnetic hysteresis and allows us to calculate the shape of magnetic hysteresis loops along different directions of the sample. The Stoner Wohlfarth model expresses the total energy of a magnetic system as the sum of the magnetostatic energy in the applied field (i.e., Zeeman energy) and the anisotropy energy.⁶⁷ The orientation of the magnetization vector at any given field is then derived by energy minimization, and the shape of the hysteresis loops can be calculated by determining the projection of this magnetization vector along the measurement direction.

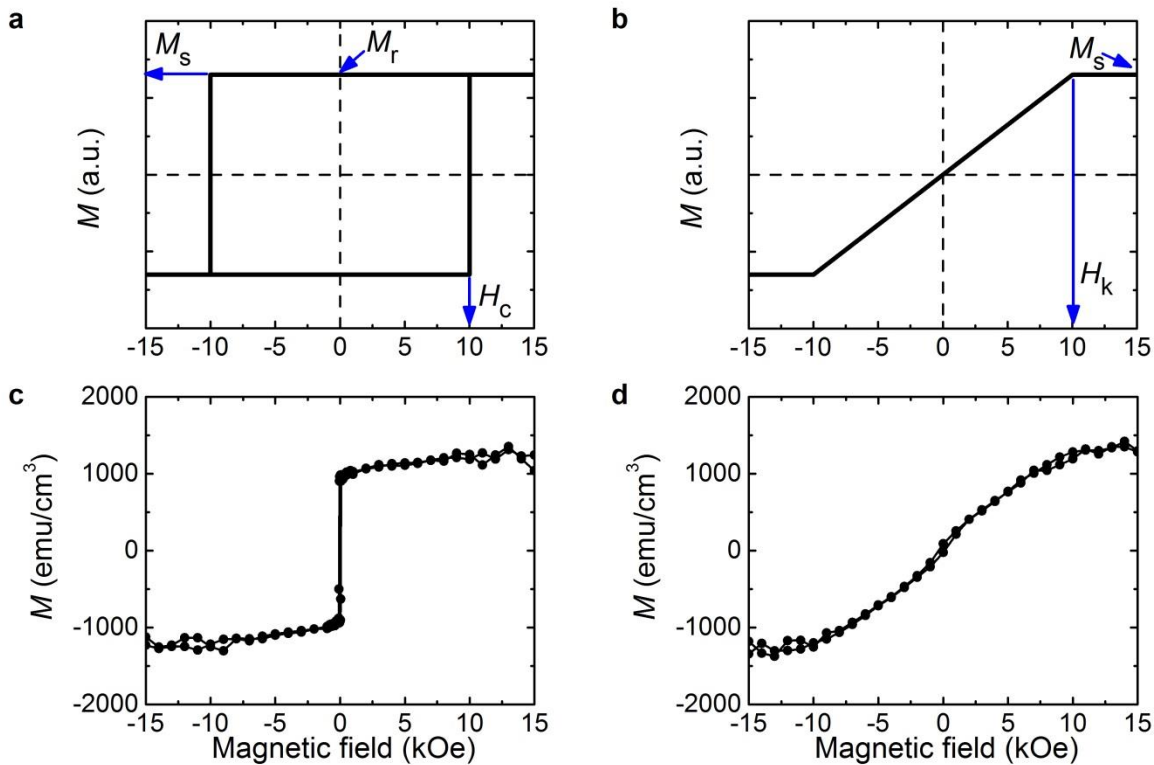


Figure 2-3: Magnetic hysteresis loops: Stoner Wohlfarth model versus reality (a) Easy and (b) hard axis hysteresis loop derived from Stoner Wohlfarth model assuming uniaxial magnetic anisotropy. The main characteristics of the hysteresis loop; the saturation magnetization M_s , the remanent magnetization M_r and the coercivity H_c are indicated. (c) Representative easy and (d) hard axis hysteresis loop measured on Pt/Co/gadolinium oxide films by vibrating sample magnetometry. Adapted with permission from Reference [68].

Figure 2-3 shows magnetic hysteresis loops derived from the Stoner Wohlfarth model for a sample with uniaxial magnetic anisotropy K_u . The main characteristics of hysteresis loops are the saturation magnetization M_s , the remanent magnetization M_r and the coercivity H_c . The coercivity H_c is given by the field at which the magnetization switches, i.e., passes through $M = 0$. M_s corresponds to the largest value of magnetization in a hysteresis loop which is achieved when the magnetization vector is fully aligned with the applied field. In contrast, M_r refers to the magnetization that remains when the field is reduced to zero and the remanent to saturation magnetization ratio M_r/M_s is then a measure of the squareness of the hysteresis loop.

Hysteresis loops measured along the easy axis (Figure 2-3(a)) exhibit a square shape, indicating that full saturation magnetization is retained even after the field is reduced to zero. Depending on the prior magnetization direction of the sample, there are two distinct magnetization states at zero field, and a field H_c is required to switch between the two states. This dependence on the magnetization history is called magnetic hysteresis and forms the basis of magnetic data storage, where the two magnetization states correspond to “bit 0” and “bit 1”.

The situation is very different for hysteresis loops measured at an angle to the easy axis. The further away from the easy axis, the smaller M_r/M_s and the opening of the hysteresis loops. Finally, hysteresis loops measured along the hard axis exhibit zero magnetization at zero field, and a field H_k , the so called saturation field, is required to fully saturate the magnetization (Figure 2-3(b)). H_k is directly related to the uniaxial anisotropy of the sample, which is why it is sometimes also referred to as the anisotropy field. According to the Stoner Wohlfarth model, $K_u = H_k M_s / 2$. Therefore, the uniaxial anisotropy K_u can be determined quantitatively by measuring a single hard axis hysteresis loop. Small deviations between the modeled (Figure 2-3(b)) and the measured (Figure 2-3(d)) hysteresis loops are likely due to spatial inhomogeneity and small misalignment with respect to the hard axis orientation.

The Stoner Wohlfarth model also predicts that the coercivity H_c of easy axis hysteresis loops is equivalent to H_k . However, in practice, this is rarely observed because macroscopic samples typically exhibit multiple domains and not just a single domain, as is assumed by the Stoner Wohlfarth model. As a result, magnetization reversal occurs by domain nucleation and expansion rather than by coherent rotation, and H_c is significantly smaller than H_k (compare Figure 2-3(a) and (b)). In the samples investigated in this thesis, H_k is typically 1000s of Oe but H_c is only a few 100 Oe. H_c can then be used as a tool to extract information about domain expansion in the thin film.

In summary, magnetic hysteresis loops are an invaluable tool to analyze the magnetic properties of magnetic materials. In Chapters 4 through 7 we make extensive use of

magnetic hysteresis loops to investigate magnetic anisotropy, saturation magnetization and domain nucleation and growth in magnetic thin films.

2.3 Thermally Activated Domain Wall Motion

In ferromagnetic materials, the magnetic moments align with each other even in the absence of an external magnetic field. However, not all moments have to be aligned in the same direction. In most cases, the ferromagnet is made up of a number of small regions. These regions are referred to as magnetic domains and within each magnetic domain, all the moments are aligned with each other and point in the same direction. But between different domains, no such alignment exists and the moments point in different directions. In thin films with strong PMA, the magnetization can either point into or out of the film plane, i.e., either up or down, such that adjacent domains are magnetized opposite to each other. This explains why most ferromagnetic specimens show little or no net magnetization in the absence of an external field. Within each domain, the magnetization is saturated, but since the magnetization differs from domain to domain, the overall net magnetization of the specimen is close to zero.⁵⁶

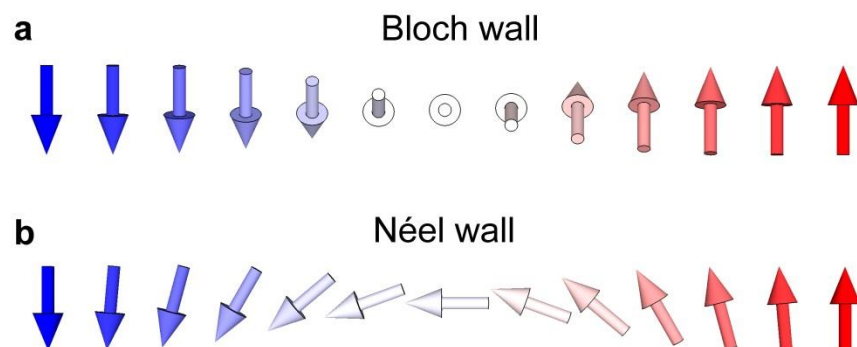


Figure 2-4: Néel and Bloch domain walls. Schematics of the configuration of magnetic moments in a (a) Bloch and (b) Néel domain wall.

The boundary between two adjacent domains is referred to as a magnetic domain wall (DW). DWs have a finite width within which the magnetic moments gradually rotate from the magnetization orientation of the first domain to the orientation of the second domain. Typically, magnetic domains prefer to align their magnetization with the easy axes of the sample. In a specimen with uniaxial anisotropy this means that domains are either

magnetized parallel or antiparallel to the easy axis and the magnetic moments in the DW rotate by 180 °. There are two types of 180 ° DWs; Bloch walls and Néel walls. In Bloch walls, the magnetic moments rotate in a plane parallel to the plane of the DW, whereas in Néel walls, the magnetic moments rotate in a plane perpendicular to the plane of the DW (Figure 2-4).

The formation of DWs in a ferromagnetic material costs energy. In a DW, the magnetic moments rotate gradually to accommodate the change in magnetization direction. Due to the gradual rotation, the moments are neither parallel to the easy axis nor are they aligned with each other, which results in an energy penalty from anisotropy energy and exchange interaction. The anisotropy energy favors narrow DWs in which the magnetic moments are closely aligned with the easy axis. In contrast, exchange interaction favors wide DWs with neighboring moments aligned nearly parallel to each other. The equilibrium width of a DW is then given by minimizing the total energy cost from anisotropy and exchange interaction. For a Bloch wall, the DW elastic energy density ε_{el} and the DW width δ are:⁵⁶

$$\varepsilon_{el} = 4\sqrt{AK_u}, \quad \delta = \pi\sqrt{A/K_u} \quad (2.3)$$

Here A is the exchange stiffness and K_u is the uniaxial magnetic anisotropy constant.

Since the formation of DWs is associated with an energy cost, the question is why most ferromagnetic specimens are in a multi domain state in the absence of an external field. The answer is that domain formation greatly reduces the demagnetization field and therefore the magnetostatic energy of the sample.⁶⁹ The demagnetization field originates from free magnetic moments at the sample surface. Replacing a single domain by multiple domains of opposite magnetization orientation can greatly reduce the overall demagnetization field. The number of domains in a ferromagnetic specimen is then governed by the balance between magnetostatic energy, originating from the demagnetization field, and the cost of introducing DWs.⁶⁹

In any given sample, the balance of anisotropy, exchange and magnetostatic energy determine the configuration of the DWs in the sample. In thin films with strong PMA, DWs

are very narrow and typically less than 10 nm wide.⁷⁰ In these samples, the Bloch configuration is generally favored,⁷¹ but it has recently been shown that in multilayers with asymmetric interfaces a new type of DW, that behaves like a Néel wall, can be stabilized by the Dzyaloshinskii-Moriya interaction.^{72,73}

When an external field is applied to a demagnetized ferromagnet, the domains which are favorably aligned with the external field grow at the expense of other domains. The domain growth occurs via DW motion. The external field results in a torque on the magnetic moments of the wall and drives the DW forward.²⁹ In most cases, the energy to move DWs through a ferromagnetic specimen is much lower than the energy required to macroscopically rotate the magnetization.⁶⁹ This explains why the actually observed coercivity is usually much lower than the one predicted by the Stoner Wohlfarth model (see Section 2.2).

The motion of a DW through a magnetic material is subject to a number of internal and external factors. In real samples, DWs do not move freely, defects such as surface roughness, grain boundaries, precipitates and inclusions result in spatial variations of the magnetic properties which pin the DWs at the corresponding local maxima and minima of the DW energy landscape.⁵⁶ Figure 2-5 shows two types of defects in a magnetic material that can inhibit DW motion. A local reduction in magnetic anisotropy can reduce the DW energy ε_{el} creating a well that traps the DW at the defect position. In contrast, a local increase in magnetic anisotropy, increases ε_{el} and acts as a barrier that prevents the DW from moving through the defect. For a Bloch wall in a magnetic thin film with strong PMA, the pinning field H_{pin} , resulting from a local anisotropy modification ΔK_u , is given by:⁷⁴

$$H_{pin} = \frac{\Delta K_u}{8\pi M_s} \frac{2\delta}{\lambda} \tanh\left(\frac{\lambda}{2\delta}\right) \quad (2.4)$$

Here, it is assumed that the change in magnetic anisotropy ΔK_u occurs over a length λ (see Figure 2-5). From Equation (2.4) it can be seen that H_{pin} does not only depend on the change in magnetic anisotropy, but also on the length scale over which this change occurs. The larger the gradient $\Delta K_u/\lambda$, the larger the pinning field. Moreover, if λ is much smaller

than the width of the DW δ , then H_{pin} is simply given by ΔK_u .⁷⁴ However, if λ is much larger than the DW width δ , then the pinning field goes to zero.⁷⁴

$$\lim_{\lambda \rightarrow 0} H_{pin} = \frac{\Delta K_u}{8\pi M_s}; \quad \lim_{\lambda \rightarrow \infty} H_{pin} = 0 \quad (2.5)$$

Thus, a DW will only be pinned by a local anisotropy modification if the length scale over which the modification occurs is on the same order as the DW width,⁷⁴ which is typically less than 10 nm.⁷⁰

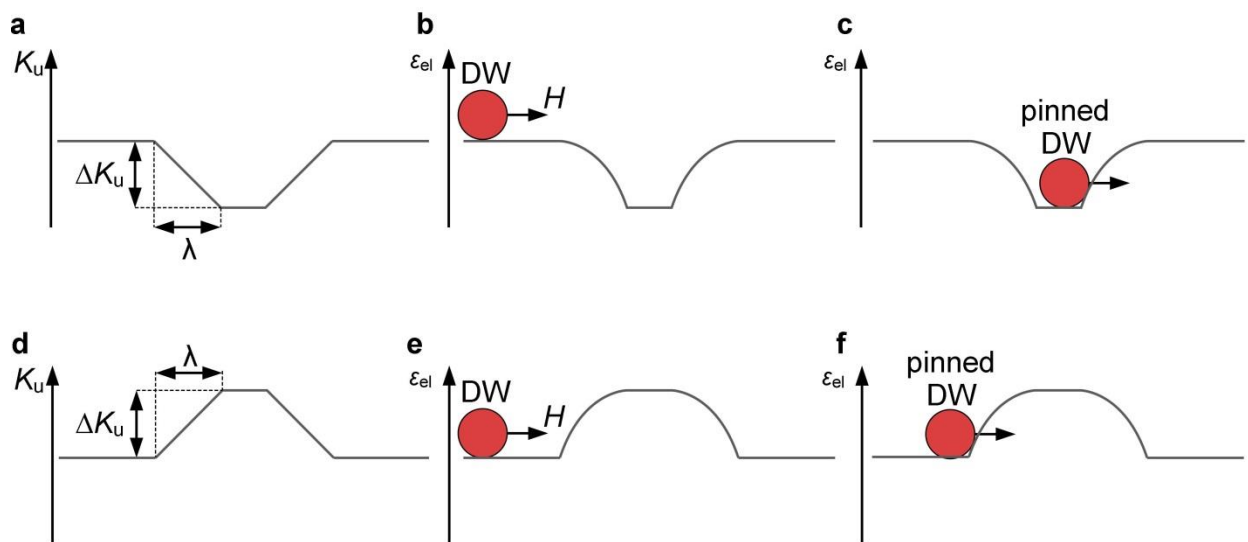


Figure 2-5: Domain wall pinning sites arising from local anisotropy modifications. One dimensional representation of a field (H) driven domain wall (DW) moving through the DW energy (ε_{el}) landscape (b,c and e,f) in the vicinity of a local anisotropy (K_u) modification (a,d). In (a-c) K_u is locally reduced by ΔK_u and gives rise to an energy well in the DW energy landscape which traps the DW at the defect location. In contrast, in (d-e) K_u is locally enhanced by ΔK_u , which gives rise to a barrier in the DW energy landscape and blocks the DW from moving through the defect. λ refers to the length scale over which the anisotropy modification occurs.

In the presence of a distribution of such pinning sites, it can be expected that a DW moves irregularly, in a series of so called Barkhausen jumps, from defect to defect site.⁵⁶ In

thin films with strong PMA, the field-driven motion of DWs can be treated within the framework of elastic interfaces driven by a force through a weakly disordered medium.^{70,75} Here, the DWs represent quasi-1D interfaces and the ultra-thin magnetic film can be treated as a quasi-2D Ising system with weak disorder due to its nanoscale inhomogeneities.⁷⁰ At zero temperature the DW will be pinned for all driving fields H below the critical depinning field H_{dep} .^{70,75,76} However, at finite temperatures, thermal activation allows the DW to move even for fields H below the critical depinning field H_{dep} .^{70,75,76} In fact, a finite DW velocity is expected for all nonzero driving fields.

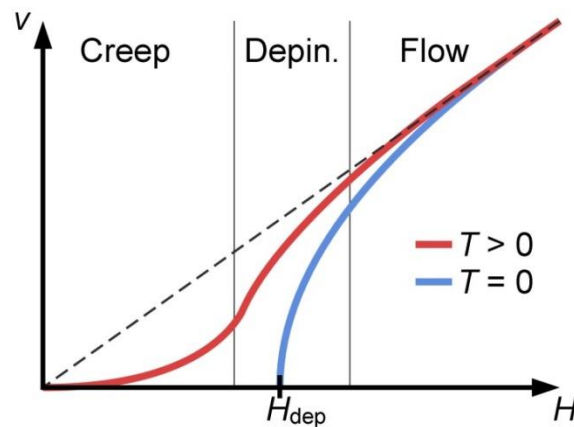


Figure 2-6: Regimes of domain wall motion. Theoretically predicted field-velocity (H - v) characteristic for a field-driven DW moving at zero and finite temperature T in an ultra-thin magnetic film with weak disorder. At zero temperature the system exhibits pinning with a critical depinning field H_{dep} . The three expected regimes of DW motion; creep, depinning and flow are labeled. Adapted from Reference [76].

Depending on the ratio H/H_{dep} , three regimes of DW motion are typically distinguished (see Figure 2-6). The thermally activated DW motion at small driving fields ($H/H_{\text{dep}} \ll 1$) is referred to as the DW creep regime.⁷⁵ On the other hand, if the driving field is far beyond the critical pinning field ($H/H_{\text{dep}} \gg 1$), pinning becomes irrelevant and the DW moves by viscous flow.⁷⁰ In between these two regimes is the depinning regime with $H/H_{\text{dep}} \approx 1$. Here, we will focus on the DW creep regime.

In the creep regime, DW motion is thermally activated and the DW velocity v follows an Arrhenius type relationship:⁷⁵

$$v = v_0 \exp\left(-\frac{E_a}{kT}\right) \quad (2.6)$$

Where E_a is the activation energy barrier for DW motion, T is the sample temperature and k is the Boltzmann constant. Equation (2.6) shows that in the creep regime, the DW velocity is exponentially sensitive to temperature T and activation energy E_a . E_a depends on the driving field, the configuration of the DW, the characteristics of the pinning sites and the magnetic properties of the sample. It can be expressed as follows:^{76,77}

$$E_a \propto U_{dep} \left(\frac{H_{dep}}{H}\right)^{1/4} \quad (2.7)$$

Here, U_{dep} is the collective pinning energy which is related to the pinning barrier height and H_{dep} is the critical depinning field. As expected, the activation energy decreases and thus the DW velocity increases with increasing driving field H .

U_{dep} and H_{dep} then depend critically on the DW configuration which is in turn determined by the magnetic properties of the sample:⁷⁷

$$H_{dep} \propto \frac{1}{M_s} \left(\frac{f_{dep}^2}{\varepsilon_{el}}\right)^{\frac{1}{3}} \quad \text{and} \quad U_{dep} \propto (f_{dep}^2 \varepsilon_{el})^{\frac{1}{3}} \quad \text{with} \quad f_{dep} \propto \frac{\varepsilon_{el,2} - \varepsilon_{el,1}}{\delta} \quad (2.8)$$

Here, δ is the DW width, f_{dep} is the pinning force of a single pinning site and $\varepsilon_{el,2} - \varepsilon_{el,1}$ is the local modification in the DW elastic energy density produced by the pinning site.

By expressing δ and ε_{el} in terms of the saturation magnetization M_s , the perpendicular magnetic anisotropy constant K_u and the exchange stiffness A allows us to rewrite E_a in terms of these fundamental magnetic properties of the sample. Assuming Bloch DWs (Equation(2.3)) and using Equations (2.7) and (2.8) it is found that:⁷⁸

$$E_a \propto K_u^{9/8} \approx K_u \quad (2.9)$$

Thus, the activation energy for DW creep is approximately a linear function of the anisotropy constant K_u . A reduction of K_u is expected to enhance the DW velocity whereas an increase in K_u is expected to reduce the DW velocity in the film. These results will be of particular importance for Chapters 4 and 5, where voltage-induced magnetic anisotropy modifications are used to control DW motion.

2.4 The Magneto-electric Effect in Metal Ferromagnets

Spintronics is an emerging field within nanoelectronics which aims to exploit the electron charge and spin degree of freedom for novel device applications. In fact, by coupling magnetic and transport properties, spintronic devices have become promising candidates for ultra-low power memory and logic applications.^{23-25,79} It is therefore not surprising, that one of the most promising spintronic technologies is magnetic random access memory (MRAM), a potential low-power successor for static and dynamic random access memory.^{27,28} In MRAM, information is stored in the resistance state of magnetic tunnel junctions (MTJs), which consist of two ferromagnetic electrodes separated by a thin insulating barrier. The resistance state of an MTJ depends on the relative orientation of the magnetization vector of the two electrodes and can be toggled by switching the magnetization orientation in one of the two electrodes.⁸⁰ The success of MTJs and many other spintronic devices therefore hinges on devising the most efficient way to control the orientation of the magnetization vector.^{26,27}

Historically, spintronic devices relied on magnetic fields to switch the magnetization. Magnetic fields however are associated with high power consumption and are notoriously hard to localize, which necessitates complex device architecture.^{23,26} Switching the magnetization by spin polarized current via spin transfer torques,⁸¹ provides a significant step forward by improving device scalability and reducing power consumption.^{27,28} However, far greater power efficiency could be achieved by using a gate voltage to control the magnetization via electric field effects.^{27,31,32}

The underlying physical phenomenon coupling magnetization and electric field is the so called magneto-electric effect.^{36,82,83} Magneto-electric coupling has stimulated broad interest in controlling a wide range of magnetic properties such as saturation magnetization,^{36,38,84} exchange bias,^{85,86} DW motion,^{77,87-91} and spin transport,^{92,93} via gate voltage (see Figure 2-7). Here, we focus on voltage control of magnetic anisotropy, because

fundamentally magnetic anisotropy determines the all-important orientation of the magnetization vector.

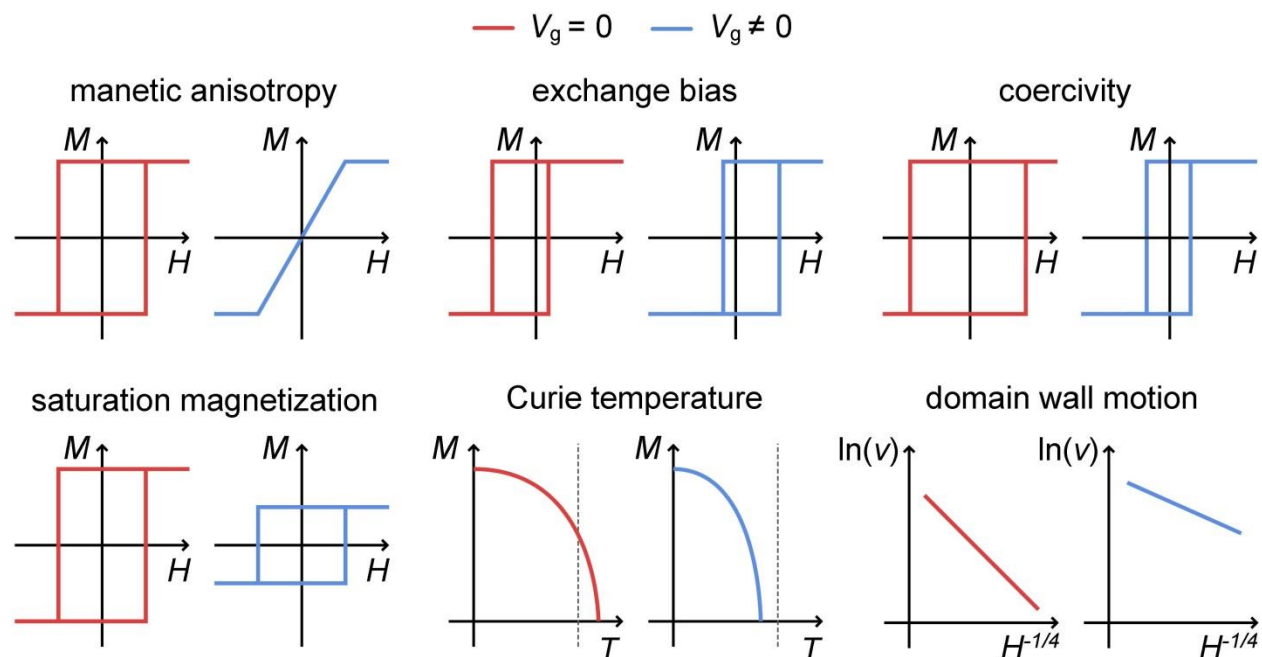


Figure 2-7: Magneto-electric control of magnetic properties. Examples of magnetic properties that can be controlled via gate voltage V_g in magneto-electric materials. M corresponds to magnetization, H to the magnetic field, T is the temperature and v is the domain wall velocity.

A variety of magneto-electric coupling mechanisms have been proposed to control magnetic anisotropy in ferromagnetic thin films. Generally they can be separated into two categories, one based on single phase, the other based on composite magneto-electric materials.⁴⁴ Single phase materials include dilute magnetic semiconductors^{35,36,94} and multiferroic materials^{33,34}. In dilute magnetic semiconductors, a gate voltage can be used to modulate the charge carrier density which in turn modifies magnetic anisotropy.³⁸ In single phase multiferroics, a gate voltage results in ion displacement away from their equilibrium positions, which modifies exchange interaction and the magnetic properties of the material.^{33,34} Unfortunately, both single phase multiferroics and dilute magnetic semiconductors usually order well below room temperature (RT) and require complex

compounds, which presents challenges for integration with existing semiconductor processing technology.²⁶

Composite magneto-electric materials include heterostructure multiferroics consisting of bilayers of ferroelectric and ferromagnetic materials. Voltage induced piezoelectric strain in the ferromagnetic layer can then couple to the magnetic properties of the ferromagnetic layer via magnetostriction.^{33,39,95} In a variation of this approach, coupling between a ferroelectric insulator and a ferromagnetic layer can also be mediated through voltage control of the ferroelectric polarization which modifies the interface electronic structure and therefore the magnetic anisotropy of the ferromagnet.^{26,96,97} A common disadvantage of such ferroelectric/ferromagnetic heterostructures is mechanical degradation resulting from the piezoelectric voltage response of the ferroelectric layer.

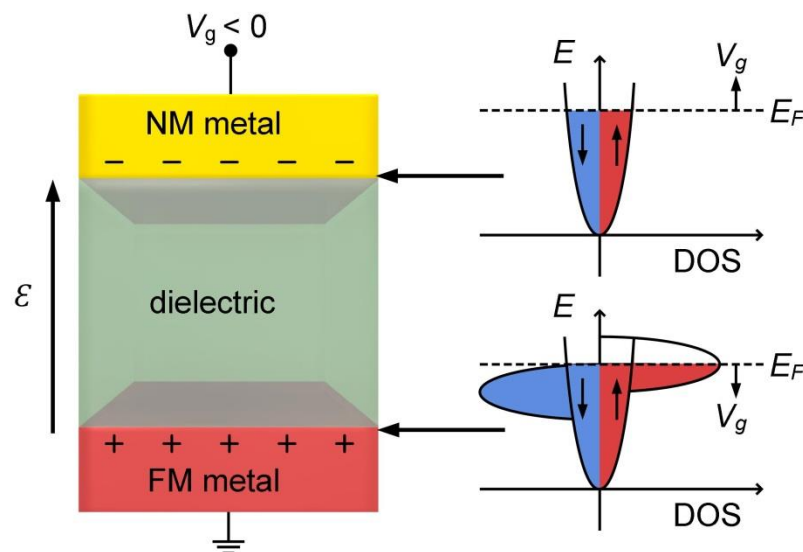


Figure 2-8: Magneto-electric coupling at ferromagnetic metal/dielectric interface. Schematic of a passive capacitor with a ferromagnetic (FM) and a nonmagnetic (NM) metal electrode separated by a dielectric layer. A gate voltage V_g generates an electric field \mathcal{E} across the device which is shielded within the first atomic layer of the metal electrodes. $V_g < 0$ results in electron accumulation (depletion) at the surface of the NM (FM) metal electrode, respectively. Changing the electron density is equivalent to moving the Fermi level E_F , which is illustrated in the band structure schematics on the right. Note the different density of states (DOS) close to E_F in the FM metal.

Here, we focus on an entirely different magneto-electric coupling mechanism (see Figure 2-8). Only recently it was found that magnetic anisotropy at the ferromagnetic metal/dielectric interface can be modulated by an electric field.⁴⁰⁻⁴² The discovery of this magneto-electric coupling mechanism has garnered a lot of research interest because it occurs at RT and requires only transition metal ferromagnets and simple dielectrics, which are compatible with existing semiconductor processing technology. Moreover, by employing ultra-thin ferromagnetic films with PMA (see Section 2.1) this magneto-electric coupling effect could allow voltage-induced switching of the magnetization between in-plane and out-of-plane orientations.⁴⁴

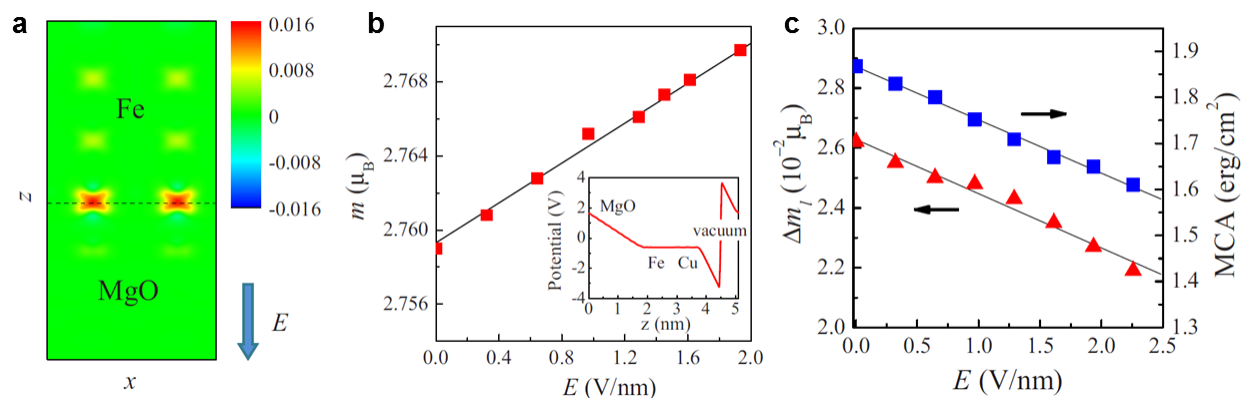


Figure 2-9: Electric field effects in Fe/MgO from first principles. (a) Electric-field-induced spin density in units of electrons/Å³ projected to the x-z plane or (010) plane of the Fe/MgO layers. The data shown is for an electric field E of 1 V/nm. The dashed line indicates the first atomic layer of Fe at the Fe/MgO interface. (b,c) Electric field dependence of the magnetic moment m (b) the orbital moment anisotropy Δm (c) and the magnetic crystalline anisotropy energy MCA (c) of a Fe atom at the Fe/MgO interface. The inset in (b) represents the calculated electrostatic potential across the sample under an electric field of 4 V/nm. Reprinted with permission from Niranjana, M. K et al. Electric field effect on magnetization at the Fe/MgO(001) interface. Appl. Phys. Lett. 96, 222504. Copyright 2010, AIP Publishing LLC.

In order to understand the microscopic origin of the field-induced anisotropy modifications, the effect of electric fields on ferromagnetic metal thin films was studied from first principles.^{44-46,98-100} When a metal is subject to an electric field, the conduction electrons screen the electric field over the screening length of the material (Figure 2-8).

However, due to their high charge carrier density, the screening length in metals is only on the order of one atomic layer, which effectively limits the magneto-electric effect to ultra-thin magnetic films.⁴⁴

Duan et al.⁴⁴ investigated electric field effects in Fe(100), Co(100) and Ni(100) films and found a variation of magnetic moment and magnetocrystalline anisotropy at the film surface. This variation was attributed to spin dependent screening in the ferromagnetic metal, which results from the different carrier densities at the Fermi level in the two spin channels (Figure 2-8).¹⁰¹ Spin dependent screening leads to a spin imbalance in the electron density at the surface and gives rise to a net surface magnetization which scales linearly with electric field (see Figure 2-9(a,b)).⁴⁴ The electric field was also found to affect the anisotropy of the orbital moments, which give rise to magnetocrystalline anisotropy (see Section 2.1). Both the orbital moment anisotropy and the MAE were found to scale approximately linearly with the electric field (see Figure 2-9(c)).⁴⁴

Later, Tsujikawa et al.⁴⁶ and Niranjana et al.⁹⁸ clarified that the change in orbital moment anisotropy, and thus magnetocrystalline anisotropy, results from changes in the relative occupation of $3d$ orbitals of Fe atoms at the surface/interface. Due to spin orbit coupling, $3d$ orbitals with different symmetry contribute differently to magnetocrystalline anisotropy, and changing their relative occupation can therefore significantly modify the anisotropy.⁹⁸ Niranjana et al.⁹⁸ also predicted that the magnitude of the anisotropy modification can be significantly enhanced by applying the electric field across a high dielectric constant material placed adjacent to the ferromagnet. For Fe/MgO they arrived at an anisotropy modification of 100fJ/Vm, five times larger than the 20fJ/Vm predicted for the Fe/vacuum interface.^{44,98}

Nakamura et al.⁴⁵ proposed an alternative mechanism for the observed changes in magnetocrystalline anisotropy. They argued that the anisotropy modifications are not the result of changes in the relative occupation of $3d$ orbitals, but rather due to electric-field-induced modifications of the band structure itself (see Figure 2-10). Although the overall band structure with and without electric field is very similar, electric-field-induced

coupling between $3d$ -orbitals and components of p -orbitals close to the Fermi level can locally split the bands and shift them relative to the Fermi level (see Figure 2-10).⁴⁵ These modifications of the $3d$ band structure are predicted to give rise to anisotropy modifications of ~ 50 f J/Vm, and at very high electric fields, they could even change the sign of the interfacial magnetic anisotropy.⁴⁵

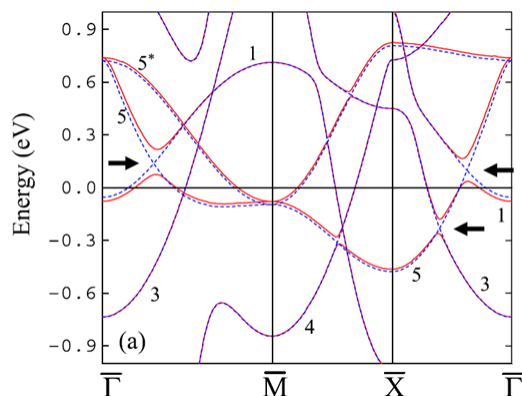


Figure 2-10: Electric field effects on the band structure of Fe. (a) Calculated minority-spin band structure along high symmetry directions for a Fe(001) monolayer in an electric field of zero (dotted lines) or 10 V/nm (solid lines). The reference energy $E = 0$ corresponds to the Fermi energy. The arrows indicate band gaps induced by the electric field and the numbers 1, 3, and 4 indicate bands corresponding to d_{z^2} , $d_{x^2-y^2}$, and d_{xy} states, respectively, and bands 5 and 5* are weakly bonding and antibonding $d_{xz,yz}$ states. Reprinted figure with permission from Nakamura, K. et al. Physical Review Letters, 102, 187201, 2009. Copyright (2009) by the American Physical Society. <http://link.aps.org/abstract/PRL/v102/p187201>

It is safe to assume that in reality, the electric field modifies both the $3d$ band structure close to the Fermi level, and the relative occupation of the $3d$ orbitals. The sign and magnitude of the magneto-electric effect thus depends on the details of the band structure at the Fermi level, which is sensitive to the magnetic material,^{44,45} the dielectric material,^{98,102} the interface oxidation state,¹⁰⁰ and adjacent metal layers⁹⁹.

The first experiments on electric field control of magnetic anisotropy in ferromagnetic metals were conducted on thin films of FePt and FePd intermetallic compounds immersed in a liquid electrolyte.⁴⁰ The FePt and FePd films exhibited strong PMA, and Weisheit et al.⁴⁰

were able to reversibly modify their coercivity by several percent, by applying a voltage across the electrolytic cell. The coercivity modifications were attributed to a electric-field-induced change in the PMA of the films.

Maruyama et al.⁴¹ significantly improved on these experiments by introducing an all solid state device design and directly demonstrating voltage-induced anisotropy modifications. The solid state device resembles a parallel plate capacitor in which one electrode has been replaced by an ultra-thin ferromagnetic metal film. Specifically, the experiments were conducted on ultra-thin Fe films grown by molecular beam epitaxy on a single crystal Au(100) substrate and covered by a thin MgO/polyimide dielectric layer.⁴¹ Voltage was applied across the dielectric via indium tin oxide gate electrodes, and the thickness of the Fe layer was chosen such that it exhibits only moderate perpendicular anisotropy, making it more susceptible to electric-field-induced effects. In this system, the change in interface magnetic anisotropy under applied bias was estimated to be ~ 90 fJ/Vm. In a quantitative experiment performed later for the Fe/MgO system, a modification of ~ 30 fJ/Vm was determined.¹⁰³

Due to its similarity to MTJs, the solid state capacitor design introduced by Maruyama et al.⁴¹ has since become the de facto standard device to study magneto-electric effects in ferromagnetic metals. For instance, Endo et al.⁴² employed the same device design to demonstrate that a similar magneto-electric effect (~ 30 fJ/Vm) can also be achieved in sputter deposited films, which greatly simplified sample preparation. Moreover, Chiba et al.⁸⁴ showed that in very thin sputtered Co films with Curie temperatures close to RT, the ferromagnetic phase transition itself can be controlled by gate voltage.

Taking a step closer towards the vision of ultra-low power spintronic devices, Nozaki et al.¹⁰⁴ directly implemented voltage control of magnetic anisotropy into magnetic tunnel junctions. Wang et al.³¹ demonstrated electric-field-assisted reversible switching in CoFeB/MgO/CoFeB tunnel junctions with PMA. Here, electric-field control of magnetic anisotropy allows switching of the magnetization configuration and tunnelling magnetoresistance at much lower magnetic fields or current densities. In a different

approach, Shiota et al.³² realized coherent precessional magnetization switching in CoFe/MgO/CoFe tunnel junctions by applying sub-nanosecond electric field pulses. In the presence of a constant magnetic field, control over the pulse duration then allowed for toggling between the parallel and antiparallel magnetization configuration of the tunnel junction. It was found, that with electric field pulses, it is possible to switch the magnetization configuration at a mere fraction of the power required for spin-transfer-torque-induced switching.³²

The experimental and theoretical results summarized in this section demonstrate that tremendous progress has been made on the path towards ultra-low power voltage-controlled spintronic devices. Nevertheless, significant hurdles remain. Most prominently, the magneto-electric effect in ferromagnet metal/dielectric bilayers is so far not strong enough to satisfy the stringent requirements of real world applications. In the results described above, effects vary between 0.01 to 0.1 erg/cm² at a field of 1V/nm (10 to 100 fJ/Vm), but for applications, for example in MRAM technology, voltage-induced anisotropy modifications on the order of 1 erg/cm² would be required. It is this gap of at least one order of magnitude, that fuels the quest for better and more efficient magneto-electric materials.

2.5 Nanoionics and Memristive Switching in Metal/Oxide/Metal Devices

The emerging field of nanoionics covers a wide range of phenomena that result from ionic migration in solid-state nanoscale systems.^{105,106} Similar to quantum confinement effects in nanoelectronics, ionic transport is drastically changed when the material dimensions are reduced to 10s of nanometers.¹⁰⁵ At this length scale, the barriers for ionic transport are greatly reduced and interface effects can become prevalent and dominate the ionic properties of the whole material.¹² These effects are expected to dramatically enhance ionic conductivity, turn materials which are ionic insulators in the bulk into good ionic conductors and significantly reduce the operational temperature of solid-state ionic devices.^{12,106-108}

Metal/oxide/metal devices are pervasive in solid state ionics and form the common basis of a wide range of applications, from oxygen sensors, to solid oxide fuel cells, and memristive switching memories.^{12,106} Memristive switching memories or memristors are true nanoscale ionic systems and typically rely on ion-migration-induced resistance changes in thin oxide films for their nonvolatile memory functionality.^{109,110} Interestingly, the materials, layer thicknesses, device structure, and electric field strength used in memristive switching devices are very similar to the ones used in the emerging field of magneto-electronics (see Section 2.4).^{41,42,84,111} Considering that memristive switching has been studied intensively since the 1960s,^{3,109} it can be expected that many of the phenomena and effects observed in memristive devices could also be relevant for magneto-electric devices and provide valuable lessons to improve magneto-electric device design. In fact, in MTJs, it has been reported that electrochemical reactions and ionic migration can modify magneto-resistance.^{112,113}

A memristors, short for memory resistor, is a two terminal device that retains either a high or low resistance state depending on the history of applied voltage and current.³ The device typically consists of two metal electrodes separated by a thin insulating layer (Figure 2-11(a)). Under bias application, voltage-driven ion migration in the insulator

results in a conductive filament between the two electrodes (see Figure 2-11(b)), which can be broken and reestablished with the bias voltage (see Figure 2-11(c,d)). Breaking and reestablishing the conductive filament then results in the characteristic hysteretic switching of the resistance state. Memristors can be categorized by their current-voltage characteristics (bipolar/unipolar) and active ionic species (anion/cation). Details about the different device categories can be found in References [3,4]. Here, our aim is to elucidate the microscopic processes, which give rise to memristive switching and which could also occur in magneto-electric devices.

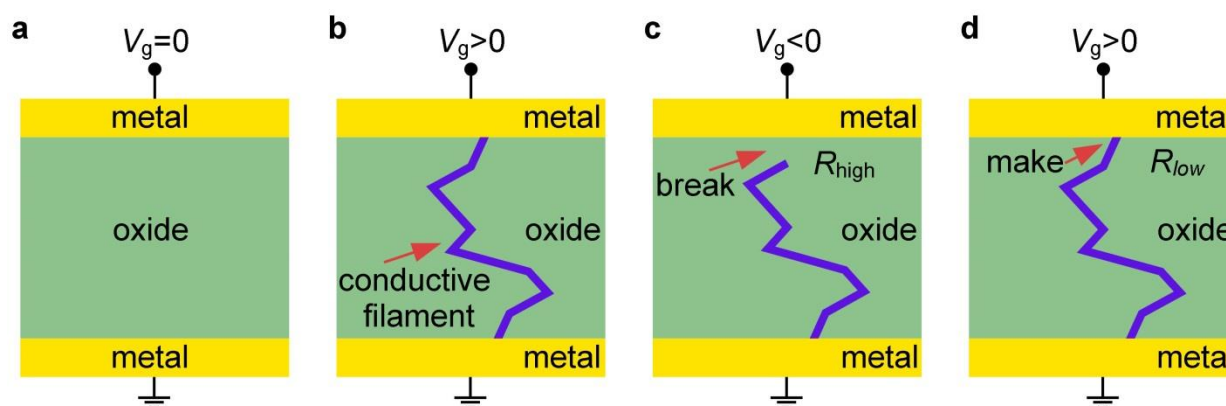


Figure 2-11: Memristive switching in metal/oxide/metal memristor. (a-d) Schematic illustration of bipolar memristive switching in a metal/oxide/metal memristor. (a) Device in its virgin state, showing two metal electrodes separated by an oxide insulator. (b) Application of a high bias voltage V_g , results in the formation of a conductive filament between the two electrodes. This process is also referred to as electroforming. (c,d) Depending on the bias polarity the filament can be broken (c) or reestablished (d) which switches the resistance state of the device from high R_{low} to low R_{high} and vice versa(b).

We focus on anion-based devices in which the oxygen anion O^{2-} , or equivalently, the positively charged oxygen vacancy V_O^{2+} , is the mobile ionic species. These devices typically rely on nanoscale metal-oxide insulators,³ which makes them most similar to magneto-electric devices. A wide range of metal-oxides have been explored in memristive devices; magnesium oxide MgO, titanium oxide TiOx, tantalum oxide TaOx and aluminum oxide AlOx are just a few of them.³ Since memristive switching originates from defects in the material and not from a particular electronic band structure, it is expected that almost all

oxide materials exhibit memristive switching.³ Currently, a complete microscopic picture of resistive switching does not exist, but the effects contributing to resistive switching are known and reasonably well understood.

A bias voltage applied across a metal/oxide/metal memristor has two main effects on the oxide; it generates an electric field and, due to the large current densities required for switching, results in Joule heating.³ Joule heating and electric field effects coexist in all memristive switching devices, but their relative contribution can vary with material system, device fabrication, and applied bias.^{3,4,114} In all cases, the combination of the two effects results in four driving forces that give rise to the redistribution of atomic species in the oxide.³ These driving forces are the electric potential gradient, the electron kinetic energy, temperature gradients, and the concentration gradients (see Figure 2-12).³

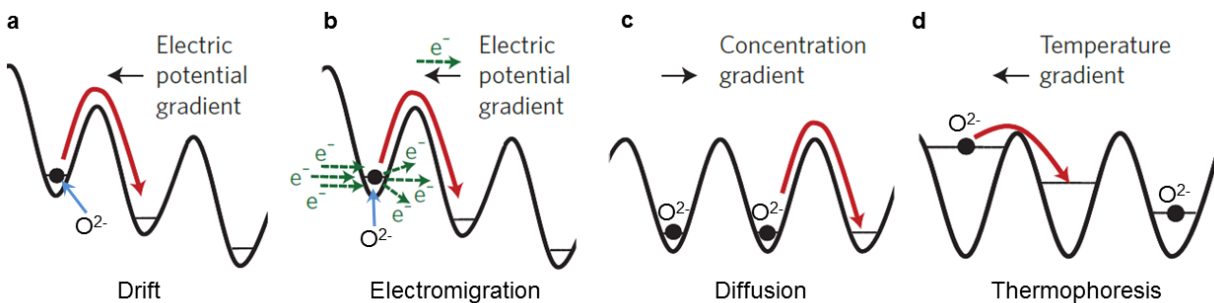


Figure 2-12: Driving forces for oxygen migration in metal/oxide/metal memristors. (a-d) Schematic illustrations of the four forces that can drive oxygen anion (O^{2-}) migration in the presence of a strong electric field. Adapted by permission from Macmillan Publishers Ltd: Nature Nanotechnology, Reference [3], copyright (2012).

In most metal-oxides, oxygen ions (or equivalently oxygen vacancies) are the mobile atomic species.^{3,115} A large potential gradient accelerates charged species such as electrons and ions in the oxide layer. For oxygen ions, the potential gradient results directly into a redistribution of atomic species via ionic drift (Figure 2-12(a)).³ For electrons however, the effect is indirect and occurs through electromigration (Figure 2-12(b)), meaning the transfer of kinetic energy from fast moving electrons to atoms in the oxide.³ Concentration gradients in the oxide layer drive diffusion of oxygen from locations with high oxygen

concentration to locations with lower oxygen concentration (Figure 2-12(c)). Joule heating, enhances both, ionic drift and diffusion, but in addition, large temperature gradients can also result in a direct transfer of atoms (Figure 2-12(d)).¹¹⁶

Rearrangement of oxygen ions inside the oxide can result in the formation of an oxygen-deficient metallic phase with reduced resistance.^{117,118} Drift and electromigration drives oxygen along the electric field direction, and temperature and concentration gradients can drive it perpendicular to that direction.³ Under prolonged voltage application, the two effects then result in the formation of a filament of the oxygen-deficient phase, which forms a conductive channel through the oxide, and switches the device resistance from high to low.^{117,118}

If we step back for a moment and compare memristors to the magneto-electric devices described in Section 2.4, we realize that the active part of the memristor is the oxide layer whereas in magneto-electric devices, the active part is the ferromagnetic metal electrode or more precisely, the electrode/oxide interface. It is therefore appropriate to focus our discussion on the processes that occur at the electrode/oxide interface before and during filament formation. In most memristive switching devices, the conductive filament is first established during a one time application of a high bias voltage, a process that is known as electroforming.

Here, we take a closer look at electroforming in Pt/TiO₂/Pt, a prototype memristive switching system (see Figure 2-13(a)).^{115,119} Triggered by the high electric field and Joule heating during electroforming, the following electrochemical reaction occurs at the anode/oxide interface (in Kröger-Vink notation):^{115,119}



This means that the oxide is reduced and oxygen gas is released at the anode/oxide interface. The anode therefore acts as a source for oxygen vacancies. Under the applied bias, the vacancies move through the oxide layer towards the cathode and accumulate at the cathode/oxide interface (Figure 2-13(b)).¹¹⁵ The vacancy motion likely occurs along

high diffusion paths in the oxide, such as grain boundaries and high dimensional defects.¹¹⁹ Due to oxygen vacancy accumulation at the cathode/oxide interface, an oxygen deficient phase grows from the cathode to the anode, forming a conducting filament (Figure 2-13(c)).¹¹⁵ Interestingly, oxygen vacancies accumulate at the cathode/oxide interface long before a conductive channel is established through the oxide. Here, we use oxygen vacancies to describe this process, but it is equivalent to think about oxygen ions moving in the opposite direction.

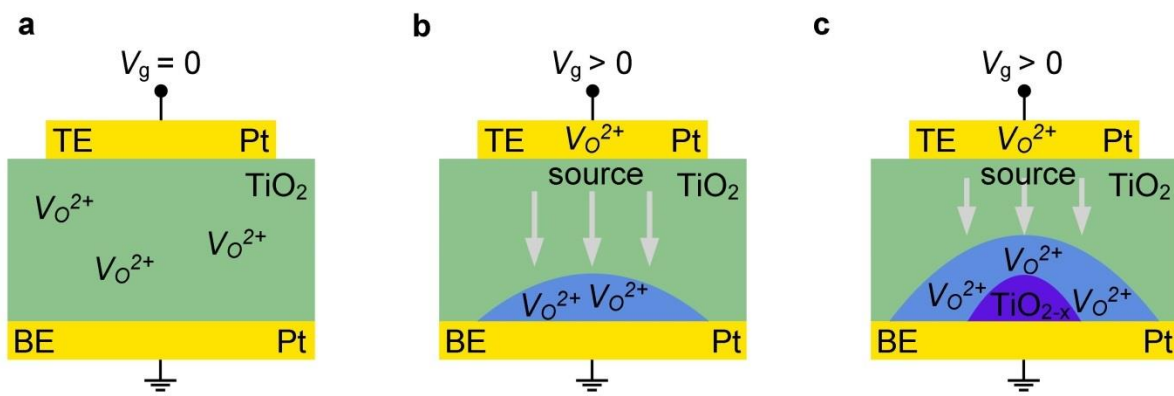


Figure 2-13: Electroforming in Pt/TiO₂/Pt memristors. (a-c) Schematic illustration of conductive filament formation in TiO₂. The filament is made up of oxygen deficient TiO_{2-x} and grows from the cathode to the anode. The grey arrows indicate the drift direction of oxygen vacancies under the applied bias V_g . TE refers to the top electrode and BE to the bottom electrode. Adapted from Reference [115]

The evolution of oxygen gas at the anode has been verified in multiple experiments and often manifests itself in the formation of oxygen gas bubbles and physical damage to the electrodes (see Figure 2-14).^{115,118,119} Yang et al.¹¹⁹ found that if positive bias is applied to the top electrode (i.e., top electrode is anode), oxygen anions drift towards it and discharge to form oxygen gas. The oxygen gas is then released and numerous large gas bubbles form underneath the top electrode (Figure 2-14(e)). If instead negative bias is applied to the top electrode (bottom electrode is the anode), then oxygen gas bubbles form at the bottom electrode, underneath the oxide layer. Since a higher gas pressure would be needed to form oxygen bubbles underneath the oxide layer, the bubbles are smaller and less numerous

(Figure 2-14(b)).¹¹⁹ In devices with nanoscale lateral dimensions bubble formation is not observed, because at the nanoscale oxygen gas can escape at the electrode edge, due to the significantly reduced diffusion length.¹¹⁹

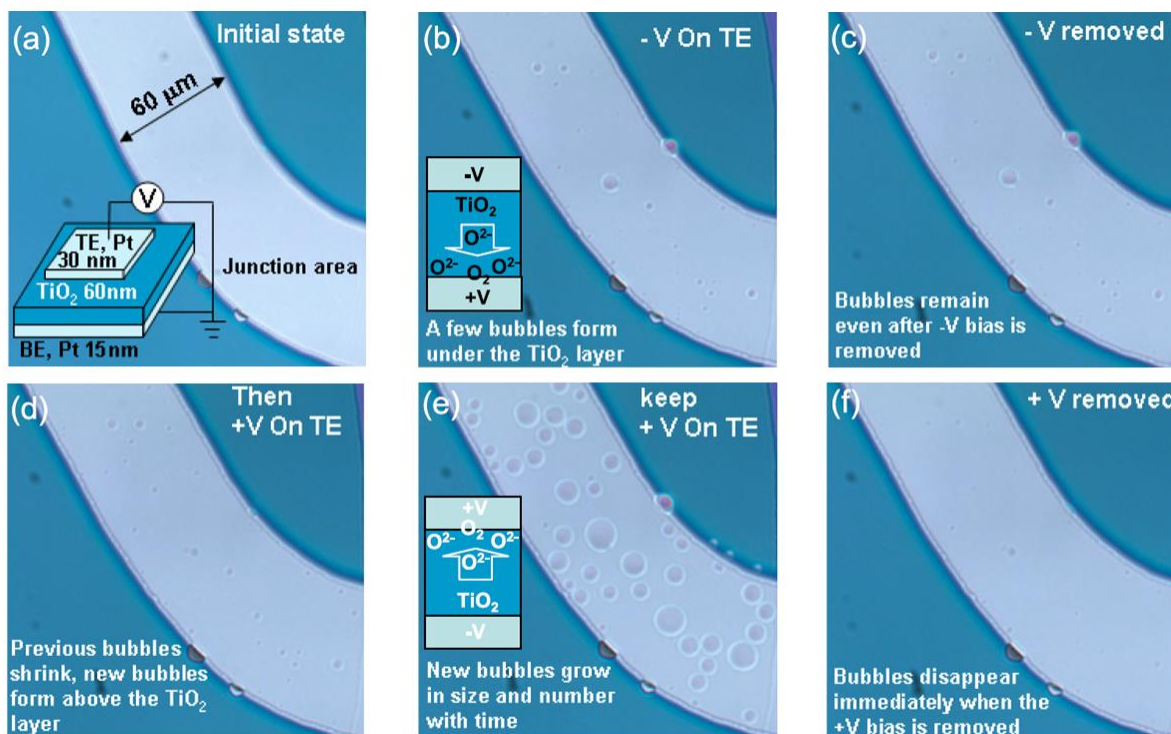


Figure 2-14: Oxygen gas evolution during electroforming of Pt/TiO₂/Pt memristors. Optical micrographs showing the virgin device (a) and the oxygen gas bubble behavior under negative bias (b,c) and under positive bias (d-f). The inset of (a) shows a schematic of the Pt/TiO₂/Pt device and the insets in (b) and (e) show schematically the migration of oxygen anions under negative and positive bias, respectively. See description in (b-f) for details on bubble behavior. The abbreviation TE refers to the top Pt contact. Adapted from Yang, J. J. et al. The mechanism of electroforming of metal oxide memristive switches, *Nanotechnology*, 20, 215201 (2009). Copyright IOP Publishing. Reproduced by permission of IOP Publishing. All rights reserved.

Oxygen evolution during electroforming shows that the oxygen kinetics in memristive switching devices can be affected by the partial pressure of oxygen in atmosphere. The device kinetics are thus not only contingent on oxygen migration through the oxide layer, but also depend on oxygen gas adsorption, decomposition, and integration at the

electrodes.¹¹⁵ Similar to solid oxide fuel cells and oxygen gas sensors, the electrode morphology and the triple phase boundary likely play a crucial role in the exchange of oxygen with ambient atmosphere.^{120,121}

Under the assumption that the rate limiting step is ionic transport through the oxide, the dynamics of memristive switching can be modeled by thermally activated hopping of oxygen ions in the potential landscape of an ionic solid.^{3,122} For memory applications, a combination of short switching times τ_{switch} on the nanosecond time scale and long retention times $\tau_{\text{retention}}$ on the order of years, is desired. At first this appears difficult to realize, considering that engineering a device for fast oxygen transport would not only reduce the switching time, but also the retention time. However, Strukov et al.¹²² showed that the desired behavior can indeed be achieved by exploiting nonlinear ionic transport.

In the context of metal/oxide/metal memristors, this would require that oxygen transport is an order of magnitude faster under an applied bias than in its absence. Assuming that oxygen ions exhibit a mobility μ and move by a distance L during switching, we can find expressions for τ_{switch} and τ_{ret} .¹²² Under an applied bias, oxygen moves at a drift velocity v_{drift} and the switching time is given by $\tau_{\text{switch}} = L/v_{\text{drift}}$. In the absence of a bias voltage, the device loses its state due to diffusion of oxygen ions back to their equilibrium distribution. With a diffusion constant D for oxygen ions, the retention time is then $\tau_{\text{ret}} = L^2/D$. Due to the high electric fields used in memristive switching, the drift velocity depends exponentially on the electric field \mathcal{E} .³ Moreover, ionic drift and diffusion depend exponentially on the temperature T in the active region of the device.³ For a memristor, the ratio $\tau_{\text{ret}}/\tau_{\text{switch}}$ can therefore be written as:¹²²

$$\frac{\tau_{\text{ret}}}{\tau_{\text{switch}}} \propto L \exp\left(\frac{\mathcal{E}}{\mathcal{E}_0}\right) \exp\left(\frac{E_a}{kT_{\text{ret}}} - \frac{E_a}{kT_{\text{switch}}}\right) \quad (2.11)$$

Here, \mathcal{E}_0 is a characteristic electric field, E_a is the activation energy for oxygen motion and T_{ret} and T_{switch} are the temperature in the active device region during switching and state retention, respectively. Since electric field and temperature (Joule heating) are much larger during switching, Equation (2.11) explains the nanosecond timescale switching and

$\tau_{\text{ret}}/\tau_{\text{switch}} > 10^{10}$ that is typically observed in metal/oxide/metal resistors.¹²² Interestingly, since the bias voltage is responsible for the electric field \mathcal{E} and via Joule heating for the difference between T_{switch} and T_{ret} , v_{drift} and $\tau_{\text{ret}}/\tau_{\text{switch}}$ depend super-exponentially on the bias voltage.³ Therefore, even a small increase in bias voltage can dramatically improve the switching kinetics.

In summary, metal/oxide/metal memristors exhibit a wide range of defect-driven phenomena, ranging from electrochemical reactions at the electrodes to ionic transport through the oxide layer. These defect-driven effects are very general and are expected to occur in almost all oxide materials. Memristors have been studied intensively for decades, and today, the origin and kinetics of the switching process are reasonably well understood. The research done on memristive switching could therefore provide a treasure trove of information for other emerging fields that rely on similar metal/oxide/metal devices.

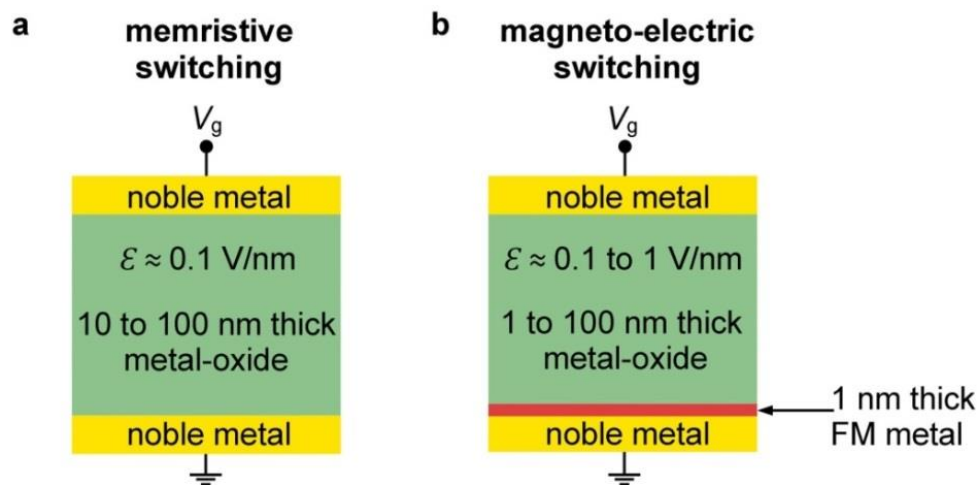


Figure 2-15: Comparison between memristive and magneto-electric devices. Device schematics, including typical oxide thicknesses and electric fields \mathcal{E} , of metal/oxide/metal devices used for memristive switching (a) and magneto-electric switching (b). The device in (b) exhibits a thin ferromagnetic (FM) metal layer between oxide and bottom electrode.

Here, it is worthwhile to once again consider the similarity between devices used for memristive switching (see Figure 2-15(a)) and voltage control of magnetism (see Figure 2-15(b) and Section 2.4). It is perplexing that essentially the same device, operated under

similar conditions, is treated as an ionic device for memristive switching and as a purely electronic device for magneto-electric switching. Would it be so surprising to discover, that after all, the devices exhibits both electronic and ionic effects simultaneously?

2.6 Motivation: A First Experiment with Unexpected Results*

Based on the discussion on magneto-electric effects in ferromagnetic metals (see Section 2.4), we performed an initial experiment with the aim to compare our results with theoretical predictions and previous work in the field. For this purpose, we selected Ag(100)/Fe/MgO a high quality, single crystal magnetic thin film system compatible with the same Fe bottom electrode and MgO gate oxide, that was used in previous experimental and theoretical studies.

The Ag(100)/Fe/MgO samples were grown by molecular beam epitaxy (MBE) in a ultra-high vacuum (UHV) system with base pressure better than 2×10^{-10} mbar.[†] We use a simple capacitor design with a heterostructure dielectric similar to that of prior studies.^{41,42,123,124} The bottom electrode is ferromagnetic and consists of a high quality epitaxial Fe film grown in wedge geometry on an Ag(100) single crystalline substrate. The Fe wedge spans a thickness range d_{Fe} of $d_{\text{Fe}} = 0$ to 9 atomic monolayers (MLs) and was annealed in UHV for 30 min at 150 °C to improve surface morphology¹²⁵. The Fe layer is covered by a double-layer dielectric consisting of 10 nm MgO and 60 nm zirconium oxide (ZrOx). MgO grows epitaxially on Fe(100),¹²⁶ and the MgO/Fe interface exhibits strong interfacial magnetic anisotropy.⁹⁸ ZrOx was chosen because of its high dielectric constant,⁴² and grown by reactive sputter deposition from a Zr target under 4.0 scc/m O₂ flow. Indium tin oxide (ITO) gate electrodes, 70 μm wide and 30 nm thick, were sputter deposited from an ITO target and patterned by shadow mask lithography.

The magnetic properties of individual devices were probed using the scanning MOKE system described in Section 3.2.2. The coercivity H_c and remanence to saturation magnetization ratio M_r/M_s were derived from polar MOKE hysteresis loops and their

* Sections of this chapter, including figures, have been previously published in the following articles:

– Bauer, U., Przybylski, M., Kirschner, J. & Beach, G. S. D. Magneto-electric Charge Trap Memory. *Nano Lett.* **12**, 1437-1442 (2012).

† UHV film growth and initial characterization of the samples was performed in collaboration with Juergen Kirschner and Marek Przybylski at the Max Planck Institute for Microstructure Physics in Halle, Germany.

modifications, ΔH_c and $\Delta M_r/M_s$, were used to characterize the influence of a gate voltage on the magnetic properties of the Fe bottom electrode.

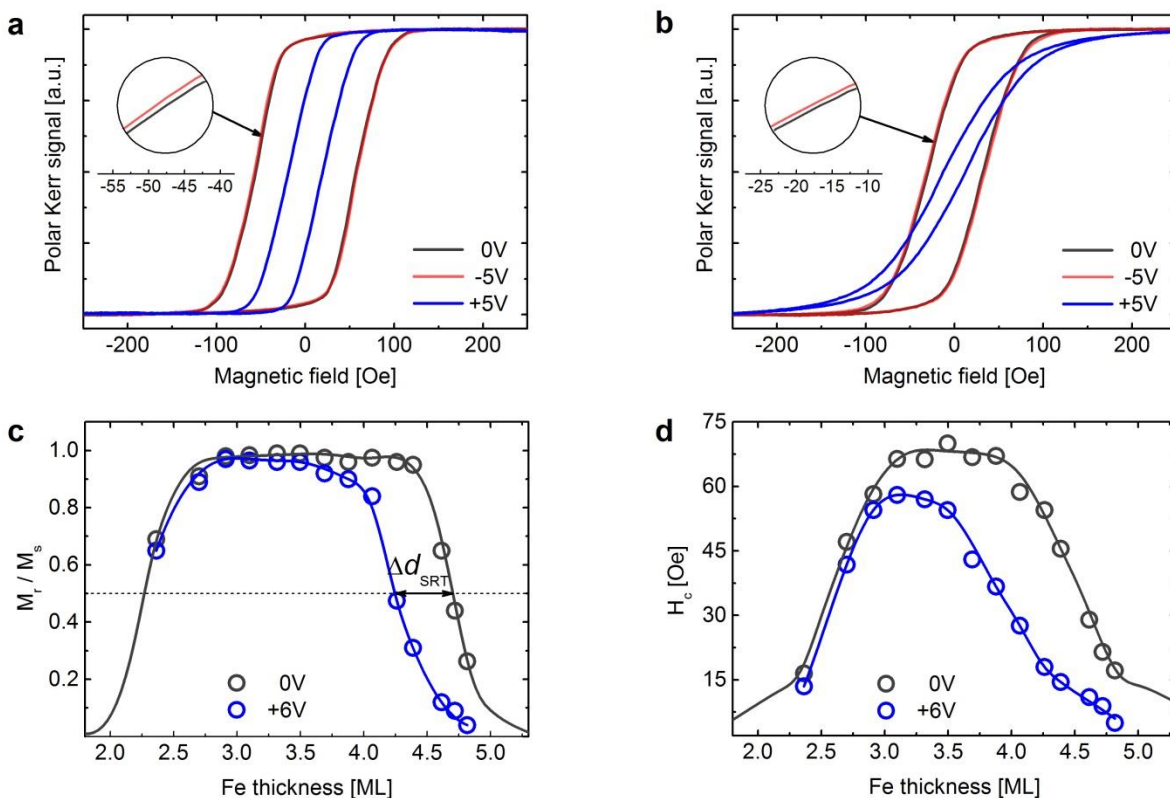


Figure 2-16: Voltage effects on the spin reorientation transition.: (a,b) Exemplary polar MOKE hysteresis loops measured under an external bias voltage of 0 V, -5 V and +5 V at 4.3 ML Fe (a) and 4.6 ML Fe (b). Inset in (a,b) shows magnified section of hysteresis loops to highlight asymmetry of bias voltage effects under inversion of bias polarity. (c,d) Thickness dependence of M_r/M_s (c) and H_c (d) on continuous Fe wedge (solid black line) and on discrete ITO electrodes at a gate voltage of 0 V (black open circles) and +6 V (blue open circles). Note, solid blue line in (c,d) is a guide to the eye and Δd_{SRT} on (c) indicates the voltage induced shift in spin reorientation thickness.

We observe a giant modification of H_c and M_r/M_s if a positive gate voltage (V_g) of just a few volts is applied to the ITO gate electrode. This modification depends strongly on Fe thickness and therefore on the strength of PMA. Exemplary hysteresis loops, at a Fe thickness of 4.3 ML and 4.6 ML showing a strong modification of $\Delta H_c = -37$ Oe or -66 % and of $\Delta M_r/M_s = -0.53$ or -78 % can be seen in Figure 2-16(a) and (b), respectively. The Fe

thickness dependence of M_r/M_s and H_c at zero bias and at $V_g = +6$ V is shown in Figure 2-16(c) and (d), respectively. From there it can be seen that up to a spin reorientation thickness of 4.7 ML Fe, the magnetization vector is aligned perpendicular to the film plane and only above this thickness prefers an orientation in the film plane. The apparent loss of perpendicular anisotropy below 2.5 ML Fe is due to the thickness dependence of the Curie temperature, which decreases below RT at this thickness.¹²⁵

The orientation of the magnetization vector in ultrathin metallic ferromagnets is often dictated by a surface contribution, K_s , to the MAE.¹²⁷ At the spin reorientation transition, perpendicular surface magnetic anisotropy K_s and shape anisotropy of the Fe film compensate each other:

$$K_s/d_{SRT} = 2\pi M_s^2 \quad (2.12)$$

Here, d_{SRT} and M_s are the spin reorientation thickness and the saturation magnetization of the Fe film, respectively. From Figure 2-16(c), application of $V_g = +6$ V shifts the spin reorientation thickness d_{SRT} downward by $\Delta d_{SRT} \approx -0.45$ ML. Taking $M_s = 1710$ G we therefore estimate the change in perpendicular surface anisotropy as $\Delta K_s = 2\pi M_s^2 \Delta d_{SRT} = 118 \mu\text{J}/\text{m}^2$. Despite the much lower applied voltage, this change is an order of magnitude larger than previously reported for Fe/MgO.⁴¹ Considering the thicknesses and dielectric constants of the MgO/ZrO₂ stack, this would correspond to a giant electric field effect on magnetic anisotropy of ~ 1000 fJ/Vm, the largest magneto-electric efficiency yet reported for any metallic system, and far beyond theoretical predictions of 100 fJ/Vm.⁹⁸

In contrast to a positive bias, application of negative bias results in only a weak modification of H_c and M_r/M_s . Under a bias voltage of -5 V, an increase of 2 % in H_c and of 3 % in M_r/M_s is observed at the same Fe thicknesses (see Figure 2-16(a,b)). These values are similar to previously reported results^{128,129} but more than one order of magnitude smaller than the changes observed here under the positive bias.

Considering the asymmetry under bias inversion, together with the giant magnitude under positive bias, it is clear that voltage-induced electron accumulation/depletion in the

Fe bottom electrode cannot alone account for the observed effects. Instead, voltage-induced defect creation in the gate oxide or at the Fe/MgO interface could be responsible for the observed modifications of magnetic properties (see Section 2.5). The presence of other voltage induced processes would also help to explain the wide range of magneto-electric efficiencies reported in the literature.^{41,42,104,123,124,128,129}

If defect creation was indeed responsible for the observed giant modification of magnetic anisotropy, we would expect the modifications of H_c and M_r/M_s to persist long after V_g is removed.¹³⁰ And that is exactly what we find experimentally. In Figure 2-17(b), a gate voltage of + 3 V is applied and results in a strong decrease of M_r/M_s . After 150 s, the voltage is removed and the evolution of M_r/M_s is monitored over time. Instead of immediately returning back to its initial value, M_r/M_s takes ~ 72 h to relax. Moreover, application of a negative bias decreases the relaxation time by an order of magnitude, while positive V_g leads to retention of $\Delta M_r/M_s$ over time.

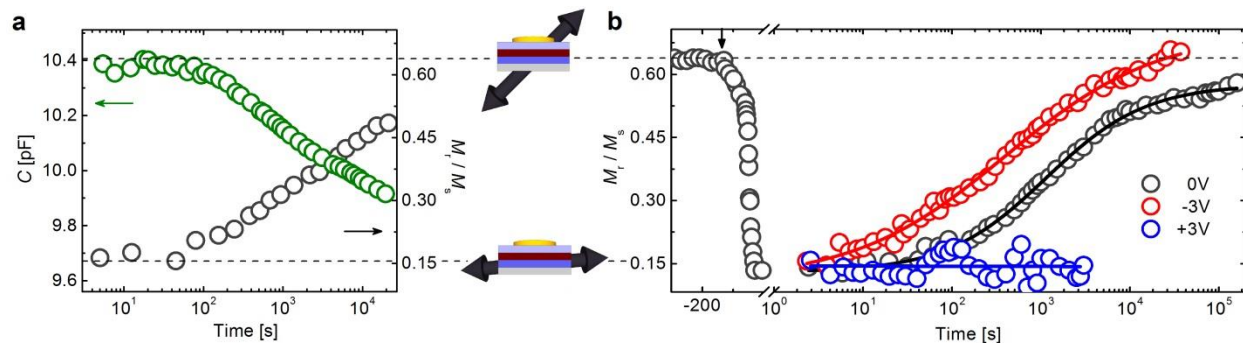


Figure 2-17: Device capacitance and magnetic anisotropy.: (a) Evolution of capacitance C and M_r/M_s over time after a bias voltage of +3 V was applied for 180 s. (b) Time dependence of M_r/M_s at 4.6 ML Fe under different bias conditions. A positive gate voltage of +3 V is applied at $t = -150$ s until $t = 0$ s such that M_r/M_s saturates. At $t = 0$ s the gate voltage is either kept constant (+3 V), inverted (-3 V) or removed (0 V) and M_r/M_s is measured over time. The device schematics in the center of the figure show the orientation of the magnetic easy axis corresponding to the indicated values of M_r/M_s .

In metal insulator metal capacitors, the presence of charged defects results in an increase in capacitance due to an increase in the polarizability of the insulating layer.^{131,132} Therefore, measurements of the device capacitance can be used to correlate the presence

of defects with changes in magnetic anisotropy. We measure an initial device capacitance of 9.7 pF at zero bias, in agreement with expectations assuming dielectric constants of $\epsilon = 10$ and $\epsilon = 25$ for the MgO and ZrO₂ layer, respectively. After applying $V_g = + 3$ V, the capacitance increased by $\Delta C = 0.73$ pF or 7.5%. This capacitance increase is accompanied by a decrease of M_r/M_s by $\Delta M_r/M_s = - 0.48$. Upon removal of V_g , both ΔC and $\Delta M_r/M_s$ decay with time (Figure 2-17(a)) at the same rate and drop to half their initial values after $\sim 3,700$ s.

The giant magnitude, retention and asymmetry shown in Figure 2-16 and Figure 2-17 clearly demonstrate that voltage-induced electron accumulation/depletion in the Fe electrode cannot explain the observed effects. Instead, our results indicate that defect related processes likely occur in the device under bias application and that these processes can dominate its magneto-electric response. The focus of the remainder of this thesis will be to characterize these novel magneto-electric processes (Chapter 4 and 5), determine their microscopic origin (Chapter 6), engineer them into a viable device technology (Chapter 7) and explore their applications beyond magnetism (Chapter 8). Since defect driven processes are likely to be accelerated in polycrystalline and amorphous films, the following chapters will focus on sputter deposited Co/gadolinium oxide films.

3 EXPERIMENTAL METHODS*

The objective of this thesis is to investigate voltage induced effects on material properties in metal/metal-oxide bilayers. This chapter covers in detail the most important experimental methods and techniques that were employed to conduct this study. Section 3.1 focusses on the sample fabrication techniques, whereas Section 3.2 describes the methods used to characterize the properties of these samples. In addition to the experimental methods described here, each of Chapters 4 through 8 starts with a short experimental methods section in which more specific details of the respective experiments are described.

* Sections of this chapter, including figures, have been previously published in the following articles:

- Bauer, U., Emori, S. & Beach, G. S. D. Voltage-gated modulation of domain wall creep dynamics in an ultrathin metallic ferromagnet. *Appl. Phys. Lett.* **101**, 172403 (2012).
- Bauer, U., Yao, L., Emori, S., Tuller, H. L., Dijken, S. van & Beach, G. S. D. Magneto-ionic control of interfacial magnetism. submitted for publication (2014).

3.1 Sample Fabrication

This section discusses the main fabrication techniques used to prepare the samples discussed in Chapter 4 through 8. All samples were deposited by magnetron sputtering (Section 3.1.1) and patterned by either shadow mask lithography (Section 3.1.2) or electron beam lithography and lift-off (Section 3.1.3). Section 3.1.2 also describes a variety of custom tools and processes that were developed for the design, fabrication and positioning of shadow masks. Finally, in Section 3.1.4, two major strategies are described to investigate voltage-induced effects in metal/metal-oxide thin films with patterned gate electrodes.

3.1.1 Sputter Deposition

Sputter deposition is a widely used thin film deposition technique. Applications in microelectronics have been the main driving force to develop and optimize sputter deposition technology over the last decades.¹³³ But sputter deposition also plays a critical role in a wide range of other areas, such as the information recording, optical coating, automotive, and biomedical industry.¹³³ Sputter deposition is a physical vapor deposition technique that relies on bombardment with energetic ions to eject atomic species from the surface of a target material.¹³³ The ejected atoms then impinge on the surface of a substrate where they form a thin film. The great advantage of sputter deposition is its versatility and flexibility. Virtually all classes of solid materials, including metals, oxides, and semiconductors, can be sputter deposited.¹³³ Moreover, sputter deposition is compatible with high/ultra-high vacuum conditions and micro/nano lithography techniques.

All the samples studied in Chapters 4 through 8 were deposited by sputter deposition, using the high vacuum magnetron sputtering system shown in Figure 3-1 and described in References [68,134,135]. The system comes equipped with four sputter guns (Figure 3-1(j)) which are used to deposit multilayer film structures of up to four different materials within a single pump down. The sputter system reaches a background pressure as low as

8×10^{-8} Torr by using a combination of a mechanical pump, a turbomolecular pump and two nitrogen cold traps. Ultra-high purity Ar (99.999%) is used as the sputtering gas and depending on the target material, a sputtering pressure between 2.0 mTorr to 3.5 mTorr is maintained by controlling the pump speed at constant Ar inflow of 30.0 sccm. All materials were deposited using DC power supplies. Metals layers were deposited in pure Ar environment, whereas oxide layers were deposited reactively under a partial pressure of ultra-high purity oxygen gas (99.993%).

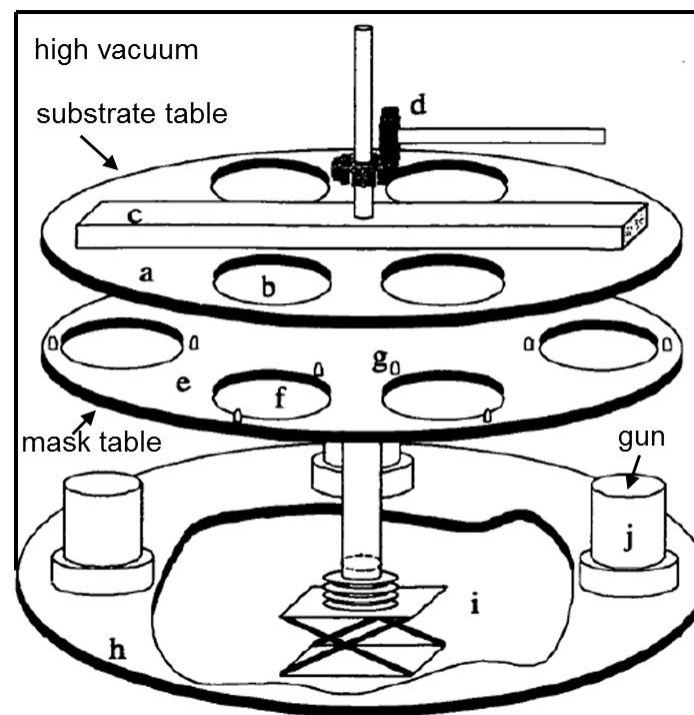


Figure 3-1: Interior of the high-vacuum magnetron sputter system.: (a) substrate table, (b) hole for mounting a substrate holder, (c) liquid nitrogen reservoir, (d) table rotation assembly, (e) mask table, (f) hole for mounting a mask, (g) pins to align the mask and substrate table, (h) chamber floor, (i) cutaway showing the jack and bellows below the chamber floor, (j) chimney and sputtering gun assembly. Adapted from References [134].

Each of the four sputter guns is mounted on the floor of the vacuum chamber and covered by a chimney, which constrains the flux of ejected target material to the its opening (see Figure 3-1(j,h)). The chimney of each gun can be opened or closed with a

pneumatically actuated shutter, to precisely control the deposition time and thus the layer thickness.

Just above the shutters, are the mask and the substrate table (see Figure 3-1(a,e)). Substrates are mounted with Cu tape on a substrate holder, which is then inserted face down in one of the four slots of the substrate table (Figure 3-1(b)). The substrate temperature can then be controlled with a liquid nitrogen reservoir on the substrate table (Figure 3-1(c)). The mask holder also exhibits individual slots (Figure 3-1(f)), which can be opened or closed with special metal inserts. By rotating the substrate table and aligning the substrate slots with their opened or closed counterparts on the mask holder, one can select the substrate holders on which material will be deposited.

Films are deposited in either one of two modes. In stationary mode, the substrate and mask table are stationary and a substrate is positioned directly above the desired sputter gun. In contrast, in rotary mode, the substrate and mask tables rotate with a period of ~ 1.7 s, which reduces the deposition rate by a factor of ~ 7 , but results in better thickness homogeneity and sub-nanometer control of film thickness. Correct alignment of the mask and substrate table allows fabrication of up to four multilayer samples with different layer thicknesses and/or layer sequences in rotary mode, in a single pump down.

Film thicknesses were determined from the deposition time and a known deposition rate. In order to determine the deposition rate for each material and deposition condition, the thickness of a film with precisely known deposition time was measured via x-ray reflectometry. The deposition rate can then be determined by dividing the film thickness by the deposition time.

All the samples discussed in Chapter 4 to 8 were deposited at RT on Si(100) wafers with a 50 nm thick thermal oxide. Ta films were grown at 2 mTorr of Ar, in rotary mode, and with a deposition rate of ~ 3 nm/min. The Pt, Co and Gd layers were deposited at 3 mTorr of Ar, in rotary mode, and with deposition rates of ~ 2 nm/min, ~ 1 nm/min and ~ 3 nm/min, respectively. The Au electrodes were grown at 3.5 mTorr of Ar, in stationary mode and with a deposition rate of ~ 30 nm/min. And finally, the gadolinium oxide (GdOx)

layers were reactively sputtered, in rotary mode, under an oxygen partial pressure of ~ 0.05 mTorr, and Ar partial pressure of 3 mTorr and with a growth rate of ~ 4 nm/min. Since the deposition rate changes over the lifetime of a target, the deposition rates differ slightly from experiment to experiment, which is why only approximate values are given here.

3.1.2 Shadow mask lithography

Shadow mask lithography is a very simple and yet powerful technique to pattern microstructures with high throughput and at low cost.¹³⁶ The technique relies on reusable masks which exhibits apertures corresponding to the desired features. The mask faces the deposition source and is placed in close contact with the sample such that during deposition, material is only deposited in the sample areas exposed by the apertures.

Compared to electron beam lithography, shadow mask lithography is a parallel technique and allows single step fabrication of micron scale features.¹³⁶ The resolution of shadow mask lithography is typically a few micrometers* which is why the technique is mainly used for features tens or hundreds of μm wide. This resolution limit is given by the unavoidable gap between the mask and the sample, which also results in one of the key features of shadow mask lithography, blurring.^{136,137} Due to blurring, features patterned by shadow mask are typically enlarged compared to the corresponding mask aperture and their edges are not sharp but rather show a gradually decrease in thickness.¹³⁷ The blurred edges of gate electrodes deposited by shadow mask lithography can also be seen in the optical micrograph shown in Figure 3-4(f).

In this work, shadow mask lithography was used to pattern circular gate electrodes for magneto-electric devices. The shadow masks were made from 10 mil thick sheets of polyether ether ketone (PEEK). PEEK is an organic polymer with excellent mechanical and

* While in our experiments the resolution of shadow mask lithography is a few micrometers, more sophisticated versions of this technique allow the fabrication of structures as small as ~ 10 nm.¹³⁶

chemical resistance that is also compatible with ultra-high vacuum conditions.¹³⁸ A Universal Laser Systems laser cutter with a 60 W CO₂ laser was used to cut circular apertures into the PEEK sheets. For this purpose, a design file with a centered square lattice of dots with a 500 μm spacing was created. The size of each dot was chosen to be smaller than the size of a single pixel at the maximum resolution of the laser cutter. This dot size guarantees that at each dot, the laser cutter only makes a single piercing shot, resulting in a circular aperture in the PEEK sheet. The diameter of each aperture can then be controlled simply by adjusting the laser power. Figure 3-2 shows that the aperture diameter can be varied from 30 μm to 100 μm by increasing the laser power from 12.5% to 25% of maximum output.

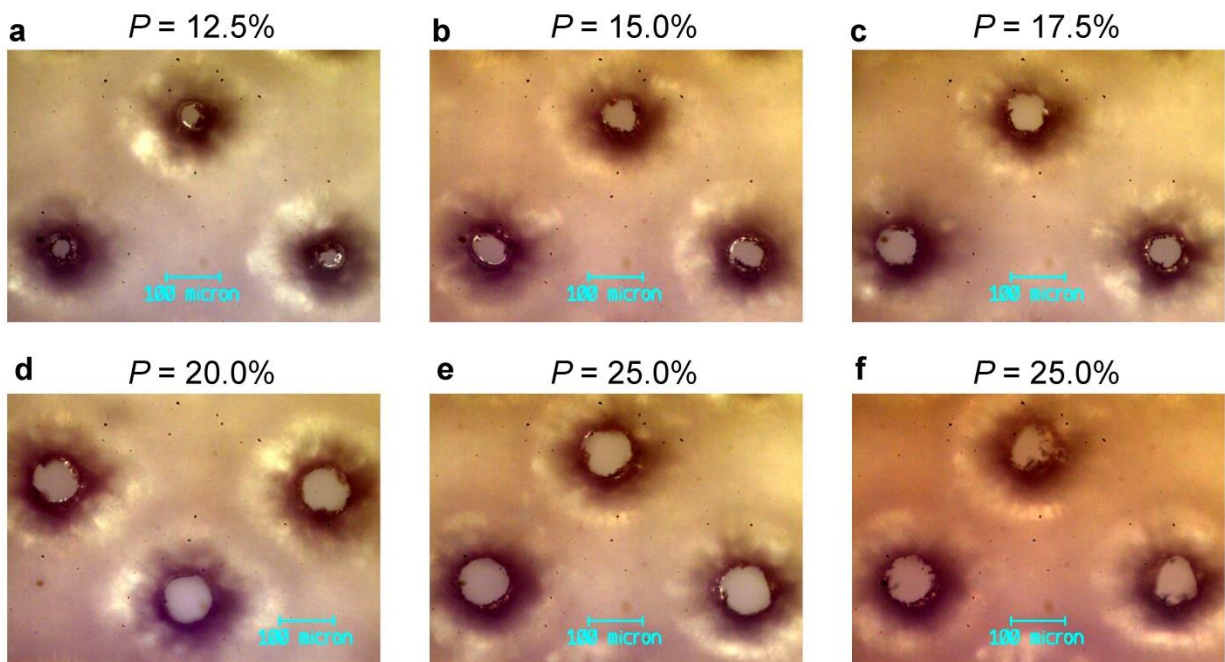


Figure 3-2: Shadow mask fabrication. (a-f) Optical micrographs of a 10 mil thick PEEK film in which three apertures were patterned with a laser cutter at varying laser power P . The PEEK silms in (a-e) were sonicated in isopropanol after laser cutting, whereas the micrographs in (f) was taken right after laser cutting, before sonication.

One side of the PEEK sheet is polished which reduces mechanical damage when it is in contact with the sample. During laser cutting, the unpolished side of the PEEK faces

towards the laser, which guarantees that the apertures diameter is at a minimum on the polished side of the sheet, which will be in contact with the sample surface during deposition. Typically, apertures were cut within a 22 mm by 22 mm area of the PEEK sheet, which resulted in ~ 700 apertures on each mask (Figure 3-4 (e)). After laser cutting, the PEEK masks were sonicated in isopropanol for ~ 1 minute to remove debris and residual material from the apertures (see Figure 3-2(e,f)).

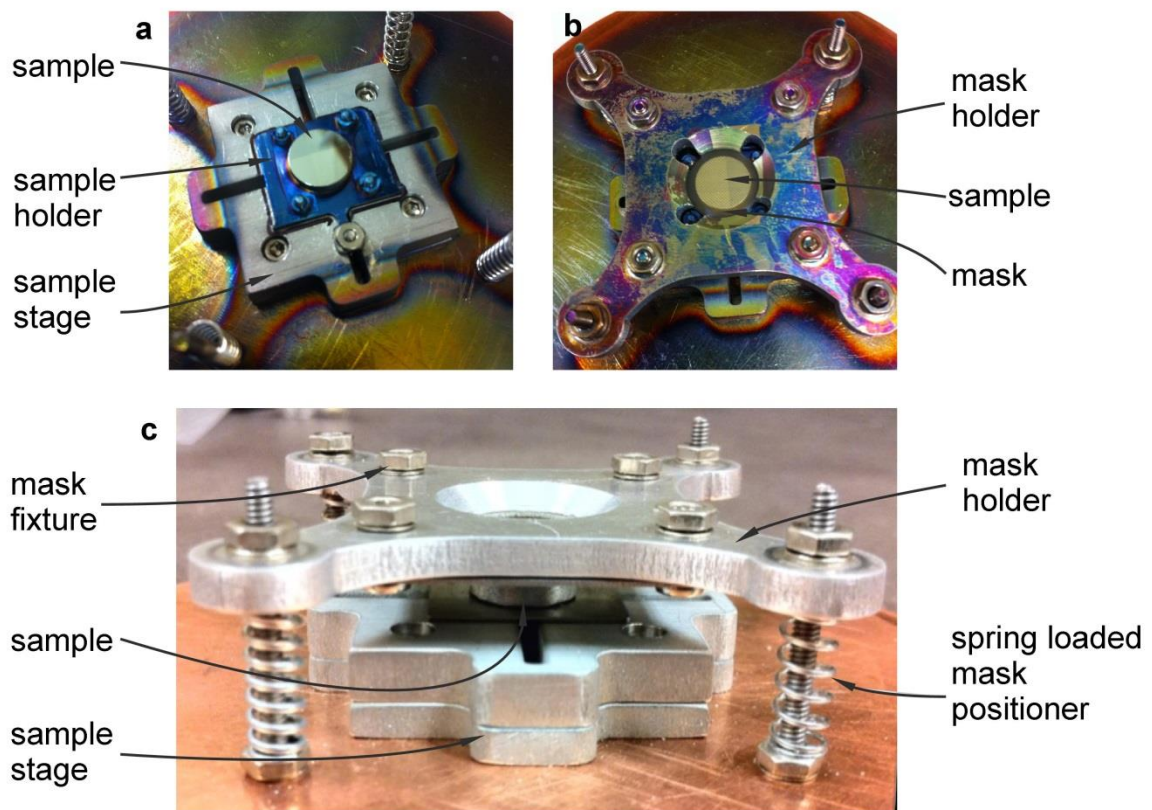


Figure 3-3: Shadow mask positioner for single crystal metal substrates. (a) Shown is a top view of the lower part of the mask positioner. A single crystal metal substrate its mounted on its custom made sample holder and fixed onto the sample stage. (b) Top view of the complete mask positioner, showing the mask holder with a PEEK mask in close contact to the single crystal substrate. (c) Side view of the mask positioner, showing the mask holder mounted on spring-loaded screws, which are used to position the mask in close contact to the sample. The mask positioner is mounted on a 3 inch Cu disk which can be directly inserted in one of the substrate slots of the magnetron sputter system described in Section 3.1.1.

For samples grown on robust Si substrates, close contact between shadow mask and sample can be achieved by taping the samples directly on the polished side of the PEEK mask. However, for samples grown on soft and fragile single crystal metal substrates, it can be challenging to position the shadow mask without damage to the sample. In order to minimize the mechanical stress on the sample, we designed a tool which allows precise positioning of the PEEK mask in very close proximity to the sample (see Figure 3-3).

The samples grown on single crystal metal substrates come on custom made sample holders, which are mounted on the sample stage of the mask positioner. Slits in the sample stage allow mounting of the samples in four different orientations with a single, low profile screw (see Figure 3-3(a)). The sample stage is surrounded by four spring-loaded screws that suspend the mask holder above the sample and keep it in the desired position (Figure 3-3(b,c)). A PEEK mask is mounted onto the lower side of the mask holder, facing the sample. By tightening the spring-loaded screws, the PEEK mask can be moved closer to the sample surface. The approach is halted when the mask is in close proximity, but does not yet exert mechanical stress on the single crystal sample.

Figure 3-4 illustrates the steps necessary to deposit gate electrodes on top of an oxide layer via shadow mask lithography. First, a PEEK shadow mask (see Figure 3-4 (e)) with the desired aperture diameter is placed in close contact with the sample (Figure 3-4 (b)). In order to keep the gap between mask and sample at a minimum, Cu tape is used to fix the sample directly on the backside of the PEEK mask. The backside of the peek mask is polished which reduces mechanical damage when it is in close contact with the sample. The electrode material is then sputter deposited (see Section) through the shadow mask (Figure 3-4(c)). Material is deposited on the sample only right underneath the mask apertures, everywhere else, the material is deposited on the mask. After deposition, the mask is removed from the sample which reveals the array of patterned electrodes on the sample (Figure 3-4(d)). The masks can be reused for future depositions.

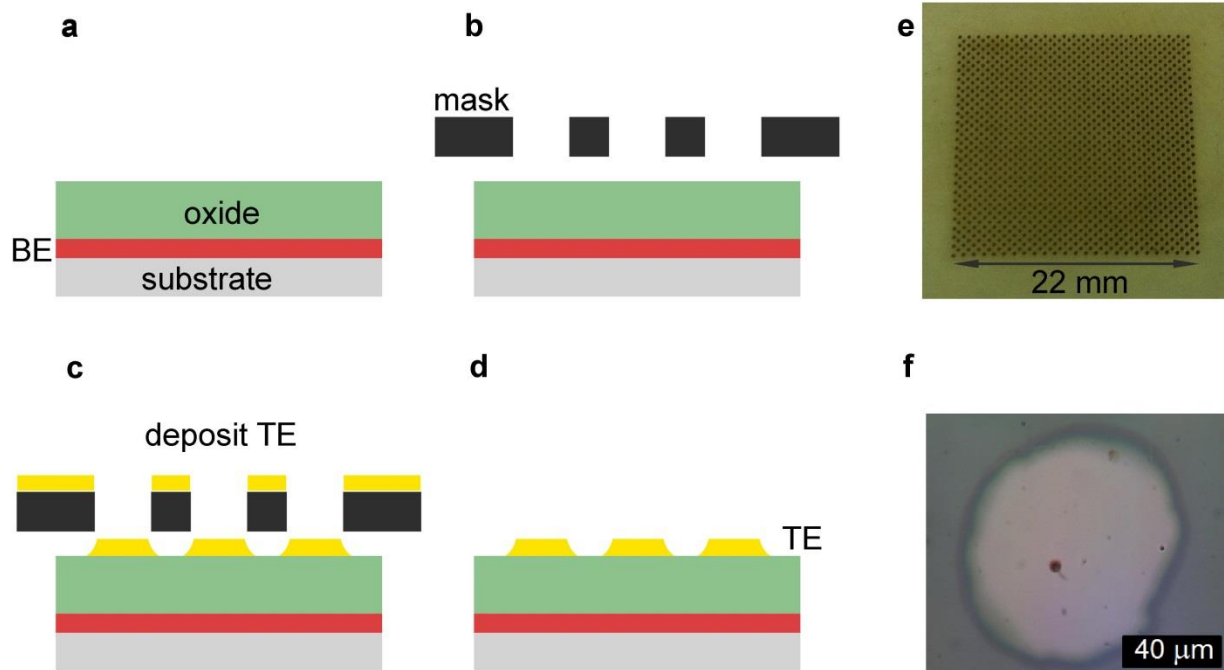


Figure 3-4: Shadow mask lithography. (a-d) Schematics of the fabrication steps necessary to pattern the top electrodes (TE) of magneto-electric devices by shadow mask lithography. The devices consist of a ferromagnetic bottom electrode (BE) and a gate oxide deposited on a thermally oxidized Si substrate. (e) Image of a shadow mask made of PEEK with ~ 700 apertures of $\sim 100 \mu\text{m}$ diameter. (f) Optical micrograph of a representative electrode deposited through the mask shown in (e).

3.1.3 Electron beam lithography and lift off

In electron beam lithography, a focused electron beam is used to write patterns into an electron-sensitive film called resist.¹³⁹ Exposure to electrons modifies the chemical properties of the resist and makes the exposed area either more soluble (positive resist) or less soluble (negative resist).¹³⁹ The written pattern is then revealed by removing the soluble part of the resist in a development step. Due to its flexibility and high resolution, electron beam lithography is widely used at universities and laboratories.¹³⁹ Compared to shadow mask lithography, electron beam lithography offers much higher resolution ($\sim 10 \text{ nm}$) but suffers from significantly lower throughput and higher cost.¹³⁹

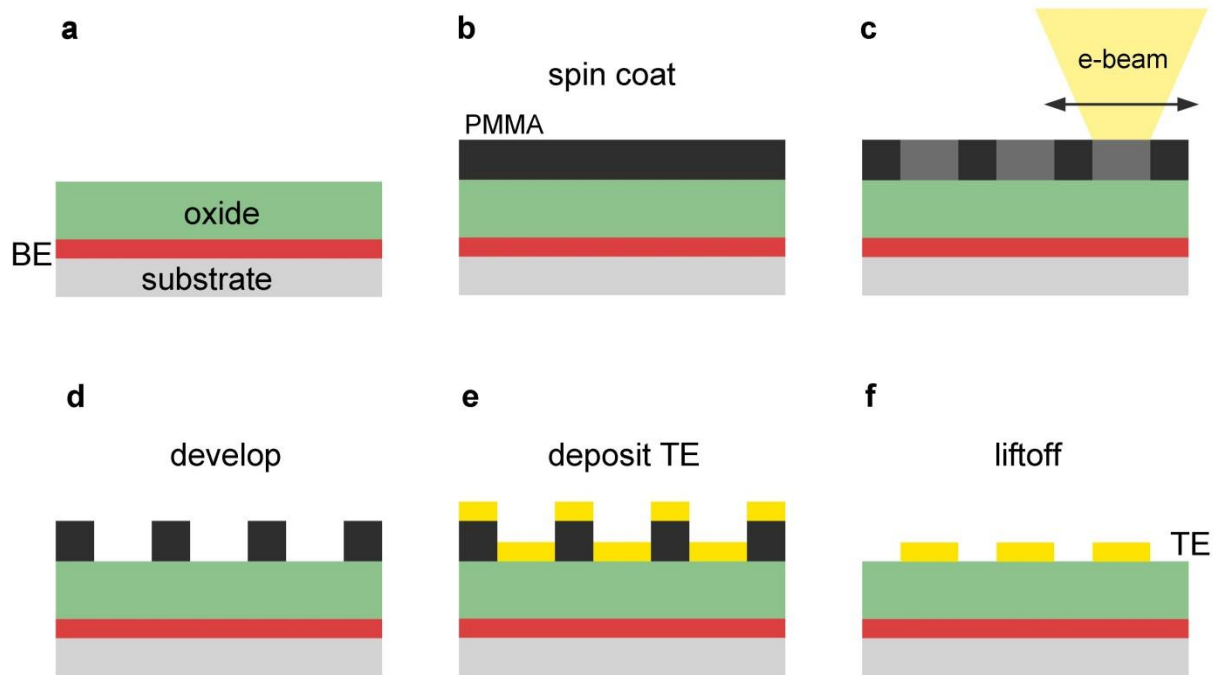


Figure 3-5: Electron beam lithography and lift-off. (a-f) Schematics of the fabrication steps necessary to pattern the top electrodes (TE) of magneto-electric devices by electron beam lithography. The devices consist of a ferromagnetic bottom electrode (BE) and a gate oxide deposited on a thermally oxidized Si substrate.

In this work, we use electron beam lithography, sputter deposition (Section 3.1.1), and lift-off to pattern magnetic nanowires devices (see Chapter 5), and micron scale gate electrodes with sharp edges (see Chapter 5, 6). Figure 3-5 shows the fabrication steps necessary to pattern gate electrodes on top of a metal/metal-oxide bilayer. First, the oxide layer is spin-coated with a 100 -200 nm thick layer of poly(methyl methacrylate) (PMMA) (Figure 3-5(b)), which acts as a positive resist in electron beam lithography. The PMMA layer is then baked to relax the polymer chains into an ordered array.¹³⁹ A relatively low baking temperature and time of 90 °C and 1 minute were chosen to prevent annealing of the underlying metal/metal-oxide bilayer during baking.

The electrode pattern is written with a Raith 150 scanning electron beam writer with an acceleration voltage of 10kV and an aperture size of 30 μm or 60 μm (Figure 3-5(c)). After writing, the pattern is developed by immersing the samples in a 3:1 (by volume) solution of isopropanol and methyl isobutyl ketone (MIBK) which removes the PMMA in the areas exposed to the electron beam (Figure 3-5(d)). In order to remove residual resist at the bottom of the patterned structures, the sample is descummed for 2 s in an oxygen plasma asher at 50 W. The electrode material is then deposited by magnetron sputtering (Figure 3-5(e)). In a final step, called lift-off, the excess sputtered material is removed together with the remaining PMMA and only the patterned electrodes remain (Figure 3-5(f)).

3.1.4 Sample structure and layout

The aim of this thesis is to investigate the voltage-induced effects on material properties in metal/metal-oxide bilayers. Chapters 4 through 7 focus on voltage effects on magnetism whereas in Chapter 8 the broader effects on material properties are explored. Common to all experiments is a simple device design, which resembles that of a parallel plate capacitor. In this case, the bottom electrode of the capacitor is made up of an ultra-thin ferromagnetic metal layer, which is separated from a noble metal top electrode by a thin gate oxide (see Figure 3-6(e)).

In order to investigate voltage-induced effects on a variety of material properties, the device needs to be optimized not only for good electrical properties such as low leakage current and high breakdown voltage, but also for the desired magnetic, ionic, optical and mechanical properties. This optimization typically requires adjusting layer thicknesses, material composition and introducing additional layers into the stack.

All the samples used in this work were deposited by sputter deposition and share the same layer sequence (see Figure 3-6(e)). The bottom electrode is made up of a Ta/Pt/Co trilayer which is directly deposited on a Si(100) substrate with a 50 nm thick thermally grown oxide layer. The role of the thermally grown SiO_2 layer is to insulate the bottom

electrode from the bulk of the substrate. The 4 nm thick Ta layer serves a double purpose; it guarantees good adhesion between SiO₂ and the bottom electrode and introduces a (111)-texture in the following Pt/Co layer.¹⁴⁰⁻¹⁴² In the (111)-textured Pt/Co layer the 3 nm thick Pt promotes PMA in the Co layer through Pt 5*d* - Co 3*d* hybridization at the Pt/Co interface.⁶¹ In addition to the Pt/Co interface, hybridization between the Co 3*d* and the O 2*p* orbitals at the Co/GdOx interface also contributes strongly to PMA.^{47,64,89,143}

The strength of PMA in the Co layer can be tuned by changing the Co thickness. In the Pt/Co/GdOx system, the Co layer exhibits PMA in a thickness range of ~ 0.7 nm to ~ 1.3 nm, with the maximum PMA of ~ 7×10⁶ erg/cm³ occurring at 0.9 nm. For our experiments, we use Co films of either 0.9 nm or 1.0 nm thickness, to maximize PMA. In addition to promoting PMA, the GdOx layer also acts as a high-*k* gate oxide and insulates the bottom electrode from the top electrode.¹⁴⁴ During the course of the experiments described in Chapter 4 to 8 the GdOx thickness was varied between 3 nm and 40 nm. Consistent with an interface mediated effect, no dependence of PMA on the GdOx thickness was found in this thickness range.

The top electrodes consist of a Ta/Au stack. The role of the 1 nm to 2 nm thick Ta layer is to improve adhesion between the GdOx and Au, which reduces damage to the electrodes when they are contacted with microprobe tips. As a noble metal, Au is unaffected by voltage-driven chemical reactions and provides good electrical contact in air. Au was also chosen because of its sharp drop in reflectivity in the mid visible light range.^{145,146} The relatively low reflectivity allows us to probe the magnetic properties of the Co layer with a 532 nm laser even for 5 nm to 12 nm thick Au layers.

The simplest way to fabricate such devices is to deposit the bottom electrode and gate oxide layer as a continuous film on the insulating substrate (Figure 3-6(a,b)). After breaking vacuum, the top electrode layer is deposited and patterned into circular electrodes (see Figure 3-6(c)), by using either shadow mask lithography (Section 3.1.2) or electron beam lithography and lift-off (Section 3.1.3). The continuous oxide layer protects the bottom electrode from atmosphere during the lithography step. An electrode diameter

of $\sim 100\ \mu\text{m}$ was found to be ideal, because the electrodes are large enough to accommodate the MOKE laser spot and microprobe tips, and small enough to operate the device at very low leakage current.⁸⁹ The simplicity however comes at a price. Since the bottom electrode is sandwiched between the insulating substrate and the gate oxide layer, it is difficult to make electrical contact to it. Two strategies are employed to overcome this problem; the first relies on locally breaking-down the gate oxide (Figure 3-6), whereas the second requires an additional lithography step (Figure 3-7).

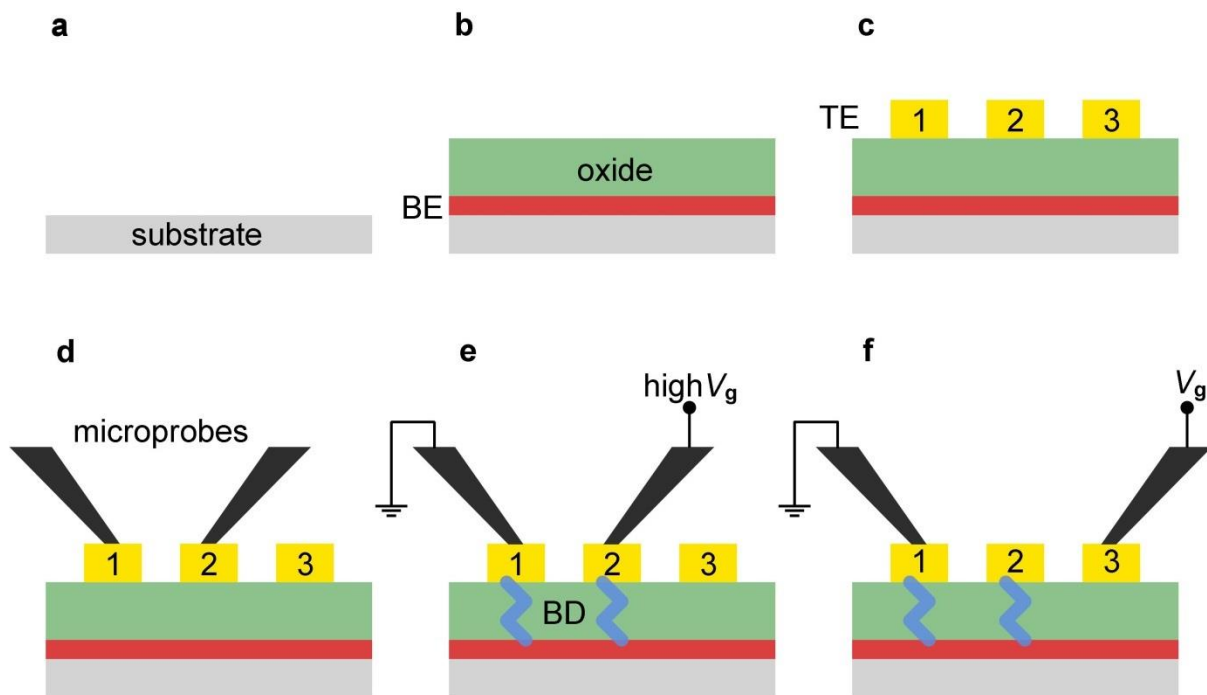


Figure 3-6: Procedure to contact the bottom electrode in thin film capacitors. (a) Thin film capacitors are deposited on a thermally oxidized Si(100) substrate. (b) The ultra-thin Ta/Pt/Co bottom electrode (BE) and GdOx gate oxide are deposited on the substrate. (c) Ta/Au top electrodes (TEs) are deposited on the oxide by shadow mask lithography to complete the capacitor design. Three exemplary TEs, electrode 1, 2 and 3 are shown. (d) Electrode 1 and 2 are contacted with BeCu microprobes. (e) Electrode 1 is grounded while a high gate voltage V_g is applied to electrode 2. The high V_g results in dielectric breakdown (BD) and formation of a conductive filament through the oxide. (f) The microprobe on electrode 1 grounds the BE through the conductive filament, while the second microprobe can be used to apply V_g to other TEs such as electrode 3.

Figure 3-6 illustrates the steps required to employ the first strategy. In order to make electrical contact to the bottom electrode, two top electrodes are contacted with microprobe tips (see Figure 3-6(d)). With the microprobes, one of the electrodes is grounded, whereas a gate voltage V_g is applied to the other one (see Figure 3-6(d)). At a high V_g , the gate oxide underneath the two electrodes will undergo hard dielectric breakdown (BD), resulting in a conductive filament between each of the two top electrodes and the bottom electrode (Figure 3-6(e)).¹⁴⁷ The microprobe used to apply high V_g is then used to contact other top electrodes, while the other microprobe remains in place to ground the bottom electrode through the conductive filament. With this procedure performed once at the beginning of an experiment, the voltage response can be investigated at several top electrodes. However, due to re-oxidation of the conductive filament over time,^{109,118} the contact to the bottom electrode has to be reestablished regularly.

The second strategy avoids this problem by introducing a dedicated contact pad for the bottom electrode (see Figure 3-7). To achieve this, shadow mask lithography is used to deposit a macroscopic Ta(5 nm)/Pt(10 nm) contact pad on one end of the insulating substrate (Figure 3-7(a,b)). Half of this contact is then again blocked by a shadow mask during deposition of the bottom electrode and oxide layers (Figure 3-7(c)). As a result, the bottom electrode and the contact pad overlap with each other, such that the bottom electrode can be easily contacted by landing a microprobe on the contact pad (Figure 3-7(e)). With one microprobe positioned on the contact pad, a second microprobe can then be used to study the voltage response on top electrodes distributed all across the oxide film. This strategy provides superior electrical contact, which more than compensates for the required extra step during sample fabrication.

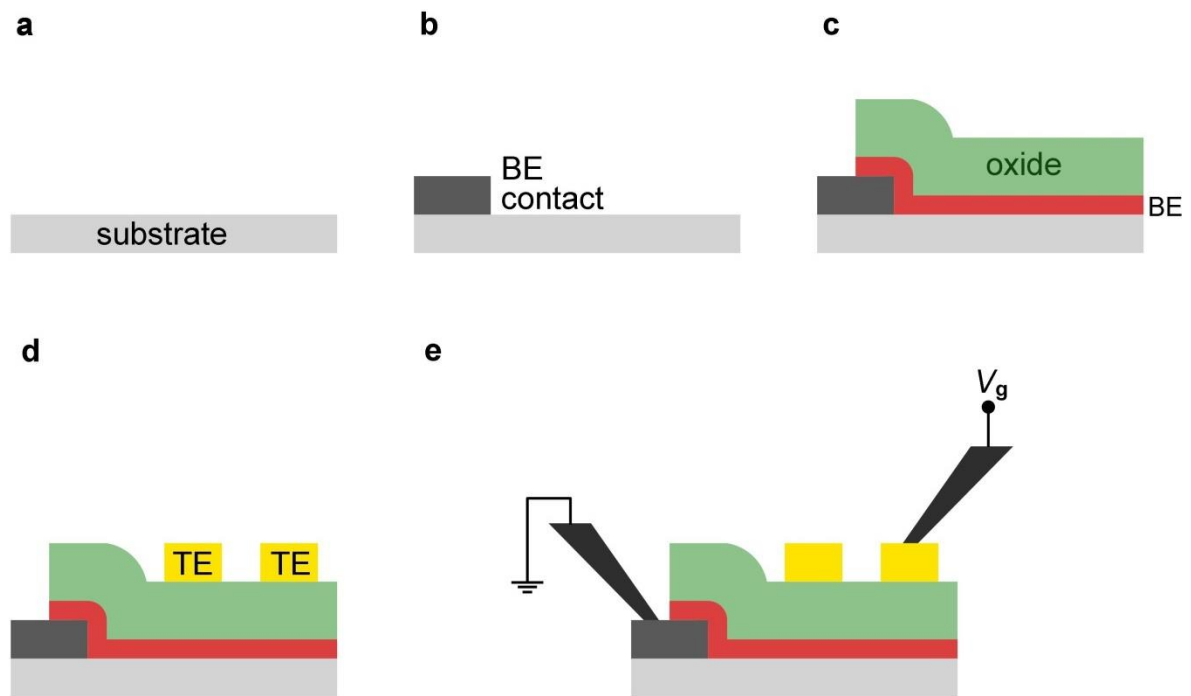


Figure 3-7: Improved procedure to contact the bottom electrode in thin film capacitors. (a) Thin film capacitors are deposited on a thermally oxidized Si(100) substrate. (b) A macroscopic Ta/Pt contact pad is patterned via shadow mask lithography. (c) The ultra-thin Ta/Pt/Co bottom electrode (BE) and GdOx gate oxide are deposited on the substrate while half the contact pad is blocked off with a mask. (d) The capacitor design is completed by deposition Ta/Au top electrodes (TEs) on the oxide layer by shadow mask lithography. (e) A BeCu microprobe is landed on the contact pad to ground the BE, while a second BeCu microprobe is used to apply a gate voltage V_g to one of the TEs.

3.2 Sample Characterization

This section described the main characterization techniques used to investigate the samples discussed in Chapter 4 through 8. Apart from vibrating sample magnetometry (Section 3.2.5), all experiments were performed on the time-resolved scanning magneto-optic Kerr effect system discussed in Section 3.2.2. This system offers optical and electrical access to the sample, allows application of in-plane and out-of-plane magnetic fields and control over the sample temperature. With this setup, the magnetic properties of a sample and its modifications under voltage, temperature, and illumination can be probed via the magneto-optic Kerr effect, which is explained in Section 3.2.1. Finally, a range of novel techniques is discussed that allow the study of magnetic DWs (Section 3.2.3) and magnetic anisotropy (Section 3.2.4), with spatial and temporal resolution.

3.2.1 Magneto-optic Kerr Effect

Magneto-optic Kerr effect (MOKE) polarimetry is an important tool to study the magnetic properties of magnetic thin films and microstructures. The popularity of the technique stems from its versatility and monolayer sensitivity, which allows the measurement of magnetic hysteresis loops even on ultra-thin magnetic structures.⁶⁵ In contrast to vibrating sample magnetometry (see Section 3.2.5), a MOKE polarimeter allows acquisition of magnetic hysteresis loops on short time scales (< 1 s), but the MOKE signal does not provide a quantitative measure of the sample magnetization.

The MOKE refers to the change in polarization that occurs when linearly polarized light is reflected off a magnetized surface. Figure 3-8(a) shows a schematic of the experimental setup typically used for MOKE polarimetry.⁶⁵ A Glan-Thompson polarizer is used to linearly polarize the light from a laser source. When the linearly polarized light is reflected from a magnetic thin film, interaction between the light and the magnetization results in a rotation of the polarization axis (i.e., the Kerr rotation) and a slight ellipticity (i.e., the Kerr ellipticity).⁶⁹ The reflected light then passes through a second polarizer, the so called

analyzer, which is set at a small angle δ from cross polarization with the incident polarizer. As a result of the nearly perpendicular polarization axes, this setup is very sensitive to the Kerr rotation Φ' . The measured Kerr intensity is then of the form:¹⁴⁸

$$J = J_0(\delta^2 + 2\delta\Phi') \quad (3.1)$$

If instead a quarter wave plate is inserted between the sample and the analyzer (see Figure 3-9), Kerr rotation Φ' and Kerr ellipticity Φ'' are interchanged and the measured intensity is proportional to the Kerr ellipticity.⁶⁵

$$J = J_0(\delta^2 + 2\delta\Phi'') \quad (3.2)$$

Whether Kerr rotation or ellipticity results in a larger intensity depends on the angle of incidence, the laser wavelength and the magnetic material.¹⁴⁹ But in both cases, the detected signal is proportional to the magnetization of the thin film, and magnetic hysteresis loops can be measured by recording the Kerr intensity, while sweeping the external magnetic field. Since MOKE is an optical technique, it is only sensitive to the magnetic material within the penetration depth of the laser light, which is ~ 5 nm in transition metal ferromagnets.⁶⁵ Because of this surface sensitivity, MOKE is sometimes also referred to as the surface magneto optical Kerr effect (SMOKE).⁶⁵

Fundamentally, MOKE results from a combination of spin orbit coupling and the net spin polarization in a ferromagnetic metal.¹⁵⁰ The difference in spin polarization results in different absorption coefficients for left and right circularly polarized light in the ferromagnet.¹⁵¹ Since linear polarized light can be treated as the sum of left and right circularly polarized light, the different attenuation of the two components in the ferromagnet results in a rotation of the polarization axis and a slight ellipticity.⁶⁹ An in depth discussion of the microscopic and macroscopic origin of MOKE can be found elsewhere.^{65,150-152}

Typically three cases are distinguished for MOKE; the polar, longitudinal and transverse Kerr effect. If the magnetization is perpendicular to the film plane, the polar Kerr effect (Figure 3-8(b)) is measured. The longitudinal Kerr effect (Figure 3-8(c)) can be

measured if the magnetization is in the film plane and parallel to the plane of incidence of the light. But if instead the magnetization is in the film plane but perpendicular to the plane of incidence, the transverse Kerr effect is measured (Figure 3-8(d)). Due to its dependence on the square of the refractive index of the magnetic thin film, the polar Kerr effect is typically an order of magnitude larger than the other Kerr effects.¹⁵² Since all samples investigated in this thesis exhibit PMA, the MOKE signal is due to the polar Kerr effect and hysteresis loops are measured by sweeping a magnetic field perpendicular to the film plane.

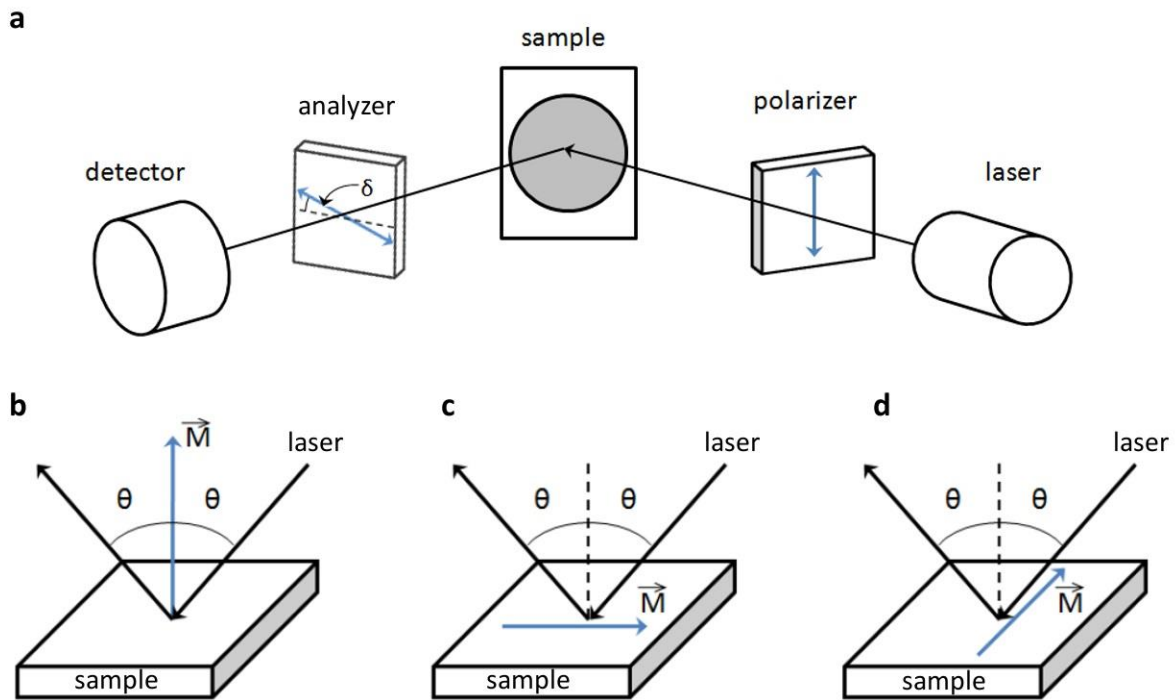


Figure 3-8: The magneto-optic Kerr effect. (a) Schematic of the optical setup required for MOKE polarimetry on a magnetic thin film. The blue arrows indicate the polarization axis of the polarizer and analyzer and δ specifies the angle from cross polarization. Not shown is the magnetic field which is usually applied parallel or perpendicular to the sample plane. (b-d) Schematics of polar (b), longitudinal (c) and transverse MOKE (d). Shown are the incident and reflected laser light (with incidence angle θ) and the magnetization vector \vec{M} . Adapted with permission from Reference [153].

3.2.2 Time-Resolved Scanning Magneto-optic Kerr Effect System

Time-resolved scanning MOKE adds a focused probe laser, a high resolution scanning stage and a high bandwidth detector to the standard MOKE setup (see Section 3.2.1), which allows probing of magnetic properties and imaging of DW dynamics in ferromagnetic thin films and microstructures with high spatial and temporal resolution.¹⁵⁴ The scanning MOKE system used in this work is based on the setup described by Nistor et al.¹⁵⁴. It relies on a continuous wave probe laser and achieves high temporal resolution by using a detector system and electromagnet with high speed response.¹⁵⁴ The spatial resolution of the system is diffraction-limited but a resolution of $\sim 3 \mu\text{m}$ can be readily achieved in practice.

In addition to its high spatial and temporal resolution the advantage of scanning MOKE is its versatility and flexibility. Conventional MOKE microscopy only allows static imaging of domain configurations, and the field driving DW motion is turned off during imaging.^{75,77,91} In contrast, scanning MOKE can be used to investigate DWs dynamically, while they are driven by field or current. DW dynamics can also be investigated by electrical techniques, such as the anomalous Hall effect. Electrical techniques however, typically allow detection of magnetic DWs only at specific locations and often require the use of special device geometries and structures to facilitate the measurement.^{73,91} In comparison, scanning MOKE is an optical technique and allows investigation of almost arbitrary sample geometries, does not require modifications to the sample structure, and allows probing at any location of the sample, as long as optical access to the magnetic layer is possible.

Figure 3-9 shows the schematics of the time-resolved scanning MOKE system used in this work. Since all samples investigated in this work exhibit PMA, the system is set up in polar MOKE geometry (see Section 3.2.1) with the laser in perpendicular incidence on the sample. A continuous wave laser diode (CrystaLaser) with 532 nm wavelength is used as the MOKE probe. The laser light is initially collimated by a 10x beam expander and two polarizers, labeled attenuator and polarizer in Figure 3-9, are used to attenuate and

linearly polarize the light. By rotating the attenuator with respect to the polarizer, the laser power incident on the sample can be varied from 1 mW to 10 mW. A 10x objective lens is mounted on linear piezoelectric drive which is used to focus the laser to a $\sim 3 \mu\text{m}$ diameter spot on the sample. The laser spot size is determined with the “knife edge” technique¹⁵⁴ by scanning the spot across a sharp lithographic feature on the sample. Since the objective lens is in relative close proximity to the electromagnets, it is surrounded by high permeability μ metal to shield it from magnetic fields and minimize the Faraday effect inside the objective lens.

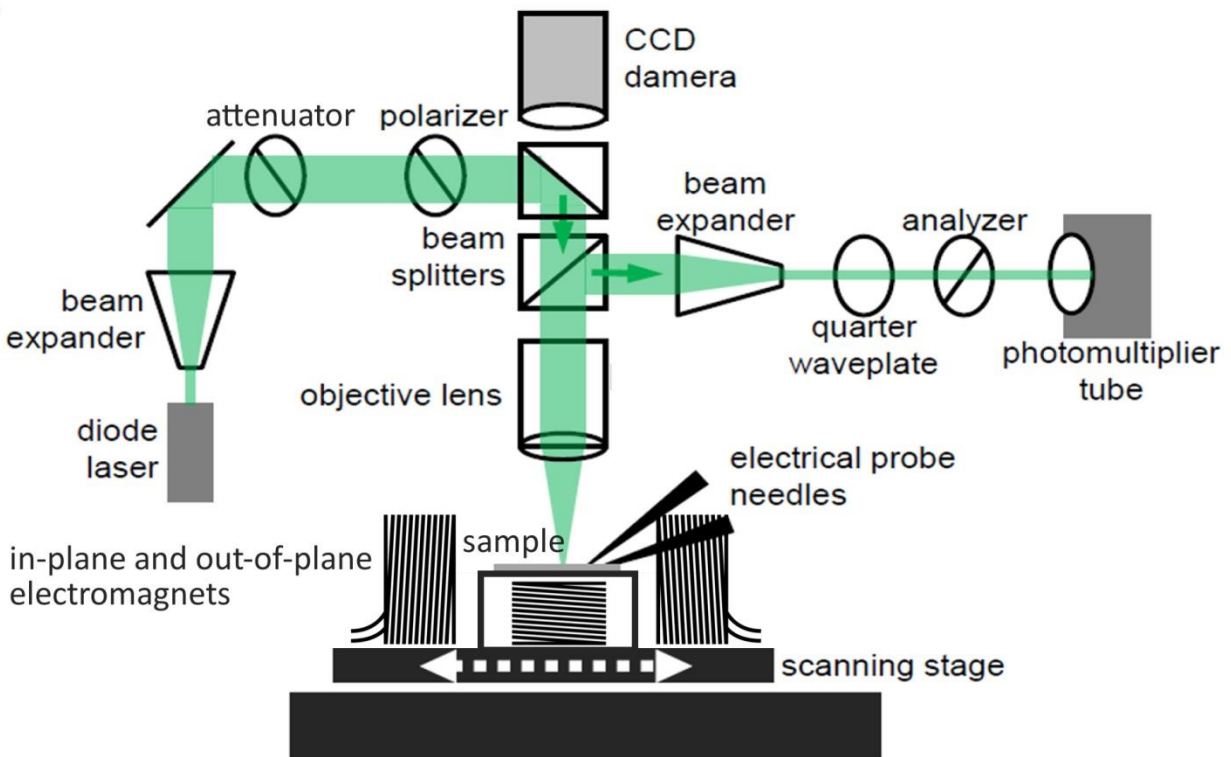


Figure 3-9: Scanning magneto-optic Kerr effect system. Schematic of the scanning MOKE system showing the path of the laser through the MOKE optics (highlighted in green), microprobes for electrical contact and electromagnets to apply magnetic field parallel and perpendicular to the sample. Adapted with permission from Reference [68].

The laser light reflected from the sample, passes through a quarter wave plate and the analyzer before reaching the photomultiplier tube detector. The quarter wave plate allows

us to measure Kerr ellipticity rather than Kerr rotation,⁶⁵ which results in a significantly larger MOKE signal from the investigated samples. The detector signal is then amplified by a Stanford SR560 low noise voltage preamplifier, digitized, and recorded by a LabVIEW program. With this setup, a signal to noise ratio > 20 can be readily achieved on Pt/Co/GdO_x films without averaging.

The sample is mounted on a AeroTech A3200 high resolution (50 nm) scanning stage, which allows positioning of the MOKE laser spot on the sample by moving the stage with respect to the “stationary” laser. The sample temperature is controlled to within ± 0.1 °C by a thermoelectric module placed underneath the sample. A K-type thermocouple measures the temperature right next to the sample substrate, and thermal paste guarantees good thermal contact between the thermoelectric module, sample substrate, and thermo couple. Unless otherwise stated, all the measurements presented in this work were performed at RT.

The scanning stage layout is modular and allows the use of different electromagnets, which are mounted directly on the scanning stage. For most of the measurements described in this work, an out-of-plane magnet with ~ 300 μ s rise time and a maximum field of 650 Oe was employed. However, for the MOKE technique described in Section 3.2.4, two electromagnets are required. Here, a large in-plane magnet capable of applying ~ 6000 Oe in the sample plane was used together with an out-of-plane air coil positioned right underneath the sample.

Electrical contact to the sample is made with up to 4 Signatone microprobe positioners, which are mounted on the scanning stage. The sample and microprobe tips are imaged through a CCD camera, which allows precise positioning of the probes on the sample. Mechanically compliant BeCu microprobes with ~ 15 μ m tip diameter and low contact resistance are used for voltage application, while relatively stiff W microprobes with ~ 25 μ m tip diameter are used to mechanically create DW nucleation sites.^{89,90} With the exception of Figure 7-4, a Keithley 2400 Sourcemeter is used to apply voltage and simultaneously monitor the current flow through the device. Usually, the current

compliance is set to $\sim 1 \mu\text{A}$ to protect the magneto-electric devices from hard dielectric BD. In Figure 7-4, the voltage waveform and short voltage pulses were applied with a Stanford DS345 function generator. For all investigated devices, the specified gate voltage V_g is applied to the top electrode, while the bottom electrode is grounded.

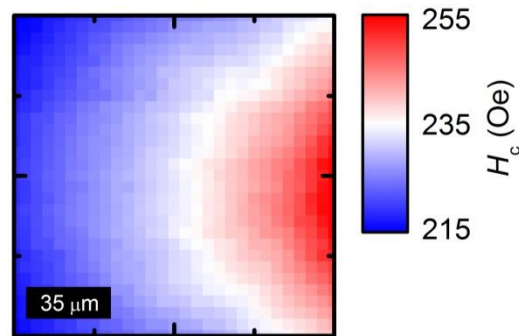


Figure 3-10: Scanning MOKE map. Map of a Pt/Co/GdO_x film showing the spatial dependence of the coercivity H_c close to an artificial nucleation site.

Apart from data acquisition, the LabView program also controls the electromagnets and the scanning stage, which allows partial automation of complex data acquisition tasks. Section 3.2.3 describes in detail how the time-resolved scanning MOKE system can be used to investigate DW dynamics and to image domain expansion in magnetic thin films. Another important capability of the system is to map out the magnetic properties across a magnetic thin film (see Figure 3-10). For this purpose, magnetic hysteresis loops can be measured locally by positioning the probe spot in the desired location and acquiring MOKE signal while sweeping the out-of-plane magnetic field. Local magnetic properties such as the coercivity and the remanence to saturation magnetization ratio can be extracted from the hysteresis loop. By measuring hysteresis loops across a two dimensional grid, these properties can then be mapped across the sample, with each point on the grid corresponding to a pixel of the final image.

3.2.3 Domain Wall Dynamics in Magnetic Thin Films Measured via MOKE

Measuring DW dynamics in continuous magnetic thin films typically relies on the presence of naturally occurring DW nucleation sites, which are randomly distributed across the film.^{75,91,155} This reliance on random nucleation sites presents a severe limitation when DW dynamics needs to be investigated in a specific location of the film, or close to certain features, such as gate electrodes. Here, we demonstrate a novel technique to characterize magnetic DW motion in continuous magnetic thin films. This technique allows us to reversibly create artificial nucleation sites with micrometer precision, image domain expansion from the nucleation site, and extract DW velocities. Figure 3-11 shows a schematic of the experimental setup and an exemplary data set from Ta(4 nm)/Pt(3 nm)/Co(1 nm)/GdO_x(40 nm) films. A 25 μm diameter blunt W microprobe is used to generate an artificial DW nucleation site through application of a local mechanical stress.^{89,90} After initially saturating the film magnetization, a reversed magnetic field step H is applied perpendicular to the film plane using an electromagnet with ~300 μs rise time. The driving field nucleates a reversed domain underneath the W probe tip, which then expands radially across the film. Magnetization reversal was detected via the polar MOKE signal using the ~3 μm wide focused laser spot positioned by a high-resolution scanning stage (see Section 3.2.2). Exemplary time-resolved MOKE transients are shown in Figure 3-11(b) for several positions of increasing distance from the W probe tip. Each transient corresponds to the averaged signal acquired from 50 reversal cycles to account for stochasticity, and hence represents the integrated probability distribution of switching times at a given location.¹⁵⁶ The mean reversal time ($t_{1/2}$), taken as the time at which the probability of magnetization switching is 50 %, increases linearly with increasing distance from the nucleation site, as expected for DW propagation. The sharp transitions in these averaged transients indicate that DW motion is highly repeatable from cycle to cycle.

Magnetic DW velocity is measured by acquiring time-resolved MOKE signal transients at several positions along a line extending radially from the artificial nucleation site. The mean magnetization reversal time $t_{1/2}$ is the extracted from each MOKE transient and

plotted as a function of distance from the nucleation site (see Figure 3-11(c)). The DW velocity is then given by the inverse slope of the linear fit of $t_{1/2}$ versus position. The offset from the origin in Figure 3-11(c) is likely due to the small uncertainty in position of the nucleation site due to the finite size of the W microprobe.

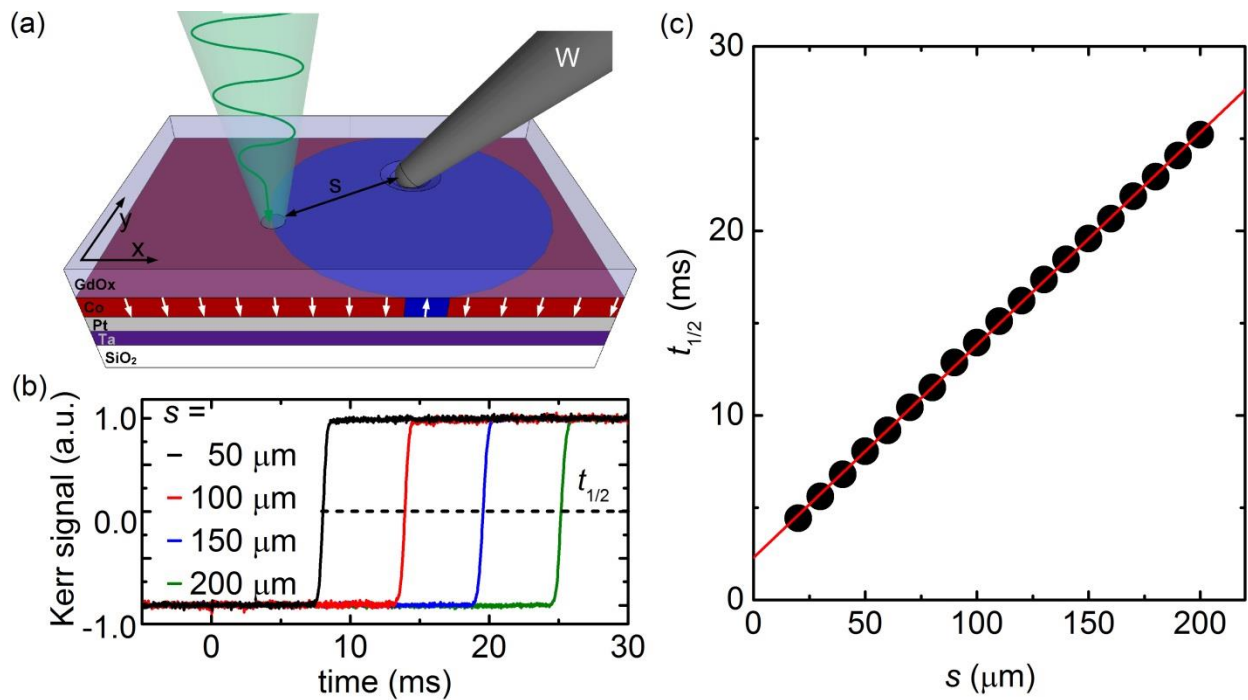


Figure 3-11: Domain wall velocity measurements in magnetic thin films. (a) Experiment schematic showing Pt/Co/GdOx structure, W microprobe to create artificial DW nucleation site and focused MOKE laser probe. (b) Normalized MOKE signal transients measured at different distances s between MOKE probing spot and artificial nucleation site. (c) Average domain wall arrival time as a function of distance from artificial nucleation site. Red line is linear fit of the data. Offset from origin is due to uncertainty in position of nucleation site due to finite size of W microprobe.

By acquiring MOKE signal transients across a two dimensional grid in the vicinity of the nucleation site, the average DW trajectory can be imaged with μm spatial and μs time resolution. Each point on the grid represents a pixel of the final magnetization image and the MOKE transient measured at each pixel contains its time evolution during domain expansion. An image of the magnetic domain at a time t after application of the reversed field step can then be reconstructed from the magnetization signal of all the pixels at that

point in time. Combining these momentary magnetization images, creates a movie of the averaged domain expansion around the nucleation site.

Figure 3-12(a)-(c) shows maps of the normalized polar MOKE signal, corresponding to the perpendicular magnetization component M_z , at several times t after application of a field step $H = 170$ Oe. Here, MOKE signal transients were acquired over a $300 \mu\text{m} \times 300 \mu\text{m}$ grid area and each pixel corresponds to the averaged measurements of 50 reversal cycles. The images show that a reversed domain indeed nucleates beneath the W probe tip and expands radially and isotropically with time. Natural nucleation sites elsewhere in the film are sufficiently distant such that no other DWs reach the probed region under the conditions examined. The remarkably sharp and azimuthally-uniform (averaged) DW propagation front suggests smooth DW motion via thermally-activated creep through a fine-scale disorder potential. While DW creep is stochastic on the scale of the disorder potential, DW propagation is deterministic at the micrometer-scale resolution of this experiment.

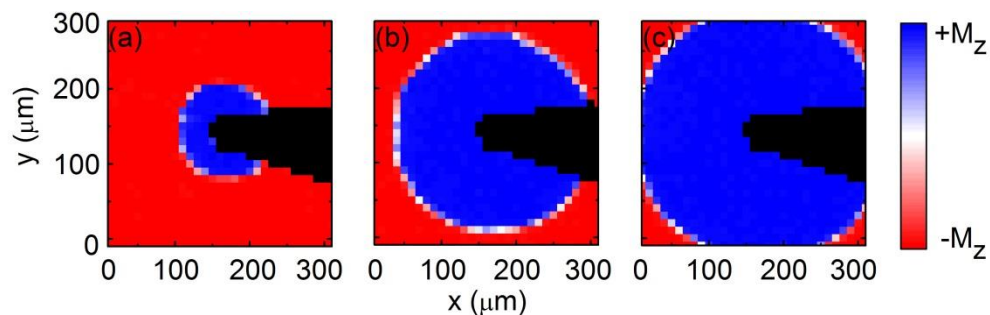


Figure 3-12: Time and space resolved magnetization maps. Polar MOKE maps, showing domain expansion from artificial nucleation site at $t = 6.3$ ms (a), 11.9 ms (b) and 14.7 ms (c) after application of magnetic field step. Black triangular area on right side of (a)-(c) and corresponds to W microprobe tip. The maps were measured at a driving field of $H = 170$ Oe and $T = 35$ °C

3.2.4 Local Probing of Magnetic Anisotropy via Polar MOKE

We have developed a MOKE-based technique that allows local measurement of the anisotropy field H_k and provides direct, quantitative and local access to PMA. In contrast to

the vibrating sample magnetometry (see Section 3.2.5), this MOKE-based technique has the advantage of spatial resolution, allowing local probing of H_k and therefore PMA with micrometer resolution. Spatially resolved measurements are of particular interest for voltage control of magnetic anisotropy where the anisotropy modifications are typically limited to the area of small gate electrodes which is inaccessible by other techniques such as vibrating sample magnetometry.

A schematic of the experimental setup and a representative measurements are shown in of the MOKE-based technique are shown in Figure 3-13. The setup is designed for samples with PMA, i.e., uniaxial magnetic anisotropy with an easy axis perpendicular to the film plane. A focused laser with a $\sim 3 \mu\text{m}$ diameter probe spot is positioned on the area of interest and used to locally probe M_z , i.e., the out-of-plane magnetization component, via polar MOKE. We then exploit the high-sensitivity of the polar MOKE signal to measure M_z versus a hard-axis field H_x , to determine the anisotropy field H_k .

In order to enhance the signal to noise ratio, we apply a periodic waveform of positive and negative perpendicular field pulses H_z with a small air coil (Figure 3-13(b)) and measure the polar MOKE signal using a lock-in amplifier phase-locked to the H_z drive waveform. This signal is measured continuously while an in-plane field H_x is slowly swept. As long as H_x is below a sample-dependent threshold, magnetic hysteresis loops have unity M_r/M_s , (Figure 3-13(d)), so that the H_z waveform periodically switches the canted magnetization vector between states with positive M_z and negative M_z . The resulting polar MOKE signal waveform, shown schematically in Figure 3-13b, therefore takes the form of a square wave with an amplitude proportional to

$$M_z = M_s \cos(\arcsin(H_x/H_k)) \quad (3.3)$$

This expression corresponds to the easy-axis magnetization component in the presence of a hard-axis field H_x , obtained using the Stoner Wohlfarth single domain model (see also Section 2.2) that considers the Zeeman energy and uniaxial anisotropy energy. Equation

(3.3) was used to fit the experimental data (normalized lock-in signal versus H_x) to extract the anisotropy field H_k .

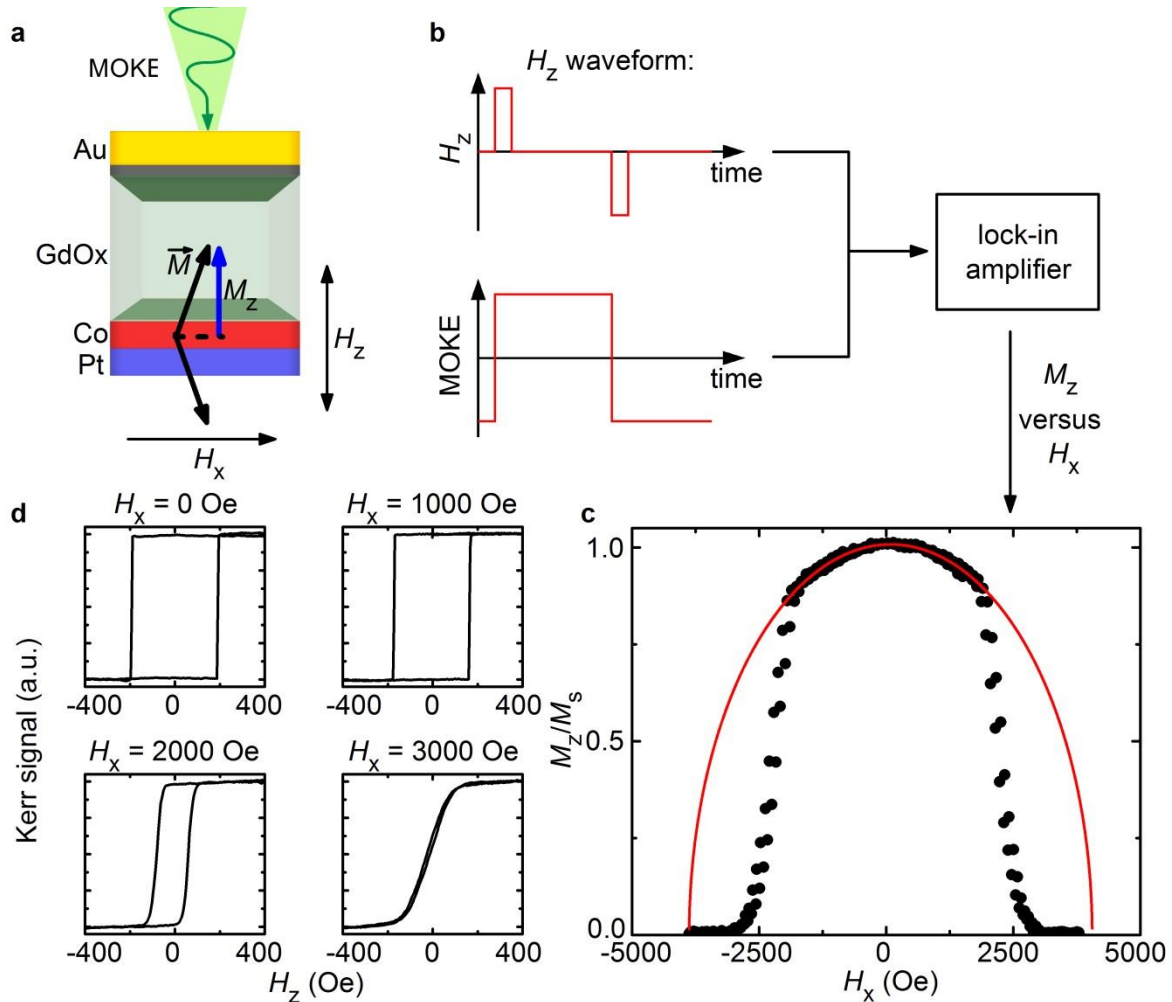


Figure 3-13: Local probing of magnetic anisotropy by polar MOKE. (a) Experiment schematic showing Pt/Co/GdOx film with perpendicular magnetic anisotropy, focused laser to acquire polar MOKE signal, in-plane magnetic field H_x to tilt the magnetization vector \vec{M} away from the easy axis and out-of-plane field H_z to switch the perpendicular component M_z of the magnetization. (b) H_z waveform used to switch M_z and the corresponding polar MOKE signal. A lock-in amplifier is used to extract the MOKE signal corresponding to M_z . (c) Representative data set measured on Ta(4 nm)/Pt(3 nm)/Co(0.9 nm)/Gd(0.9 nm)/GdOx(3 nm) films showing the normalized polar MOKE signal corresponding to M_z plotted as a function of the in-plane field H_x . The solid red line is a fit with the Stoner Wohlfarth model. (d) Polar MOKE hysteresis loops measured at increasing in-plane field H_x .

A representative dataset for a Ta(4 nm)/Pt(3 nm)/Co(0.9 nm)/Gd(0.9 nm)/GdO_x(3 nm) film is shown in Figure 3-13(c). We find that up to $H_x = 2000$ Oe the experimental data are well fit by the Stoner Wohlfarth model, beyond which the polar hysteresis loops under H_x are no longer square. Above $H_x = 2000$ Oe the experimental data drop much faster than expected from the Stoner Wohlfarth model. This deviation is attributed to the formation of a multi domain state in the Co film above $|H_x| = 2000$ Oe, such that the Stoner Wohlfarth model will no longer apply. The formation of a multi domain state is evident in Figure 3-13(d), which shows out-of-plane demagnetization at zero H_z above $H_x = 2000$ Oe.

The fit within the region $|H_x| < 2000$ Oe in Figure 3-13c allows determination of H_k with high fidelity. The fit shown here yields $H_k = 4000$ Oe which agrees well with $H_k = 3500$ Oe extracted from hard axis hysteresis loops measured by vibrating sample magnetometry, for the same sample. The data shown in Figure 3-13(d) also shows a small lateral shift of $\sim 100 - 200$ Oe, which we attribute to drift of the zero point calibration of the home made Gauss probe.

In summary, the here described MOKE-based technique allows local probing of the anisotropy field H_k with micrometer spatial resolution and produces results in good agreement with H_k determined by vibrating sample magnetometry.

3.2.5 Vibrating Sample Magnetometry

Vibrating sample magnetometry (VSM) is a simple and versatile technique that allows precision measurements of the magnetic moment of a magnetic sample in a uniform magnetizing field.¹⁵⁷ The technique is widely used to measure magnetic hysteresis loops by using an electromagnet to stepwise sweep the magnetizing field. For a measurement, the magnetic sample of interest is mounted on a glass rod and placed inside the uniform magnetizing field of an electromagnet. The glass rod with the sample is then vibrated sinusoidally, which results in a periodic change of the magnetic flux and therefore an induced voltage in a set of pickup coils placed in proximity to the vibrating sample. The induced voltage is directly proportional to the magnetic moment of the sample and the

proportionality factor between magnetization and induced voltage is determined from a standard sample of known magnetization. The technique is capable of detecting changes in magnetization as small as 10^{-5} to 10^{-6} emu.¹⁵⁷ VSM can also be used to characterize magnetic anisotropy by rotating the magnetic sample and measuring hysteresis loops at different angles to the magnetizing field. The anisotropy field H_k can then be extracted from hard axis hysteresis loops.

The magnetic thin films investigated here, have a typical thickness of ~ 1 nm and are deposited on ~ 380 μm thick Si wafers. Due to the small volume of magnetic material, several ~ 5 by 5 mm pieces of the sample are stacked on top of each other to increase the VSM signal. Acquiring a single hysteresis loop requires several minutes and typically two hysteresis loops are measured per sample; one with the magnetic field parallel and the other with the magnetic field perpendicular to the film plane. In order to determine the normalized magnetization (emu/cm^3) of the magnetic thin film, its volume is calculated by multiplying the film area and thickness. The film thickness is typically known and the film area is extracted from the weight of the samples by using the density of Si and the thickness of the Si wafer. All the VSM measurements presented in this thesis were performed at RT.

4 VOLTAGE CONTROL OF DOMAIN WALL MOTION*

Many proposed spintronic devices rely on DW dynamics to achieve logic and nonvolatile memory functionalities.²³⁻²⁵ Achieving efficient electrical control of DWs is essential to realizing high-performance solid-state operation of such devices. Much work has focused on using spin-polarized electric currents to manipulate magnetic DWs via spin-transfer torques.^{29,30} While significantly more efficient than conventional magnetic fields, this mechanism remains dissipative and often suffers from a high critical current for DW displacement. The introduction of voltage-gated effects is therefore highly desirable and would enable low power and high performance operation of DW based devices.

Voltage-gated control of the magnetization is most often achieved using complex materials such as multiferroic oxides,³⁴ magnetic semiconductors,^{36,37} or strain-coupled

*Sections of this chapter, including figures, have been previously published in the following articles:

- Bauer, U., Emori, S. & Beach, G. S. D. Electric field control of domain wall propagation in Pt/Co/GdOx films. *Appl. Phys. Lett.* **100**, 192408 (2012).
- Bauer, U., Emori, S. & Beach, G. S. D. Voltage-gated modulation of domain wall creep dynamics in an ultrathin metallic ferromagnet. *Appl. Phys. Lett.* **101**, 172403 (2012).

magnetostrictive/piezoelectric composites.³³ In particular, in strain-coupled magnetostrictive/piezoelectric composites, voltage-gated control of DW motion has been successfully demonstrated,^{87,88,158-160} but unfortunately, these materials pose challenges to integration with semiconductor processing technology.

Recently, it was shown that magnetic anisotropy at the interface between an ultrathin metallic ferromagnet and an oxide dielectric can be modulated by an applied electric field.^{31,32,40-42,111} This effect has been exploited to realize magnetization switching in MTJs^{31,32} and nonvolatile control of the magnetization vector in magneto-electric charge trap memory cells.¹¹¹ However, such control of magnetic anisotropy should also allow for electric field control of DW dynamics.^{77,89-91,161}

Here, we examine DW dynamics in an ultrathin Co film under the influence of an electric field applied across a gate dielectric. In Section 4.2, we demonstrate that a gate voltage can enhance or retard DW propagation in Pt/Co/GdOx films, leading to a linear modulation of the propagation field for DW creep motion.⁸⁹ By contrast, no clear influence on DW nucleation is observed due to the stochastic nature of nucleation events throughout the film.⁸⁹

In section 4.3, we present direct space- and time-resolved measurements of DW dynamics, spanning more than four decades in DW velocity. By measuring the velocity scaling with temperature, driving field, and gate voltage, we verify domain expansion via thermally-activated creep dynamics and derive an experimentally-motivated expression to incorporate magneto-electric effects into the creep equation of motion.⁹⁰ We show that an electric field linearly modulates the activation energy barrier E_a that governs DW creep, and identify consequent limitations to the efficiency of voltage-controlled DW motion.⁹⁰ Significant voltage-induced velocity enhancement can be achieved in the low-velocity regime, but the efficiency is diminished at high velocities where E_a is correspondingly small, which limits voltage control of fast DW motion.⁹⁰ Understanding these limitations is critical for assessing the potential of voltage-gated DW devices.

4.1 Experimental Methods:

Experiments were performed on perpendicularly-magnetized Ta(4 nm)/Pt(3 nm)/Co(1 nm)/GdOx(40 nm) films (see Figure 4-1(a)) grown at RT on a Si(100) substrate with a 50 nm thick thermally grown oxide layer. Here, the GdOx layer serves as a high-k gate dielectric¹⁴⁴ while simultaneously promoting PMA in the Co film due to Co-O interfacial hybridization.^{8,9,98} The metal layers were grown by DC magnetron sputtering at 3 mTorr of Ar with a background pressure of $\sim 1 \times 10^{-7}$ Torr. The GdOx layer was reactively sputtered at an oxygen partial pressure of $\sim 5 \times 10^{-5}$ Torr. After breaking vacuum, 100 μm diameter Ta(1 nm)/Au(5 nm) gate electrodes were deposited through a shadow mask. The metal gate was thick enough to provide good electrical contact but thin enough to allow optical access to the Co film.⁶⁵

Magnetic properties were characterized using the polar MOKE and VSM. VSM measurements yielded an in-plane saturation field $H_k \sim 6$ kOe, indicating strong PMA and a saturation magnetization M_s of ~ 1200 emu/(cm³ of Co), suggesting minimal Co oxidation during growth of the GdOx overlayer. Polar MOKE measurements were performed using a 532 nm diode laser attenuated to 1 mW, focused to a ~ 3 μm diameter probe spot and positioned by a high resolution scanning stage (see Section 3.2.2 for details). The switching field H_c and remanence to saturation magnetization ratio M_r/M_s were derived from hysteresis loops measured at a 17 Hz sweep rate. A mechanically-compliant 15 μm diameter BeCu probe tip was used to apply a gate voltage V_g to the top electrode, while a 25 μm diameter blunt W microprobe was used to mechanically generate local DW nucleation sites.

4.2 Electric Field Control of Domain Wall Propagation

The voltage response of the DW propagation field was investigated in the Ta/Pt/Co/GdOx films described in Section 4.1. The as-deposited films exhibit strong PMA and square out-of-plane hysteresis loops (see Figure 4-1(b)). The switching field is stochastic, with H_c ranging from 240 to 280 Oe depending on the location on the film and at any given location varies by ± 10 Oe from cycle to cycle (see Figure 4-1(b)), which suggests magnetization reversal limited by random nucleation throughout the film.

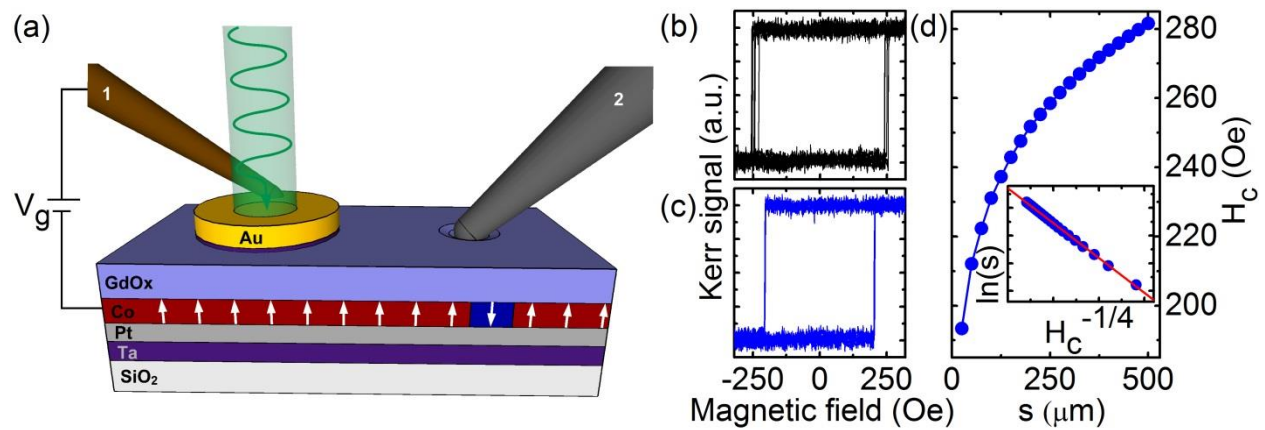


Figure 4-1: Domain wall propagation field measurements. (a) Schematic illustration of experimental setup including gated Pt/Co/GdOx structure, focused laser beam to measure polar MOKE hysteresis loops, BeCu microprobe (1) to apply gate voltage V_g and W microprobe (2) to create local DW nucleation site to switch between DW nucleation and DW propagation limited magnetization reversal. White arrows illustrate local orientation of magnetization vector and DW nucleation beneath W probe tip. (b) Superposition of 6 individual MOKE hysteresis loops without landing W microprobe and (c) with W microprobe landed. (d) Switching field H_c as a function of distance s between MOKE probing spot and tip of landed W microprobe. Inset of (d) shows same data but with $\ln(s)$ plotted as function of $H_c^{-1/4}$.

When a W microprobe is landed with small mechanical overdrive on the GdOx surface in the vicinity of the MOKE spot (see Figure 4-1(a)), the hysteresis loops change markedly. As shown in Figure 4-1(c), H_c drops to ~ 210 Oe at a distance of $50 \mu\text{m}$ from the location of the W tip, while the switching field distribution is greatly reduced. Moreover, H_c increases

monotonically as a function of distance s from the W microprobe tip as shown in Figure 4-1(d), indicating expansion of a circular domain centered at the contact point as the field is swept. This behavior can be explained by the creation of a local nucleation site with a reduced nucleation threshold upon application of a local mechanical stress. In this case, H_c is determined by the propagation field required to drive domain expansion via DW motion. The narrow spread in H_c from cycle to cycle after creating the local nucleation site is consistent with DW creep through a fine scale disorder potential. In Figure 4-1(d), inset, we show that H_c and s are related via a scaling relation $\ln(s) \sim H_c^{-1/4}$, which is identical to the scaling relation between DW velocity and applied field in the two-dimensional creep regime.⁷⁵ The distance s and the average DW velocity \bar{v} during domain expansion are related by $s = \bar{v} \tau$, where τ is a time constant related to the field sweep rate. Thus, the observed scaling supports the identification of H_c as the DW propagation field.

We find that if the W microprobe overdrive is not too great, the sample returns to its original higher H_c state when the microprobe is lifted and the stress is relieved, which shows that no permanent damage arises from landing the W probe. This simple technique thereby provides a means to separately examine nucleation-limited and propagation-limited DW dynamics and the influence of a gate voltage on these processes.

In order to measure the voltage dependence of H_c in the nucleation and propagation-limited cases, we have used a second microprobe to apply a gate voltage to the Au gate electrode (Figure 4-1(a)). This second probe tip was a more mechanically-compliant BeCu probe, which could be brought into electrical contact with the Au electrodes without causing any changes to the measured hysteresis loops. Figure 4-2 shows H_c measured at the center of a Au gate electrode as a gate voltage V_g was cycled from + 7.5 V to - 7.5 V before (Figure 4-2(a)) and after (Figure 4-2(b)) landing a W probe $\sim 80 \mu\text{m}$ away from the Au gate. Hysteresis loops were measured after every 0.5 V step by averaging 50 reversal cycles to account for stochasticity in the nucleation-limited case. In the DW nucleation limited regime, i.e., without landing the W microprobe, we observe a random fluctuation of H_c of about 8 Oe throughout the measurements despite signal averaging, but with no clear

correspondence to the applied gate voltage (see Figure 4-2(a)). The lack of a clear correlation between H_c and V_g suggests that the distribution of random nucleation events throughout the Co film rather than within the area covered by the gate electrode dominates magnetization reversal.

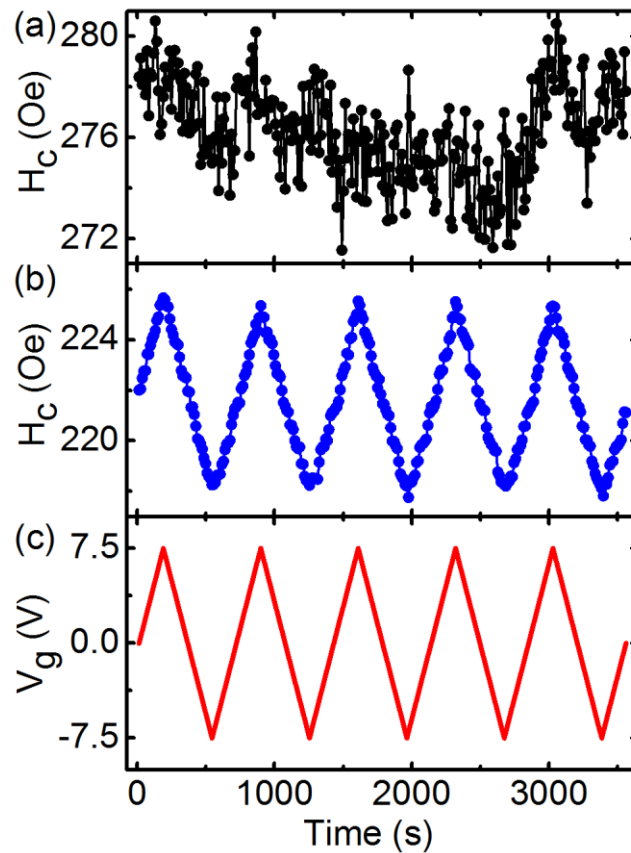


Figure 4-2: Voltage dependence of switching field. Switching field H_c in (a) DW nucleation and (b) DW propagation limited regime (i.e., W microprobe landed at $s \sim 80 \mu\text{m}$) and (c) gate voltage V_g plotted as a function of time. V_g is ramped between -7.5 V and +7.5V for 5 cycles and 50 MOKE hysteresis loops are averaged after every 0.5 V step in V_g .

When a local nucleation site is created by the W microprobe close to the gate electrode, a clear modulation of H_c by V_g becomes apparent (Figure 4-2(b)). In this case H_c tracks V_g linearly and reversibly over a range of ~ 8 Oe, corresponding to a slope of ~ 0.5 Oe/V. Negative V_g reduces H_c and therefore enhances DW propagation whereas positive V_g

increases H_c and therefore retards DW propagation in the Co film. As DW propagation occurs by creep dynamics, the DW velocity v can be expressed by an Arrhenius relation, $v \propto \exp(-E_a/kT)$, where k is the Boltzmann constant, T the temperature and E_a the activation energy for DW propagation. Moreover, $E_a \propto (H_{\text{crit}}/H)^{1/4}$ where H is the applied magnetic field and H_{crit} is a characteristic depinning field that scales with the DW elastic energy density $\varepsilon_{\text{el}} \sim (AK_u)^{1/2}$.⁷⁵ Here, A is the exchange constant and K_u is the uniaxial anisotropy constant. Since E_a scales with K_u , modulation of K_u by an electric field at the Co/GdOx interface correspondingly changes the DW creep velocity and therefore modifies the DW propagation field at a fixed distance from the nucleation site.

The MOKE measurements in this section were limited to the acquisition of magnetic hysteresis loops and therefore the DW propagation field. However, the here described technique to reversibly create nucleation sites, facilitates time-resolved MOKE measurements in continuous magnetic thin films and allows us to directly investigate electric field effects on DW velocity in Section 4.3.

4.3 Electric Field Control of Domain Wall Velocity

DW motion in the Ta/Pt/Co/GdOx films described in Section 4.1 was studied using the technique introduced in Section 3.2.3 and described schematically in Figure 4-3(a). A W microprobe was used to generate an artificial DW nucleation site. After initially saturating the film magnetization, a magnetic field step H can then be used to nucleate a reversed domain underneath the W probe and expand it radially across the film. Magnetization reversal was detected via the polar MOKE signal using the scanning MOKE system described in Section 3.2.2. Exemplary time-resolved MOKE transients are shown in Figure 4-3(b) for several positions of increasing distance from the W probe tip. As expected for DW propagation, the mean magnetization reversal time ($t_{1/2}$) increases linearly with increasing distance from the nucleation site.

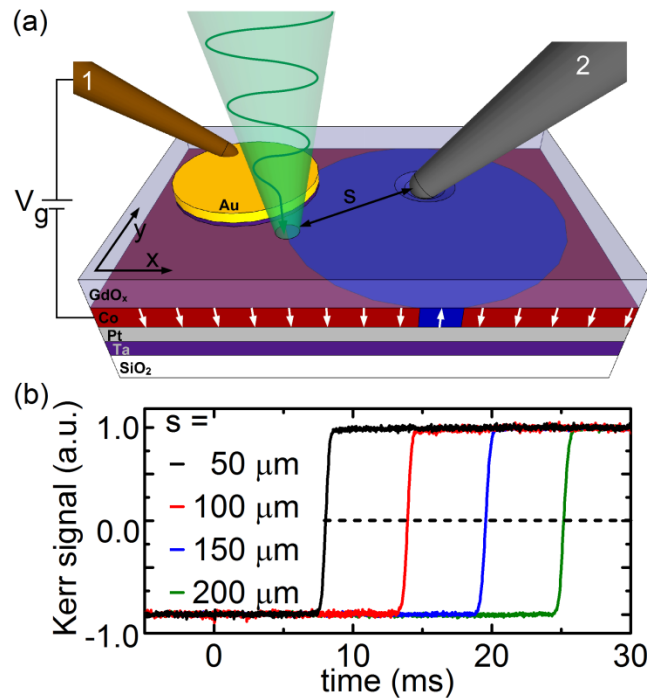


Figure 4-3: Domain wall velocity measurements. (a) Experiment schematic showing Pt/Co/GdOx structure, (1) BeCu microprobe for voltage application, (2) W microprobe to create artificial DW nucleation site and focused MOKE laser probe. (b) Normalized MOKE signal transients measured at different distances s between MOKE probing spot and artificial nucleation site.

By acquiring MOKE signal transients across a two dimensional grid in the vicinity of the nucleation site, the average DW trajectory can be imaged with μm spatial and μs time resolution. Figure 4-4(a)-(c) shows maps of the normalized polar MOKE signal, corresponding to the perpendicular magnetization component M_z , at several times t after application of a field step $H = 170$ Oe. Figure 4-4(d) shows a corresponding contour map of the mean reversal time $t_{1/2}$ over the same $300 \mu\text{m} \times 300 \mu\text{m}$ grid area. Here each pixel corresponds to the averaged measurements of 50 reversal cycles. These images show that a reversed domain nucleates beneath the W probe tip and expands radially and isotropically with time. Natural nucleation sites elsewhere in the film are sufficiently distant such that no other DWs reach the probed region under the conditions examined. The remarkably sharp and azimuthally-uniform (averaged) DW propagation front suggests smooth DW motion via thermally-activated creep through a fine-scale disorder potential. While DW creep is stochastic on the scale of the disorder potential, DW propagation is deterministic at the micrometer-scale resolution of the present experiments.

The dotted circle in Figure 4-4(a) outlines the position of a Ta/Au electrode located $\sim 50 \mu\text{m}$ from the artificial nucleation site. In the absence of a gate voltage, the propagating DW passes unimpeded underneath the electrode. In Figure 4-4(e)-(g) a mechanically-compliant $15 \mu\text{m}$ diameter BeCu probe tip was gently landed on the electrode to apply a gate voltage V_g without creating an additional nucleation site. In the experiments presented here, V_g was limited to ± 8 V to minimize charge trapping and associated irreversibility in the gate oxide.^{89,111} Figure 4-4(e)-(g) shows maps of M_z for $V_g = 8$ V at exactly the same t as the $V_g = 0$ maps of Figure 4-4(a)-(c). Comparison reveals that at $V_g = 8$ V, domain expansion is impeded underneath the electrode whereas it occurs unimpeded outside of the electrode area. The mean switching time $t_{1/2}$ versus position, plotted in Figure 4-4(h), highlights the effect of V_g on DW propagation under the gate electrode. At $V_g = 0$, $t_{1/2}$ increases linearly with distance from the nucleation site with the same slope inside and outside the electrode area. However, the slope in the electrode area increases for $V_g = 8$ V and decreases for $V_g = -8$ V, indicating that v increases for $V_g < 0$ and decreases for $V_g > 0$.

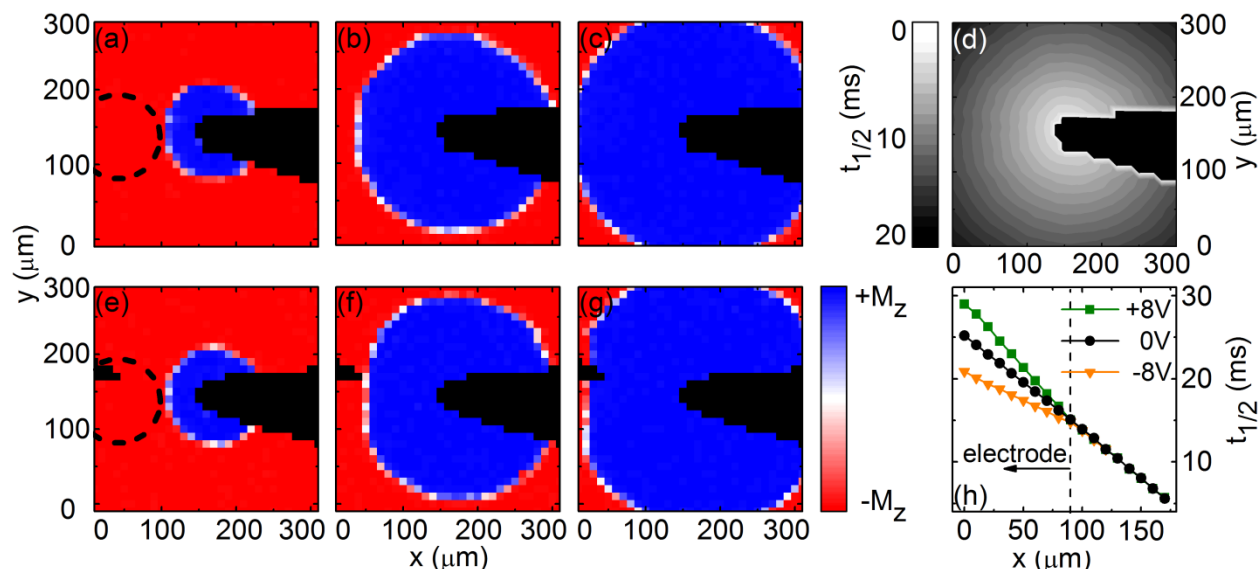


Figure 4-4: Domain expansion under bias voltage. Polar MOKE maps, showing domain expansion from artificial nucleation site at $t = 6.3$ ms ((a), (e)), 11.9 ms ((b), (f)) and 14.7 ms ((c), (g)) after application of magnetic field step, at $V_g = 0$ ((a)-(c)) and at $V_g = 8$ V ((e)-(g)). (d) Contour map showing mean switching time ($t_{1/2}$) with $V_g = 0$. (h) Line scan of $t_{1/2}$ across gate electrode at $V_g = -8$, 0 and $+8$ V for another device with larger distance between electrode and nucleation site. Black triangular area on right side of (a)-(g) and on left side of (e)-(g) corresponds to W and BeCu microprobe tip, respectively. Dashed black line in (a), (e) outlines gate electrode. All measurements at $H = 170$ Oe and $T = 35$ °C.

To better understand the observed DW dynamics and the role of V_g on those dynamics we measured v as a function of H , V_g , and substrate temperature T . DW velocity was determined from a linear fit of $t_{1/2}$ versus position for typically 9 measurements of $t_{1/2}$ over a distance of 80 μm across the electrode, on a line extending radially from the artificial nucleation site. In the creep regime of DW dynamics, DW motion is thermally activated and follows an Arrhenius-type relation $v \propto \exp(-E_a(H)/kT)$. Here, k is the Boltzmann constant, T the temperature and E_a the activation energy barrier for DW propagation. E_a is expected to follow a scaling law $E_a \propto (H_{crit}/H)^\mu$ where H_{crit} is a characteristic depinning field, and the scaling exponent $\mu = 1/4$ for a one-dimensional elastic line in a two-dimensional disorder potential.⁷⁵

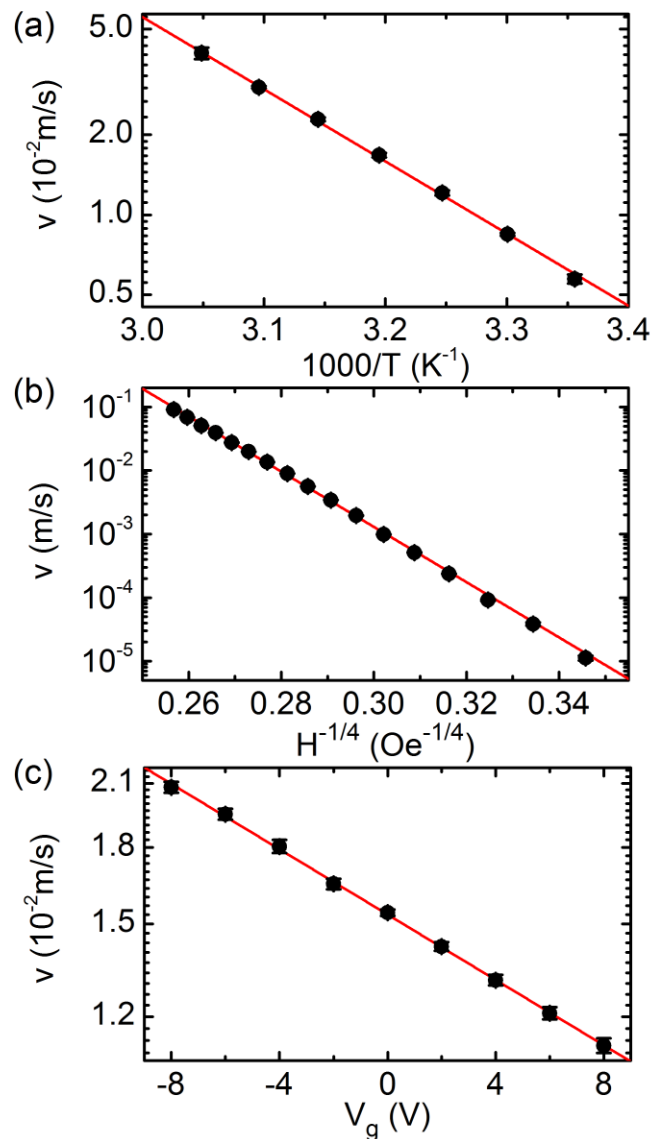


Figure 4-5: Temperature, field and voltage dependence of domain wall velocity. DW velocity v as a function of (a) temperature (T) at $H = 170$ Oe and $V_g = 0$ V, (b) magnetic field (H) at $T = 35$ °C and $V_g = 0$ V and (c) gate voltage (V_g) at $H = 170$ Oe and $T = 35$ °C. Red lines are linear fits. Error bars in (a) and (b) are smaller than symbols.

We first measured $v(T)$ at $H = 170$ Oe and $V_g = 0$ V, spanning a temperature range from 25°C to 55 °C, controlled using a thermoelectric module stable to within ± 0.1 °C. Within this range of T , the velocity spans nearly an order of magnitude. As seen in Figure 4-5(a), $\ln(v)$ scales linearly with T^{-1} , confirming Arrhenius-like behavior.¹⁶² The slope corresponds

to $E_a = (0.54 \pm 0.01)$ eV, or ~ 20 kT . In Figure 4-5(b), we plot the dependence of v on H over a driving field range from 70 Oe to 230 Oe, corresponding to a change in v by almost four decades. Within this range, the dependence of v on H is well-described via a scaling relation $\ln(v) \propto H^{-1/4}$, consistent with two-dimensional DW creep dynamics.⁷⁵

Having established that DW motion is indeed in the thermally-activated creep regime, we proceed to examine the dependence of v on V_g . The depinning field H_{crit} is a function of the DW elastic energy density $\varepsilon_{\text{el}} = 4(AK_u)^{1/2}$ and the DW width $\delta = (A/K_u)^{1/2}$, where A is the exchange constant and K_u is the uniaxial anisotropy constant.⁷⁵ Therefore, H_{crit} is expected to scale with K_u and voltage induced changes to K_u are expected to result in a direct modification of E_a and therefore of v . In Figure 4-5(c) the dependence of v on V_g is shown at $H = 170$ Oe and $T = 35$ °C. The DW velocity v can be modified by a factor of two in a bias range of $V_g = -8$ to $+8$ V. Due to limited charge trapping likely at the Co/GdOx interface,⁸⁹ we find that the v versus V_g curves often show small hysteresis. Therefore, we plot v averaged over several forward and reverse V_g cycles. Figure 4-5(c) shows that $\ln(v)$ and therefore E_a scale approximately linearly with V_g . To accurately access the scaling exponent would require measurements over several decades in v which is experimentally inaccessible. However, in the investigated bias range the scaling relation for v can be expanded to include V_g :

$$v(V_g, H, T) \propto \exp\left(-\left(1 + \frac{\alpha}{d_{\text{GdOx}}}V_g\right)E_{a,0V}(H)/kT\right) \quad (4.1)$$

Here, d_{GdOx} is the GdOx thickness, α is a magneto-electric coefficient and $E_{a,0V}$ is the activation energy barrier at $V_g = 0$ V. From the linear fit in Figure 4-5(c), the previously determined E_a at $V_g = 0$ V, and taking $d_{\text{GdOx}} = 40$ nm, we find $\alpha = (8.1 \pm 0.5) \times 10^{-2}$ nm/V.

Given the full functional dependence of v on H , T and V_g , it is now possible to investigate in more detail the efficiency of voltage control of DW motion across the parameter space. Equation (4.1) suggests that the relative influence of V_g on v scales with $E_{a,0V}$. The relative DW velocity enhancement, defined here as the ratio between DW velocity at $V_g = -4$ V (v_{-4V}) and at $V_g = 0$ V (v_{0V}) was determined at $T = 35$ °C for H spanning 100 to

230 Oe. As H increases, v_{0V} increases exponentially but the relative enhancement v_{-4V}/v_{0V} decreases (see Figure 4-6(a)). At $v_{0V} \approx 2 \times 10^{-4}$ m/s, corresponding to $H = 100$ Oe, we find a voltage-induced velocity enhancement of $\sim 34\%$ at $V_g = -4$ V. However, this same V_g , leads to only a $\sim 14\%$ velocity enhancement at $v_{0V} \approx 1 \times 10^{-1}$ m/s, corresponding to $H = 230$ Oe. Therefore, the efficiency of voltage control of DW motion decreases with increasing DW velocity due to the correspondingly lower activation energy barrier.

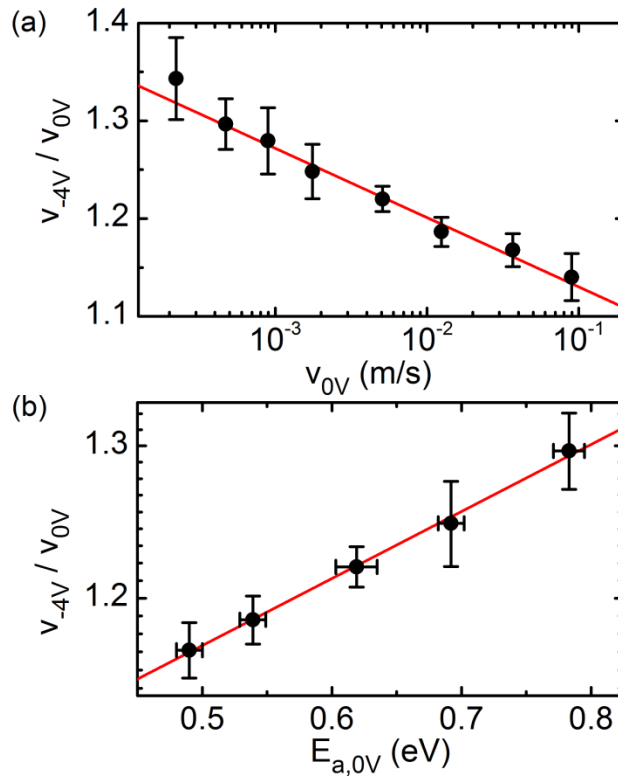


Figure 4-6: Efficiency of voltage control of domain wall motion. (a) Ratio between DW velocity at $V_g = -4$ V (v_{-4V}) and at 0 V (v_{0V}) as a function of DW velocity v_{0V} . (b) Subset of same data plotted versus activation energy barrier at $V_g = 0$ V ($E_{a,0V}$). Red lines are linear fits.

This behavior follows directly from Equation (4.1) an increase in H results in a decrease of $E_{a,0V}$ which then reduces the effect of V_g on the creep velocity. The ratio v_{Vg}/v_{0V} can be expressed as

$$\ln(v_{Vg}/v_{0V}) = -\alpha V_g E_{a,0V} / d_{GaOx} kT \quad (4.2)$$

Therefore, $\ln(v_{-4V}/v_{0V})$ is expected to decrease linearly with $E_{a,0V}$ at a slope proportional to α . We have determined $E_{a,0V}$ through direct Arrhenius analysis of $\ln(v)$ versus T^{-1} curves, such as shown in Figure 4-5(a), at $H = 110, 130, 150, 170$ and 200 Oe. We find that within the measurement accuracy α is independent of H . By plotting v_{-4V}/v_{0V} directly as a function of $E_{a,0V}$ (see Figure 4-6(b)) we find that indeed, v_{-4V}/v_{0V} decreases with decreasing $E_{a,0V}$. The linear fit in Figure 4-6(b) yields $\alpha = (9.4 \pm 2.0) \times 10^{-2}$ nm/V, which agrees well with the value determined above.

Taking^{75,77} $E_a \propto K_u$ and $K_u = K_s/d_{Co} - 2\pi M_s^2$ (with Co film thickness d_{Co} and surface anisotropy constant K_s) this α indicates ~ 9 % electric-field-induced change of E_a at 1 V/nm corresponding to a ~ 3 % change in K_s . From our VSM results above, we estimate $K_s \approx 1.3$ erg/cm², and an electric-field-induced modification of $\sim 3 \times 10^{-9}$ erg/Vcm (~ 30 fJ/Vm).

Large voltage-induced velocity enhancements up to a factor of 10 were recently reported in Refs. ⁷⁷ and ⁹¹, which might enhance the speed of DW-based devices and decrease power consumption. However, Equation (4.2) and Figure 4-6 show that this enhancement depends strongly on the velocity regime probed, and efficiency is diminished as v increases. Ref. ⁷⁷ suggested that velocity enhancement by a factor of 10^5 could be reasonably expected through materials engineering. Based on the α reported here, even at $V_g = -40$ V, corresponding to an electric field of 1 V/nm (typical BD limit for high-quality dielectrics), Equation (4.2) would require $E_{a,0V} \sim 3$ eV to achieve this enhancement. Extrapolating from Figure 4-6a, this would correspond to toggling the velocity from between $\sim 10^{-18}$ m/s and 10^{-13} m/s, timescales that are experimentally inaccessible and of questionable utility to device operation. A further increase of α by an order of magnitude would be necessary to access practical DW velocities.

4.4 Summary and Conclusion

In summary we have demonstrated direct electric field control of DW propagation in ultrathin Co films with PMA. We find that the DW propagation field linearly follows the applied gate voltage and can be enhanced and retarded by the presence of an electric field at the Co/GdO_x interface. Moreover, we demonstrate voltage control of DW creep dynamics and characterize the efficiency of the effect. DW velocity can be controlled by a linear modulation of the activation energy barrier via voltage-induced changes to the interfacial anisotropy. At low DW speeds corresponding to a large activation energy barrier, DW velocity can be significantly modified by a gate voltage. However, at higher speeds the efficiency of voltage control is diminished due to the simultaneous decrease in activation energy, which limits the utility of the effect in high-speed DW-based device applications. An orders of magnitude improvement in the magneto-electric response would be necessary to achieve voltage control of DWs moving at device relevant velocities. Up to now, magneto-electric coupling in metals has been achieved by charging or discharging a ferromagnetic thin film that acts as one plate of a capacitor. Since the charge density of a metal can be varied only slightly, the change in magnetic anisotropy achievable by this approach is typically small and fundamentally limited. As we will see in Chapter 5, the necessary improvement in the magneto-electric response requires an entirely different magneto-electric coupling mechanism and a novel device design.

5 VOLTAGE-CONTROLLED DOMAIN WALL TRAPS*

Electrical control of magnetism has the potential to bring about revolutionary new spintronic devices,^{23-25,36,163} many of which rely on efficient manipulation of magnetic DWs in ferromagnetic nanowires.²³⁻²⁵ Magnetic anisotropy in ultrathin metallic ferromagnets can be tuned by an electric field,⁴⁰⁻⁴² opening the door to ferromagnetic field-effect devices in which a gate voltage can control the magnetic state.^{31,32,111} Magneto-electric coupling in metals has until now been achieved by charging up a ferromagnetic thin film that acts as one plate of a capacitor. Electron accumulation or depletion of the ferromagnet can alter its magnetic properties,^{40-42,84} but since the charge density of a metal can be varied only slightly, the change in MAE is small and fundamentally limited. In Chapter 4 we used this mechanism to modulate DW velocity in nanometer-thick Co films,^{77,89-91} but the effects were relatively modest and limited to the slow, thermally-activated creep regime ($\mu\text{m/s}$ –

* Sections of this chapter, including figures, have been previously published in the following articles:

- Bauer, U., Emori, S. & Beach, G. S. D. Electric field control of domain wall propagation in Pt/Co/GdOx films. *Appl. Phys. Lett.* **100**, 192408 (2012).
- Bauer, U., Emori, S. & Beach, G. S. D. Voltage-controlled domain wall traps in ferromagnetic nanowires. *Nat. Nanotechnol.* **8**, 411-416 (2013).

mm/s) where velocity is exponentially sensitive to surface anisotropy.⁹⁰ By contrast, practical devices require manipulation of DWs traveling at tens to hundreds of m/s, which would require much stronger anisotropy modifications. Interestingly, Section 5.2 identifies two regimes of voltage effects in the Pt/Co/GdOx system. In the low voltage regime, the DW propagation field varies linearly and reversibly with voltage (see Chapter 4).⁸⁹ However, at higher voltages a much larger change of magnetic anisotropy is observed and allows nonvolatile switching of the magnetic state.⁸⁹ These nonvolatile changes occur preferentially at the edge of the gate electrodes, indicating an ionic rather than electronic origin (see Section 5.3).¹⁴³

PMA in Co/metal-oxide bilayers derives from interfacial Co-O hybridization,⁴⁷ and slight changes to the interfacial oxidation state have a pronounced impact on PMA.^{9,47} We propose that by using a gate oxide with high ionic mobility, one can electrically displace O²⁻ at the Co/oxide interface^{3,4,118,119} and thereby not just tune the anisotropy, but remove and reintroduce its very source. Section 5.4 shows that using a rare-earth gate oxide and providing a high-diffusivity path for ionic exchange, allows toggling of magnetic anisotropy at the nanoscale. We harness this effect to create unprecedentedly strong voltage-controlled DW traps that function as nonvolatile, electrically programmable and switchable pinning sites. Section 5.5 demonstrates that pinning strengths of at least 650 Oe can be readily achieved, enough to bring to a standstill DWs travelling at speeds of at least ~20 m/s. Moreover, since the effect does not rely on maintaining an electrical charge, these voltage-induced changes persist at zero bias, enabling nonvolatile switching and state retention in the power-off state. Finally, in Section 5.6, we exploit this new magneto-ionic effect to demonstrate a prototype nonvolatile memory device in which DW traps facilitate bit selection in a nanowire register.

This chapter highlights a new opportunity to merge nanoionics^{3,4} and nanomagnetism into novel ‘magneto-ionic’ devices that offer an attractive alternative to magneto-electric composites that rely on complex oxides (piezoelectrics or ferroelectrics) to achieve similar functionality^{87,88,158-160}.

5.1 Experimental Methods

Ta/Pt/Co/GdOx films were prepared by DC magnetron sputtering at RT under 3 mTorr Ar with a background pressure of $\sim 1 \times 10^{-7}$ Torr, on thermally-oxidized Si(100) substrates. GdOx layers were deposited by reactive sputtering from a metal Gd target at an oxygen partial pressure of $\sim 5 \times 10^{-5}$ Torr. Layer thicknesses were determined from the deposition rate of each material, which was calibrated by x-ray reflectivity.

Magnetic properties of the Ta/Pt/Co/GdOx films were characterized by VSM (see Section 3.2.5). The Ta(4 nm)/Pt(3 nm)/Co(1 nm)/GdOx(40 nm) films used in Section 5.2 and Section 5.3 exhibited an in-plane saturation field $H_k \sim 6$ kOe and the Ta(4 nm)/Pt(3 nm)/Co(0.9 nm)/GdOx(3 nm) structures used in Sections 5.4 to 5.6 exhibited $H_k > 10$ kOe, indicating strong PMA. Both structures show saturation magnetization of ~ 1200 emu/(cm³ of Co) which suggests minimal Co oxidation during growth of the GdOx overlayer.

For the Ta(4 nm)/Pt(3 nm)/Co(1 nm)/GdOx(40 nm) films used in Section 5.2 and 5.3, 100 μ m diameter Ta(1 nm)/Au(5 nm) electrodes were deposited through a shadow mask. In contrast, the gate electrodes on the Ta(4 nm)/Pt(3 nm)/Co(0.9 nm)/GdOx(3 nm) films in Section 5.4 were patterned using electron beam lithography and lift-off. The metal electrodes in Samples A and B consisted of a Ta(2 nm)/Au(12 nm) sputter-deposited stack.

The nanowire devices used in Section 5.5 and 5.6 were also fabricated using electron beam lithography and lift-off, and were prepared in three steps; the nanowire was patterned first, followed by the Cu nucleation lines, and finally the gate electrodes. DWs were nucleated in these devices by the Oersted field from a 25 ns-long current pulse (~ 100 mA) injected through the Cu line.

Polar MOKE measurements were made using a 532 nm diode laser attenuated to 1 mW, focused to a ~ 3 μ m diameter probe spot and positioned by a high resolution (50 nm) scanning stage (see Section 3.2.2 for details). The Ta/Au gate electrodes were thick enough to permit robust electrical contact, but thin enough that polar MOKE measurements could be made directly through the electrodes at the 532 nm wavelength.

Magnetic hysteresis loops were measured and the DW propagation field was determined at a fixed sweep rate of the magnetic field of 28 kOe/s. The electromagnet used in this work had a rise time of $\sim 300 \mu\text{s}$, and a maximum amplitude of 650 Oe, which limited the maximum DW trapping potential that could be measured.

The DW velocity in continuous film samples was measured using the technique described in detail in Section 3.2.3. The DW velocity in nanowire samples was measured in the following way.¹⁶⁴ A reversed domain was nucleated at the right end of the magnetic nanowire by the Oersted field of a 25 ns-long current pulse I_{nuc} ($\sim 100 \text{ mA}$) injected through a Cu line orthogonal to the magnetic nanowire (see Figure 5-11(a)). The reversed domain was then expanded by an applied perpendicular magnetic field H , thereby driving an initialized DW along the nanowire away from the nucleation line as shown in Figure 5-11(a). Time-resolved MOKE transients, corresponding to the averaged signal acquired from 500 reversal cycles, were measured along the nanowire in $2 \mu\text{m}$ steps. Similar to the continuous magnetic film samples, the DW velocity is determined from a linear fit of the mean reversal time $t_{1/2}$ versus position.

5.2 Two Regimes of Voltage Response

Expanding on the results described in Chapter 4, the magneto-electric response of Ta(4 nm)/Pt(3 nm)/Co(1 nm)/GdOx(40 nm) films was investigated in a wider voltage range. Consistent with Section 4.2, we find that voltage-induced changes to H_c are reversible as long as $|V_g| < 8$ V (electric field < 0.2 V/nm), indicating that no significant charge trapping occurs in the GdOx layer or at the Co/GdOx interface.^{111,124} However, at higher V_g , irreversibility appears in the H_c versus V_g response, and the change in H_c depends on V_g and the voltage dwell time. Figure 5-1 shows H_c (Figure 5-1(a)), M_r/M_s (Figure 5-1(b)), and the leakage current I (Figure 5-1(c)), measured as V_g was ramped to increasing positive and increasing negative voltage for two separate electrodes, beginning from the virgin state. For positive V_g up to 8 V, we find that H_c increases linearly with V_g , with $M_r/M_s = 1$ and $I < 100$ pA. Between + 8 and + 15 V, H_c starts to deviate from its linear dependence on V_g and after an initially slow decrease, H_c drops dramatically by ~ 120 Oe or ~ 60 % above +12 V. At the same time M_r/M_s decreases significantly from 1 to 0.2 and I increases up to 40 nA. Above $V_g = + 15$ V we observe hard BD of the GdOx dielectric as can be seen from the jump in I to the externally set current limit of 0.5 μ A.¹⁴⁷ After dielectric BD, H_c and M_r/M_s remain at their diminished values and no significant change is observed within hours after the BD occurred. Under negative V_g the devices show markedly different behavior, with no significant deviation from the linear dependence of H_c on V_g until dielectric BD occurs at $V_g = - 11$ V. Also, no change in M_r/M_s is observed under negative V_g .

From these observations, we separate the electric field effects into 3 regimes. In regime I, between $V_g = - 8$ V to + 8 V, DW propagation can be reversibly controlled by an electric field at the Co/GdOx interface, and H_c follows V_g linearly. In regime II, ($V_g = + 8$ V to + 15 V), H_c and M_r/M_s decrease significantly and irreversibly. In Regime III, corresponding to $V_g < - 11$ V and $V_g > + 15$ V, hard dielectric BD of the GdOx layer occurs, and no further changes in hysteresis characteristics are induced.

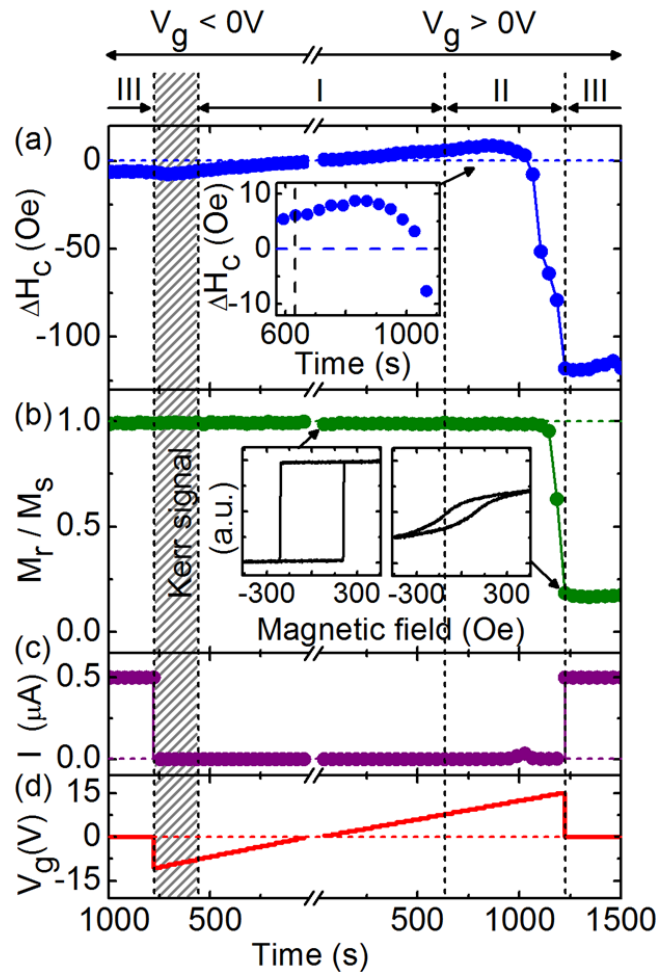


Figure 5-1: Different regimes of voltage modification of magnetic properties. (a) Modification of switching field H_c (i.e., ΔH_c), (b) remanence to saturation magnetization ratio M_r/M_s , and (c) leakage current I (clamped at $0.5 \mu\text{A}$) as a function of time while gate voltage V_g is ramped in steps of 0.5 V every $\sim 40 \text{ s}$ (d). Left and right half of figure correspond to two different devices, measured under increasing negative and positive V_g , respectively. W microprobe is landed at $s \sim 80 \mu\text{m}$ and 250 MOKE hysteresis loops are averaged and I is measured after every voltage step. Effects in regime I are linear and reversible. Regime II (enlarged in inset of (a)) is marked by the onset of irreversibility and, at higher V_g , a steep drop in H_c and M_r/M_s . Regime III corresponds to hard dielectric breakdown. Dashed area highlights lack of regime II for negative V_g . Insets in (b) show representative hysteresis loops at indicated points.

Since the strongest modifications of H_c and M_r/M_s in regime II occur at V_g close to regime III, it is likely that their origin is related to processes occurring during or directly

preceding hard dielectric BD. Hard dielectric BD is typically preceded by a soft BD which is associated with trapped charge generation in the dielectric layer.¹⁴⁷ Trapped charges have previously been shown to result in strong modifications of magnetic anisotropy in ultrathin Fe films and could therefore explain the irreversible character of the modifications of H_c and M_r/M_s , observed here.¹¹¹ However, changes in O^{2-} coordination at the Co/GdOx interface could also play an important role in the observed effects.¹⁴⁷ Oxygen vacancy $V_{O^{2+}}$ generation is often a precursor of dielectric BD in high-k gate oxides¹⁶⁵ and $V_{O^{2+}}$ would migrate predominantly to the Co/GdOx interface due to the high positive V_g . Since hybridization between Co $3d$ and O $2p$ orbitals is expected to play a crucial role in the PMA of the Co film,^{8,9,166} the PMA should be very sensitive to changes in interface oxygen stoichiometry.^{8,9,98} Accumulation of oxygen vacancies at the interface could therefore significantly contribute to the observed loss of PMA in regime II. Moreover, hysteresis loops are only sensitive to changes at the interface between GdOx and the Co film but not to changes at the interface between GdOx and the gate electrode, which could explain why regime II is only observed at positive V_g .

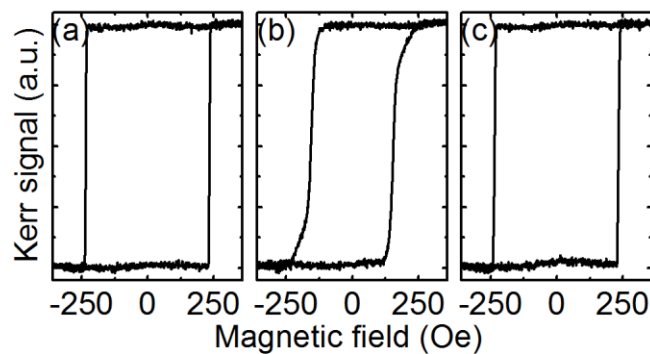


Figure 5-2: Nonvolatile switching of the magnetic state. Evolution of MOKE hysteresis loops measured for Pt/Co/GdOx/Ta/Au structure with reduced GdOx thickness of 3 nm. (a) Before application of gate voltage V_g , (b) after application of $V_g = + 1.8$ V for 60 s and (c) after subsequent application of $V_g = - 1$ V for 15

Interestingly, the dramatic changes in H_c and M_r/M_s observed for positive V_g in Region II can be partially or even fully reversed by application of a negative V_g so long as hard BD has not been reached. In addition, the timescale and voltage levels necessary for these

changes can be significantly reduced by reducing the GdOx thickness. Figure 5-2 shows a series of hysteresis loops measured for a Pt/Co/GdOx device with 3 nm thick GdOx. The (propagation-limited) H_c is 235 Oe before application of a gate voltage (Figure 5-2(a)). $V_g = +1.8$ V was then applied for 60 s and then set to zero, after which H_c decreased to 160 Oe (Figure 5-2(b)). This nonvolatile change in coercivity was retained until a negative gate voltage of -1 V was applied for 15 s, after which the coercivity returned to its initial state (Figure 5-2(c)). It has been shown previously that the charge trapping and vacancy migration that occurs during soft BD of a dielectric can be reversed under appropriate conditions.^{109,118} This behavior could therefore be exploited as a novel nonvolatile magneto-electric coupling mechanism.

5.3 The Role of the Electrode Edge

In the previous section, we reported on large, nonvolatile modifications of the switching field H_c and the remanence to saturation magnetization ratio M_r/M_s at high positive voltage, close to dielectric break down (BD).⁸⁹ We suggested that the observed strong modifications were due to voltage-driven migration of mobile ionic species within the continuous GdOx layer, which is expected to occur close to dielectric BD.^{109,118,165} In this section, we provide additional details about the high voltage case and investigate the spatial distribution of the anisotropy modifications across the electrode area.

Using the Ta(4 nm)/Pt(3 nm)/Co(1 nm)/GdOx(40 nm) films from Section 5.2, dielectric BD of the GdOx layer was induced by ramping V_g with a constant rate of ~ 3 V/s from 0 V to high positive or negative voltage. In Figure 5-3, we correlate the change in magnetic properties that occurs under high voltage stress and subsequent dielectric BD with the simultaneously appearing physical degradation of the gate electrode.

For dielectric BD at high negative bias (~ -20 V), physical damage of the gate electrode is very limited and only occurs in the immediate area (upper left corner) in which the BeCu micro probe was landed to apply the gate voltage (see Figure 5-3(a,b)). After BD, no polar Kerr signal could be obtained in the contact area, but in its vicinity, the coercivity H_c is significantly reduced which indicates that this area now acts as a nucleation site (see Figure 5-3(c,d)).

In contrast, for BD at high positive voltage ($\sim +20$ V), physical damage of the gate electrode is widespread and often large parts of the gate electrode are blown off of the GdOx layer (see Figure 5-3(e,f)). After BD, hysteresis loops measured within the damaged area of the electrode show a strong reduction in M_r/M_s which indicates a strong reduction in PMA (see Figure 5-3(g,h)). Moreover, we note that the strongest modifications of M_r/M_s usually occur in the areas close to the electrode edge and the effects are somewhat reduced towards the electrode center.

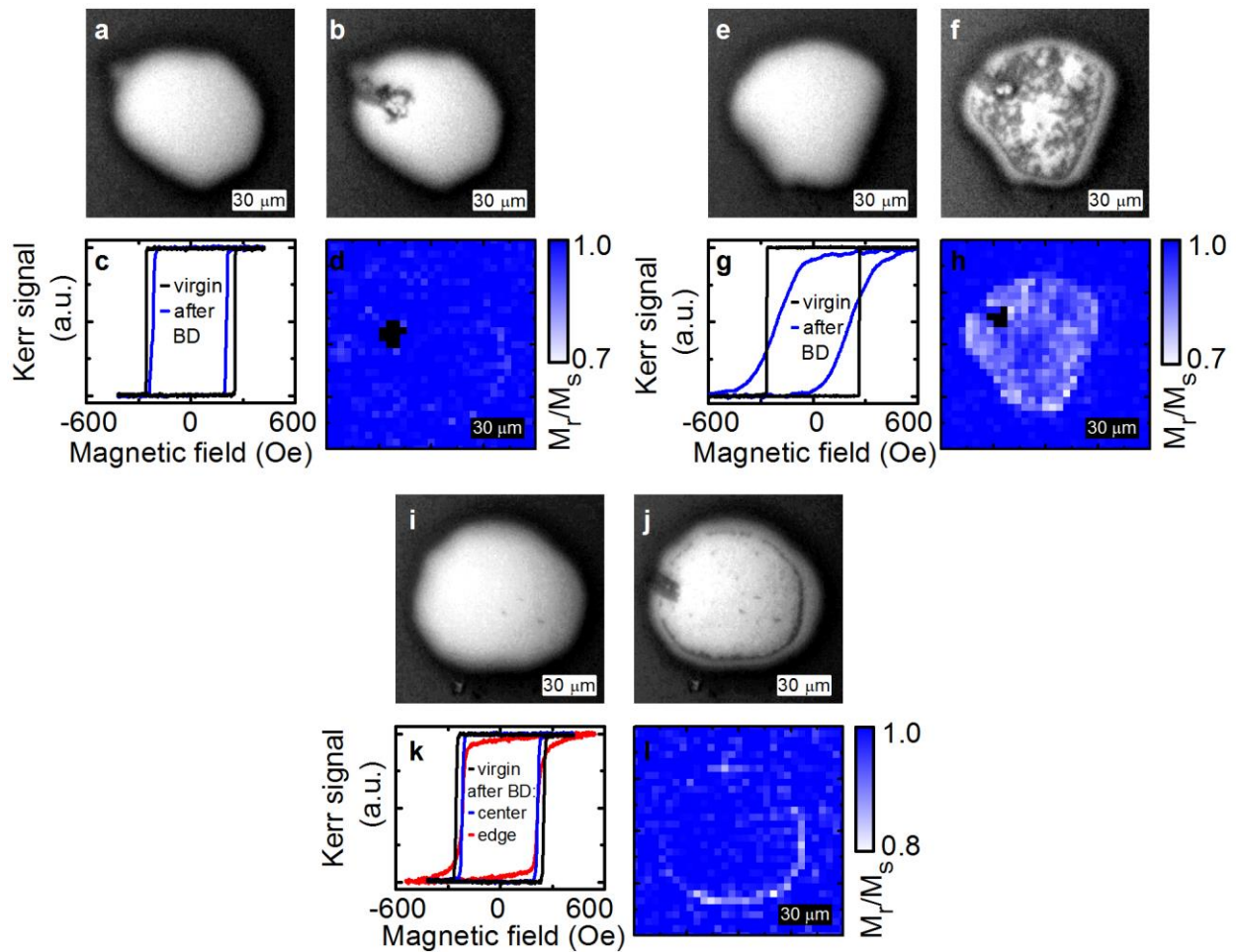


Figure 5-3: Anisotropy modification and physical electrode degradation at high voltage. (a-d) Behavior under high negative bias stress: Optical micrographs showing Ta/Au gate electrode in virgin state (a) and after dielectric breakdown (BD) (b). Hysteresis loops measured in center of gate electrode in virgin state and after BD (c) and M_r/M_s map after BD (d) showing same area as seen in (b). (e-h) Behavior under high positive bias stress (fast voltage ramp): Optical micrographs showing gate electrode in virgin state (e) and after BD (f). Hysteresis loops measured in center of gate electrode in virgin state and after BD (g) and map of M_r/M_s (h) showing same area as (f). (i-l) Behavior under high positive bias stress (slow voltage ramp): Optical micrographs showing gate electrode in virgin state (i) and after BD (j). Hysteresis loops measured in center of gate electrode in virgin state and in center and at the edge of electrode after BD (k) and map of M_r/M_s (l) showing same area as (j). Note, black points in (d) and (h) indicate regions where no polar Kerr signal could be obtained after BD.

Based on this observation, the voltage ramp rate was reduced to $\sim 1 \text{ V} / 30 \text{ s}$, which reduced the voltage at which dielectric BD occurred to $\sim 15 \text{ V}$ (due to time dependence of dielectric BD, lower voltage ramp rate usually results in lower BD voltage¹⁶⁷). In this case, physical damage of the gate electrode occurs predominantly at the electrode edge (see Figure 5-3(i,j)) and similarly M_r/M_s and therefore PMA is reduced predominantly at the edge of the gate electrode (see Figure 5-3(k,l)).

Figure 5-3 shows that the electrode damage exhibits clear polarity dependence under high bias stress. Moreover it shows a direct correspondence between the area in which electrode damage occurs (i.e., where electrode material was removed) and the area in which the magnetic properties are modified, which suggests a common origin. In particular Figure 5-3(i-l), shows that the mechanism responsible for electrode damage and modification of magnetic properties occurs most efficiently at the electrode perimeter, where gas phase, electrolyte and electrode coincide and electrochemical reactions occur most efficiently.¹²¹ These observations suggest the presence of a mobile ionic species which is either released or incorporated into the GdOx depending on the polarity of the bias voltage. Since rare-earth Gd-based oxides are well-known oxygen ion conductors,^{3,4,168} O^{2-} presents the most likely candidate for the mobile ionic species.

Under fast voltage ramp to high positive bias we see widespread damage across the electrode consistent with O_2 release and blow-off of electrode material, as described in references.^{109,118,119,165,169} The low oxygen permeability of Au supports this interpretation.¹⁷⁰ Oxygen gas release from the GdOx and the resulting modification of O^{2-} stoichiometry in the GdOx film should significantly impact magnetic anisotropy, which is consistent with the observed modifications of M_r/M_s in the areas in which electrode damage occurred.

In contrast, at high negative bias, oxygen incorporation instead of release is expected which would explain the absence of wide spread physical damage of the electrode. Since incorporated oxygen would have to move through the thickness of the GdOx layer before reaching the Co/GdOx interface, modifications of the magnetic properties are likely

preempted by break down of the GdOx layer through an electronic avalanche process directly underneath the BeCu probe.

For the Ta/Pt/Co/GdOx films investigated here, high voltages are required to overcome the high diffusion resistance of the continuous GdOx film. The high voltage typically results in dielectric BD of the GdOx layer and degradation and damage of the device. However, by engineering the device for efficient ionic transport, the diffusion resistance could be significantly reduced and it should be possible to achieve strong, reliable and nondestructive switching of magnetic anisotropy at much lower voltages.

5.4 Voltage Controlled Domain Wall Traps in Magnetic Thin Films

The results from Section 5.2 and 5.3 showed that at high voltages, close to dielectric BD, strong nonvolatile modifications of magnetic anisotropy can be achieved in the Pt/Co/GdOx system. Here, we investigate the voltage response of two different device geometries to demonstrate that optimizing the device for ionic transport opens the door for efficient and nondestructive switching of magnetic anisotropy at low voltages. On Ta(4 nm)/Pt(3 nm)/Co(0.9 nm)/GdOx(3 nm) films, a second 30 nm thick GdOx overlayer and a Ta/Au metal gate were deposited and patterned into two different geometries. In Sample A (see Figure 5-4(b)), the GdOx overlayer is continuous and the Ta/Au layer is patterned into an array of 100 μm -diameter electrodes, while in Sample B (Figure 5-4(c)), the GdOx and Ta/Au layer are patterned together into such an array. The gate structure is nominally identical for these two samples, but the devices on Sample B exhibit an open oxide edge around the electrode perimeter, which is not present in Sample A.

The influence of a gate voltage on DW propagation was investigated using the technique^{89,90} described schematically in Figure 5-4(a). A stiff W microprobe was used to create an artificial domain nucleation site in the vicinity of a gate electrode through application of a local mechanical stress. A second, mechanically-compliant BeCu probe was used to gently contact the electrode and apply a gate voltage V_g . Magnetization reversal was locally probed using a scanning MOKE polarimeter.⁹⁰ Figure 5-4(d) shows hysteresis loops for Sample A measured near the center of a gate electrode located $\sim 100 \mu\text{m}$ from an artificial nucleation site, with $V_g = 0 \text{ V}$, $+6 \text{ V}$ and -7 V . The coercivity H_c varies linearly and reversibly with V_g at a slope of $\sim 0.5 \text{ Oe/V}$, consistent with the influence of electron accumulation/depletion on DW creep.^{77,89,91}

The behavior of Sample B is remarkably different. Under negative gate voltage, H_c increases with time at a rate that increases with increasing $|V_g|$. In contrast to Sample A, when V_g is removed the higher H_c state is retained. As seen in Figure 5-4(e), H_c increases by $\sim 230 \text{ Oe}$ after applying $V_g = -6 \text{ V}$ for 180 s. This change is 2 orders of magnitude larger and

of opposite sign compared to Sample A at the same V_g . Subsequent application of positive $V_g = +6V$ for 300 s returns H_c to within 10 Oe of its initial state. H_c can be cycled in this way many times and remains stable at $V_g = 0$ for at least several days.

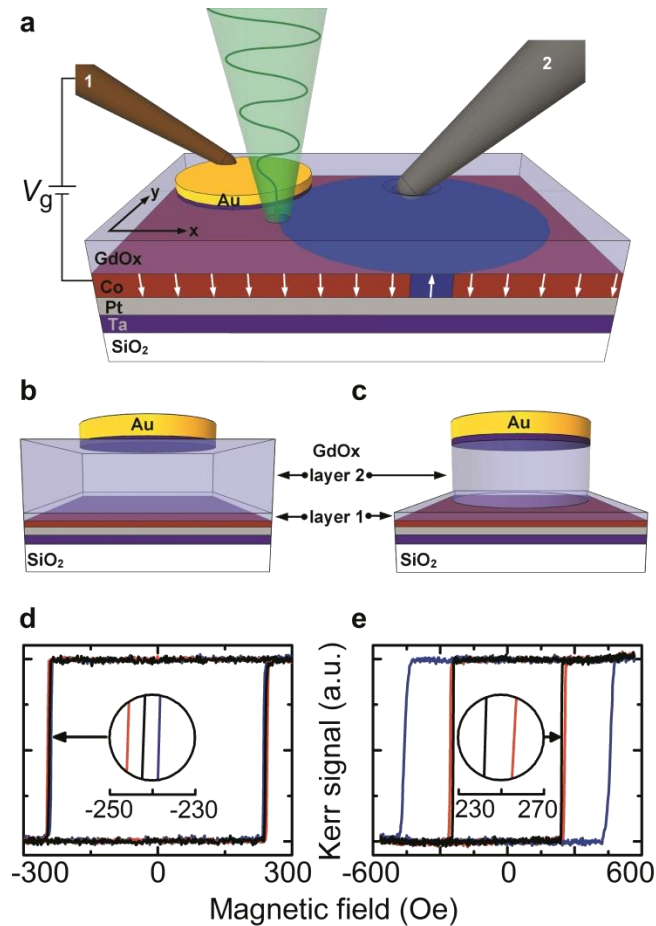


Figure 5-4: Experiment schematics and magnetic hysteresis loops. (a) Schematic showing Ta/Pt/Co/GdOx structure, BeCu microprobe for voltage application (1), W microprobe to create artificial DW nucleation site (2) and focused MOKE laser probe (green cone) to map out (x, y) magnetic domain expansion. (b,c) Device schematic showing double-layer GdOx dielectric with continuous second layer (Sample A) (b) and patterned second layer (Sample B) (c). (d,e) Hysteresis loops for Sample A (d) with $V_g = 0$ V (solid black line), -7 V (solid blue line) and $+6$ V (solid red line) and for Sample B (e) in virgin state (solid black line) and after $V_g = -6$ V for 180 s (solid blue line) and $V_g = +6$ V for 300 s (solid red line). Insets show magnified section of hysteresis loops.

Spatially resolved measurements of H_c further elucidate these results. Figure 5-5(b-e) show maps of H_c in the vicinity of a gate electrode on Sample B. In the virgin state (Figure 5-5(b)), H_c increases monotonically and continuously with distance from the artificial nucleation site located to the right of the imaged region, as expected for a circularly-expanding domain.^{89,90} H_c at the gate electrode center is ~ 230 Oe. After negative V_g application (Figure 5-5(c)), H_c increases abruptly at the electrode perimeter and is uniformly enhanced to ~ 460 Oe across the electrode area. After positive V_g application (Figure 5-5(d)) H_c returns to within a few per cent of its initial value, with only a small stepwise increase visible at the electrode edge.

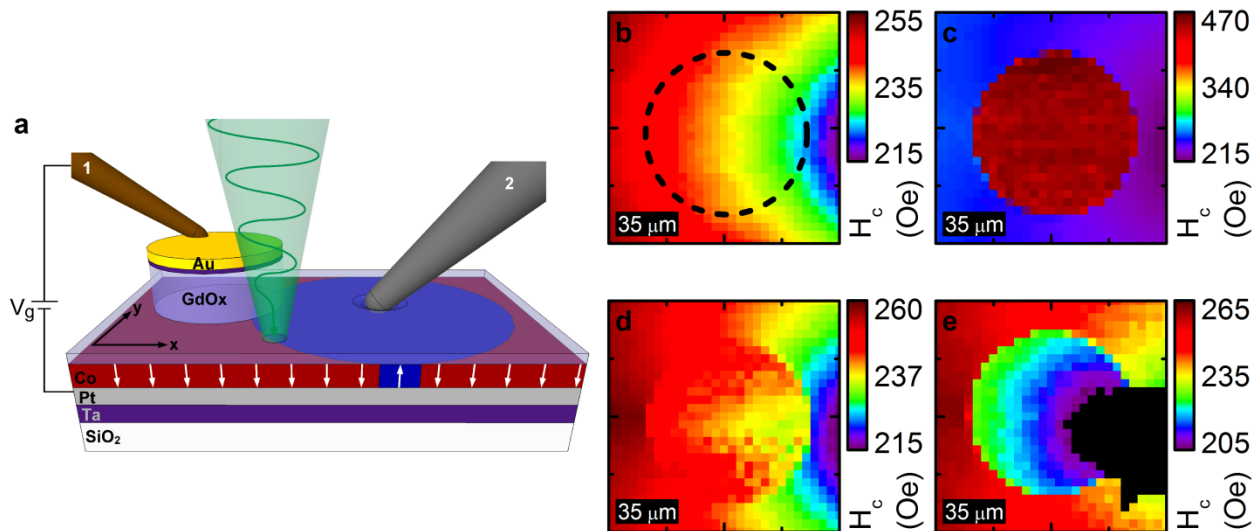


Figure 5-5: Domain wall propagation. (a) Experiment schematic showing Pt/Co/GdOx structure on Sample B, BeCu microprobe for voltage application (1), W microprobe to create artificial DW nucleation site (2) and focused MOKE laser probe to locally measure hysteresis loops in order to map out (x,y) the coercivity H_c . White arrows illustrate local orientation of magnetization vector during expansion of domain from artificial nucleation site. (b-e) Maps of H_c around gate electrode on Sample B with device in virgin state (b), after $V_g = -6$ V for 180 s (c,e) and after $V_g = +6$ V for 300 s (d). Artificial nucleation site is located to the right of imaged region (b-d) or inside electrode area (e). All measurements at $V_g = 0$ V. Note very different scale in (c). Dashed black line in (b) indicates perimeter of gate electrode.

Prior to acquiring the data in Figure 5-5(e), the electrode was switched back to a high-coercivity state with $H_c \sim 460$ Oe. Then the W microprobe tip was used to generate an artificial nucleation site inside the electrode and H_c was again locally mapped. Here, H_c is lower inside the electrode than outside, and a clear step is again seen at the perimeter. In this case the step is less than in Figure 5-5(c) because of the reduced nucleation threshold at the first W probe landing site to the right of the electrode. Comparing Figure 5-5(c) and Figure 5-5(e), the voltage-induced enhancement in H_c is evidently due to modified domain expansion across the device area.

Figure 5-6 shows space and time-resolved images of domain expansion in Sample B at zero V_g that reveal the origin of the H_c enhancement. At each pixel, the magnetization was first saturated and then a reverse field $H = +170$ Oe was applied while acquiring a time-resolved MOKE signal transient. Fifty reversal cycles were averaged at each position, from which the average trajectory of the expanding domain was reconstructed. Figure 5-6(a-d) each shows a sequence of snapshots of domain expansion at increasing times after field-step application. In the virgin state (see Figure 5-6(a)), the DW passes unimpeded underneath the gate electrode. However, in the high- H_c state, domain expansion is blocked at the electrode edge, regardless of whether the artificial nucleation site is outside (Figure 5-6(b)) or inside (Figure 5-6(c)) the electrode.

After switching the device to its high H_c state, the DW velocity inside and outside of the gate electrode was determined. Time-resolved MOKE signal transients were acquired along a line extending radially from the artificial nucleation site located either outside or inside of the electrode. Figure 5-7(b) shows the mean reversal time $t_{1/2}$ as a function of distance from the nucleation site, for both cases. As expected, $t_{1/2}$ increases linearly with distance from the nucleation site. In fact, $t_{1/2}$ increases with exactly the same slope outside and inside of the electrode, which shows that the DW velocity is $\sim 1.5 \times 10^{-2}$ m/s in both cases.

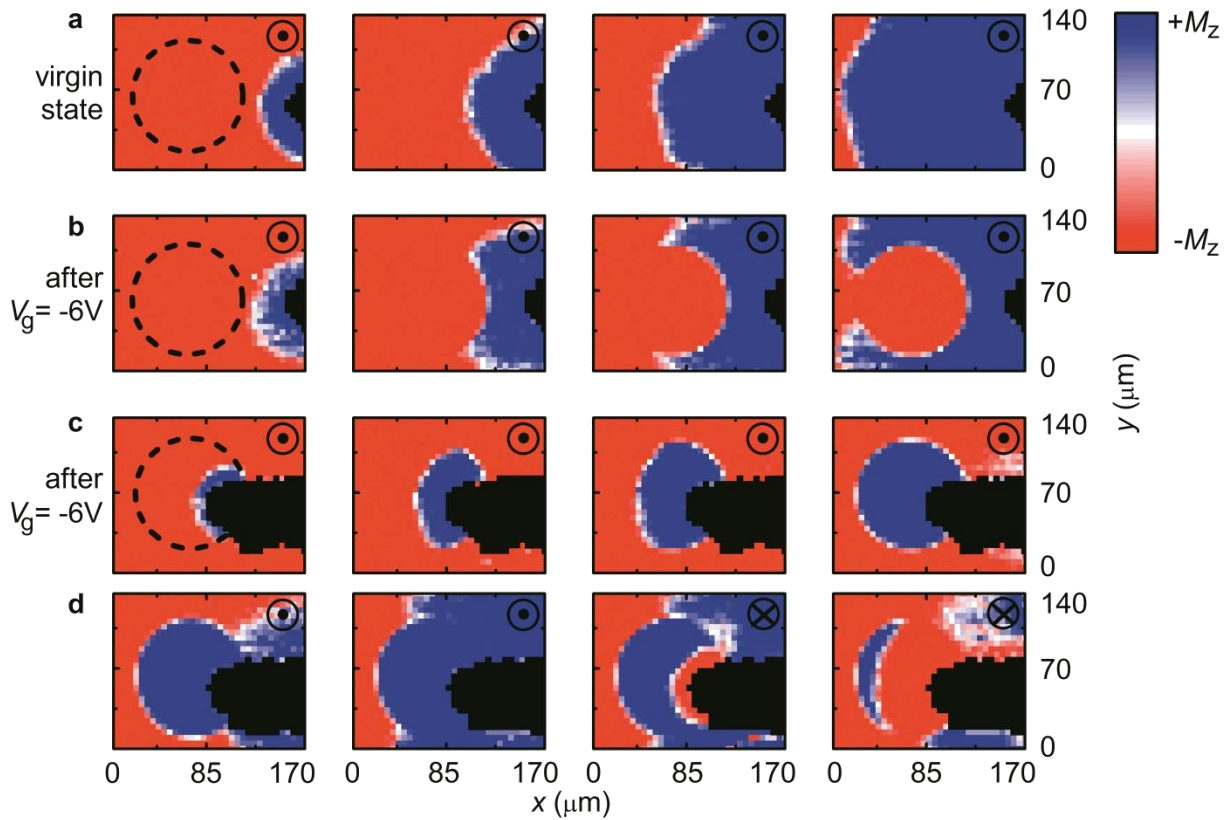


Figure 5-6: Space and time resolved domain expansion. (a-d) Sequences of polar MOKE maps showing domain expansion on Sample B with increasing time (left to right) under driving field $H = 170$ Oe. Sequence (a) shows virgin device state whereas sequences (b-d) correspond to high- H_c state with $H_c = 460$ Oe after application of $V_g = -6$ V for 180s. All maps (a-d) measured at $V_g = 0$ V with artificial nucleation site either outside (a,b) or inside (c,d) of electrode. Domain expansion in (d) is continuation of (c) with reversed H direction from second map on. Sequences (a), (b) and (c) span 9.8 ms, 9.8 ms and 4.2 ms, respectively. Sequence (d) spans 12.2 ms and H was reversed after 6.2 ms. Symbol in upper right corner of each map (a-d) indicates H direction, dashed black line in (a-c) shows outline of gate electrode and black map area (a-d) corresponds to W microprobe used to create artificial nucleation site.

The DW creep velocity depends exponentially on the activation energy E_a and is therefore very sensitive to the uniaxial anisotropy constant K_u and saturation magnetization M_s . Since the DW creep velocity is unchanged underneath the electrode in the high- H_c state, the irreversible changes that block DW propagation after voltage application occur only at the electrode perimeter. This indicates formation of either a

potential barrier or a potential well depending on whether the local anisotropy energy is enhanced or reduced by voltage application. The panels in Figure 5-6(d) show a continuation of the sequence in Figure 5-6(c) after subsequent application of a negative field step. If the electrode perimeter acted as a potential barrier, the domain within the electrode should collapse inward as the DW retreats from the electrode edge. However, the DW remains pinned at the electrode perimeter, and reversal inside the electrode instead proceeds by nucleation of a reversed domain underneath the W probe tip. We therefore conclude that the electrode perimeter acts as a strong DW trap.

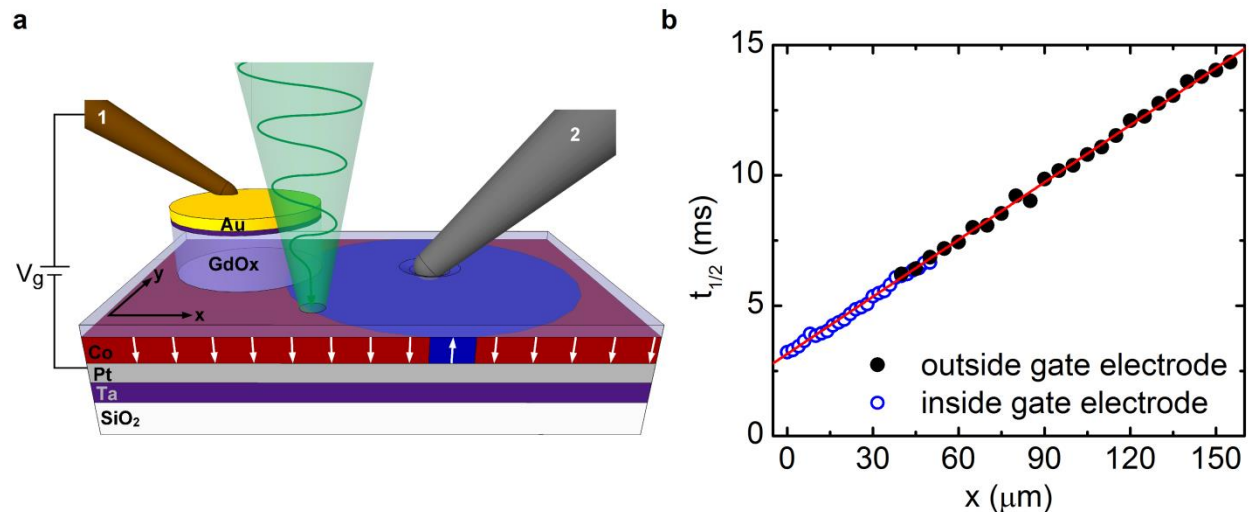


Figure 5-7: Domain wall velocity inside and outside of electrode. (a) Experiment schematic showing Pt/Co/GdOx structure on Sample B, BeCu microprobe for voltage application (1), W microprobe to create artificial DW nucleation site (2) and focused MOKE laser probe to measure MOKE transients. White arrows illustrate local orientation of magnetization vector during expansion of domain from artificial nucleation site. (b) Mean magnetization reversal time $t_{1/2}$ as a function of position, extracted from MOKE transients measured at $H = 170$ Oe along a radial line from the artificial nucleation site, after setting DW trap by applying $V_g = -6$ V for $t = 180$ s. The nucleation site is located outside/inside the gate electrode to measure $t_{1/2}$ versus position outside/inside of the electrode area, respectively. Red line is linear fit to data. Note that the x position is arbitrary and has been shifted for clarity.

The nonvolatility of this effect and its localization at the electrode perimeter, where the electrostatic field is weaker than it is at the interior, indicate that electric-field-induced electron accumulation/depletion cannot be responsible. Rather, the timescale of trap creation (seconds), together with the unprecedentedly-strong influence on DW propagation, suggest an ionic rather than electronic origin. Rare-earth Gd-based oxides are well-known solid state ionic conductors in which high O^{2-} vacancy mobility is often exploited for, e.g., memristive switching devices^{3,4} and oxygen exchange in solid oxide fuel cells.¹⁶⁸ In thin-film amorphous metal oxides ionic exchange is particularly efficient, and occurs readily at RT.^{4,118,119} As PMA in Co/metal-oxide bilayers is highly sensitive to interfacial oxygen coordination,^{9,47} we suggest that O^{2-} vacancy transport in the GdOx permits voltage-controlled O^{2-} accumulation or depletion near the Co/GdOx interface, which consequently alters the local magnetic energy landscape. Negative V_g is expected to drive O^{2-} towards the Co/GdOx interface, and overoxidation of the Co would decrease both PMA^{19,20} and the saturation magnetization. The resulting decrease in magnetic energy density confined to a very short length scale near the electrode edge would produce a DW trap consistent with our observations.

Indeed, the electrode edge corresponds to the triple phase boundary (TPB) where O_2 gas, O^{2-} ion-conducting and electron-conducting phases meet and electrochemical reactions occur most efficiently.¹²¹ Since DW traps are only generated near the TPB, the open oxide edge in Sample B likely provides the necessary high diffusivity path for O^{2-} ions to the Co/GdOx interface. Since bulk diffusion is typically much slower than surface diffusion,¹⁷¹ the timescale for these effects should be correspondingly longer for Sample A, consistent with the lack of irreversibility at low voltage in that sample.

5.5 Voltage Controlled Domain Wall Traps in Magnetic Nanowires

Voltage-gated DW traps can not only be used to control DW propagation in continuous magnetic thin films (see Section 5.4), but also allow efficient control of DWs in magnetic nanowires (see Figure 5-8 and Figure 5-9). A 500 nm wide, 30 μm long Ta(4 nm)/Pt(3 nm)/Co(0.9 nm)/GdOx(3 nm) nanowire was fabricated with a 5 μm wide GdOx(30 nm)/Ta(2 nm)/Au(12 nm) gate electrode at its center, and DW nucleation lines at either end (see Figure 5-8(a)).

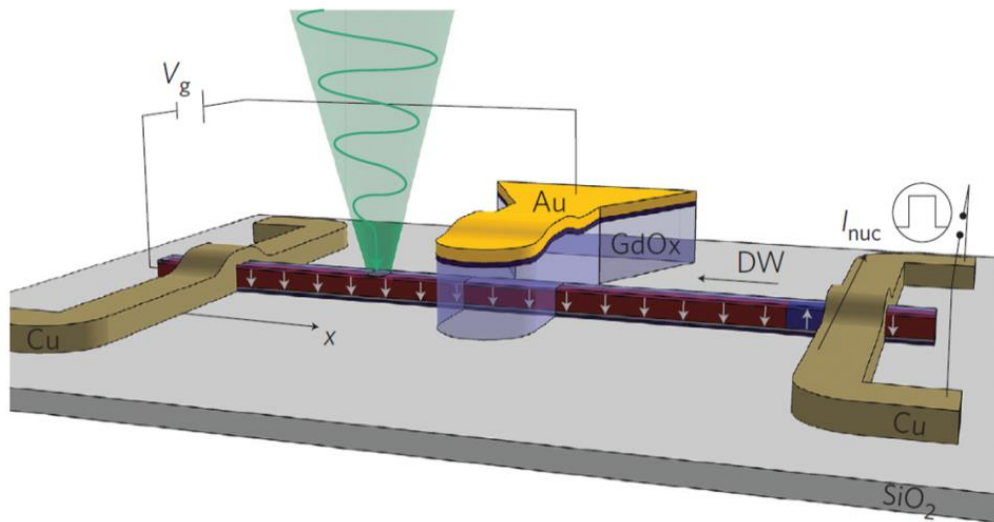


Figure 5-8: Nanowire conduit with integrated domain wall trap. (a), Device schematics showing 30 μm long and 500 nm wide Ta/Pt/Co/GdOx nanowire conduit with orthogonal Cu lines at each end (for DW initialization through current pulse I_{nuc}) and 5 μm wide GdOx/Ta/Au gate electrode at center of wire. Green cone represents focused MOKE laser probe.

Figure 5-9(a-f) shows the DW propagation field H_{prop} versus position, measured by first nucleating a DW at one end of the nanowire with a current pulse through the Cu line, and then sweeping H while detecting DW propagation using MOKE. In the virgin state (Figure 5-9(a,d)) DWs propagate freely underneath the gate. After applying $V_g = -5$ V for 60 s and then setting V_g to zero, H_{prop} for leftward-propagating DWs (Figure 5-9(b)) exhibits a large step at each edge of the gate, while for rightward-propagating DWs (Figure 5-9(e)) there is

a single step at the left side of the gate. This behavior indicates the presence of localized DW traps at the right and left edges of the gate, with pinning strengths of ~ 300 Oe and 400 Oe, respectively. As seen in Figure 5-9(c,f), the traps can be subsequently removed by application of a positive gate voltage.

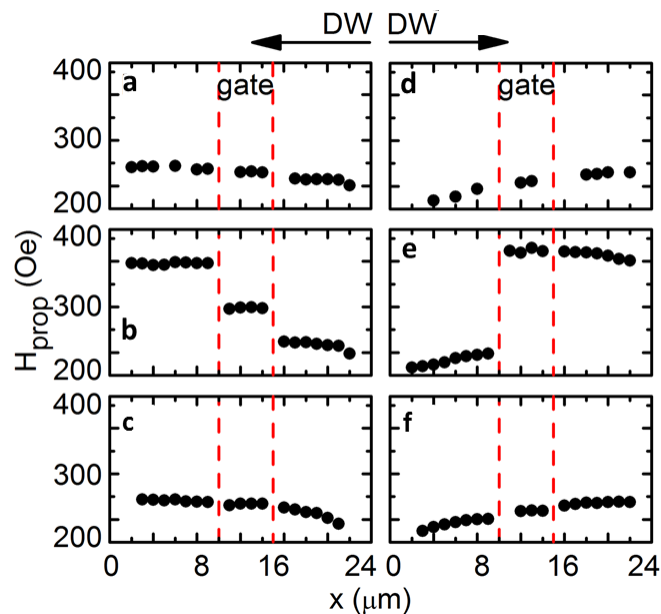


Figure 5-9: Control of domain wall propagation in magnetic nanowire conduits. (a-f), DW propagation field along nanowire for device in virgin state (a,d), after application of $V_g = -5$ V for 60s (b,e) and after application of $V_g = +6$ V for 120s (c,e) with DW initialization from right end (a-c) or left end (d-f) of nanowire. All measurements at $V_g = 0$ V.

By reducing the gate width to 800 nm (Figure 5-10(a)), directional asymmetry in H_{prop} was greatly reduced, suggesting that the traps begin to overlap at this length scale. Figure 5-10(b) shows that H_{prop} can be programmatically set to any desired level up to at least 650 Oe (the limit of our electromagnet), by controlling the integrated voltage dwell time and in Figure 5-10(c), H_{prop} was repeatedly cycled between ~ 250 Oe and 450 Oe to demonstrate the robustness of the switching mechanism. Finally, Figure 5-10(d) and Figure 5-10(e) show that once set, H_{prop} remains stable at zero bias for more than 24 h.

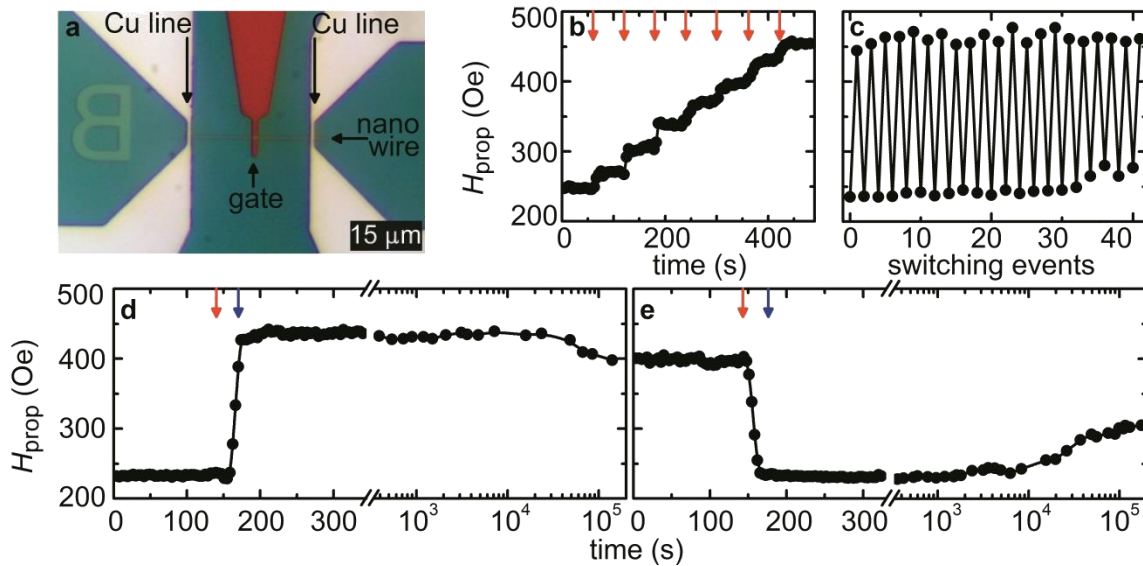


Figure 5-10: Properties of domain wall traps in nanowire conduits. (a) Optical micrograph showing Ta/Pt/Co/GdOx nanowire conduit with Cu lines and GdOx/Ta/Au gate with reduced width of 800 nm. (b) Stepwise increase of DW trap pinning strength due to application of 5 s long voltage pulses of $V_g = -3$ V (red arrows). (c) Twenty switching cycles of DW trap pinning strength between ~ 250 Oe and ~ 450 Oe. (d,e) First switching cycle of virgin device. Retention of pinning strength over 48 h after application of $V_g = -5$ V for 30 s (d) and then after $V_g = +5$ V for 30 s (e). Red/blue arrows in (d,e) indicate time of bias application/removal, respectively.

To demonstrate the viability of DW traps to control DWs moving at device relevant speeds, MOKE transients were measured along the nanowire before and after a DW trap was activated underneath the gate electrode (see Figure 5-11(a)). It can be seen that in the absence of a DW trap, $t_{1/2}$ increases linearly with distance from the nucleation site (see Figure 5-11(b)). At the maximum available field of $H = 650$ Oe, we find a DW velocity of ~ 20 m/s from the slope of $t_{1/2}$ versus position. After a DW trap is created and set to a pinning strength of > 650 Oe (beyond the maximum available H), the DW still moves with a velocity of ~ 20 m/s, but only up to the gate electrode. Beyond the gate electrode, no magnetization reversal is observed. This shows that even at ~ 20 m/s, DWs still come to a standstill upon entering the voltage-controlled trap.

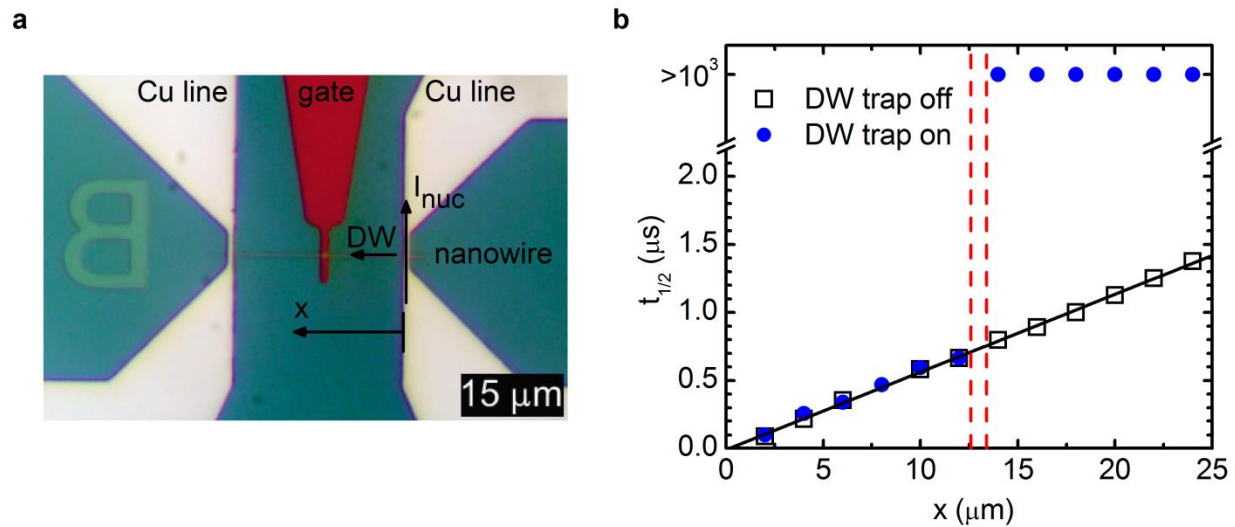


Figure 5-11: Trapping high velocity domain walls. (a) Device schematic showing 500 nm wide Pt/Co/GdOx nanowire with Cu lines at each end for DW initialization and 800 nm wide GdOx/Ta/Au gate to program DW trap. A reversed domain is nucleated at the right end of the magnetic nanowire by the Oersted field of a current pulse I_{nuc} injected through the Cu line on the right. The initialized DW is then driven along the nanowire, away from the nucleation line (in positive x -direction) by a perpendicular magnetic field H . (b), Mean reversal time $t_{1/2}$ extracted from time-resolved MOKE transients measured along the nanowire at a driving field $H = 650$ Oe before and after setting DW trap underneath gate electrode. Dashed red line outlines gate electrode position and black line is linear fit to data.

5.6 Prototype Nanowire Register

Finally, we demonstrate a n -bit nonvolatile memory cell based on $n-1$ gate electrodes programmed as a cascaded sequence of DW traps with successively increasing pinning strength. An arbitrary bit sequence can then be written using a sequence of n global field pulses with successively decreasing amplitude. To write a bit pattern, a new DW is initialized with the injection line prior to each field pulse and the pulse amplitudes are such that the m th pulse drives the initialized DW past the first $m-1$ DW traps but not past the m th trap.

Figure 5-12(a) shows a micrograph of a 3-bit register, with each bit separated by a gate electrode. DWs are nucleated using the Cu nucleation line to the right, and the right and left DW traps are set to pinning strengths of 450 Oe and 550 Oe, respectively. Three field pulses $|H| = 635$ Oe, 505 Oe and 325 Oe are used to write the three bits, with the pulse polarity determining the polarity of the corresponding bit. Field pulse sequences and MOKE maps for all possible domain states are shown in Figure 5-12(b-h), where the down-saturated state was used as a reference to extract the differential MOKE signal.

A complimentary field pulse sequence is used to read out the bits. Here, read-out is done by MOKE with the laser spot placed on the first bit, but this could in principle be done all-electrically via a magnetic tunnel junction. For the read out process, bit 1 is read and then set to a reference state. Subsequent bits are read out in sequence by applying read and reset field pulses of equal amplitude but opposite polarity for each bit. To read the m th bit, the pulse amplitude is between the pinning strengths of the $m-1$ th and m th DW trap. If the state of the m th bit is different from the reference state, the read pulse sweeps the DW from the $m-1$ th DW trap through the first bit where it is detected. Afterwards, the reset pulse, accompanied by a DW nucleation pulse, resets all previously read bits to the reference state. Otherwise the read and reset pulses have no effect.

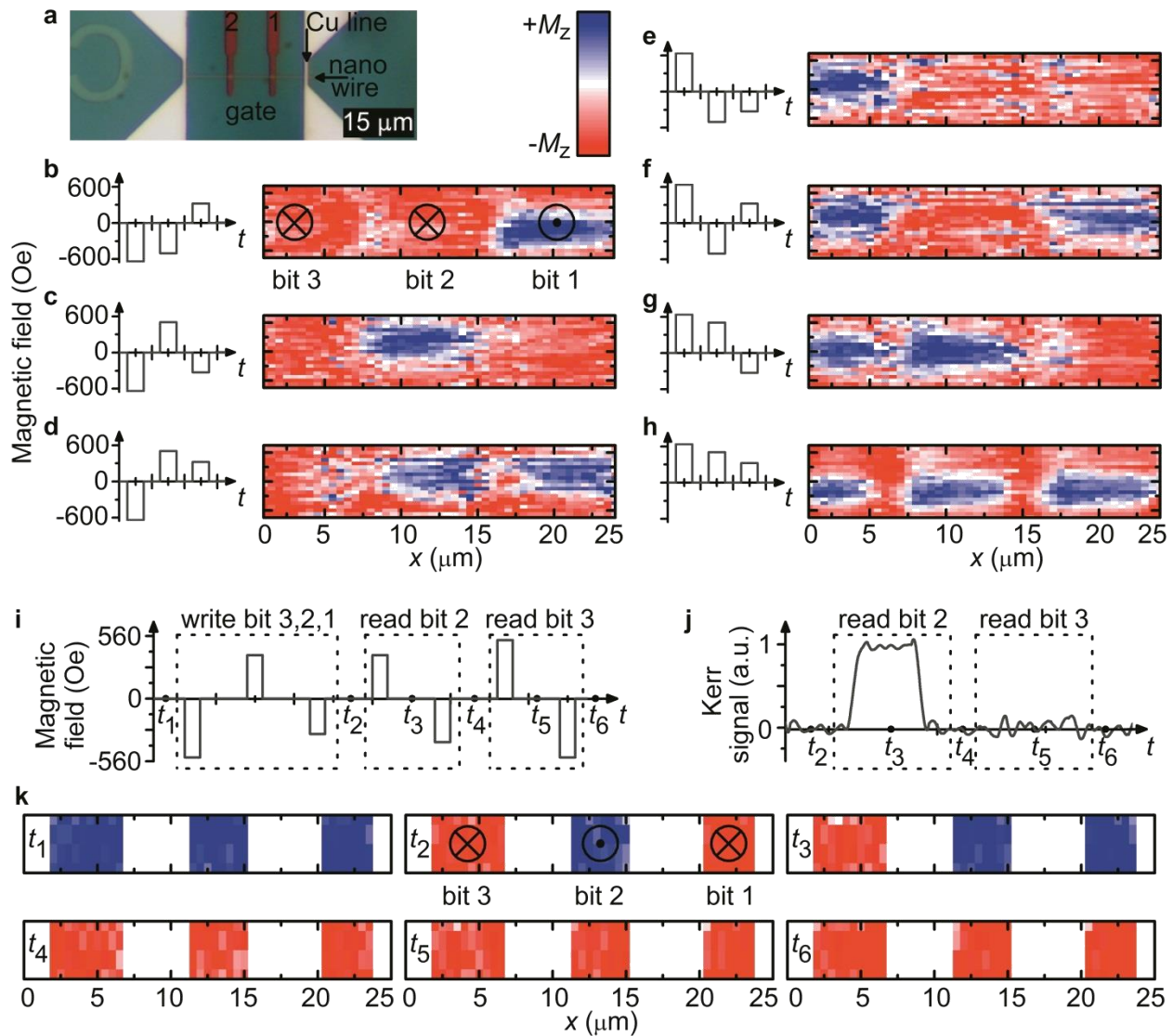


Figure 5-12: Domain wall trap based 3-bit register. (a) Optical micrograph showing 3 bit register consisting of Ta/Pt/Co/GdOx nanowire conduit with Cu lines and two 800 nm wide GdOx/Ta/Au gates. (b-h) Magnetic field pulse sequence (2 ms pulse duration) and Kerr images of nanowire register in the corresponding 3-bit state. (i) Magnetic field pulse sequence (2 ms pulse duration) to write and subsequently read out 3-bit register. (j) Kerr signal during read out of 2nd and 3rd bit. (k) Kerr images of the nanowire device at different times t_1 - t_6 during the write and read out process. Symbols in Kerr images of (b) and (k) indicate magnetization direction of individual bits and white area in (k) corresponds to area of nanowire obstructed by gates and Cu lines.

The read out process for the 3-bit register is demonstrated in Figure 5-12(i-k), where the reference state (bit 1) is chosen to be magnetization down. An array of such devices could be driven by a single global field source, with any particular nanowire register addressed as above, while all other registers are placed in an inactive state by setting all DW traps to a high-pinning state. Although a practical device will require significantly increasing the switching speed of the voltage-controlled traps, these results demonstrate that voltage-controlled DW traps can be used to realize novel devices.

5.7 Summary and Conclusion

In this chapter, we show that a voltage can generate giant, nonvolatile switching of magnetic properties at the nanoscale by modulating interfacial chemistry rather than charge density. We demonstrate that a functionally-active gate dielectric allows the creation of voltage-controlled DW traps that are nonvolatile, programmable, and switchable. We explain the observed effects in terms of enhanced ionic mobility in the gate oxide, which permits voltage-controlled changes to interfacial ionic coordination with a consequent modification of interfacial magnetic anisotropy. The localization of this change to a narrow region at the electrode edge leads to sharp voltage-controlled magnetic potential wells with unprecedented pinning strength. While the voltage-induced effects observed here occur over relatively long timescales, ionic transport can occur at the nanosecond timescale in, e.g., memristive switching devices.^{4,110} Optimization of the gate oxide materials and structure based on design principles that are already well-established in solid-state ionic devices should permit fast voltage-induced changes to the Co/oxide interface and therefore rapid switching of magnetic properties. The merger of magnetic and solid-state ionic materials represents a novel class of functional materials that offers an alternative to traditional magneto-electric composites based on complex oxides. By replacing ferroelectric or piezoelectric materials with simple oxide dielectrics, magneto-ionic composites could allow realization of high-performance magneto-electric devices using fabrication conditions compatible with complementary metal-oxide semiconductor processing.

6 MAGNETO-IONIC CONTROL OF INTERFACIAL MAGNETISM*

In metal/oxide heterostructures, rich chemical,^{1,2} electronic,³⁻⁵ magnetic⁶⁻⁹ and mechanical^{14,15} properties can emerge from interfacial chemistry and structure. The possibility to dynamically control interface characteristics with an electric field paves the way towards voltage control of these properties in solid-state devices. For example, ferromagnetic metal/metal-oxide bilayers such as Co/AlO_x and CoFe/MgO exhibit strong PMA derived from interfacial Co-O hybridization.^{8,9} The ability to toggle interfacial PMA with a gate voltage would dramatically reduce switching energies in spintronic devices, and could enable new device architectures exploiting local gating of magnetic properties.^{31,32,41,44,89,111,143,172-175} Most work on voltage control of magnetic anisotropy in metal/metal-oxide bilayers has focused on charge accumulation or band shifting in the metal layer.^{31,32,41,44} However, the results from Chapter 5 and other experimental reports of

* Sections of this chapter, including figures, have been previously published in the following articles:

- Bauer, U., Yao, L., Emori, S., Tuller, H. L., Dijken, S. van & Beach, G. S. D. Magneto-ionic control of interfacial magnetism. submitted for publication (2014).

irreversibility, and anisotropy changes much larger than theoretically predicted,^{111,172} suggest ionic effects may be important and in some cases even dominant.^{89,143,173-175} Nonetheless, electric field driven oxygen migration in metal/metal-oxide bilayers is difficult to observe directly, and its impact on magnetic properties has not yet been established.

In this chapter, we observe for the first time, *in situ* voltage-driven O²⁻ migration in a Co/metal-oxide bilayer and show that electrical switching of the interfacial oxidation state allows for voltage control of magnetic properties to an extent never before achieved through conventional magneto-electric coupling mechanisms. In Section 6.2 we use cross-sectional transmission electron microscopy and high-resolution electron energy loss spectroscopy, to track the position of the oxidation front in a Co/GdO_x bilayer before and after voltage application and show that the oxidation front can be reversibly controlled by changing the polarity of the gate voltage.

The thermally-activated nature of ion migration is exploited in Section 6.3 to dramatically increase the switching efficiency by activating oxygen migration in the bulk of the GdO_x. We toggle interfacial MAE by an unprecedented >0.6 erg/cm² at a voltage of just 4V, yielding a magneto-electric efficiency >5000 fJ/Vm. These giant anisotropy modifications establish magneto-ionic coupling as a powerful new mechanism for voltage control of magnetism and allow us to completely remove and restore PMA in a thin Co layer.

By varying temperature and interface structure, Section 6.4 relates the motion of the oxidation front to voltage-induced anisotropy changes, and shows that increasing the temperature by just ~100 °C above ambient reduces the timescale of these effects by ~4 orders of magnitude. Finally, in Section 6.5, we introduce a general method to reversibly imprint material properties through local activation of ionic migration, which we use to locally pattern magnetic anisotropy and create DW conduits in continuous magnetic films. These results suggest a path towards voltage-programmable materials based on solid-state switching of interface oxygen chemistry.

6.1 Experimental Methods

Ta(4 nm)/Pt(3 nm)/Co(0.9 nm)/GdO_x(3 nm) films were prepared by DC magnetron sputtering at RT under 3 mTorr Ar with a background pressure of $\sim 1 \times 10^{-7}$ Torr, on thermally-oxidized Si(100) substrates. For the samples described in Figure 6-5, the top GdO_x layer was 30 nm thick. All GdO_x layers were deposited by reactive sputtering from a metal Gd target at an oxygen partial pressure of $\sim 5 \times 10^{-5}$ Torr.

Gate electrodes of GdO_x(30 nm)/Ta(2 nm)/Au(12 nm) were patterned on the (4 nm)/Pt(3 nm)/Co(0.9 nm)/GdO_x(3 nm) films using electron beam lithography and lift-off. For the samples in Section 6.4 with a Gd metal spacer layer and the 30 nm thick GdO_x top layer, Ta(2 nm)/Au(12 nm) electrodes were deposited through a shadow mask.

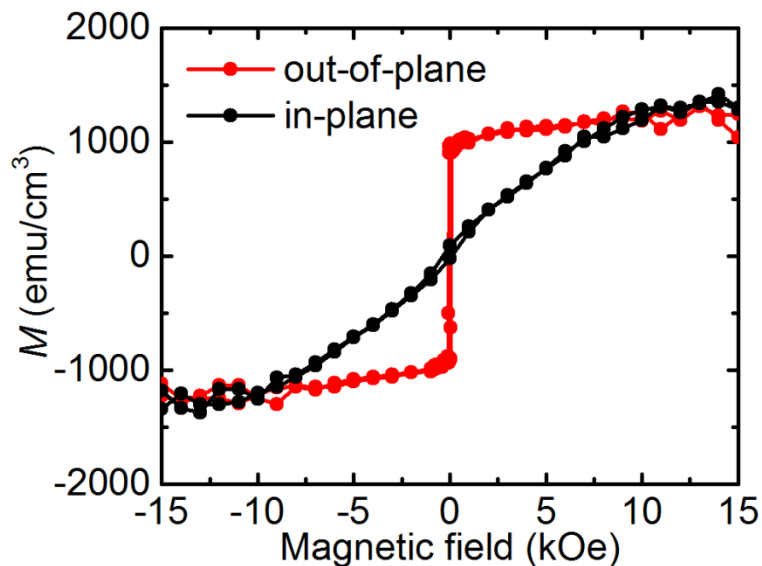


Figure 6-1 Vibrating sample magnetometry. In-plane and out-of-plane hysteresis loops of Ta(4 nm)/Pt(3 nm)/Co(0.9 nm)/GdO_x(3 nm) film measured by vibrating sample magnetometry.

The magnetic properties of Ta(4 nm)/Pt(3 nm)/Co(0.9 nm)/GdO_x(3 nm) films were characterized by VSM (see Figure 6-1). The films exhibited an in-plane saturation field H_k of

~10 kOe and a saturation magnetization M_s of ~1300 emu/(cm³ of Co) which suggests minimal Co oxidation during growth of the GdOx overlayer.

Microstructural analysis and electron energy loss spectroscopy (EELS)* were performed on a JEOL 2200FS transmission electron microscope (TEM) with double Cs correctors, operated at 200 keV. A cross-sectional TEM specimen was fabricated from a patterned Si/SiO₂/Ta(4 nm)/Pt(3 nm)/Co(0.9 nm)/GdOx(30 nm)/Ta/Au sample using the following steps: First, a Si substrate was glued to the top surface of the sample and the Si/multilayer/Si sandwich was subsequently cut into thin slices. Next, a thin slice was polished into a wedge by a MultiPrep polishing machine (Allied High-Tech). After gluing the specimen to a half TEM Cu grid, it was further polished by Ar ion milling. Before mounting the grid onto an *in situ* electrical probing holder (HE150, Nanofactory Instruments AB), the Si was unglued from the wedge using acetone. After Si removal, a piezo-controlled Pt/Ir tip with a diameter of about 40 nm was able to contact the patterned electrode on top of the GdOx layer. Slight bending of the sample was observed after contact, but the structural integrity of the layers remained intact (Figure 6-2(b)). Silver paste was used to make electrical contact between the bottom electrode of the layer structure and the Cu grid. The thickness of the TEM specimen was estimated to be less than 30 nm by measuring the intensity ratio of the plasmon loss and the zero-loss peaks in EELS. For the analysis of EELS core-loss peaks, background subtraction was performed using a power-law fit. The lateral resolution of STEM-EELS characterization was about 0.25 nm.

Polar MOKE measurements were made using a 532 nm diode laser attenuated to 1 mW, except where noted. The laser was focused to a ~3 μm diameter probe spot and positioned by a high resolution scanning stage with integrated temperature control (see Section 3.2.2 for details). Gate voltage was applied using a mechanically-compliant BeCu microprobe. Mechanically-generated nucleation sites created for the measurements in Figure 6-3 were prepared by applying mechanical stress to the film surface using a stiff W

* Transmission electron microscopy and electron energy loss spectroscopy were performed in collaboration with Lide Yao and Sebastiaan van Dijken at Aalto University, Finland.

microprobe tip. Magnetic hysteresis loops were measured at a sweep rate of 28 kOe/s, using an electromagnet with a rise time of $\sim 300 \mu\text{s}$ and a maximum amplitude of 650 Oe.

The time-resolved domain expansion snapshots in Figure 6-9, Figure 6-11 and Figure 6-12 were obtained by, at each pixel, first saturating the magnetization and then applying a reverse field step ($H=90$ Oe in Figure 6-11, and $H=42$ Oe in Figure 6-12) while acquiring a time-resolved MOKE signal transient. Five reversal cycles were averaged at each pixel, from which the average trajectory of the expanding domain was reconstructed (see Section 3.2.3 for more details).

Time resolved MOKE transients along a line extending radially from a nucleation site were used to determine the DW velocity reported in Figure 6-12(g) (see Section 3.2.3 for details on the technique). At each position, 25 reversal cycles were acquired and averaged, yielding the cumulative probability distribution of switching times. The mean reversal time $t_{1/2}$, taken as the time at which the probability of magnetization switching is 50 %, was plotted versus position, and the slope used to determine the mean velocity.

To estimate the laser-induced temperature increase ΔT , we used the temperature dependence of the coercivity of a sub micrometer patterned feature. We first measured H_c versus substrate temperature, using a temperature-controlled stage and a low incident laser power ($<1\text{mW}$) for the MOKE probe spot, and then measured H_c versus incident laser power P , at a fixed substrate temperature. We estimate that $P = 1$ mW corresponds to a negligible ΔT whereas $P = 10$ mW corresponds to a ΔT of at least ~ 20 °C.

6.2 *In situ* Tracking of the Oxidation Front

Ta(4 nm)/Pt(3 nm)/Co(0.9 nm)/GdOx(3 nm) films sputter-deposited on thermally-oxidized Si were used to demonstrate that a gate voltage results in migration of the oxidation front in Co/GdOx bilayers. The films exhibit strong PMA with an in-plane saturation field $H_k \sim 10$ kOe (see Figure 6-1). Square 200 μm x 200 μm GdOx(30 nm)/Ta/Au gate electrodes were patterned on top of the film for voltage application, with the bottom metal stack used as counter electrode. Figure 6-2(a) shows a high-resolution cross-sectional TEM micrograph of the layer structure, with the thin Co layer embedded between polycrystalline Pt and GdOx layers.

Spatially resolved EELS experiments were carried out in scanning TEM (STEM) mode on the same cross section to measure the chemical profile and to detect changes induced by a gate voltage V_g .^{*} Voltage was applied by contacting the top electrode *in situ* with a Pt/Ir tip as shown in the inset of Figure 6-2(a) (see SI for details). Figure 6-2(b) shows representative STEM-EELS spectra with O K-edges and Co white lines from a location in the center of the Co layer. The evolution of the O K-edge and Co L₃-edge count rates along a line profile perpendicular to the layers is shown in Figure 6-2(c). The Co layer is clearly distinguished, with no O detected within the Co layer and a sharp rise in the O signal at the Co/GdOx interface. Figure 6-2(d,e) shows STEM-EELS scans after applying a negative bias of -3V, and -5V, respectively, each for ~ 100 s, with a polarity that drives O²⁻ towards the Co layer. The data show a clear progression of the oxygen front into the Co layer, with a significant O signal detected near the center of the Co layer after -3V, and at the bottom Co/Pt interface after -5V. The appearance of an O K-edge signal at the center of the Co layer after the application of -3V can also be inferred from the spectra in Figure 6-2(b). Finally, Figure 6-2(f) shows that Co oxidation is reversible under positive bias, and that the O²⁻ content in the Co layer can be toggled repeatedly by cycling V_g .

^{*} Transmission electron microscopy and electron energy loss spectroscopy were performed in collaboration with Lide Yao and Sebastiaan van Dijken at Aalto University, Finland.

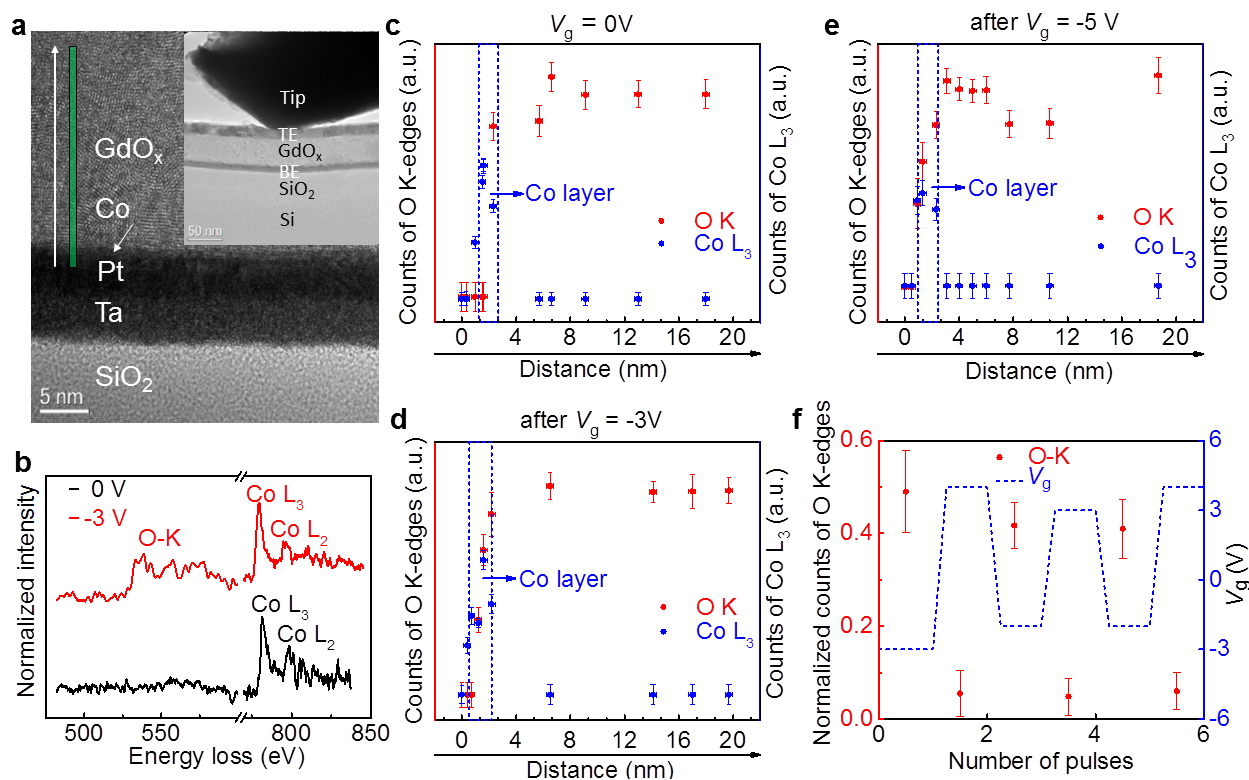


Figure 6-2: Cross-sectional TEM and EELS analysis. (a) High-resolution TEM image of the SiO₂/Ta/Pt/Co/GdO_x layer structure. STEM-EELS spectra were measured along green line, starting from the Pt/Co interface as indicated by white arrow. Inset in (a) Shows contact between the Pt/Ir probe of the *in situ* TEM holder and the Ta/Au top electrode (TE). The Ta/Pt/Co bottom electrode is indicated by BE. (b), STEM-EELS spectra of the O-K edges and the Co-L_{2,3} edges from a location in the center of the Co layer before (black) and after (red) applying a negative bias of -3V. (c-e) O K-edge and Co L₃-edge count rates along a similar line profile as indicated in (a). The data are obtained before the application of a bias voltage (c) and after applying -3V (d) and -5V (e), respectively. (f) O K-edge counts in the middle of the Co layer normalized to the O K-edge signal in the GdO_x layer following three cycles of alternating positive and negative bias voltage.

Figure 6-2 shows that a gate voltage indeed results in migration of the oxidation front in Co/GdO_x bilayers and that the position of the oxidation front can be reversibly controlled by changing the bias polarity. In order to directly link voltage-induced oxygen migration with modifications in magnetic anisotropy, the magneto-electric response of the same samples is investigated in Section 6.3 and 6.4.

6.3 Thermally Activated Anisotropy Modifications

We examined the impact of voltage-induced O^{2-} migration on magnetic properties using a scanning MOKE polarimeter with a $\sim 3 \mu\text{m}$ laser spot to locally probe hysteresis characteristics. Figure 6-3(a) maps the coercivity H_c in the vicinity of a gate electrode, shown schematically in Figure 6-3(b). Prior to measurement, a domain nucleation site was created nearby using a mechanical microprobe^{89,90,143} so that H_c represents the DW propagation field,^{89,90,143} which is highly sensitive to the MAE landscape.

In the virgin state (see Figure 6-3(a)), H_c is uniform across the measured area, reflecting a DW propagation field of $\sim 200 \text{ Oe}$ due to fine-scale disorder. After applying $V_g = -4\text{V}$ for 240s and then setting $V_g = 0\text{V}$, H_c exhibits an abrupt step at the electrode edge (see Figure 6-3(c)) and increases to $\sim 340 \text{ Oe}$ beneath the electrode. Similar behavior has been observed previously¹⁴³ and attributed to O^{2-} migration near the electrode perimeter, where ionic transport is typically most efficient¹⁷¹. This would locally reduce the MAE energy by over-oxidizing the Co interface^{8,9}, creating potential wells at the electrode edge (Figure 6-3(d)) that trap propagating DWs, increasing H_c . We verified that the DW propagation field at the interior of the electrode remained unchanged after V_g application by mechanically creating a nucleation site inside the electrode. The observed magnetic behavior is thus consistent with the schematic MAE landscape in Figure 6-3(d). The lack of irreversible MAE changes at the electrode interior suggests the timescale for bulk O^{2-} diffusion is much longer than at the electrode perimeter, where the open oxide edge (Figure 6-3(b)) provides a high-diffusivity path¹⁷¹. The high ionic mobility observed in Figure 6-2 is likewise probably aided by the high surface to volume ratio of the polished TEM specimen, since the activation energy for surface diffusion is typically lower than for bulk¹⁷¹. Voltage-induced O^{2-} migration, however, need not be limited to the oxide edge. Due to the thermally-activated nature of ion migration, voltage application at elevated temperature should result in exponentially higher O^{2-} drift velocities,¹⁷¹ and activation of bulk O^{2-} migration on an observable timescale.

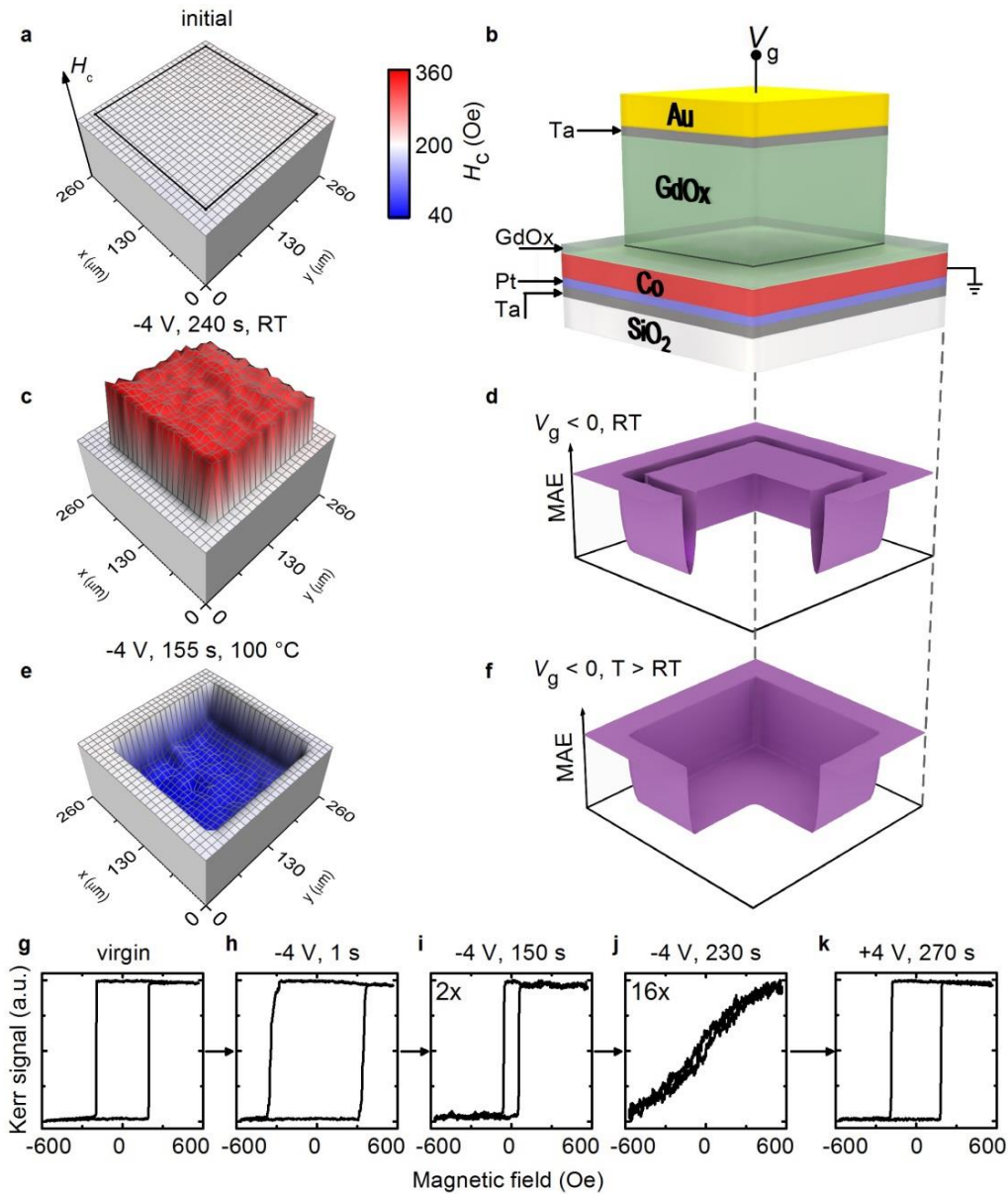


Figure 6-3: Device schematics and voltage control of magnetic anisotropy. (a) Topographic map of the coercivity (H_c) in the virgin state, in the vicinity of a gate electrode. (b) Schematic view of gate electrode structure. (c). and (d). show H_c and the implied magnetic anisotropy energy (MAE) landscape, respectively, after applying a gate voltage $V_g = -4$ V for 240 s at room temperature (RT); (e). and (f). show the same after applying $V_g = -4$ V for 155 s at 100°C . (g-k), Polar MOKE hysteresis loops measured at RT at the center of the gate electrode showing the device in its virgin state (g), after applying $V_g = -4$ V at 100°C for 1 s (h), 150 s (i) and 230 s (j), and after applying $V_g = +4$ V at 100°C for 270 s (k). Note that the Kerr signal intensity in (i) is reduced by a factor of 2 and in (j) by a factor of 16, as indicated by inset number.

Before we characterized the voltage response at elevated temperature, the effects of elevated temperature on magnetic properties was investigated in the absence of a bias voltage. H_c was measured inside the gate electrode while the sample temperature was controlled using a thermoelectric module stable to within ± 0.1 °C. Upon slowly increasing the temperature from a base level of 37 °C to 100 °C (see Figure 6-4), a monotonic decrease of H_c from ~ 200 Oe to ~ 120 Oe is observed. The reduction in H_c is consistent with the thermally activated nature of DW motion in this field range.^{89,90} Once the final temperature of 100 °C is reached, H_c does not show any further modifications and remains stable over time. After ~ 45 minutes the temperature is slowly reduced back to its initial value which is accompanied by a simultaneous increase in H_c back to its initial value of ~ 200 Oe. The lack of a permanent modification of H_c after the heat treatment shows that exposure to 100 °C does not result in any permanent modifications of magnetic anisotropy in the Pt/Co/GdOx samples.

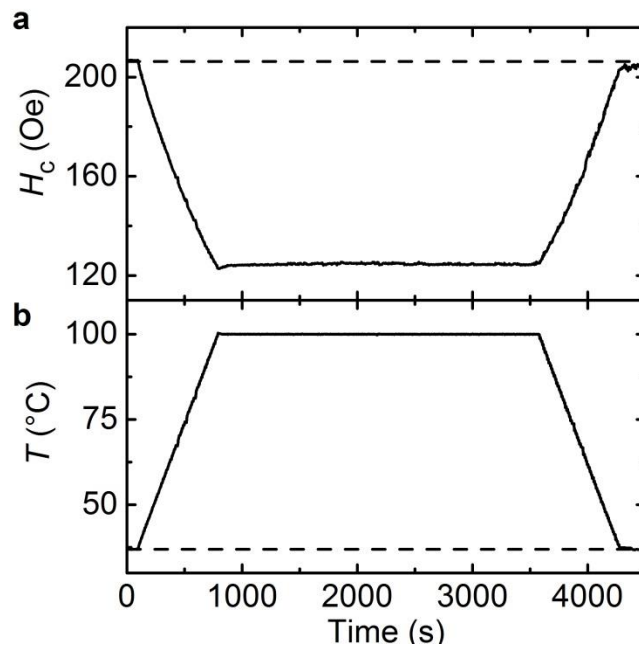


Figure 6-4: Lack of annealing at 100 °C. (a) Coercivity H_c measured as a function of time while the sample temperature T was varied as plotted in (b). (b) Sample temperature as a function of time.

Figure 6-3(e) shows a H_c map after applying $V_g = -4$ V for 155 s at $T = 100$ °C, and then cooling the sample back to RT at $V_g = 0$ V. In this case, H_c outside the electrode is unchanged, confirming that the elevated temperature alone does not irreversibly change the magnetic properties (see Figure 6-4). However, beneath the electrode H_c drops to ~ 50 Oe, indicating that DWs nucleate and propagate there at a much lower field, and are impeded by an anisotropy step at the electrode edge. This implies a significant MAE reduction across the electrode area, shown schematically in Figure 6-3(f), consistent with overoxidation of the Co interface^{8,9}.

As seen in Figure 6-3(g-k), the voltage-induced MAE change at $T = 100$ °C is progressive. Here, we sequentially applied $V_g = -4$ V for a fixed dwell time at $T = 100$ °C, and then cooled the sample to RT with $V_g = 0$ V to measure a hysteresis loop beneath the electrode. We observe an initial increase in H_c due to DW trap formation at the electrode perimeter, which occurs within 1 s of V_g application in contrast to the several minutes required at RT (see Figure 6-3(c)). With increasing voltage dwell time H_c then drops dramatically, indicating a rapid reduction of PMA across the electrode. The saturation MOKE signal also declines, by nearly a factor of 2 after ~ 150 s (see Figure 6-3(i)), suggesting increasing Co oxidation. After several minutes (Figure 6-3(j)), PMA is lost entirely. Remarkably, PMA can be completely restored by reversing the bias polarity, as seen in Figure 6-3(k) after applying $V_g = +4$ V for 270 s at 100 °C.

The results in Figure 6-3(g-k) can be used to estimate the voltage-induced modification of the interfacial MAE. With a thickness d_{Co} of 0.9 nm, an in-plane saturation field H_k of ~ 10 kOe and a saturation magnetization M_s of ~ 1300 emu/(cm³ of Co), the uniaxial magnetic anisotropy $K_u = (H_k M_s)/2$ of the Co film is 6.5×10^6 erg/cm³ and its interfacial magnetic anisotropy $K_s = (K_u + 2\pi M_s^2) d_{Co}$, is ~ 1.5 erg/cm². Assuming that the voltage-induced changes to M_s are negligible, we can use $\Delta K_s = \Delta K_u d_{Co} = \Delta H_k M_s d_{Co}/2$ to determine the change in interfacial magnetic anisotropy. Here, $\Delta H_k = 10600$ Oe is the sum of the initial in-plane saturation field of ~ 10 kOe (see Figure 6-1) and the lower limit (limited by our electromagnet) of the out-of-plane saturation field after voltage application of 600 Oe (see

Figure 6-3(j)). Based on these numbers, we estimate a lower limit of the change in interfacial MAE of $> 0.6 \text{ erg/cm}^2$, or $\sim 5000 \text{ fJ/Vm}$, which corresponds to the largest magneto-electric coupling efficiency yet reported.

6.4 Magnetic Anisotropy and the Position of the Oxidation Front

To correlate magnetic anisotropy with the location of the oxidation front, we used a Gd spacer to control the distance between Co and the Gd/GdO_x interface. Here, GdO_x was grown as a continuous 30nm-thick layer before depositing Ta/Au electrodes to prevent DW trap formation at the edges. Figure 6-5(a-d) shows the nominal sample structure and corresponding hysteresis loops for four samples with increasing Gd spacer thickness d_{Gd} . With a thin Gd spacer, PMA is diminished as evidenced by a significant drop in the remanent magnetization ratio M_r/M_s (see Figure 6-5(b)), but as d_{Gd} is increased further, PMA again increases (Figure 6-5(c-d)). The recovery of PMA for thicker metal overlayers differs from the behavior reported in References [8,9] for Pt/Co/Al/AlO_x but is consistent with the results in Reference [176] for that system. We obtained similar results for other metal-oxides including Pt/Co/Zr/ZrO_x and Pt/Co/Ta/TaO_x, and find this behavior to be rather general. Although the origin of this nonmonotonic anisotropy variation is not well understood, it is fortuitous because it allows us to determine sensitively the position and direction of motion of the oxidation front.

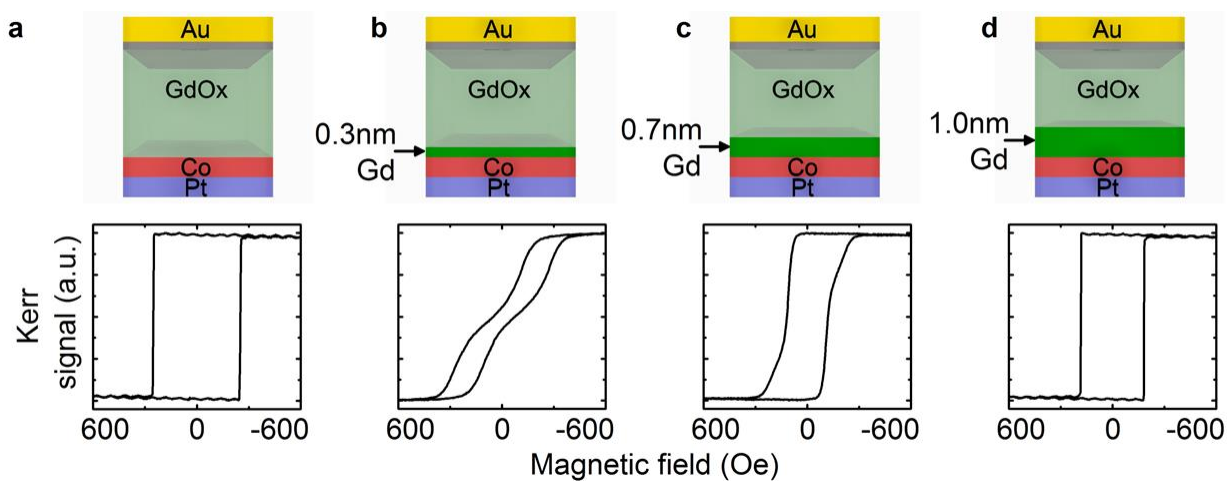


Figure 6-5: Voltage-induced propagation of oxidation front. (a-d), Schematics of Pt/Co/Gd/GdO_x samples with different Gd spacer thicknesses (0 to 1 nm) at the Co/GdO_x interface and polar MOKE hysteresis loops corresponding to the as-deposited samples.

In Figure 6-5, hysteresis loops and M_r/M_s are used to probe magnetic anisotropy. Now, we use both VSM and the MOKE technique described in Section 3.2.4 to directly access the anisotropy field H_k and its variation with applied voltage. In particular, we investigate how the voltage response depends on the initial position of the oxidation front in the Co/Gd/GdO_x stack.

Figure 6-6(a) shows H_k versus d_{Gd} for these samples, extracted from VSM hard-axis hysteresis loop measurements and from MOKE via the technique described in Section 3.2.4. The data for both techniques show the same trend and are in good agreement with each other. The small differences between VSM and MOKE measurement are attributed to the local nature of the MOKE technique and the difference in probed area. We note that for the sample with $d_{\text{Gd}} = 0.3$ nm, H_k cannot be extracted by MOKE because in this sample $M_r/M_s < 1$ (see Figure 6-5(b)) even at $H_x = 0$.

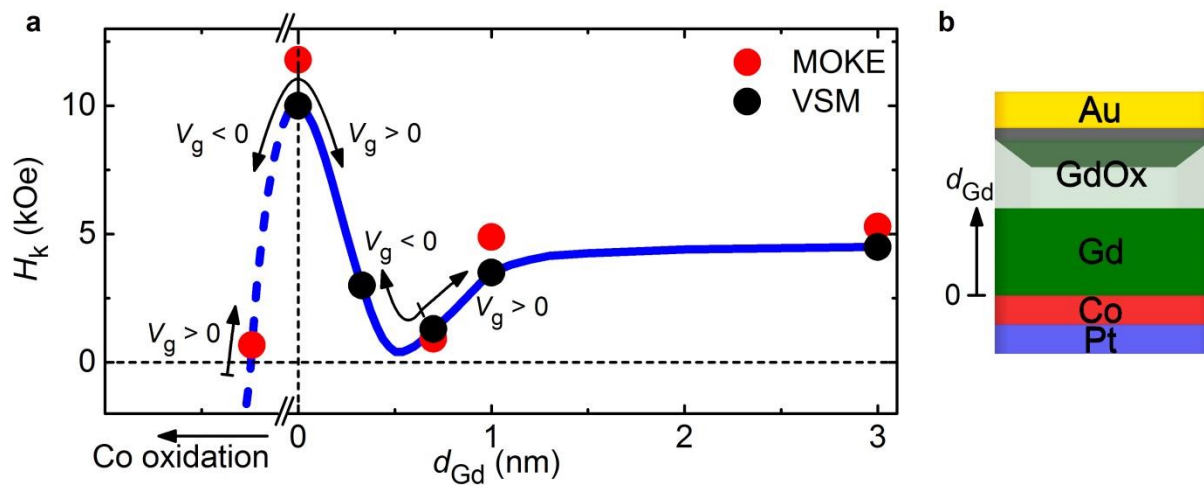


Figure 6-6: Anisotropy transition in Pt/Co/Gd/GdO_x films. (a) Plot of the anisotropy field H_k as a function of position of the oxidation front in the Pt/Co/Gd/GdO_x stack. Where possible, H_k was extracted from both MOKE and VSM measurements. The solid and dashed blue lines are a guide to the eye and the black arrows highlight the response to positive and negative voltage V_g at different positions along the anisotropy transition. (b) Schematic of the Pt/Co/Gd/GdO_x structure with Ta/Au electrodes. d_{Gd} refers to thickness of the Gd spacer layer and more general to the distance between the oxidation front and the Co layer.

Starting from $d_{\text{Gd}} = 0$, where $H_k \approx 10$ kOe, H_k decreases rapidly with increasing Gd spacer thickness and goes through a minimum where $H_k \approx 1$ kOe, then increases again with further increase of d_{Gd} before it saturates above $d_{\text{Gd}} = 1$ nm at $H_k \approx 5$ kOe. This nonmonotonic dependence of H_k on d_{Gd} agrees well with what was inferred from the trend of M_r/M_s in the hysteresis loops in Figure 6-5.

From the discussion in Sections 6.2 and 6.3, it is also known, that if the Co layer itself is oxidized, PMA decreases rapidly and eventually disappears completely with increasing oxidation. Taking d_{Gd} to be more generally the distance between the Co layer and the metal/metal-oxide interface, this then corresponds to $d_{\text{Gd}} < 0$. This allows us to extend schematically the dependence of magnetic anisotropy on the position of the oxidation front in Co/Gd/GdOx, which is illustrated by dashed and solid blue lines in Figure 6-6(a).

Based on the full dependence of PMA on the position of the oxidation front in Co/Gd/GdOx, we consider here the voltage response at different starting points for d , which correspond to different points along the anisotropy transition in Figure 6-6(a). From the discussion in Sections 6.2, it is expected that negative gate voltage V_g drives the oxidation front closer to the Co layer whereas positive V_g drives it further away, corresponding to decreasing and increasing d , respectively. Therefore, it can be anticipated that the sign of the magneto-electric response should itself depend on the starting state: it can be either positive or negative depending on the local slope of H_k versus d , and even change sign during voltage application if V_g is sufficient to drive the system through the maximum or minimum of H_k versus d_{Gd} in Figure 6-6(a).

We first consider again the Ta(4 nm)/Pt(3 nm)/Co(0.9 nm)/Gd(0.7 nm)/GdOx(30 nm) sample described in Figure 6-5. The PMA of the as-deposited sample (Figure 6-7(c)) is near the minimum of H_k versus d_{Gd} in Figure 6-6(a). Evolution of the hysteresis loop characteristics is then observed at RT, after positive and negative V_g application at $T = 100$ °C. It is found that a positive gate voltage $V_g = +6$ V, which should draw O^{2-} away from the Co layer and thus increase d , causes the out-of-plane loop squareness to increase (Figure 6-7(d)), consistent with increased PMA strength. Under negative bias of $V_g = -6$ V, M_r/M_s

initially drops (Figure 6-7(b)), indicating a reduction in PMA, but with sustained voltage application, the hysteresis loop again becomes square, indicating a subsequent increase in PMA (Figure 6-7(a)). Figure 6-7(e) shows a time sequence of M_r/M_s for this sample under negative bias $V_g = -6$ V, where the nonmonotonic evolution of M_r/M_s with time is clearly apparent.

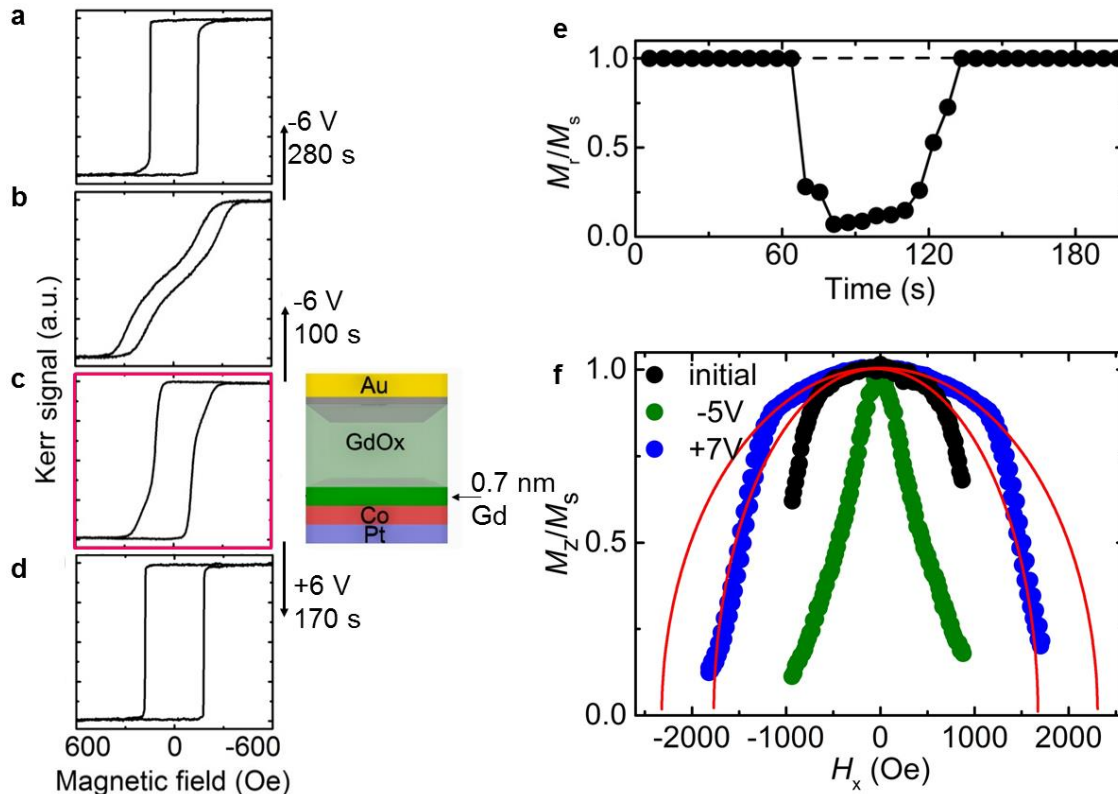


Figure 6-7: Nonmonotonic Voltage Response of Magnetic Anisotropy. (a-d) Hysteresis loops measured at room temperature for the Ta(4 nm)/Pt(3 nm)/Co(0.9 nm)/Gd(0.7 nm)/GdOx(30 nm) films described in Figure 6-5 and shown schematically next to (c). The initial state (c) has full remanence but is slightly sheared, indicating weakened PMA. Under positive bias (d) the loop becomes square after applying $V_g = +6$ V for 170 s at 100 °C. The loop evolution under negative bias is shown in panels (b) and (a) corresponding to $V_g = -6$ V at 100 °C for 100 s and 280 s, respectively. In this case, the loop shows first a reduction in M_r/M_s , and then recovery of strong PMA. The full evolution of M_r/M_s during application of $V_g = -6$ V at 100 °C is shown in panel (e). (f) MOKE anisotropy measurements performed at room temperature, in virgin state and after application of $V_g = -5$ V for 120 s and $V_g = 7$ V for 240 s at 70 °C. The anisotropy measurements confirm the voltage-induced anisotropy modifications inferred from the hysteresis loops in (b) and (d).

Figure 6-7(f), shows the results of local MOKE anisotropy measurements performed at RT, before and after a bias voltage was applied at $T = 70\text{ }^\circ\text{C}$. Application of positive bias of $\sim 7\text{ V}$ for 4 minutes results in an increase of H_k from 1700 Oe to 2300 Oe, whereas application of a negative bias of -5 V for 2 minutes clearly reduces H_k . These H_k measurements directly confirm the presumed variation in anisotropy energy inferred from the modification of M_r/M_s under positive and negative bias.

Together, these data show that voltage application follows the H_k versus d_{Gd} trend near the anisotropy minimum in Figure 6-6(a) indicated schematically by the black arrows shown on that figure in the vicinity of $d_{\text{Gd}} = 0.7\text{ nm}$. Notably, the sign of the magneto-electric coefficient changes with time in a way that is well understood from the functional form of H_k versus d .

In Figure 6-8, we show that the voltage response is nonmonotonic also in the low- d regime in the vicinity of the anisotropy maximum in Figure 6-6(a). Here, we focus on Ta(4 nm)/Pt(3 nm)/Co(0.9 nm)/GdOx(3 nm) films with thin Ta/(1.5 nm)/Au(5 nm) electrodes, which will be described in detail, in Sections 7.2 and 7.3. On these films, near the electrode perimeter the Co is partially oxidized in the virgin state, while near the center of the electrode the magnetic properties indicate minimal oxidation of Co in the virgin state. Therefore, it is possible to examine initial states corresponding to $d_{\text{Gd}} \approx 0$ and $d_{\text{Gd}} < 0$ (i.e., partially oxidized Co) using the same device, simply by probing the voltage response either at the electrode center or the electrode edge, respectively.

The electrode center initially exhibits PMA with square out-of-plane hysteresis loops. Figure 6-8(c) shows results of a local anisotropy measurement at the electrode center using the MOKE technique described in Section 3.2.4. The fit to these data using Equation (3.3) yields $H_k = 14\text{ kOe}$. In the virgin state, the electrode center region is therefore near the peak in H_k versus d_{Gd} in Figure 6-6(a), where $d_{\text{Gd}} \approx 0$. Thus both positive and negative V_g should cause a reduction of PMA and H_k if applied for a sufficiently long time that the system is driven to one side or the other of the anisotropy maximum.

Figure 6-8(a) shows the evolution of M_r/M_s under positive and negative bias, where V_g was applied and hysteresis loops were measured continuously at RT. The positive and negative bias measurements were performed on separate devices so as to start from the virgin state for both bias polarities. Likewise, when V_g was ramped from 0 V to -2 V within ~ 1 minute, M_r/M_s also declined abruptly, indicating a reduction in PMA consistent with our observations in Section 6.3. For the positive bias case, V_g was ramped from 0 V to +2.5 V in ~ 4 minutes, during which M_r/M_s was relatively constant until after ~ 200 s it dropped precipitously, indicating a significant reduction of PMA. Therefore, under either bias polarity, M_r/M_s is eventually reduced, indicating a reduction in PMA.

The variation of PMA inferred from variations in M_r/M_s in Figure 6-8(a) were directly confirmed using local MOKE anisotropy measurements, shown in Figure 6-8(d,e). In these measurements, starting from the virgin state, bias voltage was applied and then removed prior to the drop in M_r/M_s so that the MOKE technique in Section 3.2.4 could be applied. In this case, even though the loops remain square, H_k has been significantly reduced under gate voltage application of either polarity, dropping to $H_k = 6500$ Oe in the positive bias case (Figure 6-8(d)) and to $H_k = 700$ Oe in the negative bias case (Figure 6-8(e)). Therefore, under both bias polarities, which should either drive O^{2-} into the Co layer or drive the oxide boundary away from the Co layer, the PMA eventually declines. This behavior is indicated schematically in Figure 6-6(a) by the black arrow near $d=0$.

Finally, in Figure 6-8(b), we perform measurements similarly to those in Figure 6-8(a), but examining the RT response of M_r/M_s near the electrode edge. Here, the initial state corresponds to an oxidized Co layer with $d_{Gd} < 0$, as described in more detail in Section 7.2. The hysteresis loop in the initial state show $M_r/M_s \approx 0.1$. A ramp up in V_g from 0 V to 3 V, which should draw O^{2-} away from the Co layer, and increase d , gives rise to an increase in loop squareness and M_r/M_s , indicating an increase in PMA. This behavior is indicated schematically by the black arrow on Figure 6-6(a). With increasing dwell time, M_r/M_s then begins to drop to below 1, consistent with crossing the maximum of H_k in the anisotropy transition at $d_{Gd} = 0$.

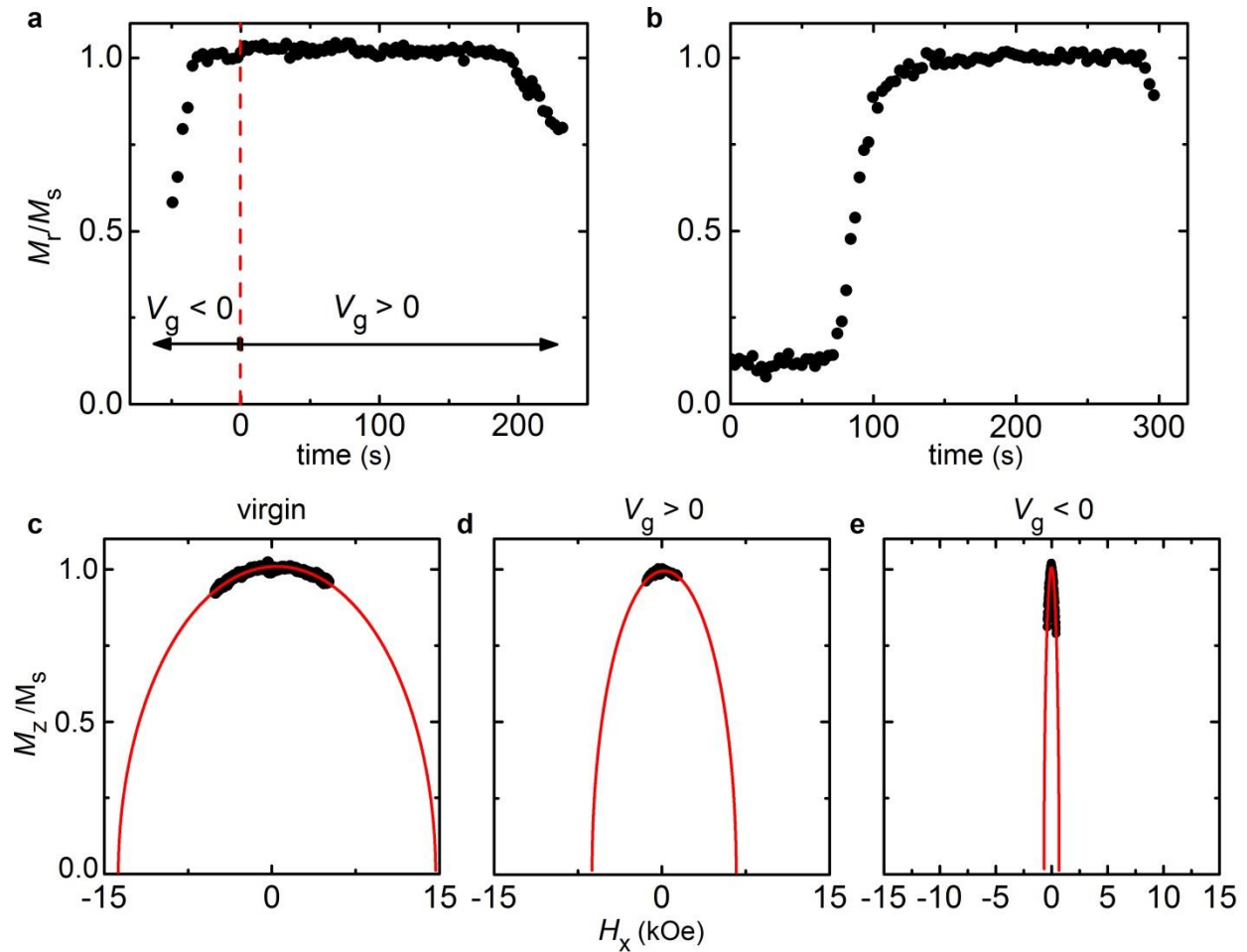


Figure 6-8: Voltage response at center and edge of Au electrodes. (a) Evolution of remanence to saturation magnetization ratio M_r/M_s under positive and negative gate voltage V_g for Ta(4nm)/Pt(3nm)/Co(0.9nm)/GdOx(3nm) films with Ta(1.5 nm)/Au(5 nm) electrodes. Here, M_r/M_s is probed at the center of the electrode. The red dashed line indicates the virgin state of the electrode center. (b) Evolution of M_r/M_s under positive V_g , where M_r/M_s is probed at the electrode edge. (c-d) The normalized polar MOKE signal corresponding to the out-of-plane magnetization M_z at electrode center is plotted as a function of in-plane field H_x in the virgin state (c), after positive V_g (d) and after negative V_g application (e). The solid red lines are fits with the Stoner Wohlfarth model.

The voltage-response of the three samples is summarized in Figure 6-6(a) schematically, with black arrows showing the trends of the perpendicular anisotropy energy under positive and negative bias, depending on the starting position of d . It can be seen, that depending on the position of the oxidation front, both positive and negative V_g

can result in an increase or decrease of PMA, i.e., the magnitude and sign of the magneto-electric coefficient depends on the local slope of H_k versus d . For all of these samples, the voltage response of the anisotropy can be well-understood in terms of the H_k versus d_{Gd} characteristic determined from as-deposited samples, indicating that the gate voltage indeed changes d_{Gd} dynamically by moving the position of the oxidation front. In this magneto-ionic system, the polarity of the magneto-electric coefficient is therefore not coupled to the polarity of the gate voltage but solely determined by the position of the oxidation front with respect to the Co layer.

6.5 Laser Defined Anisotropy Patterns and Domain Wall Conduits

Finally, we demonstrate local MAE patterning using the MOKE laser spot to locally heat the sample and activate oxygen migration under V_g . Using the devices in Figure 6-3(b), we first apply $V_g < 0$ at RT to create a potential well at the electrode perimeter, evidenced by a jump in H_c beneath the electrode (Figure 6-11(a)). This isolates the electrode area from DW motion in the adjacent Co film. With V_g applied, we then increase the MOKE laser power P from 1mW to 10mW, corresponding to a local temperature rise of $\sim 20^\circ\text{C}$ (see Section Experimental Methods6.1). This causes H_c and M_r/M_s to drop dramatically underneath the laser spot (Figure 6-11(a)), and this change is retained when V_g is removed and P decreased to 1 mW. Due to this local anisotropy reduction, the illuminated spot acts as a domain nucleation site. Figure 6-9(a-d) shows space- and time-resolved images of domain expansion in the electrode area at increasing times after a reversed magnetic field-step is applied. It can be seen that indeed, magnetic DWs nucleate at the laser-defined position (Figure 6-9(a)) and then expand radially across the Co film (see Figure 6-9(b-d)).

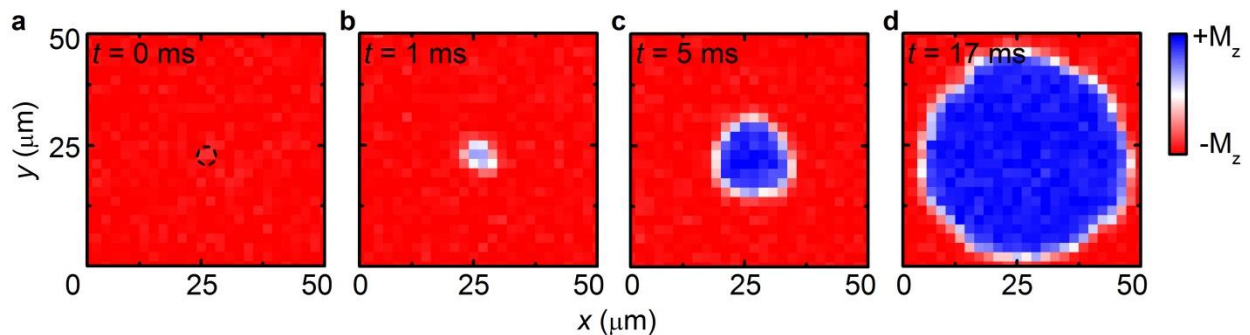


Figure 6-9: Laser-defined domain wall nucleation site. (a-d) Polar magneto-optical Kerr effect maps showing domain expansion inside electrode area with increasing time t after applications of a reversed magnetic field step of 90 Oe. The dashed black line in (a) outlines the area exposed for 100 s to the 10 mW laser spot at a gate voltage -3 V. All maps were acquired at room temperature and under zero bias

To elucidate the individual roles of V_g and P we create a laser-induced DW nucleation site in one corner of an electrode, and then place the laser spot in the diagonally opposite corner (see Figure 6-10(a)). H_c then corresponds to the field necessary to propagate DWs

from one corner of the electrode to the other. Figure 6-10(b-d) show H_c as a function of V_g at $P = 1$ mW and $P = 10$ mW. At $P = 1$ mW (Figure 6-10(b)), H_c follows the applied voltage showing modifications of ~ 1 Oe/V and then returns close to its initial value at zero bias. This volatile and weak voltage response is consistent with the influence of electric-field-induced charge accumulation on DW propagation,⁸⁹ and shows that the small ΔT at $P = 1$ mW is not sufficient to facilitate the voltage-driven O^{2-} migration necessary to produce nonvolatile PMA changes.

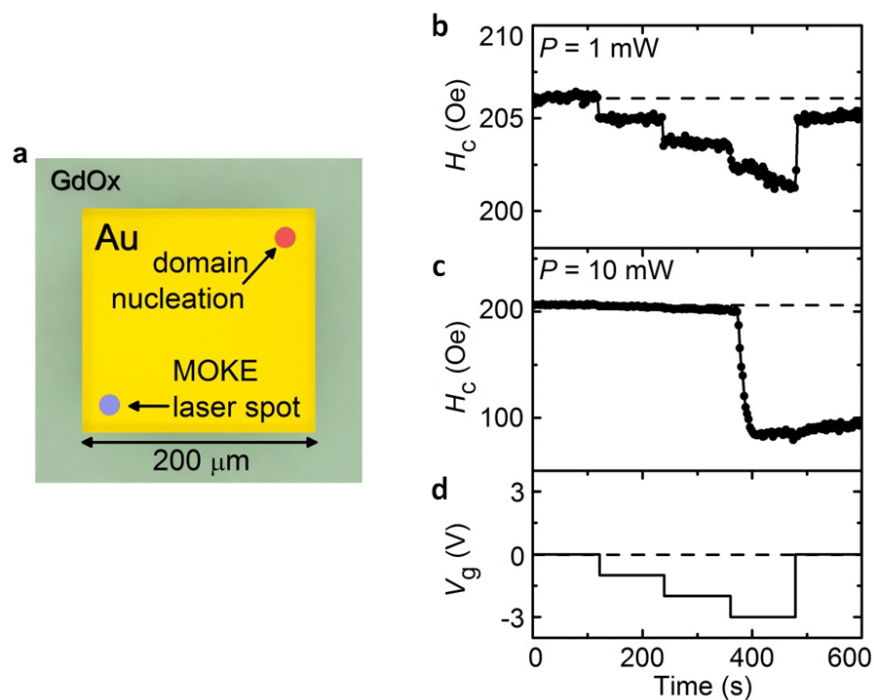


Figure 6-10: Effects of combined gate voltage and laser illumination. (a) Schematic of a Pt/Co/GdOx device with Au electrode, showing the position of the MOKE laser probe spot and the laser-generated domain nucleation site inside the electrode area. (b-d) Voltage dependence of coercivity H_c as a function of V_g (d) at an incident laser power P of 1 mW (b) and 10 mW (c).

The behavior at $P = 10$ mW is very similar, but only up to $V_g = -2$ V (Figure 6-10(c)). At -3 V, H_c suddenly drops from ~ 200 Oe to ~ 80 Oe. This large change in H_c indicates that instead of propagating across the electrode, domains now nucleate directly underneath the laser spot due to a strong PMA reduction, there. Thus, Neither V_g nor high P alone is

sufficient to cause irreversible changes to PMA, but when both are sufficiently high (see Figure 6-10), laser-induced heating activates voltage-driven O^{2-} migration, which facilitates local MAE imprinting.

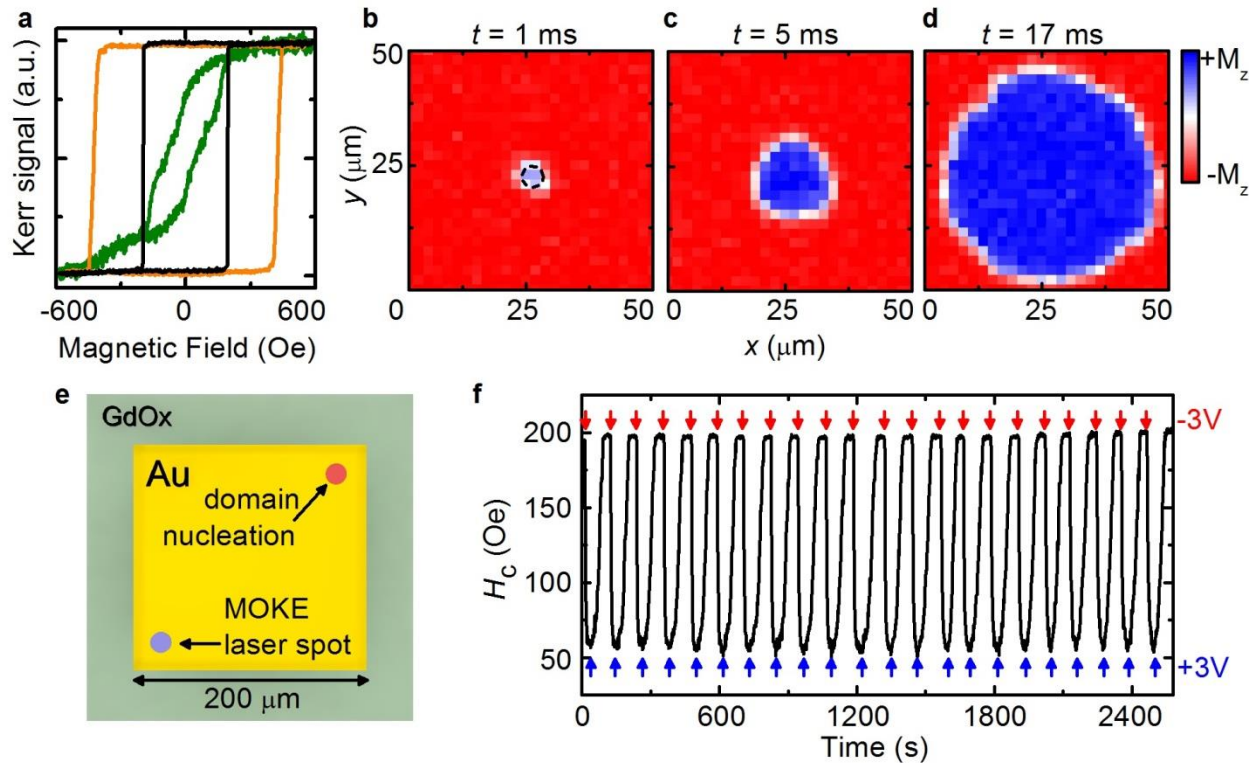


Figure 6-11: Effects of voltage and laser illumination on magnetic anisotropy. (a) Polar MOKE hysteresis loops measured inside gate electrode with the device in its virgin state (black line), after application of a gate voltage $V_g = -3V$ for 90 s (orange line) and after application of $V_g = -7V$ for 180 s under laser illumination (green line). (b-d) Snapshots of domain expansion around a laser-induced nucleation site, at the indicated times following application of a reverse field step of 90 Oe at $t=0$. All snapshots were acquired at zero bias. The dashed black line in (b) outlines the area exposed for 100 s to the 10 mW laser spot at a gate voltage $-3V$. (e). Schematic showing top view of an electrode in which a laser-induced nucleation site has been created at the upper-right corner, and the probe laser spot is positioned at the bottom left corner. (f) Voltage dependence of coercivity H_c as a function of V_g , corresponding to the schematic experiment geometry in (e), as V_g is cycled between $\pm 3V$.

To demonstrate the reversibility of this MAE imprinting, we first created a laser-induced DW nucleation site in one corner of an electrode and then placed the laser spot in the diagonally opposite corner (Figure 6-11(e)) with $P = 10$ mW. At $V_g=0$ the higher laser power alone has no effect on H_c , which is determined by the field necessary to propagate a DW from the far corner. But with $V_g = -3$ V, H_c and M_r/M_s drop dramatically, indicating that instead of propagating across the electrode, DWs nucleate directly underneath the laser spot due to the local PMA reduction. Positive bias restores M_r/M_s and H_c to their initial values and H_c can be toggled repeatedly in this manner as V_g is cycled between +3V and -3V (see Figure 6-11(f)).

Finally, we imprint more complex anisotropy patterns that allow for spatial control of magnetization dynamics. In Figure 6-12, we define a conduit in which DWs are injected from a laser-written nucleation site and propagate along a pre-defined path. At $V_g = -3$ V, a point inside the electrode area was illuminated at $P=10$ mW for 100 s to produce a DW nucleation site. The laser was then scanned along an L-shaped line in 1.25 μm steps with a variable dwell time to produce a conduit of reduced MAE (Figure 6-12(a)). Figure 6-12(a-f) shows time-resolved MOKE images of field-driven domain expansion in the patterned region (see Methods). Here, a reverse domain nucleates at the laser-defined nucleation site (Figure 6-12(b)) and expands preferentially along the laser-written conduit (Figure 6-12(c-f)). The degree of confinement depends on the difference in MAE in the film and in the patterned region, which determines the difference in creep velocity along and orthogonal to the conduit. The DW velocity follows $v \propto \exp(-E_a(H)/k_B T)$, where the activation energy $E_a(H) \propto H^{-1/4}$ depends on the MAE.⁹⁰ Figure 6-12(g) shows that the slope of $\ln(v)$ versus $H^{-1/4}$, and hence the activation energy that determines the DW velocity, can be precisely tuned to control the DW dynamics. By reducing the anisotropy in the conduit we enhance the velocity by up to a factor of ~ 160 . The MAE can be further reduced, but in this case nucleation along the conduit is observed.

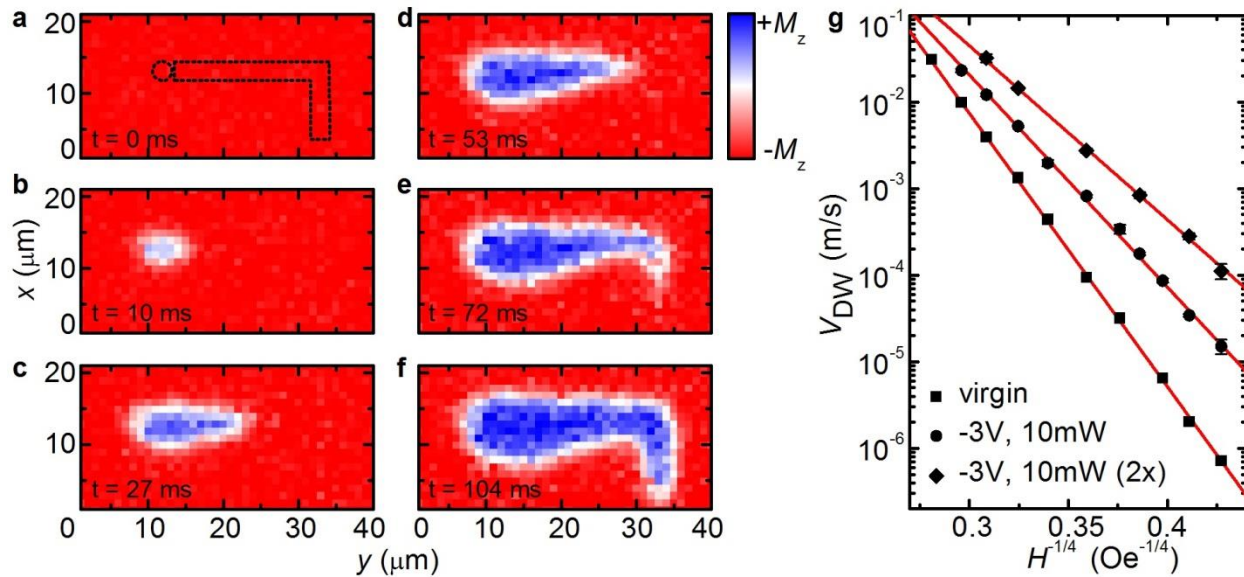


Figure 6-12: Laser-defined anisotropy patterns and domain wall conduits. (a-f), Time-resolved polar MOKE maps showing domain expansion in laser-defined domain wall conduit with increasing time t after application of a magnetic driving field $H = 42$ Oe. Dashed black lines in (a) outline area exposed by laser spot with 10 mW incident power, under gate voltage $V_g = -3$ V. The dashed circle was exposed for 100 s while dashed, L-shaped line was scanned in $1.25 \mu\text{m}$ steps with 65 s exposure at each point. All maps were acquired under zero bias. (g). Domain wall velocity as a function of magnetic field H in virgin film and along conduit exposed at 10 mW incident power under $V_g = -3$ V for 60 s and 65 s.

We note that local MAE patterning has previously been demonstrated using local ion beam irradiation,^{177,178} but has never been realized in a nondestructive and completely reversible way. Here, the spatial resolution is limited by the laser spot size to a few μm . However, this resolution limit could easily be overcome by instead heating the sample globally and writing the anisotropy pattern locally using, e.g. a conductive atomic force microscopy (AFM) tip to apply V_g with high spatial resolution.

6.6 Summary and Conclusion

The results presented in this chapter show that interfacial chemistry in metal/metal-oxide bilayers can be electrically-gated using an all-solid-state device, operating at low voltage and within the typical operating temperature range of common semiconductor electronics. Specifically for Co/metal-oxide bilayers, where interfacial MAE is sensitive to interface oxygen coordination, we observe *in situ* voltage-driven O²⁻ migration and show that oxygen migration allows for unprecedentedly strong voltage control of magnetic properties. Consistent with the thermally activated nature of ion migration, we show that relatively small changes in temperature can improve device response times by orders of magnitude and allow voltage control of magnetic properties in the bulk of the gate oxide, which was previously inaccessible. Based on these results, considerable further improvement in switching time can be anticipated by using materials and/or devices with even a modestly lower energy barrier for ionic migration. In a first step, Chapter 7 demonstrates magneto-ionic switching at the microsecond timescale.

Although this chapter focused on magnetic properties, reversible voltage-gated control of oxygen stoichiometry in metal/metal-oxide bilayers makes a wide range of materials properties and effects amenable to solid-state electrical control. These results thus suggest a path towards electrically gating a variety of phenomena governed by metal/oxide interfaces, and provide a novel means to locally and reversibly imprint material properties by local activation of ionic migration. The exciting prospect of dynamically programming material properties other than magnetic anisotropy is explored in detail in Chapter 8.

7 FAST SWITCHING OF MAGNETIC PROPERTIES*

In computing applications such as memory and logic chips, devices operate at gigahertz frequencies requiring nanosecond switching from the underlying technology.^{3,4} However, in less time constraint applications, switching at the microsecond timescale is more than adequate and the availability of low power voltage control of material properties has the potential to be a transformative technology. So far, we observed voltage-induced effects that occurred over relatively long timescales of 10s or 100s of seconds, but ionic transport can occur at the nanosecond timescale in, e.g., memristive switching devices.^{4,110} Having established that the dramatic, nonvolatile modifications of magnetic anisotropy occur through a thermally-activated process, consistent with voltage-induced O^{2-} migration, we aim to significantly reduce the switching time by further optimizing the device structure for efficient ionic transport.

* This chapter consists of material from the following publications:

- Bauer, U., Yao, L., Emori, S., Tuller, H. L., Dijken, S. van & Beach, G. S. D. Magneto-ionic control of interfacial magnetism. submitted for publication (2014).

In Section 7.2 we present a novel device structure employing a thinner gate oxide and porous electrodes which reduces the barrier for oxygen migration and dramatically enhances the triple phase boundary length. Based on these devices, we show in Section 7.3 a reduction of the magneto-ionic switching time by 6 orders of magnitude and demonstrate unprecedentedly strong switching of magnetic anisotropy at the milli- and microsecond timescale at voltage as low as 3V.

7.1 Experimental Methods

Ta(4 nm)/Pt(3 nm)/Co(0.9 nm)/GdOx(3 nm) films were prepared by DC magnetron sputtering at RT under 3 mTorr Ar with a background pressure of $\sim 1 \times 10^{-7}$ Torr, on thermally-oxidized Si(100) substrates. The GdOx layer was deposited by reactive sputtering from a metal Gd target at an oxygen partial pressure of $\sim 5 \times 10^{-5}$ Torr. Gate electrodes of Ta(1.5 nm)/Au(5 nm) were directly deposited on top of the Ta(4 nm)/Pt(3 nm)/Co(0.9 nm)/GdOx(3 nm) films through a shadow mask.

Polar MOKE measurements were made using a 532 nm diode laser attenuated to 1 mW. The laser was focused to a ~ 3 μm diameter probe spot and positioned by a high resolution scanning stage with integrated temperature control (see Section 3.2.2 for details). Magnetic hysteresis loops were measured at a sweep rate of 170 kOe/s and gate voltage was applied using a mechanically-compliant BeCu microprobe. The magnetic properties of Ta(4 nm)/Pt(3 nm)/Co(0.9 nm)/GdOx(3 nm) films were characterized by the MOKE technique described in Section 3.2.4 which yielded an in-plane saturation field H_k of ~ 14 kOe.

For the time resolved MOKE transients shown in Figure 7-4, a 100 ms long voltage pulse with an amplitude of 3 V or 4V was applied while the out-of-plane magnetization was probed by polar MOKE. A small out-of-plane background field of 40 Oe was applied to saturate the magnetization once PMA was established with the voltage pulse.

7.2 Engineering Magneto-ionic Devices for Fast Switching

In order to facilitate fast magneto-ionic switching at RT and low V_g , the device structure was engineered to enhance ionic exchange and reduce the O^{2-} diffusion barrier. The GdO_x thickness was decreased from tens of nanometers to 3 nm and on the resulting $Ta(4nm)/Pt(3nm)/Co(0.9nm)/GdO_x(3nm)$ films, thinner $Ta(1.5nm)/Au(5nm)$ gate electrodes were sputter-deposited through a shadow mask (Figure 7-1(a)). AFM shows that near its center the electrode is continuous with relatively low roughness (Figure 7-1(b)), allowing robust electrical contact by the mechanical microprobes. However, shadowing at the electrode perimeter results in a thickness gradient such that over an extended region the Au film thickness is near the percolation threshold. AFM images here (Figure 7-1(c)) show percolated island growth where the electrode is electrically contiguous but structurally porous. The porous microstructure should extend the lateral extent of the triple phase boundary, where gas phase, electrode, and electrolyte coincide and where ionic exchange is most efficient, while the thinner GdO_x underneath should permit more rapid O^{2-} diffusion.

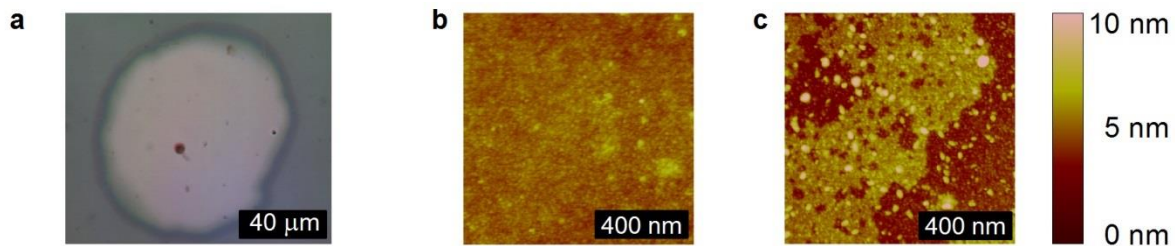


Figure 7-1: Imaging shadow masked Au electrodes (a) Optical micrograph showing shadow masked 100 μm diameter $Ta(1.5\text{ nm})/Au(5\text{ nm})$ gate electrode on $Ta(4\text{ nm})/Pt(3\text{ nm})/Co(0.9\text{ nm})/GdO_x(3\text{ nm})$ film. (b,c) Atomic force microscopy image taken at the center (b) and at the edge (c) of a gate electrode.

Initially the $Ta(4nm)/Pt(3nm)/Co(0.9nm)/GdO_x(3nm)$ films show square out-of-plane hysteresis loops with a remanence to saturation magnetization ratio $M_r/M_s = 1$ and a coercivity $H_c \approx 250\text{ Oe}$, everywhere, and these properties remain unchanged after prolonged exposure to atmosphere under ambient conditions. However, after depositing

the gate electrodes on the films, and again exposing the samples to ambient, we observe a time evolution of the magnetic properties in the vicinity of the electrode edge. Figure 7-2(a) shows line scans of M_r/M_s across an electrode at increasing times Δt after exposure to atmosphere. Up to $\Delta t = 20$ h, $M_r/M_s = 1$ across the whole electrode, after 22 h of exposure, a clear reduction of M_r/M_s can be seen at the edge of the Au electrode. As Δt increases, the reduction in M_r/M_s drops further, and the width of the modified area gradually increases. After $\Delta t = 118$ h, Figure 7-2(a) shows that M_r/M_s is reduced to ≈ 0 within the outermost 15 μm of the Au electrode, indicating a strong reduction of PMA in this area.

Figure 7-2 (b-d) and Figure 7-2(e-g) show exemplary hysteresis loops measured outside of, at the edge and inside of the Au electrode at $\Delta t = 25$ h and $\Delta t = 118$ h, respectively. Interestingly, there is no change in magnetic properties away from the electrodes, indicating that the 3 nm thick GdOx layer is sufficient to protect the Co film from oxidation in atmosphere in the absence of the Ta/Au electrode overlayer. However, PMA is clearly lost at the electrode edge, as evidenced by the hysteresis loops in Figure 7-2(c,f). We also note a gradual reduction in H_c at the electrode center, which is considerable after 118 h in the hysteresis loop in Figure 7-2(g). However, since the initial-state coercivity corresponds to the DW nucleation field threshold, the reduction in H_c near the electrode center is likely due not to a local reduction of PMA there, but rather a reduction in the nucleation field near the electrode edge so that H_c near the center reflects the DW propagation field, which is lower in these films than the nucleation field.^{89,90}

The reduction in PMA near the electrode edge is consistent with the effects of overoxidation of the Co at the Co/GdOx interface, which was observed in Section 6.3 after negative bias application. We suggest that this behavior indicates that there is spontaneous oxidation of the Co film localized near the electrode perimeter. The fact that a positive bias voltage applied to the gate electrode, which should drive O^{2-} away from the Co layer, fully restores PMA to this region (see Figure 7-4), supports this interpretation.

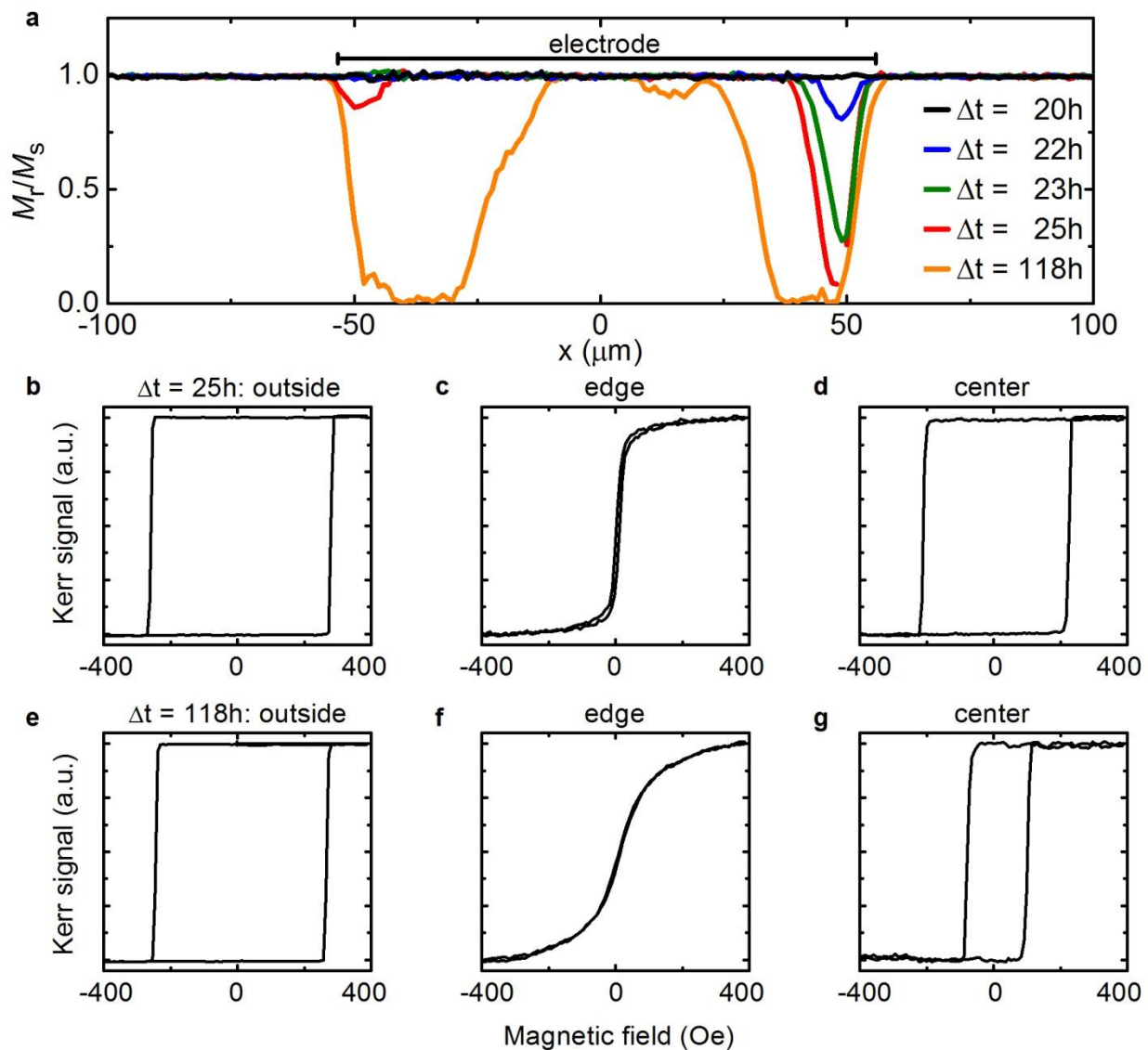


Figure 7-2: Effect of electrode porosity on magnetic properties. (a) For Ta(4nm)/Pt(3nm)/Co(0.9nm)/GdOx(3nm) films, line scans of the remanence to saturation magnetization ratio M_r/M_s were measured across shadow masked Ta(1.5nm)/Au(5nm) electrodes after exposure to atmosphere for times Δt . (b-d) Representative hysteresis loops measured outside (b), at the edge (c) and at the center (d) of the electrode at $\Delta t = 25$ h. (e-g) Representative hysteresis loops measured outside (e), at the edge (f) and at the center (g) of the electrode at $\Delta t = 118$ h.

We note, that similar films without Au electrodes have been found to remain stable under ambient atmosphere exposure for at least two years. Therefore, it is quite surprising that adding a porous Au layer on top of the GdOx leads to spontaneous oxidation over such a short timescale. We suggest that the behavior observed here indicates that the oxygen affinity of the Co film beneath the triple phase boundary region is sufficient to drive O^{2-} diffusion through the thin GdOx layer, resulting in spontaneous Co oxidation under ambient conditions. Since this is not the case away from the electrodes, this suggests that the rate limiting step is not O^{2-} diffusion, but rather ionic exchange at the electrolyte/gas phase interface, which is catalyzed by the presence of metallic Au that can act as a source of electrons.

In summary, the here described devices with thin gate oxide and porous Au electrodes allow us to investigate voltage-induced effects at different oxidation states of the Co/GdOx interface, by probing the edge or the center of the electrodes (see Section 6.4). But even more exciting, the presence of spontaneous overoxidation of the Co/GdOx interface holds the promise of fast magneto-ionic switching, which is explored in detail in Section 7.3.

7.3 Microsecond Switching of Magnetic Anisotropy

So far, voltage-induced effects occurred over relatively long time scales of 10s or 100s of seconds, but ionic transport can occur at the nanosecond timescale in, e.g., memristive switching devices.^{4,110} From memristive switching (see Section 2.5), it is well known that the timescale for voltage-driven ion migration exhibits a super-exponential dependence on temperature and electric field.¹²² Therefore, faster magneto-ionic switching should be readily achieved by further increasing T and V_g . Figure 7-3 shows that indeed at $T = 120$ °C and $V_g = 12$ V, the timescale for anisotropy switching drops to < 10 ms, compared to ~ 100 s at 100 °C and 6V (see Figure 6-7), and in contrast to the inaccessibly-long timescales required at RT in these devices (see Figure 6-3).

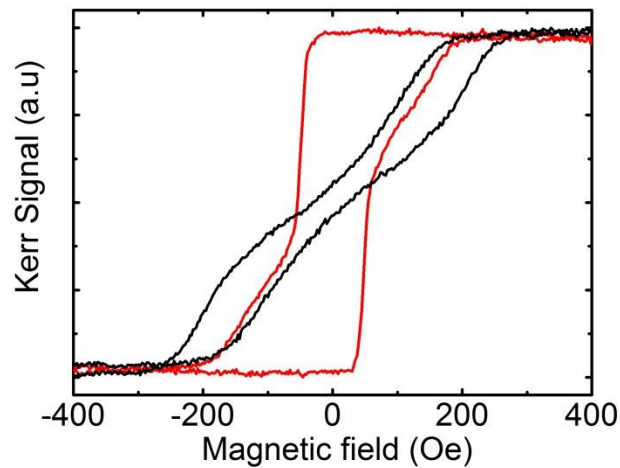


Figure 7-3: Anisotropy switching via short voltage pulses at elevated temperature. Magnetic hysteresis loops measured via the polar magneto-optic Kerr effect, before (black line) and after (red line) application of a 10 ms long voltage pulse of 12 V at 120 °C.

To achieve similar response at RT and low V_g , we use the Ta(4 nm) /Pt(3 nm)/Co(0.9 nm)/GdOx(3 nm) films with shadow-masked Ta(1.5 nm)/Au(5 nm) described in Section 7.2. These films were optimized for efficient O^{2-} transport by decreasing the oxide and electrode thicknesses.

At the electrode center these films exhibit square hysteresis loops, indicating strong PMA in the virgin state. Indeed, using the MOKE technique described in Section 3.2.4, we find a large anisotropy field of $H_k \approx 14$ kOe (see Figure 7-4(b)). Figure 7-4(a) shows hysteresis loops measured near the electrode center in the virgin state and after sequentially applying $V_g = +2$ V and $V_g = -2$ V at room-temperature. It can be seen that under these conditions, the easy axis switches between out-of-plane and in-plane within ~ 10 s, ten times faster than for the devices in Figure 6-3 at higher T and V_g .

By applying $V_g = -2$ V in the virgin state and removing the bias just before M_r/M_s drops below unity, we can establish a lower limit for the voltage-induced anisotropy modification. Using MOKE, we now find an anisotropy field H_k of only 700 Oe (see Figure 7-4(b)), corresponding to a reduction of $\Delta H_k \approx 13$ kOe. This ΔH_k corresponds to a modification of interfacial magnetic anisotropy of $\Delta K_s \approx 0.8$ erg/cm². Most remarkably, this giant modification of magnetic anisotropy is achieved at RT and at a bias voltage of only -2V.

In the absence of a bias voltage, PMA is stable with time at the electrode interior and away from the electrodes. However, within a ~ 15 μ m region at the electrode perimeter, PMA is spontaneously diminished after exposure to ambient for ~ 24 hours, consistent with overoxidation of the Co/GdOx interface (see Section 7.2). Hysteresis loops measured near the electrode perimeter in the virgin device state confirm the lack of PMA, there (see Figure 7-4(c)). Figure 7-4(d) show hysteresis loops measured at the same position after sequentially applying $V_g = +2$ V, $V_g = -1.5$ V and $V_g = +2$ V at room-temperature. Again, the easy axis switches between in-plane and out-of-plane within ~ 10 s. Moreover, the MAE can be repeatedly cycled with voltage, as seen in Figure 7-4(e), which plots M_r/M_s as V_g was cycled between +2 V and -1.4 V. Here, smaller V_g was used under negative bias to slow the downward transition of M_r/M_s and stop its progression at a point where the out-of-plane magnetization could still be saturated so that M_r/M_s could be computed.

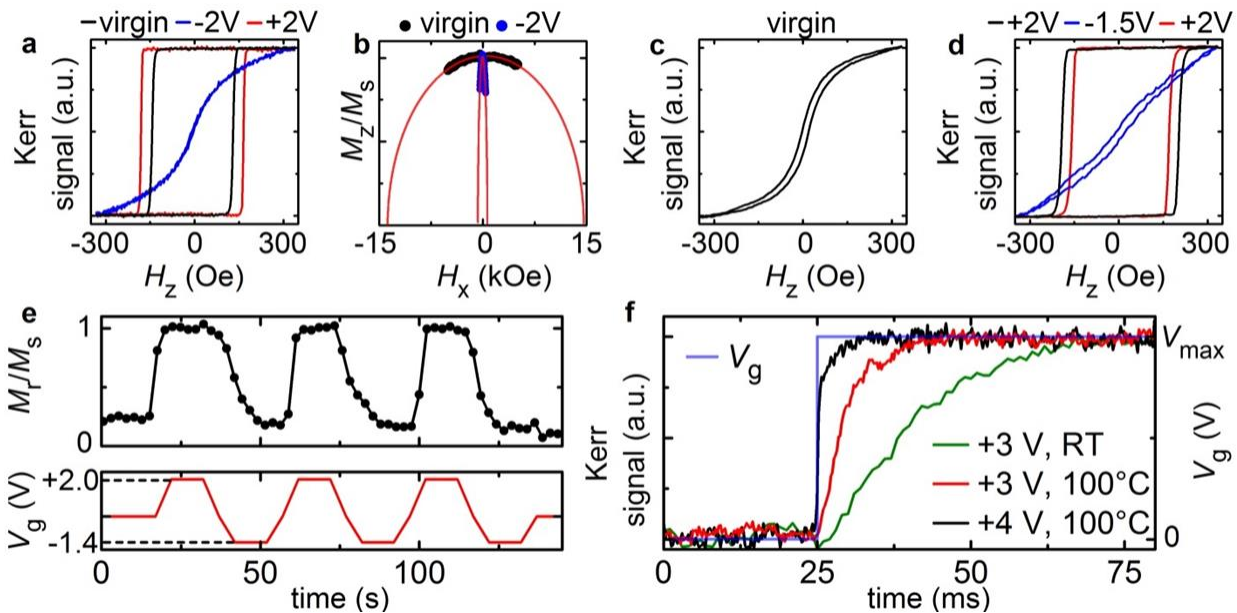


Figure 7-4: Fast anisotropy switching by engineering electrode and oxide. (a) Polar MOKE hysteresis loops measured at the electrode center of Ta(4nm)/Pt(3nm)/Co(0.9nm)/GdOx(3nm) films with shadow-masked Ta(1.5 nm)/Au(5 nm) electrodes. Hysteresis loops were first measured in the virgin state and after sequential application of a gate voltage of $V_g = -2V$ and $V_g = +2V$ for 10s at room temperature (RT). (b) The perpendicular magnetization component M_z measured as a function of in-plane field H_x in the virgin state and after application of $V_g = -2V$ at RT. The red lines are fits with the Stoner Wohlfarth model. (c,d) Polar MOKE hysteresis loops measured at the electrode edge in the virgin state (c) and after subsequent application of $V_g = +2 V$, $V_g = -1.5 V$ and $V_g = +2 V$ for 10s each at RT (d). (e) Three voltage-induced switching cycles of the remanence to saturation magnetization ratio M_r/M_s measured at the electrode edge at RT. (f) Transients showing polar MOKE signal during application of a V_g pulse at RT and at 100 °C. A perpendicular bias field of $H_z = 40$ Oe is applied to orient the magnetization in a well-defined direction as the voltage generates PMA. V_{max} refers to the amplitude of the voltage pulse.

Since Co redox reactions are dramatically enhanced close to the electrode perimeter, it follows that voltage pulses significantly shorter than the 10 s long pulses used above, could be sufficient to switch the MAE. Figure 7-4(f) shows time-resolved measurements of voltage-induced MAE switching that directly yield the switching speed. In these measurements, the film was initially in the low-anisotropy state (similar to Figure 7-4(c)), and the polar MOKE signal was followed in time as a fast-risetime voltage step $V_g > 0$ was

applied to generate PMA. A small perpendicular bias field was applied during measurement, so that as the MAE transitions from in-plane to out-of-plane, the magnetization orients in a well-defined direction. The polar MOKE signal transients in Figure 7-4(f) show that when V_g is applied the out-of-plane magnetization component rapidly increases and saturates, indicating a transition to PMA. The MOKE transient for $V_g = +3$ V at RT exhibits a risetime of ~ 25 ms, similar to the switching time achieved in Figure 7-3 at $T = 120$ °C and $V_g = +12$ V in the case of thicker GdOx and Au electrodes. The switching speed is further increased by increasing either T or V_g , dropping to ~ 700 μ s at 100 °C and +4 V. The remarkable reduction in switching time, by ~ 6 orders of magnitude compared to the same T and V_g in Figure 6-3, together with the unprecedented degree by which the MAE can be switched, indicates that magneto-ionic coupling offers a promising new route towards magneto-electric devices.

7.4 Summary and Conclusions

In summary, we show that the timescale of magneto-ionic effects can be improved by 6 orders of magnitude by taking relatively simple steps to optimize the device structure for efficient voltage-driven oxygen migration. Simply by employing thinner gate oxides and porous electrodes, magnetic properties can be switched at the microsecond timescale over a 15 μm wide area. Based on these results, considerable further improvement in switching time can be reasonably anticipated by examining oxides with higher ionic conductivity, or designing gate oxide heterostructures that include separately optimized oxygen storage and ion conducting layers. The design principles to optimize magneto-ionic devices are already well-established in solid-state ionics and should permit even faster voltage-induced changes to the Co/oxide interface and therefore rapid switching of magnetic properties. The here achieved dramatic reduction in switching times together with the prospect of further improvements, highlight the potential of magneto-ionics as a serious candidate for next generation memory and logic technology.

8 VOLTAGE CONTROL OF ELECTRICAL RESISTANCE

Memristors or “memory resistors” are true nanoscale ionic systems and often rely on ion-migration-induced resistance changes in thin oxide films for their nonvolatile memory functionality.^{109,110} Memristive switching devices are of great interest in computer technology due to their potential integration into next generation nonvolatile memories. Memristor technology is nonvolatile, scalable down to less than 10 nm, and offers low-power nanosecond-timescale switching.^{3,4,115}

Throughout this thesis we have highlighted the similarity between the devices used in memristive switching and their counterparts used in spintronics or more specifically in magneto-electronics (see Sections 2.4 and 2.5). Both fields rely on metal/oxide/metal devices which are made from very similar materials, exhibit similar layer thicknesses and are subject to the same high electric field. Based on this understanding, we postulated the magneto-ionic effect and argued that voltage-driven ion migration and electrochemical interface reactions should also be considered in magneto-electric devices and might even dominate their voltage response (see Chapter 5). Having spent Chapters 5 through 7 to prove the concept of magneto-ionic coupling and establish it as a powerful new mechanism for voltage

control of magnetism, we are now in a position to fully close the circle and demonstrate memristive switching in magneto-electric devices.

In Section 8.2 we show, that in the same ferromagnetic metal/oxide/metal devices that were used to demonstrate the magneto-ionic effect, we can also observe bistable nonpolar memristive switching. In fact, after electroforming, the devices resistance can be electrically switched by 5 orders of magnitude. This switching behavior is consistent with our previous observations of voltage-driven motion of the oxidation front and suggests a memristive switching mechanism based on oxygen anions.

Section 8.3 reveals that in addition to the resistance across the oxide layer, it is also possible to reversibly switch the lateral resistance in the ferromagnetic bottom electrode. By integrating this new resistive switching mechanism into magnetic nanowire devices we demonstrate its potential for applications requiring novel micro and nanoscale electrical switches.

It is truly remarkable that in the same ferromagnetic metal/oxide/metal devices we can not only observe two distinct memristive switching mechanisms with changes in resistance of up to 5 orders in magnitude, but also find unprecedentedly strong voltage effects on magnetic properties. This multifunctionality, crossing material properties and research fields, clearly highlights the impact and potential of solid state switching of oxygen stoichiometry as a route towards voltage programmable nano materials.

8.1 Experimental Methods

Continuous thin films of Ta(4 nm)/Pt(3 nm)/Co(0.9 nm)/GdOx(33 nm) were prepared by DC magnetron sputtering at RT under 3 mTorr Ar with a background pressure of $\sim 1 \times 10^{-7}$ Torr, on thermally-oxidized Si(100) substrates. GdOx layers were deposited by reactive sputtering from a metal Gd target at an oxygen partial pressure of $\sim 5 \times 10^{-5}$ Torr. On top of the GdOx layer, 100 μm diameter Gd(2 nm)/Au(12 nm) gate electrodes were deposited through a shadow mask. Layer thicknesses were determined from the deposition rate of each material, which was calibrated by x-ray reflectivity.

In addition to the continuous thin film samples, nanowire devices were fabricated in 4 steps using electron beam lithography and lift-off. First 500 nm wide, 50 μm long Ta(4 nm)/Pt(3 nm)/Co(0.9 nm)/GdOx(3 nm) nanowires were patterned. Then, two sets of 50 nm thick Cu contacts were deposited on the nanowire, one spaced 50 μm apart and the other spaced 40 μm apart. These contacts provide the 4 terminals required to probing the resistance of the nanowire. Next, the nanowire was covered by 30 nm GdOx. On top of the GdOx layer 30 μm wide Ta(2 nm)/Au(12 nm) gate electrodes were deposited at the center of the nanowire. The aim of this device structure is to avoid the open GdOx edge right underneath the electrode perimeter (see Section 5.5), such that the oxygen stoichiometry can be modified uniformly across the whole electrode.

The electrical properties of the continuous thin film samples* were probed at RT, in the dark and under medium vacuum conditions to reduce the influence of illumination and atmospheric oxygen on device characteristics. Mechanical microprobes were used to contact the Au top electrodes and the Ta/Pt/Co bottom electrode which is common to all devices (see Section 3.1.4). Current-voltage characteristics were measured with an Agilent 4156C semiconductor parameter analyzer and a Keithley 487 picoammeter. Constant

*The electrical properties and resistive switching behavior of the continuous thin film samples were investigated in collaboration with Henrique L. Gomes and Paulo R. F. Rocha at the University of the Algarve in Faro, Portugal.

current stress (CCS) during electroforming was sustained with the Agilent 4156C semiconductor parameter analyzer and the device capacitance was probed with a Fluke PM6306 RCL meter at zero bias and an AC amplitude of 300 mV.

The resistance of the nanowire samples was measured in ambient atmosphere and 4 terminal geometry with a Keithley Sourcemeter 2400. For resistance measurements the 4 Cu electrodes were contacted with mechanical microprobes and sense currents of $-5 \mu\text{A}$ to $+5 \mu\text{A}$ were applied through the two outer electrodes. The two inner electrodes were used to measure the voltage drop along the wire, resulting from the sense current and the resistance was extracted from linear fits of voltage versus sense current. In order to control the oxygen stoichiometry at the Co/GdO_x interface, gate voltages V_g were applied between the Ta/Au top electrode and the magnetic nanowire at 120 °C and for each device state, the nanowire resistance was extracted as described above. In all cases, positive bias refers to the top Au electrode being positive with respect to the Ta/Pt/Co bottom electrode.

Polar MOKE measurements were made on the nanowire samples, using a 532 nm diode laser attenuated to 1 mW. The laser was focused to a $\sim 3 \mu\text{m}$ diameter probe spot and positioned by a high resolution scanning stage with integrated temperature control (see Section 3.2.2 for details).

8.2 Voltage Control of Vertical Resistance*

The electrical properties of Ta(4 nm)/Pt(3 nm)/Co(0.9 nm)/GdOx(33 nm) with 100 μm wide Gd(2 nm)/Au(12 nm) gate electrodes were investigated to demonstrate the close link between memristive switching and the magneto-ionic effect. Here, voltages V_g and currents I_V are applied and measured between the top and bottom electrode of the metal/oxide/metal devices and the resistance state of a device then refers to the resistance across the oxide layer, i.e., the vertical resistance R_V of the device.

In the virgin state, the devices show high vertical resistance R_V of ~ 100 GOhm at a voltage of 1 V. Cyclic voltammetry measurements performed in a voltage range of ± 2 V show nearly rectangular curves indicating the devices behave like ideal passive capacitors (see Figure 8-1(a)). The rounded corners are likely the result of power loss during charge and discharge of the capacitor due to series resistance originating from the electrical contacts and electrodes. The rapid rise in current above ± 1.5 V could also indicate the emergence of ionic processes in the GdOx layer, above that voltage.

Assuming ideal behavior we can determine the device capacitance C geometrically from Equation (8.1) and from Figure 8-1(a) using Equation (8.2) :

$$C = \varepsilon_0 \varepsilon_r F / d_{\text{GdOx}} \quad (8.1)$$

$$C = I_V / dV_g / dt \quad (8.2)$$

Here, ε_0 is the permittivity of free space, ε_r is the dielectric constant of GdOx, which typically is ~ 16 .^{179,180} F is the electrode area and d_{GdOx} is the thickness of the GdOx layer. In Equation (8.2) dV_g/dt corresponds to the voltage scan rate of ~ 0.4 V/s. With both equations we arrive at a similar device capacitance of ~ 35 pF.

**The electrical properties and resistive switching behavior was investigated in collaboration with Henrique L. Gomes and Paulo R. F. Rocha at the University of the Algarve in Faro, Portugal.

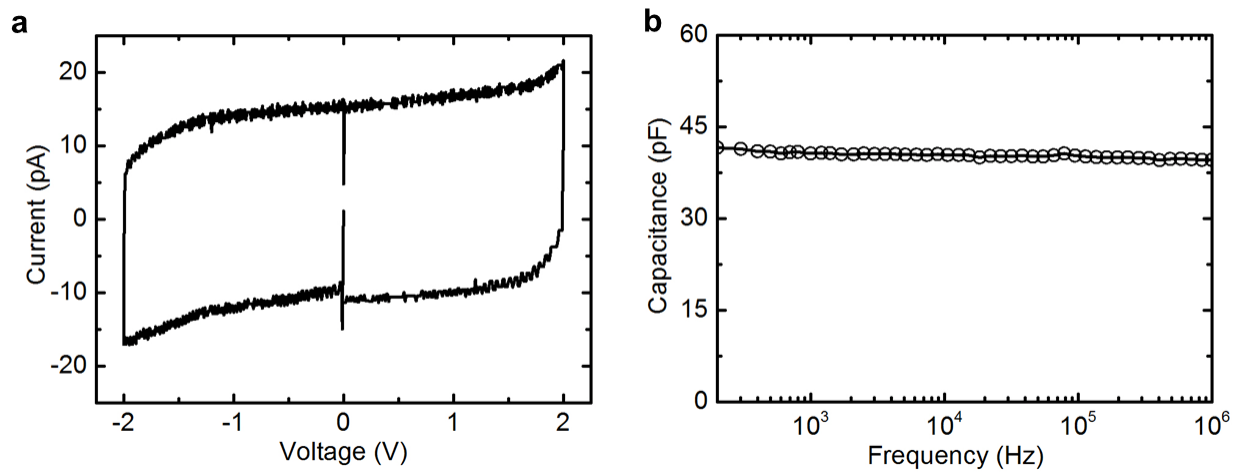


Figure 8-1: Electrical characterization of virgin device state. (a) Cyclic voltammetry curve measured at a voltage scan rate of 0.4V/s and (b) capacitance frequency characteristic measured at zero bias with an AC amplitude of 0.3V on Ta(4 nm)/Pt(3 nm)/Co(0.9 nm)/GdO_x(33 nm) with 100 μm wide Gd(2 nm)/Au(12 nm) gate electrodes.

These results are in good agreement with the capacitance measurements performed in Figure 8-1(b) which yield $C \approx 40$ pF across the entire frequency range from 200 Hz to 1 MHz. The flat frequency dependence of C confirms the nearly ideal capacitor behavior at low bias voltages. These results are consistent with our conclusions in Section 5.2, where at low bias voltages; we attributed voltage-induced changes to magnetic properties to electron accumulation/depletion in the Co electrode.

To turn metal/oxide/metal capacitors in to programmable memristive switching devices usually requires a so called electroforming step, consisting of either sweeping V_g to high bias voltages or applying CCS.^{109,119,181,182} Here we find that both methods can be used to turn the nearly insulating virgin devices into a memristive memory with a high resistance (OFF) and low resistance (ON) state.

Figure 8-2 shows electroforming of the Pt/Co/GdO_x/Gd/Au capacitors under CCS. A current stress of 500 pA is applied and the voltage across the device is monitored over time. We find that the voltage increases continuously over time until it reaches a critical value of ~ 3 V after ~ 1.1 s. Above this critical value, the voltage required to sustain the

constant current of 500 pA suddenly drops, indicating the formation of a conducting path through the GdOx layer. The device has now been electroformed and is in its low resistance or ON state.

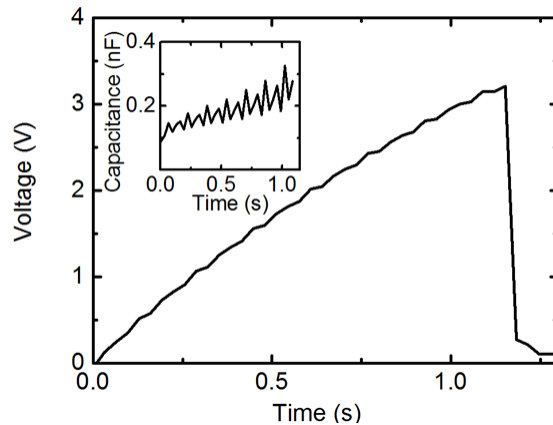


Figure 8-2: Electroforming via constant current stress. The voltage across a Ta(4 nm)/Pt(3 nm)/Co(0.9 nm)/GdOx(33 nm)/Gd(2 nm)/Au(12 nm) capacitor is monitored over time, while a constant currents stress of 500 pA is applied. The inset shows the device capacitance derived from the slope of voltage versus time in the main figure.

In electroforming via CCS, the current is kept constant and therefore changes in the slope dV_g/dt correspond to changes in device capacitance (see Equation (8.2)). The capacitance during CSS is plotted in the inset of Figure 8-2 and increases steadily while the voltage approaches its critical value. This increase in capacitance can be attributed to charge trapping and defect formation/migration in the oxide layer, which typically precedes the formation of a conductive path through the oxide layer.^{118,131,132,147,165,182}

Alternatively, the devices can be electroformed by sweeping V_g from 0 to +12 V or 0 to -12 V while the compliance current is set to $I_V = 10$ mA. While this method results in switchable devices, the power dissipated during electroforming is much higher in the voltage sweeping method than in the CCS method.¹⁸² Therefore we rely on the CCS method to keep device degradation to a minimum.

After electroforming, the Pt/Co/GdOx/Gd/Au devices are in their low resistance ON state and exhibit reliable resistive switching. In the ON state, a sweep of V_g beyond a so

called RESET voltage of typically 2 V to 5 V results in an abrupt drop in the current through the device, corresponding to a transition from the low resistance ON state to the high resistance OFF state (see Figure 8-3(a)). Similarly, in the OFF state, a sweep of V_g beyond the so called SET voltage of 7 V to 10V results in an abrupt increase in the current and thus a transition from the OFF back to the ON state (not shown here). At $V_g = 1$ V, the resistance in the OFF state is $R_V \approx 50$ MOhm whereas in the ON state $R_V \approx 500$ Ohm, implying resistance switching by 5 orders in magnitude (see Figure 8-3(b)).

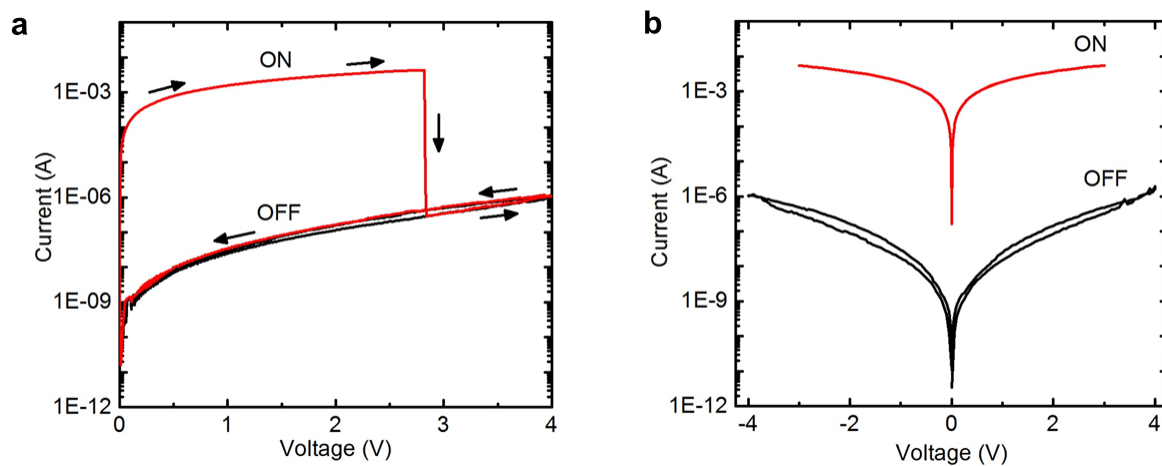


Figure 8-3: Memristive switching in Pt/Co/GdO_x/Gd/Au devices. (a) Current-voltage characteristic showing transition from low resistance ON state to high resistance OFF state (RESET) during a positive voltage sweep. (b) Current-voltage characteristic of ON and OFF state. The Ta(4 nm)/Pt(3 nm)/Co(0.9 nm)/GdO_x(33 nm)/Gd(2 nm)/Au(12 nm) devices were initially electroformed under constant current stress of 500 pA.

Although the SET and RESET processes occur most reliably under positive bias, we find that sweeping V_g to negative bias during the SET and RESET process can also switch the device between the ON and OFF state. In fact, we observe that all combinations of bias polarities during SET/RESET, i.e., positive/positive, negative/negative, negative/positive and positive/negative, give rise to resistive switching. This polarity independence of the switching characteristics suggests that the memristive switching observed here, is of the bistable nonpolar type.³

The microscopic origin of nonpolar switching is still controversial, but it is generally assumed that the formation of conductive filaments in the oxide layer is due to the combined effect of Joule heating and electric field (see Section 2.5).^{3,109} In nonpolar switching electroforming is typically explained in a two-step process, where a purely electronic effect establishes a hot electronic filament and the resulting high current densities then drive changes in material composition through heat-assisted ionic motion.^{3,116} The RESET switch then results from thermal rupture of the conducting filament, similar to a fuse, and is likely driven by heat assisted ionic motion in the concentration gradient around the filament.³

In the Pt/Co/GdOx/Gd/Au devices investigated here, we have the unique benefit of having a thin ferromagnetic layer between the oxide and the bottom electrode. With its sensitivity to interface chemistry and structure (i.e., the magneto-ionic effect) the ferromagnetic layer almost acts as a sense layer that allows us to identify voltage-induced modifications of interface composition and chemistry. Therefore, combining the results of our magneto-ionic switching experiments (Chapters 5 and 6) with the results of our memristive switching experiments, could grant us additional insight into the microscopic mechanisms behind nonpolar switching.

In Chapter 6, we demonstrated that oxygen anion migration is responsible for magneto-ionic coupling in Pt/Co/GdOx/Gd/Au devices. It is thus very likely that oxygen anions also give rise to memristive switching in these devices.¹⁸³ In theory, the formation of Co filaments could be a possibility,¹⁸⁴ but electroforming under positive bias is not consistent with a filament formation process based on mobile Co species.

Having established that memristive switching in Pt/Co/GdOx/Gd/Au devices is likely driven by mobile oxygen anions, it is now possible to revisit one of our first experiments on magneto-ionic switching (see Section 5.2, Figure 5-1). It is now evident, that Figure 5-1, essentially shows the evolution of the magnetic properties during electroforming with positive or negative bias. Under positive bias, significant modifications of the magnetic properties are observed long before the device switches to the low resistance ON state.

This suggests that filaments first nucleate at the Co bottom electrode and then grow towards the Gd/Au top electrode. Moreover, the spatially extended nature of the modifications in magnetic properties suggests that modifications of the oxide composition and therefore the interface oxygen stoichiometry are not limited to individual, localized filaments but likely occur across the whole electrode area. This result is very different from the simple model of local filament growth which is usually employed to explain electroforming in nonpolar switching devices.^{3,116} Preliminary results also indicate that no changes in magnetic properties occur during SET and RESET of the memristor, which suggests that filament rupture likely occurs far away from the Co layer. The structural and chemical sensitivity of ferromagnetic thin films can therefore indeed provide an additional window into the microscopic processes that give rise to memristive switching.

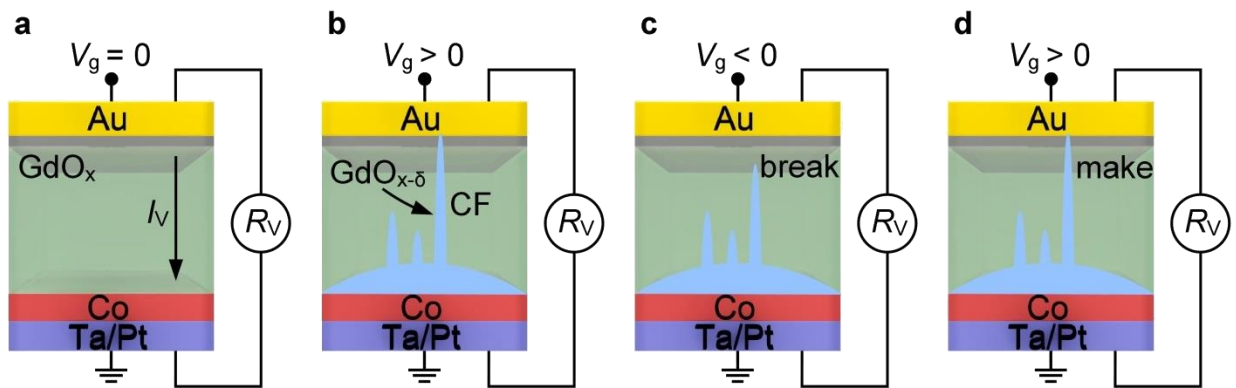


Figure 8-4: Schematics of memristive switching mechanism. Schematic illustration of the proposed memristive switching mechanism in Ta(4 nm)/Pt(3 nm)/Co(0.9 nm)/GdO_x(33 nm)/Gd(2 nm)/Au(12 nm) devices. (a) Virgin device in its insulating state. (b) After electroforming at positive voltage V_g , a conductive filament (CF) made of oxygen deficient GdO_x (GdO _{$x-\delta$}) connects the two electrodes and switches the device to the ON state. After electroforming, the filament can be broken (RESET to OFF state) and reestablished (SET to ON state) by applying (c) $V_g > 0$ or (d) $V_g < 0$, respectively. R_v is the vertical resistance and I_v the current flowing vertically through the device.

Combining our observations, it is now possible to develop a simple model for memristive switching in Pt/Co/GdO_x/Gd/Au devices (see Figure 8-4). During electroforming at positive V_g (see Figure 8-4(b)), the Gd/Au electrode likely acts as a

source for oxygen vacancies. In the applied bias, the oxygen vacancies are driven through the GdOx layer, towards the Pt/Co electrode and accumulate at the Co/GdOx interface. Due to oxygen vacancy accumulation an oxygen deficient and therefore conductive GdOx phase forms at the Co/GdOx interface and grows towards the Gd/Au electrode, such that eventually a conducting filament connects the electrodes and the device switches to the ON state. As our magnetic results suggested, the oxygen deficient GdOx phase likely forms across the whole electrode area but extended filaments grow only in certain locations, likely where their growth is aided by the availability of a high diffusion path.

Filament rupture is induced during the RESET process (Figure 8-4(c)), which switches the device to the OFF state. Due to the growth direction of the filament, rupture likely occurs in proximity to the Gd/Au electrode, where the filament diameter is expected to be smaller than closer to the Pt/Co electrode. The filament can then be reestablished by application of positive V_g . (Figure 8-4(d)). This SET process transitions the device back to the low resistance ON state.

This switching mechanism suggests that in our devices, magneto-ionic switching occurs during the slow electroforming step rather than during the fast SET and RESET steps of the memristor. In memristive switching electroforming is considered undesirable because it is slow, unpredictable, and potentially destructive to the device.¹¹⁹ The close connection between magneto-ionic switching and electroforming might therefore appear disadvantageous. However, that is not the case. It is crucial to realize that electroforming in memristive switching requires growth of a filament, and therefore ionic motion, across the whole thickness of the oxide. In magneto-ionic switching, ions need to be displaced only by atomic distances from the electrode interface, which should allow for switching times similar to the fast SET and RESET steps in memristive switching.

8.3 Voltage Control of Lateral Resistance in Nanowire Devices

In ultra-thin metal films and wires, electron scattering at surfaces and interfaces often contributes significantly to the overall resistivity.^{185,186} Modifying in interface chemistry and structure could therefore result in significant changes in resistivity. Here, we exploit our proven ability to electrically control the oxygen stoichiometry at the Co/GdOx interface (see Chapter 6) to tune the lateral resistance R_L in a Ta(4 nm)/Pt(3 nm)/Co(0.9 nm)/GdOx(3 nm) nanowire.

The experiment is schematically described in Figure 8-5(a). Under a negative bias voltage V_g oxygen anions are expected to migrate towards the Co/GdOx interface, such that under extended bias application, the Co layer itself is oxidized (Figure 8-5(b)). Due to the insulating properties of Co oxide (CoOx), migration of the oxidation front into the Co layer should then reduce the effective cross section of the metal nanowire and increase its resistance. Similar to magneto-ionic coupling, retention of the resistance modifications is expected in zero bias (Figure 8-5(c)), while a positive bias should reverse the effect (Figure 8-5(d)).

In order to verify this behavior experimentally, 50 μm long and 500 nm wide Ta(4 nm)/Pt(3 nm)/Co(0.9 nm)/GdOx(3 nm) nanowires were covered with a 30 μm wide GdOx(30 nm)/Ta(2 nm)/Au (12 nm) gate electrode, to control by voltage the oxygen stoichiometry at the Co/GdOx interface. The lateral resistance R_L of the nanowire is then measured with the four terminal technique and simultaneously magnetic hysteresis loops are acquired from the nanowire, to confirm via magneto-ionic coupling that voltage-induced changes to oxygen stoichiometry occur.

Figure 8-6 shows the evolution of the resistance R_L and coercivity H_c of the nanowire during sequential application of $V_g = -5$ V for 6 minutes and $V_g = +5$ V for 4 minutes at 120 $^\circ\text{C}$ (Figure 8-6(c)). Every 2 minutes the gate voltage was momentarily removed to facilitate measurements of R_L and H_c . Under negative bias we observe a gradual reduction of H_c from 210 Oe to 70 Oe, which is then reversed under positive bias (Figure 8-6(a)). This is

consistent with the results from Chapter 6 and confirms that the oxidation front migrates towards/away from the bottom electrode under negative/positive bias, respectively.

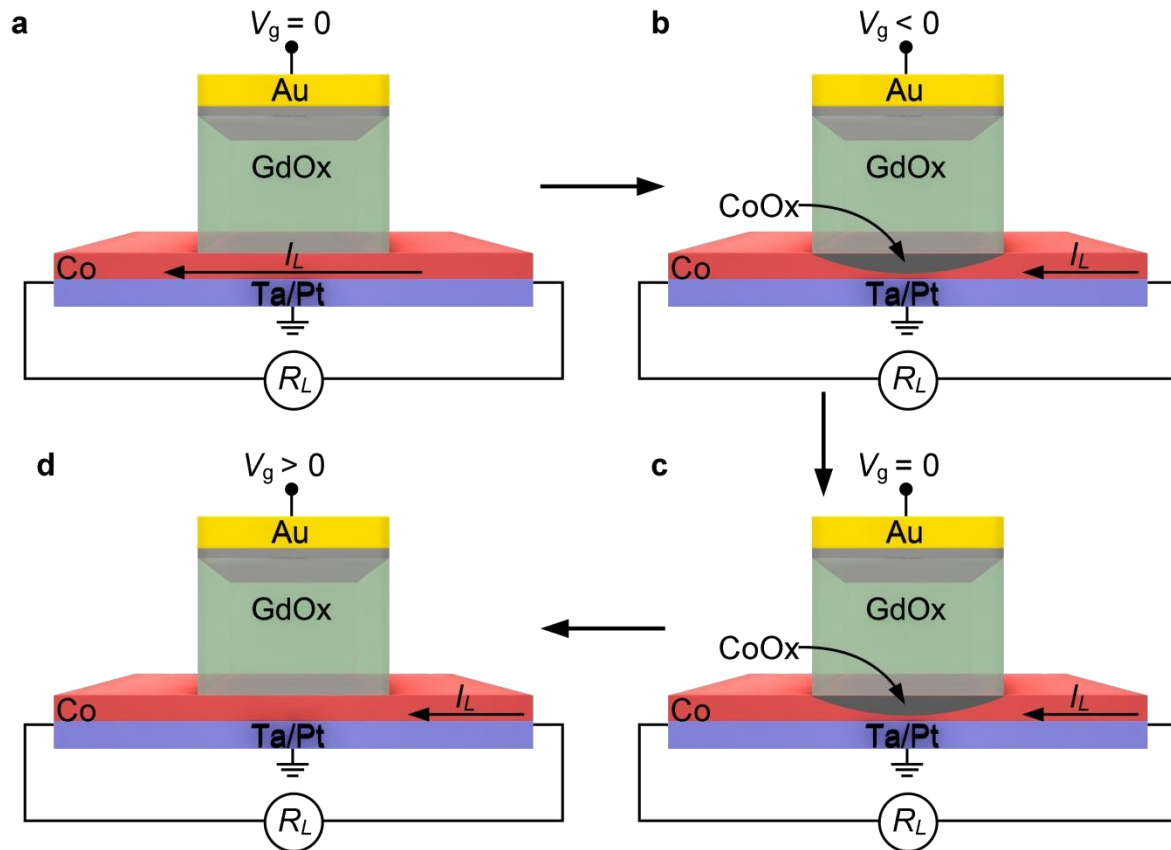


Figure 8-5: Lateral resistive switching in nanowire devices. Schematics of a Ta/Pt/Co nanowire device in the virgin state (a) and after sequential application of a voltage $V_g < 0$ (b), $V_g = 0$ (c) and $V_g > 0$ (d) to the GdOx/Ta/Au gate electrode. At $V_g < 0$, the oxidation front migrates into the Co layer and oxidizes Co to cobalt oxide (CoOx). These modifications are retained at zero bias but can be reversed at $V_g > 0$. In each device state, the lateral resistance R_L is measured based on the voltage necessary to drive the current I_L through the nanowire.

At the same time R_L increases by $\sim 4\%$ under negative bias and then returns close to its initial value under positive bias (Figure 8-6(b)). The resistance modifications are nonvolatile and remain at zero bias. This behavior is consistent with our expectation that oxidation of the Co/GdOx interface and the Co layer itself should result in a measurable increase in wire resistance. Indeed, using typical bulk values for the resistivity of Co, Pt, and

Ta of 60, 100, and 2000 n Ω m respectively, and treating the three layers as a set of three parallel resistors, we find that a 4% increase in resistance corresponds to a reduction of the Co metal thickness by ~ 0.2 nm or 20 %.

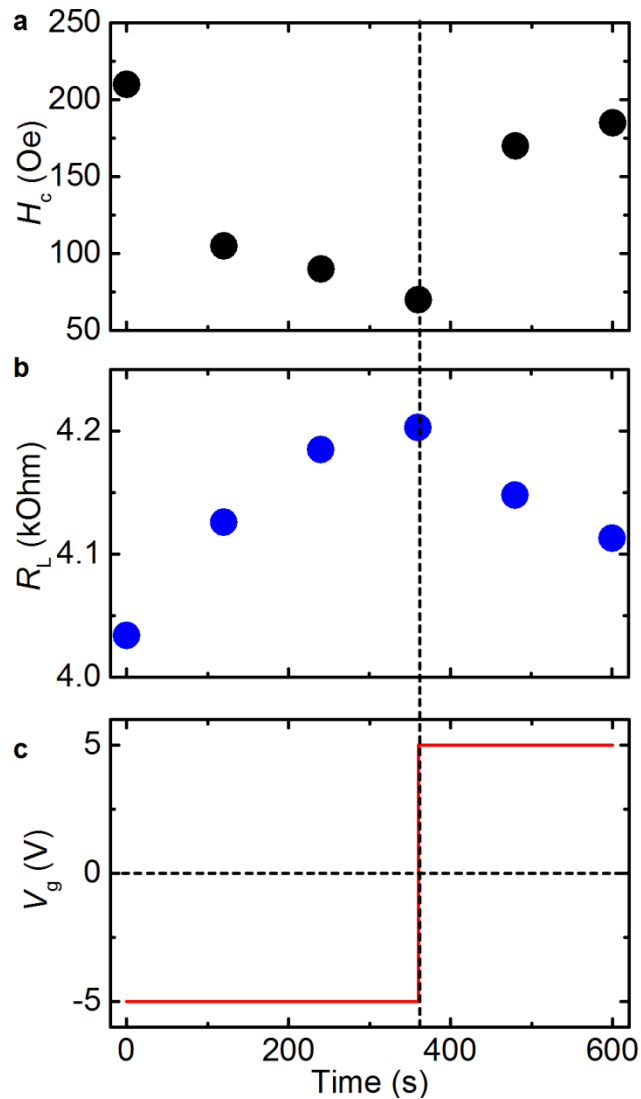


Figure 8-6: Lateral resistive switching and magnetic property modifications Evolution of the coercivity H_c (a) and lateral resistance R_L (b) under bias application (c) at 120 °C for a 500 nm wide and 50 μ m long Ta(4nm)/Pt(3 nm)/Co(0.9 nm)/GdOx(3 nm) nanowire with a GdOx(30 nm)/Ta(2 nm)/Au(12 nm) gate electrode. Error bars are smaller than the data point size.

Here we assumed a uniform reduction of the Co thickness to explain the increase in R_L , but in reality, the situation is likely more complicated. For instance, the oxygen anions could penetrate the Co film primarily along fast diffusion paths, such as grain boundaries, and therefore mainly affect electron scattering at grain boundaries.⁴⁷ Also, the effect of changes in interfacial oxygen stoichiometry on electron scatter is currently unknown. Likely, the observed increase in wire resistance is the result of a combination of several of these effects and additional experiments are necessary to separate their relative contributions.

Here, the voltage-induced effects on R_L are relatively small, but this is largely due to the presence of the thick Ta and Pt layers which are unaffected by V_g . Since the purpose of the Ta/Pt layer is to establish the correct magnetic properties, which are irrelevant for resistive switching, much larger changes in R_L could readily be achieved by simply removing those layers. We believe that given device optimization, lateral memristive switching is a very promising technology for a wide range of applications in micro and nanoscale electrical switching.

8.4 Summary and Conclusion

In summary, we observe bistable nonpolar memristive switching in the same Pt/Co/GdO_x/Au devices that were previously used to demonstrate the magneto-ionic effect. In fact, after electroforming, these devices can be electrically switched between a high and low resistance state, separated by 5 orders of magnitude in resistance. The observed switching behavior is consistent with our previous observations of voltage-driven motion of the oxidation front (see Chapter 6) and suggests that oxygen anions are also the mobile species responsible for memristive switching.

The unique combination of voltage-induced changes to electrical resistance and magnetic properties also provides a new tool to investigate the microscopic processes responsible for memristive switching. With its high sensitivity to interface chemistry and structure, a thin ferromagnetic layer sandwiched between oxide and electrodes could be used as a sense layer, providing otherwise hard to access information about structural and chemical changes at the electrode interfaces.

In addition to switching the electrical resistance between the top and bottom electrodes, we also demonstrate bistable switching of the lateral resistance in a nanowire device. Comparison of magnetic and electrical properties reveals that this effect is likely due to voltage-driven modification of the Co/GdO_x interface and likely oxidation of the Co layer itself. This lateral resistive switching mechanism provides a novel approach to realize micro and nanoscale electrical switches.

In conclusion, it is truly remarkable to observe two distinct memristive switching effects in addition to unprecedentedly strong magneto-ionic effects in exactly the same device structure. In fact we have now demonstrated that in the same device we can control by voltage; magnetic anisotropy, coercivity, saturation magnetization, DW motion, lateral electrical resistance, vertical electrical resistance and chemical composition. This multifunctionality clearly highlights the impact and potential of solid state switching of oxygen stoichiometry as a route towards voltage programmable nano materials.

9 SUMMARY AND OUTLOOK

9.1 Summary

The crossover from macroscale to nanoscale systems is characterized by the emergence of interface effects. In nanoscale materials, many physical and chemical properties are determined by the structure and composition of their interfaces. For instance, in metal/metal-oxide heterostructures, chemical,^{1,2} electronic,³⁻⁵ magnetic⁶⁻⁹ and mechanical^{14,15} properties can emerge from interfacial oxygen stoichiometry and defect structure. The possibility to dynamically control these interface characteristics with an electric field would therefore pave the way towards voltage control of these properties in solid-state devices (Figure 9-1).

The results presented in this thesis demonstrate that interfacial chemistry in metal/metal-oxide bilayers can indeed be electrically-gated using all-solid-state devices, operating at low voltage and within the typical operating temperature range of common semiconductor electronics. Our experiments focus on Co/metal-oxide bilayers that exhibit strong perpendicular magnetic anisotropy due to interfacial Co-O hybridization. In these materials we directly observe, for the first time, *in situ* voltage-driven O²⁻ migration and show that electrical switching of the interfacial oxidation state allows for voltage control of

magnetic properties to an extent never before achieved through conventional magneto-electric coupling mechanisms.

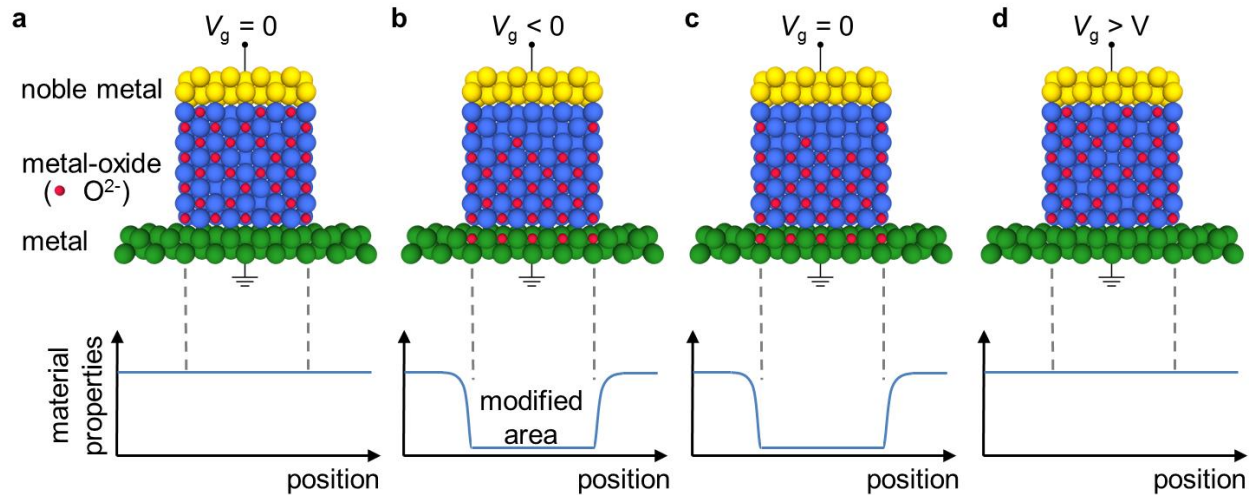


Figure 9-1: Illustration of solid-state switching of interface oxygen chemistry for voltage control of material properties Schematic illustration of a metal/oxide/metal device and its material properties in the virgin state (a) and after sequential application of negative bias (b), zero bias (c) and positive bias (d). Under negative bias, oxygen anions move towards the bottom electrode and modify the oxygen stoichiometry at the metal/metal-oxide interface, thereby modifying the properties of the bottom electrode layer underneath the electrode area (b). The changes to the metal/metal-oxide interface and material properties persist at zero bias (c) and only application of a reverse bias return the interface and the material properties back to their initial state (d). Note: Figure for illustrative purposes only. Neither layer thicknesses nor atom sizes are drawn to scale, and d and the described effects do not rely on the implied single crystal structure of the materials.

Using cross-sectional TEM and high-resolution EELS, we track *in situ* the voltage-driven migration of the oxidation front in a Co/metal-oxide bilayer, varying temperature and interface structure; we relate the migration of the oxidation front to voltage-induced anisotropy changes. We refer to this coupling between interfacial ionic species and magnetic properties as the magneto-ionic effect and show that it is capable of switching interfacial perpendicular magnetic anisotropy by an unprecedented $> 0.8 \text{ erg/cm}^2$ at just 4 V, yielding a magneto-electric efficiency of $> 5000 \text{ fJ/Vm}$. Together, our results establish magneto-ionic coupling as a powerful new mechanism for voltage control of magnetism.

Up to now, voltage control of magnetic properties in metal/metal-oxide bilayers has largely been attributed to charge accumulation or band shifting in the metal layer.^{40,41,44-46,98} Our results however, clearly show that this picture is incomplete and incapable of accounting for the observed irreversibility, and anisotropy changes much larger than the theoretically predicted 20 – 100 fJ/Vm.^{44-46,98} In order to fully describe the experimental results, the metal-oxide layer and specifically the metal/metal-oxide interface have to be considered as active device components. It then becomes clear that, in addition to electronic effects in the metal layer, voltage-driven ion migration and interface electrochemical reactions will contribute significantly to the voltage-induced modifications of magnetic properties. Depending on the voltage regime and material system, the relative contributions of these effects may vary, but as demonstrated here, by optimizing the device for efficient ion transport, the ionic contribution, can be orders of magnitude larger than the electronic contribution. Voltage-driven ion migration and interface electrochemical reactions have long been studied in solid state ionics and memristive switching devices, and the design principles established there can provide valuable lessons to improve magneto-ionic device design.

Based on these design principles, we report that relatively small changes in temperature and gate voltage can improve device response times by orders of magnitude and that by simply varying the thickness and morphology of the gate oxide and electrode, the magneto-ionic switching time drops from hundreds of seconds to hundreds of microseconds. Therefore considerable further improvements in performance and functionality can likely be anticipated by examining oxides with higher ionic conductivity, or designing gate oxide heterostructures that include separately optimized oxygen storage and ion conducting layers.

Ferromagnetic metal/metal-oxide bilayers and their unique electronic and magnetic properties are of crucial importance in the field of spintronics,^{6,21,22} which aims to exploit the electron charge and spin degree of freedom for novel, ultra-low power device application.²³⁻²⁶ The here demonstrated ability to voltage-gate the interfacial magnetic properties in these materials could dramatically reduce switching energies in spintronic devices and presents a significant step forward on the path towards all-electrical spintronic devices

Electrical control of magnetism has the potential to bring about revolutionary new spintronic devices,^{23-25,36,163} many of which rely on efficient manipulation of magnetic domain walls in ferromagnetic nanowires.²³⁻²⁵ We report for the first time that domain wall motion in ferromagnetic metal films can be controlled by an electric field. Initially, we achieve control of domain walls through voltage-mediated modification of magnetic anisotropy based on charge accumulation in metal films. However, a thorough investigation of the voltage-induced effects reveals that this mechanism is suitable only to modulate relatively slow, thermally activated domain wall motion. In order to effectively control domain walls travelling at device relevant velocities, larger voltage effects are required, which can be achieved through magneto-ionic coupling. By localizing the magneto-ionic effect to a narrow region at the electrode edge, we find that it is possible to create sharp voltage-controlled magnetic potential wells that trap domain walls and function as nonvolatile, electrically programmable, and switchable pinning sites. Pinning strengths of at least 650 Oe can be readily achieved, and are enough to bring to a standstill domain walls travelling at speeds of at least ~ 20 m/s. By integrating these voltage-controlled domain wall traps into magnetic nanowires, we demonstrate a prototype nonvolatile memory device in which the domain wall traps facilitate electrical bit selection in a magnetic nanowire register.

Based on magneto-ionic coupling, we also introduce a general method to reversibly imprint material properties through local activation of ionic migration, which we use to locally pattern magnetic anisotropy and create domain wall nucleation sites and conduits in continuous magnetic films. Since the magneto-ionic effect does not rely on maintaining an electrical charge, these anisotropy patterns persist in the power-off state but can be removed on demand by applying a reverse bias. This method therefore allows reversible patterning of magnetic microstructures without the need for lithography and materials processing.

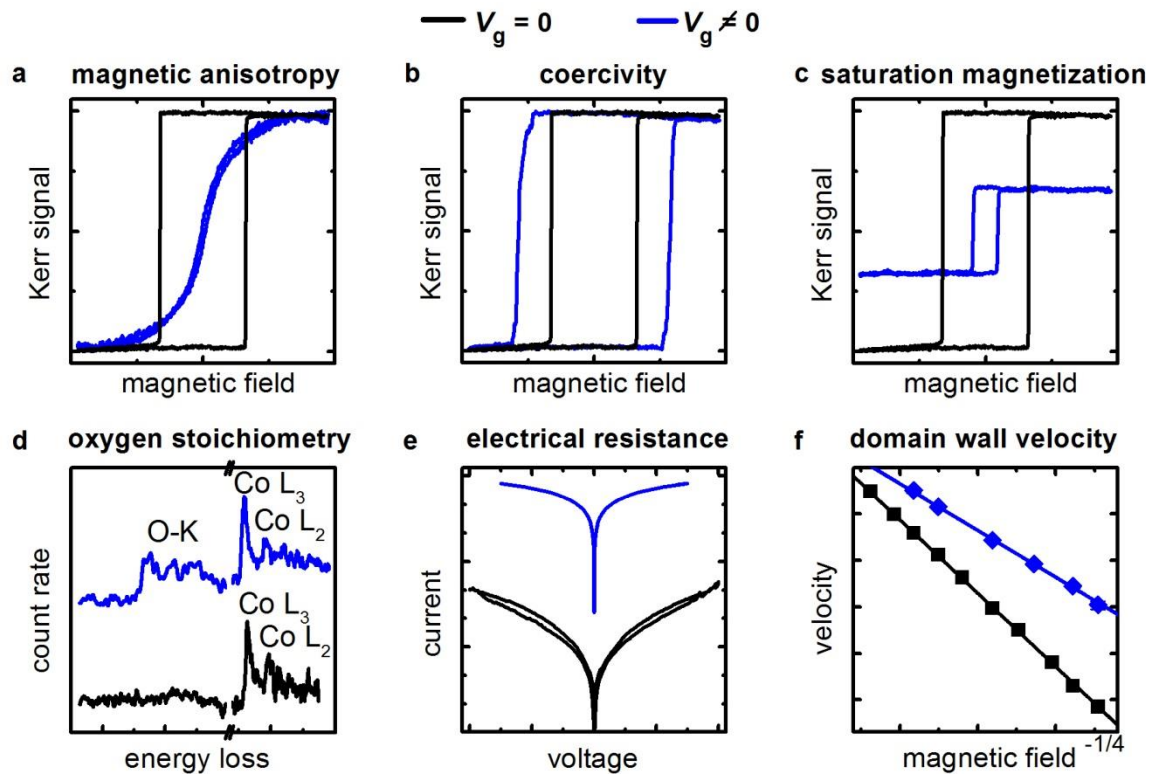


Figure 9-2: Voltage control of material properties. Overview of the material properties that we demonstrated to be amenable to nonvolatile voltage control in the Pt/Co/GdOx/Au system. For each property a representative dataset was chosen from the corresponding chapter of this thesis. See Figure 6-3 for (a-c), see Figure 6-2 for (d), see Figure 8-3 for (e) and Figure 6-12 for (f).

Most of the experiments presented in this thesis focus on magnetic properties, but the here demonstrated ability to reversibly control the interfacial oxygen stoichiometry in metal/metal-oxide bilayers at RT has implications far beyond magnetism. To highlight this potential, we show that in the same Co/metal-oxide structure we cannot only voltage-gate the magnetic properties but also the electrical resistance. In fact we have now demonstrated that in the same device we can control magnetic anisotropy, coercivity, saturation magnetization, domain wall motion, lateral electrical resistance, vertical electrical resistance, and chemical composition by gate voltage (see Figure 9-2). This multifunctionality across material properties and research fields clearly highlights the impact and potential of solid state switching of interface oxygen chemistry as a path towards voltage programmable materials

9.2 Outlook

Here we would like to present a short outlook on future work and potential applications of the results presented in this thesis.

9.2.1 A Magnetic Window into Memristive Switching

Memristive switching devices are of great technological interest due to their potential to be the next generation nonvolatile memory technology.^{3,109,110} Despite the tremendous interest in memristor technology, the physics and microscopic processes responsible for memristive switching are still not fully understood.³ One of the challenges is the unpredictability and localized nature of filament formation. Characterization of material composition, and chemistry, as well as imaging and probing of nanoscale filaments are therefore limited to very sophisticated equipment such as HRTEM and EELS.^{118,187}

Here, we propose the use of magnetic ultra-thin films as local sense layers inside memristive switching devices (see also Section 8.2). The magnetic properties of ultra-thin films are very sensitive to interface chemistry and structure and changes in these interface characteristics would immediately trigger changes in magnetic properties, which can be conveniently detected by techniques such as MOKE (see Chapter 3.2.1). The use of spatially resolved techniques such as Scanning MOKE (see Chapter 3.2.2) would then allow monitoring of interface composition and structure with spatial resolution.

Similar to tomographic imaging, integrating magnetic layers at various positions in the metal/oxide/metal stack would facilitate the imaging of memristive switching processes, section by section. By using magnetic layers that differ in their magnetic properties, several magnetic layers could even be integrated simultaneously into the same memristor device. As a simple manifestation of this idea, we imagine a memristive switching device with two magnetic layers. A layer with high coercivity H_c at the bottom electrode/oxide interface and a layer with low H_c at the oxide/top electrode interface. Due to the difference in H_c , the two layers and their magnetic properties should be distinguishable in MOKE measurements.

From the evolution of the magnetic properties at the two electrodes, it would then be possible to determine at which electrode oxygen vacancies accumulate during electroforming, where filament formation initiates and where filament rupture occurs during SET and RESET of the memristor.

We believe there is tremendous potential in the convergence of magneto-electric and memristive switching devices, and imaging memristive switching through magnetic sense layers presents a promising technique to gain additional insight into the microscopic details of memristive switching.

9.2.2 Nanosecond Magneto-Ionic Switching

With the work presented in this thesis, we have established the magneto-ionic effect as a powerful mechanism for voltage control of magnetism. Magneto-ionic coupling can control magnetic properties at an unprecedented scale, but initially had the disadvantage of being relatively slow. This changed in Chapter 7, where we were able to reduce the time required for magneto-ionic switching by 6 orders of magnitude, from hundreds of seconds to hundreds of microseconds. Although microsecond scale switching is sufficient for a wide range of application, for certain memory and logic devices, nanosecond switching would be required. Here we outline several approaches that we believe will allow significant further improvements in magneto-ionic switching times.

Since magneto-ionic switching relies on voltage-driven ion migration, further improvements in performance and functionality can likely be anticipated by increasing ionic mobility and enhancing ionic exchange. Voltage-driven ion migration has long been studied in solid state ionics and memristive switching and the design principles established there can provide valuable lessons to improve magneto-ionic device design.^{3,12,109,188}

One promising approach would be to examine oxides with higher ionic conductivity such as yttria-stabilized zirconia (YSZ),¹⁸⁹ or designing gate oxide heterostructures that include separately optimized oxygen storage and ion conducting layers. The introduction of new materials is however also associated with challenges. New materials do not only need to satisfy

the requirement for high ionic conductivity but they also have to promote the correct magnetic properties. In the case of YSZ this is possible; our preliminary experiments indicate that the Pt/Co/YSZ system exhibits strong perpendicular magnetic anisotropy.

Another promising strategy would be to engineer the concentration of oxygen defects in the oxide layer for maximum ion conductivity. This can be achieved either by doping the oxide, or by carefully controlling the oxygen partial pressure during oxide deposition.^{114,189} Both methods could result in orders of magnitude improvements in magneto-ionic switching times.

In Chapter 7 we were able to reduce the switching time by many orders of magnitude, by optimizing the layer thicknesses in the Pt/Co/GdO_x/Ta/Au stack. Nevertheless, the opportunities in further engineering device structure and layer thicknesses are far from exhausted. In particular a detailed analysis, identifying rate limiting steps and the specific role of each layer in the switching process, could result in further dramatic performance improvements.

We also expect that miniaturization of magneto-ionic devices to the nanoscale could significantly enhance the device response. In Chapter 5 it was found, that magneto-ionic switching occurs within a narrow region around the electrode edge within several seconds, but further inside, no switching was observed even within hundreds of seconds. This effect was attributed to enhanced ionic mobility and more efficient ionic exchange at the oxide edge.^{119,171} At the nanoscale, these benefits would apply to the entire device and this scaling effect alone might be sufficient to realize nanosecond switching in magneto-ionic devices.

9.2.3 Voltage Programmable Materials: Beyond Magnetism and Memristors

The physical and chemical properties of nanoscale materials derive largely from structure and composition at interfaces. The possibility to electrically modify these interfacial characteristics would provide a powerful means to control material properties. Of particular recent scientific and technological interest are metal/metal-oxide bilayers,¹⁻¹⁵ in which properties as varied as catalytic activity,^{1,2} charge and spin transport,³⁻⁶ ionic exchange,^{12,13} mechanical behavior,^{14,15} thermal conductivity^{10,11}, plasmonic response¹⁹⁰ and magnetism⁶⁻⁹ all depend sensitively on oxygen stoichiometry and defect structure at

the metal/metal-oxide interface (see Figure 9-3). Ionic transport in metal-oxides can be driven by an electric field, and O^{2-} migration is already exploited as a mechanism for resistive switching in anionic metal/oxide/metal memristors^{3,4}. However, the broader application of voltage-driven oxygen transport to control interfacial phenomena in metal/metal-oxide structures is only beginning to be explored.

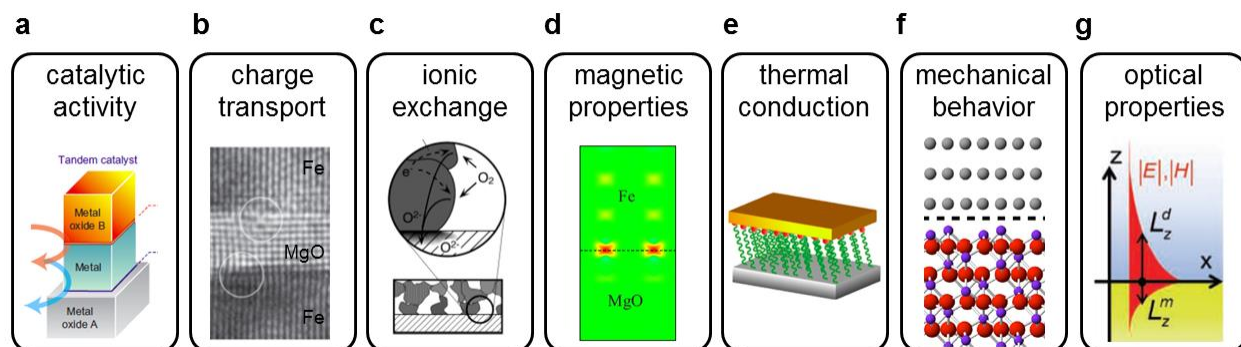


Figure 9-3: Material properties governed by metal/metal-oxide interfaces. Summary of material properties that emerge at the metal/metal-oxide interface and that could be amenable to voltage control via solid state switching of interface oxygen chemistry. The inset in (a) is reprinted with permission from Macmillan Publishers Ltd: Nature Chemistry, Reference [1], copyright (2011). The inset in (b) is reprinted by permission from Macmillan Publishers Ltd: Nature Materials, Reference [191], copyright (2004). The inset in (c) is reprinted with permission from Adler, S. B. Factors governing oxygen reduction in solid oxide fuel cell cathodes. Chem. Rev. 104, 4791-4843. Copyright (2004) American Chemical Society. The inset in (d) is reprinted with permission from Niranjana, M. K et al. Electric field effect on magnetization at the Fe/MgO(001) interface. Appl. Phys. Lett. 96, 222504. Copyright 2010, AIP Publishing LLC. The inset in (e) is reprinted by permission from Macmillan Publishers Ltd: Nature Materials, Reference [11], copyright (2012). The inset in (f) is reprinted with permission from Reference [192], Creative Commons license. The inset in (g) is reprinted from Armelles, G. et al. Magnetoplasmonics: combining magnetic and plasmonic functionalities. Adv. Opt. Mater. 1, 10-35. Copyright (2013) by John Wiley and Sons.

In this thesis we demonstrated voltage control over magnetic anisotropy, coercivity, saturation magnetization, domain wall motion, lateral electrical resistance, vertical electrical resistance and chemical composition. But considering the variety of properties and phenomena that emerge at metal/oxide interfaces this might only be the proverbial tip

of the iceberg. For instance in MTJs, interface states critically contribute to tunneling magneto resistance (TMR) and any modifications of these interfaces, such as the formation of an interfacial FeO layer,¹⁹³ is expected to dramatically alter the TMR ratio.¹⁹⁴ In addition to interface states, the barrier height in Fe/MgO/Fe tunnel junctions depends on the oxygen defect concentration in the thin MgO barrier,¹⁹¹ such that charge transport in MTJs could be tuned by voltage gating interfacial oxygen stoichiometry.

In microscale and nanoscale systems, interfaces often dictate thermal conductivity and heat flow. The interface thermal conductivity has been shown to depend on interface stiffness and thus the nature and density of interfacial bonds.¹¹ Due to the difference in energetics between metal-oxide and metal-metal bonds,¹⁹⁵ voltage control of interface oxygen stoichiometry could therefore provide a means to electrically gate interface stiffness and heat transport in micro and nanoscale devices.

Other interesting applications can be found in magneto-plasmonics, where the magneto-optical activity is greatly enhanced by the plasmon resonance.^{190,196} In these material systems, magneto-ionic coupling and voltage-driven modifications of metal/dielectric interfaces could provide a means to electrically control the optical properties of nanoscale systems.

Metal/metal-oxide bilayers are also of great importance in catalysis. Oxide supported metal catalysts are widely used in industry and it is well known that their catalytic activity emerges at the metal/oxide interface.^{1,2} Interestingly, it has been found that tuning the composition of the metal nanoparticles and the oxide support, as well as engineering their interfaces, allows control over reaction activities and selectivities.² Controlling these interface characteristics by voltage, might thus enable us to electrically control catalytic activity and chemical reactions in solid state devices.

In this thesis, we focused on voltage control of the magnetic and electrical properties of metal/metal-oxide bilayers, but as these examples show, there is tremendous potential in extending the principles demonstrated here to a wide range of material properties.

10 REFERENCES

- 1 Stair, P. C. Metal-oxide interfaces where the action is. *Nature Chem.* **3**, 345-346 (2011).
- 2 Yamada, Y. *et al.* Nanocrystal bilayer for tandem catalysis. *Nature Chem.* **3**, 372-376 (2011).
- 3 Yang, J. J., Strukov, D. B. & Stewart, D. R. Memristive devices for computing. *Nat. Nanotechnol.* **8**, 13-24 (2013).
- 4 Waser, R., Dittmann, R., Staikov, G. & Szot, K. Redox-based resistive switching memories - nanoionic mechanisms, prospects, and challenges. *Adv. Mater.* **21**, 2632 (2009).
- 5 Jeong, J. *et al.* Suppression of Metal-Insulator Transition in VO₂ by Electric Field-Induced Oxygen Vacancy Formation. *Science* **339**, 1402-1405 (2013).
- 6 Ikeda, S. *et al.* A perpendicular-anisotropy CoFeB-MgO magnetic tunnel junction. *Nat. Mater.* **9**, 721-724 (2010).
- 7 Miron, I. M. *et al.* Current-driven spin torque induced by the Rashba effect in a ferromagnetic metal layer. *Nat. Mater.* **9**, 230-234 (2010).
- 8 Rodmacq, B., Manchon, A., Ducruet, C., Auffret, S. & Dieny, B. Influence of thermal annealing on the perpendicular magnetic anisotropy of Pt/Co/AlO_x trilayers. *Phys. Rev. B* **79**, 024423 (2009).
- 9 Manchon, A. *et al.* X-ray analysis of the magnetic influence of oxygen in Pt/Co/AlO_x trilayers. *J. Appl. Phys.* **103**, 07A912 (2008).

- 10 Padture, N. P., Gell, M. & Jordan, E. H. Thermal barrier coatings for gas-turbine engine applications. *Science* **296**, 280-284 (2002).
- 11 Losego, M. D., Grady, M. E., Sottos, N. R., Cahill, D. G. & Braun, P. V. Effects of chemical bonding on heat transport across interfaces. *Nat. Mater.* **11**, 502-506 (2012).
- 12 Maier, J. Nanoionics: ion transport and electrochemical storage in confined systems. *Nat. Mater.* **4**, 805-815 (2005).
- 13 Adler, S. B. Factors governing oxygen reduction in solid oxide fuel cell cathodes. *Chem. Rev.* **104**, 4791-4843 (2004).
- 14 Zhang, W. & Smith, J. R. Nonstoichiometric interfaces and Al₂O₃ adhesion with Al and Ag. *Phys. Rev. Lett.* **85**, 3225-3228 (2000).
- 15 Howe, J. M. Bonding, Structure, and Properties of Metal-Ceramic Interfaces .1. Chemical Bonding, Chemical-Reaction, and Interfacial Structure. *Int. Mater. Rev.* **38**, 233-256 (1993).
- 16 Korotcenkov, G. *Handbook of gas sensor materials : properties, comparisons and applications*. 49 - 116 (Springer, 2013).
- 17 Korotcenkov, G. Metal oxides for solid-state gas sensors: What determines our choice? *Materials Science and Engineering B-Solid State Materials for Advanced Technology* **139**, 1-23 (2007).
- 18 Litzelman, S. J., Hertz, J. L., Jung, W. & Tuller, H. L. Opportunities and challenges in materials development for thin film solid oxide fuel cells. *Fuel Cells* **8**, 294-302 (2008).
- 19 Yamamoto, O. Solid oxide fuel cells: fundamental aspects and prospects. *Electrochim. Acta* **45**, 2423-2435 (2000).
- 20 Yang, H. X. *et al.* First-principles investigation of the very large perpendicular magnetic anisotropy at Fe vertical bar MgO and Co vertical bar MgO interfaces. *Phys. Rev. B* **84** (2011).
- 21 Ross, C. Patterned magnetic recording media. *Annu. Rev. Mater. Res.* **31**, 203-235 (2001).
- 22 Zhu, J. G. J. & Park, C. D. Magnetic tunnel junctions. *Materials Today* **9**, 36-45 (2006).
- 23 Chappert, C., Fert, A. & Van Dau, F. N. The emergence of spin electronics in data storage. *Nat. Mater.* **6**, 813-823 (2007).
- 24 Parkin, S. S. P., Hayashi, M. & Thomas, L. Magnetic domain-wall racetrack memory. *Science* **320**, 190-194 (2008).
- 25 Allwood, D. A. *et al.* Magnetic domain-wall logic. *Science* **309**, 1688-1692 (2005).
- 26 Fusil, S., Garcia, V., Barthélémy, A. & Bibes, M. Magnetoelectric devices for spintronics. *Annu. Rev. Mater. Res.* **44**, 91-116 (2014).

- 27 Wang, K. L., Alzate, J. G. & Amiri, P. K. Low-power non-volatile spintronic memory: STT-RAM and beyond. *J. Phys. D: Appl. Phys.* **46**, 074003 (2013).
- 28 Zhu, J. G. Magnetoresistive random access memory: the path to competitiveness and scalability. *Proc. IEEE* **96**, 1786-1798 (2008).
- 29 Beach, G. S. D., Tsoi, M. & Erskine, J. L. Current-induced domain wall motion. *J. Magn. Magn. Mater.* **320**, 1272-1281 (2008).
- 30 Brataas, A., Kent, A. D. & Ohno, H. Current-induced torques in magnetic materials. *Nat. Mater.* **11**, 372-381 (2012).
- 31 Wang, W. G., Li, M. G., Hageman, S. & Chien, C. L. Electric-field-assisted switching in magnetic tunnel junctions. *Nat. Mater.* **11**, 64-68 (2012).
- 32 Shiota, Y. *et al.* Induction of coherent magnetization switching in a few atomic layers of FeCo using voltage pulses. *Nat. Mater.* **11**, 39-43 (2012).
- 33 Eerenstein, W., Mathur, N. D. & Scott, J. F. Multiferroic and magnetoelectric materials. *Nature* **442**, 759-765 (2006).
- 34 Ramesh, R. & Spaldin, N. A. Multiferroics: progress and prospects in thin films. *Nat. Mater.* **6**, 21-29 (2007).
- 35 Dietl, T. A ten-year perspective on dilute magnetic semiconductors and oxides. *Nat. Mater.* **9**, 965-974 (2010).
- 36 Ohno, H. *et al.* Electric-field control of ferromagnetism. *Nature* **408**, 944-946 (2000).
- 37 Chiba, D., Yamanouchi, M., Matsukura, F. & Ohno, H. Electrical manipulation of magnetization reversal in a ferromagnetic semiconductor. *Science* **301**, 943-945 (2003).
- 38 Chiba, D. *et al.* Magnetization vector manipulation by electric fields. *Nature* **455**, 515-518 (2008).
- 39 Wang, Y., Hu, J. M., Lin, Y. H. & Nan, C. W. Multiferroic magnetoelectric composite nanostructures. *Npg Asia Materials* **2**, 61-68 (2010).
- 40 Weisheit, M. *et al.* Electric field-induced modification of magnetism in thin-film ferromagnets. *Science* **315**, 349-351 (2007).
- 41 Maruyama, T. *et al.* Large voltage-induced magnetic anisotropy change in a few atomic layers of iron. *Nat. Nanotechnol.* **4**, 158-161 (2009).
- 42 Endo, M., Kanai, S., Ikeda, S., Matsukura, F. & Ohno, H. Electric-field effects on thickness dependent magnetic anisotropy of sputtered MgO/Co₄₀Fe₄₀B₂₀/Ta structures. *Appl. Phys. Lett.* **96**, 212503 (2010).
- 43 Shiota, Y. *et al.* Voltage-assisted magnetization switching in ultrathin Fe₈₀Co₂₀ alloy layers. *Appl. Phys. Expr.* **2**, 063001 (2009).

- 44 Duan, C. G. *et al.* Surface magnetoelectric effect in ferromagnetic metal films. *Phys. Rev. Lett.* **101**, 137201 (2008).
- 45 Nakamura, K. *et al.* Giant modification of the magnetocrystalline anisotropy in transition-metal monolayers by an external electric field. *Phys. Rev. Lett.* **102**, 187201 (2009).
- 46 Tsujikawa, M. & Oda, T. Finite electric field effects in the large perpendicular magnetic anisotropy surface Pt/Fe/Pt(001): a first-principles study. *Phys. Rev. Lett.* **102**, 247203 (2009).
- 47 Manchon, A. *et al.* Analysis of oxygen induced anisotropy crossover in Pt/Co/MOx trilayers. *J. Appl. Phys.* **104**, 043914 (2008).
- 48 O'handley, R. C. *Modern magnetic materials: principles and applications*. Vol. 830622677 (Wiley New York, 2000).
- 49 Johnson, M. T., Bloemen, P. J. H., denBroeder, F. J. A. & deVries, J. J. Magnetic anisotropy in metallic multilayers. *Rep. Prog. Phys.* **59**, 1409-1458 (1996).
- 50 Néel, L. Anisotropie magnétique superficielle et surstructures d'orientation *J. Phys. Rad.* **15**, 225-239. (1954).
- 51 Gradmann, U. & Muller, J. Flat ferromagnetic epitaxial 48Ni/52Fe(111) films of few atomic layers. *Phys. Status Solidi* **27**, 313 (1968).
- 52 Carcia, P. F. Perpendicular magnetic-anisotropy in Pd/Co and Pt/Co thin-film layered structures. *J. Appl. Phys.* **63**, 5066-5073 (1988).
- 53 Carcia, P. F., Meinhaldt, A. D. & Suna, A. Perpendicular magnetic-anisotropy in Pd/Co thin-film layered structures. *Appl. Phys. Lett.* **47**, 178-180 (1985).
- 54 Zeper, W., Greidanus, F., Carcia, P. & Fincher, C. Perpendicular magnetic anisotropy and magneto-optical Kerr effect of vapor-deposited Co/Pt-layered structures. *J. Appl. Phys.* **65**, 4971-4975 (1989).
- 55 Baberschke, K. in *Band-Ferromagnetism* 27-45 (Springer, 2001).
- 56 Cullity, B. D. & Graham, C. D. *Introduction to magnetic materials*. (John Wiley & Sons, 2011).
- 57 Heinrich, B. & Cochran, J. F. Ultrathin metallic magnetic films - magnetic anisotropies and exchange Interactions. *Adv. Phys.* **42**, 523-639 (1993).
- 58 Bruno, P. Tight-binding approach to the orbital magnetic-moment and magnetocrystalline anisotropy of transition-metal monolayers. *Phys. Rev. B* **39**, 865-868 (1989).
- 59 Daalderop, G. H. O., Kelly, P. J. & Schuurmans, M. F. H. Magnetic-anisotropy of a free-standing Co monolayer and of multilayers which contain Co monolayers. *Phys. Rev. B* **50**, 9989-10003 (1994).

- 60 Weller, D. *et al.* Orbital Magnetic-Moments of Co in Multilayers with Perpendicular Magnetic-Anisotropy. *Phys. Rev. B* **49**, 12888-12896 (1994).
- 61 Nakajima, N. *et al.* Perpendicular magnetic anisotropy caused by interfacial hybridization via enhanced orbital moment in Co/Pt multilayers: Magnetic circular x-ray dichroism study. *Phys. Rev. Lett.* **81**, 5229-5232 (1998).
- 62 Kyuno, K., Yamamoto, R. & Asano, S. Theoretical-study on the magnetocrystalline anisotropy of X/Co (X = Pd, Pt, Cu, Ag, Au) multilayers. *J. Phys. Soc. Jpn.* **61**, 2099-2103 (1992).
- 63 Monso, S. *et al.* Crossover from in-plane to perpendicular anisotropy in Pt/CoFe/AlO_x sandwiches as a function of Al oxidation: A very accurate control of the oxidation of tunnel barriers. *Appl. Phys. Lett.* **80**, 4157-4159 (2002).
- 64 Rodmacq, B., Auffret, S., Dieny, B., Monso, S. & Boyer, P. Crossovers from in-plane to perpendicular anisotropy in magnetic tunnel junctions as a function of the barrier degree of oxidation. *J. Appl. Phys.* **93**, 7513-7515 (2003).
- 65 Qiu, Z. Q. & Bader, S. D. Surface magneto-optic Kerr effect (SMOKE). *J. Magn. Magn. Mater.* **200**, 664-678 (1999).
- 66 Stoner, E. C. & Wohlfarth, E. P. A mechanism of magnetic hysteresis in heterogeneous alloys. *Philos. Trans. R. Soc. London, A* **240**, 599-642 (1948).
- 67 Tannous, C. & Gieraltowski, J. The Stoner-Wohlfarth model of ferromagnetism. *Eur. J. Phys.* **29**, 475-487 (2008).
- 68 Emori, S. *Magnetic domain walls driven by interfacial phenomena* Ph.D. thesis, Massachusetts Institute of Technology, (2013).
- 69 Blundell, S. *Magnetism in condensed matter*. (Oxford University Press, 2001).
- 70 Metaxas, P. J. Creep and flow dynamics of magnetic domain walls: weak disorder, wall binding, and periodic pinning. *Solid State Physics* **62**, 75-162 (2011).
- 71 Koyama, T. *et al.* Observation of the intrinsic pinning of a magnetic domain wall in a ferromagnetic nanowire. *Nat. Mater.* **10**, 194-197 (2011).
- 72 Thiaville, A., Rohart, S., Jue, E., Cros, V. & Fert, A. Dynamics of Dzyaloshinskii domain walls in ultrathin magnetic films. *Europhys. Lett.* **100**, 57002 (2012).
- 73 Emori, S., Bauer, U., Ahn, S. M., Martinez, E. & Beach, G. S. D. Current-driven dynamics of chiral ferromagnetic domain walls. *Nat. Mater.* **12**, 611-616 (2013).
- 74 Franken, J. H., Hoeijmakers, M., Lavrijsen, R. & Swagten, H. J. M. Domain-wall pinning by local control of anisotropy in Pt/Co/Pt strips. *J. Phys.: Condens. Matter* **24**, 024216 (2012).
- 75 Lemerle, S. *et al.* Domain wall creep in an Ising ultrathin magnetic film. *Phys. Rev. Lett.* **80**, 849-852 (1998).

- 76 Chauve, P., Giamarchi, T. & Le Doussal, P. Creep and depinning in disordered media. *Phys. Rev. B* **62**, 6241-6267 (2000).
- 77 Schellekens, A., van den Brink, A., Franken, J., Swagten, H. & Koopmans, B. Electric-field control of domain wall motion in perpendicularly magnetized materials. *Nat. Commun.* **3**, 847 (2012).
- 78 Franken, J. H. *et al.* Voltage-gated pinning in a magnetic domain-wall conduit. *Appl. Phys. Lett.* **103**, 102411 (2013).
- 79 Bibes, M., Villegas, J. E. & Barthelemy, A. Ultrathin oxide films and interfaces for electronics and spintronics. *Adv. Phys.* **60**, 5-84 (2011).
- 80 Moodera, J. S., Kinder, L. R., Wong, T. M. & Meservey, R. Large magnetoresistance at room-temperature in ferromagnetic thin-film tunnel-junctions. *Phys. Rev. Lett.* **74**, 3273-3276 (1995).
- 81 Slonczewski, J. C. Current-driven excitation of magnetic multilayers. *J. Magn. Magn. Mater.* **159**, L1-L7 (1996).
- 82 Spaldin, N. A. & Fiebig, M. The renaissance of magnetoelectric multiferroics. *Science* **309**, 391-392 (2005).
- 83 Lottermoser, T. *et al.* Magnetic phase control by an electric field. *Nature* **430**, 541-544 (2004).
- 84 Chiba, D. *et al.* Electrical control of the ferromagnetic phase transition in cobalt at room temperature. *Nat. Mater.* **10**, 853-856 (2011).
- 85 Borisov, P., Hochstrat, A., Chen, X., Kleemann, W. & Binek, C. Magnetoelectric switching of exchange bias. *Phys. Rev. Lett.* **94**, 117203 (2005).
- 86 Laukhin, V. *et al.* Electric-field control of exchange bias in multiferroic epitaxial heterostructures. *Phys. Rev. Lett.* **97**, 227201 (2006).
- 87 Lahtinen, T. H. E., Franke, K. J. A. & van Dijken, S. Electric-field control of magnetic domain wall motion and local magnetization reversal. *Sci. Rep.* **2**, 258 (2012).
- 88 Lahtinen, T. H. E., Tuomi, J. O. & van Dijken, S. Pattern transfer and electric-field-induced magnetic domain formation in multiferroic heterostructures. *Adv. Mater.* **23**, 3187 (2011).
- 89 Bauer, U., Emori, S. & Beach, G. S. D. Electric field control of domain wall propagation in Pt/Co/GdOx films. *Appl. Phys. Lett.* **100**, 192408 (2012).
- 90 Bauer, U., Emori, S. & Beach, G. S. D. Voltage-gated modulation of domain wall creep dynamics in an ultrathin metallic ferromagnet. *Appl. Phys. Lett.* **101**, 172403 (2012).
- 91 Chiba, D. *et al.* Electric-field control of magnetic domain-wall velocity in ultrathin cobalt with perpendicular magnetization. *Nat. Commun.* **3**, 888 (2012).

-
- 92 Gajek, M. *et al.* Tunnel junctions with multiferroic barriers. *Nat. Mater.* **6**, 296-302 (2007).
- 93 Tsymbal, E. Y. & Kohlstedt, H. Tunneling across a ferroelectric. *Science* **313**, 181-183 (2006).
- 94 Furdyna, J. K. Diluted Magnetic Semiconductors. *J. Appl. Phys.* **64**, R29-R64 (1988).
- 95 Zavaliche, F. *et al.* Electrically assisted magnetic recording in multiferroic nanostructures. *Nano Lett.* **7**, 1586-1590 (2007).
- 96 Duan, C. G. *et al.* Tailoring magnetic anisotropy at the ferromagnetic/ferroelectric interface. *Appl. Phys. Lett.* **92**, 122905 (2008).
- 97 Duan, C. G., Jaswal, S. S. & Tsymbal, E. Y. Predicted magnetoelectric effect in Fe/BaTiO₃ multilayers: Ferroelectric control of magnetism. *Phys. Rev. Lett.* **97**, 047201 (2006).
- 98 Niranjana, M. K., Duan, C. G., Jaswal, S. S. & Tsymbal, E. Y. Electric field effect on magnetization at the Fe/MgO(001) interface. *Appl. Phys. Lett.* **96**, 222504 (2010).
- 99 Tsujikawa, M., Haraguchi, S., Oda, T., Miura, Y. & Shirai, M. A comparative ab initio study on electric-field dependence of magnetic anisotropy in MgO/Fe/Pt and MgO/Fe/Au films. *J. Appl. Phys.* **109**, 07C107 (2011).
- 100 Nakamura, K., Akiyama, T., Ito, T., Weinert, M. & Freeman, A. J. Role of an interfacial FeO layer in the electric-field-driven switching of magnetocrystalline anisotropy at the Fe/MgO interface. *Phys. Rev. B* **81**, 220409 (2010).
- 101 Zhang, S. F. Spin-dependent surface screening in ferromagnets and magnetic tunnel junctions. *Phys. Rev. Lett.* **83**, 640-643 (1999).
- 102 Shimabukuro, R., Nakamura, K., Akiyama, T. & Ito, T. Electric field effects on magnetocrystalline anisotropy in ferromagnetic Fe monolayers. *Physica E* **42**, 1014-1017 (2010).
- 103 Shiota, Y. *et al.* Quantitative evaluation of voltage-induced magnetic anisotropy change by magnetoresistance measurement. *Appl. Phys. Expr.* **4**, 043005 (2011).
- 104 Nozaki, T., Shiota, Y., Shiraishi, M., Shinjo, T. & Suzuki, Y. Voltage-induced perpendicular magnetic anisotropy change in magnetic tunnel junctions. *Appl. Phys. Lett.* **96**, 022506 (2010).
- 105 Despotuli, A. L. & Nikolaichik, V. I. A step towards nanoionics. *Solid State Ionics* **60**, 275-278 (1993).
- 106 Yamaguchi, S. Nanoionics-present and future prospects. *Sci. Tech. Adv. Mater.* **8**, 503-503 (2007).
- 107 Maier, J. Ionic transport in nano-sized systems. *Solid State Ionics* **175**, 7-12 (2004).

- 108 Tuller, H. L. Ionic conduction in nanocrystalline materials. *Solid State Ionics* **131**, 143-157 (2000).
- 109 Waser, R. & Aono, M. Nanoionics-based resistive switching memories. *Nat. Mater.* **6**, 833-840 (2007).
- 110 Yang, J. J. *et al.* Memristive switching mechanism for metal/oxide/metal nanodevices. *Nat. Nanotechnol.* **3**, 429-433 (2008).
- 111 Bauer, U., Przybylski, M., Kirschner, J. & Beach, G. S. D. Magnetoelectric charge trap memory. *Nano Lett.* **12**, 1437-1442 (2012).
- 112 Najjari, N. *et al.* Electrical switching in Fe/V/MgO/Fe tunnel junctions. *Phys. Rev. B* **81**, 174425 (2010).
- 113 Bowen, M. *et al.* Bias-crafted magnetic tunnel junctions with bistable spin-dependent states. *Appl. Phys. Lett.* **89**, 103517 (2006).
- 114 Yang, Y. C., Choi, S. & Lu, W. Oxide heterostructure resistive memory. *Nano Lett.* **13**, 2908-2915 (2013).
- 115 Jeong, D. S. *et al.* Emerging memories: resistive switching mechanisms and current status. *Rep. Prog. Phys.* **75**, 076502 (2012).
- 116 Strukov, D. B., Alibart, F. & Williams, R. Thermophoresis/diffusion as a plausible mechanism for unipolar resistive switching in metal-oxide-metal memristors. *Appl. Phys. A: Mater. Sci. Process.* **107**, 509-518 (2012).
- 117 Miao, F. *et al.* Anatomy of a nanoscale conduction channel reveals the mechanism of a high-performance memristor. *Adv. Mater.* **23**, 5633 (2011).
- 118 Kwon, D. H. *et al.* Atomic structure of conducting nanofilaments in TiO₂ resistive switching memory. *Nat. Nanotechnol.* **5**, 148-153 (2010).
- 119 Yang, J. J. *et al.* The mechanism of electroforming of metal oxide memristive switches. *Nanotechnology* **20**, 215201 (2009).
- 120 Yan, Y., Sandu, S. C., Conde, J. & Muralt, P. Experimental study of single triple-phase-boundary and platinum-yttria stabilized zirconia composite as cathodes for micro-solid oxide fuel cells. *J. Power Sources* **206**, 84-90 (2012).
- 121 Mogensen, M. & Skaarup, S. Kinetic and geometric aspects of solid oxide fuel cell electrodes. *Solid State Ionics* **86-8**, 1151-1160 (1996).
- 122 Strukov, D. B. & Williams, R. S. Exponential ionic drift: fast switching and low volatility of thin-film memristors. *Appl. Phys. A: Mater. Sci. Process.* **94**, 515-519 (2009).
- 123 Ha, S. S. *et al.* Voltage induced magnetic anisotropy change in ultrathin Fe(80)Co(20)/MgO junctions with Brillouin light scattering. *Appl. Phys. Lett.* **96**, 142512 (2010).

- 124 Bonell, F. *et al.* Large change in perpendicular magnetic anisotropy induced by an electric field in FePd ultrathin films. *Appl. Phys. Lett.* **98**, 232510 (2011).
- 125 Qiu, Z. Q., Pearson, J. & Bader, S. D. Asymmetry of the spin reorientation transition in ultrathin Fe films and wedges grown on Ag(100). *Phys. Rev. Lett.* **70**, 1006-1009 (1993).
- 126 Wulfhekel, W. *et al.* Single-crystal magnetotunnel junctions. *Appl. Phys. Lett.* **78**, 509-511 (2001).
- 127 Shen, J. & Kirschner, J. Tailoring magnetism in artificially structured materials: the new frontier. *Surf. Sci.* **500**, 300-322 (2002).
- 128 Weisheit, M. Electric field-induced modification of magnetism in thin-film ferromagnets. *Science* **315**, 1077-1077 (2007).
- 129 Fowley, C., Rode, K., Oguz, K., Kurt, H. & Coey, J. M. D. Electric field induced changes in the coercivity of a thin-film ferromagnet. *J. Phys. D: Appl. Phys.* **44**, 305001 (2011).
- 130 Liu, M., Liu, J., Wang, Q., Long, S. B. & Zhang, M. H. A metal/Al₂O₃/ZrO₂/SiO₂/Si (MAZOS) structure for high-performance non-volatile memory application. *Semicond. Sci. Technol.* **25**, 055013 (2010).
- 131 Besset, C., Bruyere, S., Blonkowski, S., Cremer, S. & Vincent, E. MIM capacitance variation under electrical stress. *Microelectron. Reliab.* **43**, 1237-1240 (2003).
- 132 Hung, C. C. *et al.* An innovative understanding of metal-insulator-metal (MIM)-capacitor degradation under constant-current stress. *IEEE Trans. Device Mater. Reliab.* **7**, 462-467 (2007).
- 133 Ohring, M. *Materials science of thin films.* (Academic press, 2001).
- 134 Price, E. P. *Characterization of transport processes in magnetic tunnel junctions* Ph.D. thesis, University of California, San Diego, (2001).
- 135 Beach, G. S. D. *The cobalt-iron metal/native oxide multilayer* Ph.D. thesis, University of California, San Diego, (2003).
- 136 Egger, S. *et al.* Dynamic shadow mask technique: A universal tool for nanoscience. *Nano Lett.* **5**, 15-20 (2005).
- 137 Vazquez-Mena, O. *et al.* Analysis of the blurring in stencil lithography. *Nanotechnology* **20**, 415303 (2009).
- 138 Thomas, S. & Visakh, P. *Handbook of engineering and specialty thermoplastics: Volume 3: Polyethers and polyesters.* Vol. 64 (John Wiley & Sons, 2011).
- 139 Landis, S. *Lithography.* (John Wiley & Sons, 2013).
- 140 Lin, C. J. *et al.* Magnetic and Structural-Properties of Co/Pt Multilayers. *J. Magn. Magn. Mater.* **93**, 194-206 (1991).

- 141 Kanak, J. *et al.* Influence of buffer layers on the texture and magnetic properties of Co/Pt multilayers with perpendicular anisotropy. *Phys. Status Solidi A* **204**, 3950-3953 (2007).
- 142 Emori, S. & Beach, G. S. D. Optimization of out-of-plane magnetized Co/Pt multilayers with resistive buffer layers. *J. Appl. Phys.* **110**, 033919 (2011).
- 143 Bauer, U., Emori, S. & Beach, G. S. D. Voltage-controlled domain wall traps in ferromagnetic nanowires. *Nat. Nanotechnol.* **8**, 411-416 (2013).
- 144 Pan, T. M. *et al.* Excellent frequency dispersion of thin gadolinium oxide high-k gate dielectrics. *Appl. Phys. Lett.* **87**, 262908 (2005).
- 145 Corti, C. & Holliday, R. *Gold: science and applications*. (CRC Press, 2010).
- 146 Saeger, K. & Rodies, J. The colour of gold and its alloys. *Gold Bull.* **10**, 10-14 (1977).
- 147 Lombardo, S. *et al.* Dielectric breakdown mechanisms in gate oxides. *J. Appl. Phys.* **98**, 121301 (2005).
- 148 Bauer, U., Choi, J., Wu, J., Chen, H. & Qiu, Z. Q. Effect of step decoration on the spin reorientation of Ni films grown on vicinal Cu(001). *Phys. Rev. B* **76**, 184415 (2007).
- 149 Zvezdin, A. K. & Kotov, V. a. c. A. *Modern magneto-optics and magneto-optical materials*. (CRC Press, 2010).
- 150 Heinrich, B. & Bland, J. Ultrathin magnetic structures II. *Sect 3*, 195-222 (1994).
- 151 Spaldin, N. A. *Magnetic materials: fundamentals and applications*. (Cambridge University Press, 2010).
- 152 Zak, J., Moog, E. R., Liu, C. & Bader, S. D. Universal approach to magneto-optics. *J. Magn. Mater.* **89**, 107-123 (1990).
- 153 Bauer, U. *Magnetic anisotropy of Fe films grown on Ag(017)* Diplom thesis, University of Würzburg, (2009).
- 154 Nistor, C., Beach, G. S. D. & Erskine, J. L. Versatile magneto-optic Kerr effect polarimeter for studies of domain-wall dynamics in magnetic nanostructures. *Rev. Sci. Instrum.* **77**, 103901 (2006).
- 155 Metaxas, P. J. *et al.* Creep and flow regimes of magnetic domain-wall motion in ultrathin Pt/Co/Pt films with perpendicular anisotropy. *Phys. Rev. Lett.* **99**, 217208 (2007).
- 156 Emori, S., Bono, D. C. & Beach, G. S. D. Time-resolved measurements of field-driven domain wall motion in a submicron strip with perpendicular magnetic anisotropy. *J. Appl. Phys.* **111**, 07D304 (2012).
- 157 Foner, S. Versatile and Sensitive Vibrating-Sample Magnetometer. *Rev. Sci. Instrum.* **30**, 548-557 (1959).

- 158 Chung, T. K., Carman, G. P. & Mohanchandra, K. P. Reversible magnetic domain-wall motion under an electric field in a magnetoelectric thin film. *Appl. Phys. Lett.* **92**, 112509 (2008).
- 159 Dean, J., Bryan, M. T., Schrefl, T. & Allwood, D. A. Stress-based control of magnetic nanowire domain walls in artificial multiferroic systems. *J. Appl. Phys.* **109**, 023915 (2011).
- 160 Lei, N. *et al.* Strain-controlled magnetic domain wall propagation in hybrid piezoelectric/ferromagnetic structures. *Nat. Commun.* **4**, 1378 (2013).
- 161 Emori, S. & Beach, G. S. D. Enhanced current-induced domain wall motion by tuning perpendicular magnetic anisotropy. *Appl. Phys. Lett.* **98**, 132508 (2011).
- 162 Emori, S. & Beach, G. S. D. Roles of the magnetic field and electric current in thermally activated domain wall motion in a submicrometer magnetic strip with perpendicular magnetic anisotropy. *J. Phys.: Condens. Matter* **24**, 024214 (2012).
- 163 Garcia, V. *et al.* Ferroelectric control of spin polarization. *Science* **327**, 1106-1110 (2010).
- 164 Emori, S., Bono, D. C. & Beach, G. S. D. Interfacial current-induced torques in Pt/Co/GdOx. *Appl. Phys. Lett.* **101**, 042405 (2012).
- 165 Pey, K. L. *et al.* Physical analysis of breakdown in high-kappa/metal gate stacks using TEM/EELS and STM for reliability enhancement (invited). *Microelectron. Eng.* **88**, 1365-1372 (2011).
- 166 Tsymbal, E. Y. & Belashchenko, K. D. Role of interface bonding in spin-dependent tunnelling (invited). *J. Appl. Phys.* **97**, 10C910 (2005).
- 167 Cheng, K. H. & Krishnamoorthy, A. Effect of ramp rate on dielectric breakdown in CU-SiOC interconnects. *Thin Solid Films* **462**, 316-320 (2004).
- 168 Beckel, D. *et al.* Thin films for micro solid oxide fuel cells. *J. Power Sources* **173**, 325-345 (2007).
- 169 Brichzin, V., Fleig, J., Habermeier, H. U., Cristiani, G. & Maier, J. The geometry dependence of the polarization resistance of Sr-doped LaMnO₃ microelectrodes on yttria-stabilized zirconia. *Solid State Ionics* **152**, 499-507 (2002).
- 170 Eberhart, M. E., Donovan, M. M. & Outlaw, R. A. Ab initio calculations of oxygen diffusivity in group-IB transition metals. *Phys. Rev. B* **46**, 12744-12747 (1992).
- 171 Balluffi, R. W., Allen, S. M. & Carter, W. C. *Kinetics of materials*. 209 - 228 (John Wiley & Sons, 2005).
- 172 Rajanikanth, A., Hauet, T., Montaigne, F., Mangin, S. & Andrieu, S. Magnetic anisotropy modified by electric field in V/Fe/MgO(001)/Fe epitaxial magnetic tunnel junction. *Appl. Phys. Lett.* **103**, 062402 (2013).

- 173 Bonell, F. *et al.* Reversible change in the oxidation state and magnetic circular dichroism of Fe driven by an electric field at the FeCo/MgO interface. *Appl. Phys. Lett.* **102**, 152401 (2013).
- 174 Tournerie, N., Engelhardt, A. P., Maroun, F. & Allongue, P. Influence of the surface chemistry on the electric-field control of the magnetization of ultrathin films. *Phys. Rev. B* **86**, 104434 (2012).
- 175 Reichel, L., Oswald, S., Fahler, S., Schultz, L. & Leistner, K. Electrochemically driven variation of magnetic properties in ultrathin CoPt films. *J. Appl. Phys.* **113**, 143904 (2013).
- 176 Lacour, D. *et al.* Magnetic properties of postoxidized Pt/Co/Al layers with perpendicular anisotropy. *Appl. Phys. Lett.* **90**, 192506 (2007).
- 177 Chappert, C. *et al.* Planar patterned magnetic media obtained by ion irradiation. *Science* **280**, 1919-1922 (1998).
- 178 Franken, J. H., Swagten, H. J. M. & Koopmans, B. Shift registers based on magnetic domain wall ratchets with perpendicular anisotropy. *Nat. Nanotechnol.* **7**, 499-503 (2012).
- 179 Pu, J., Kim, S. J., Kim, Y. S. & Cho, B. J. Evaluation of gadolinium oxide as a blocking layer of charge-trap flash memory cell. *Electrochem. Solid St.* **11**, H252-H254 (2008).
- 180 Vitale, S. A., Wyatt, P. W. & Hodson, C. J. Plasma-enhanced atomic layer deposition and etching of high-k gadolinium oxide. *J. Vac. Sci. Technol., A* **30**, 01A130 (2012).
- 181 Rocha, P. R. F. *et al.* Low-frequency diffusion noise in resistive-switching memories based on metal-oxide polymer structure. *IEEE Trans. Electron Devices* **59**, 2483-2487 (2012).
- 182 Chen, Q., Gomes, H. L., Rocha, P. R. F., de Leeuw, D. M. & Meskers, S. C. J. Reversible post-breakdown conduction in aluminum oxide-polymer capacitors. *Appl. Phys. Lett.* **102**, 153509 (2013).
- 183 Wang, J. C., Jian, D. Y., Ye, Y. R., Chang, L. C. & Lai, C. S. Characteristics of gadolinium oxide resistive switching memory with Pt-Al alloy top electrode and post-metallization annealing. *J. Phys. D: Appl. Phys.* **46**, 275103 (2013).
- 184 Aratani, K. *et al.* A novel resistance memory with high scalability and nanosecond switching. *2007 IEEE International Electron Devices Meeting, Vols 1 and 2*, 783-786 (2007).
- 185 Graham, R. L. *et al.* Resistivity dominated by surface scattering in sub-50 nm Cu wires. *Appl. Phys. Lett.* **96**, 042116 (2010).
- 186 Wu, W., Brongersma, S. H., Van Hove, M. & Maex, K. Influence of surface and grain-boundary scattering on the resistivity of copper in reduced dimensions. *Appl. Phys. Lett.* **84**, 2838-2840 (2004).

-
- 187 Yang, Y. C. *et al.* Observation of conducting filament growth in nanoscale resistive memories. *Nat. Commun.* **3**, 732 (2012).
- 188 Wachsman, E. D. & Lee, K. T. Lowering the temperature of solid oxide fuel cells. *Science* **334**, 935-939 (2011).
- 189 Jung, W., Hertz, J. L. & Tuller, H. L. Enhanced ionic conductivity and phase metastability of nano-sized thin film yttria-doped zirconia (YDZ). *Acta Mater.* **57**, 1399-1404 (2009).
- 190 Armelles, G., Cebollada, A., Garcia-Martin, A. & Gonzalez, M. U. Magnetoplasmonics: combining magnetic and plasmonic functionalities. *Adv. Opt. Mater.* **1**, 10-35 (2013).
- 191 Yuasa, S., Nagahama, T., Fukushima, A., Suzuki, Y. & Ando, K. Giant room-temperature magnetoresistance in single-crystal Fe/MgO/Fe magnetic tunnel junctions. *Nat. Mater.* **3**, 868-871 (2004).
- 192 Pilania, G. *et al.* Revisiting the Al/Al₂O₃ interface: coherent interfaces and misfit accommodation. *Sci. Rep.* **4** (2014).
- 193 Meyerheim, H. L. *et al.* Geometrical and compositional structure at metal-oxide interfaces: MgO on Fe(001). *Phys. Rev. Lett.* **87**, 076102 (2001).
- 194 Butler, W. H., Zhang, X. G., Schulthess, T. C. & MacLaren, J. M. Spin-dependent tunneling conductance of Fe vertical bar MgO vertical bar Fe sandwiches. *Phys. Rev. B* **63**, 054416 (2001).
- 195 Gundrum, B. C., Cahill, D. G. & Averback, R. S. Thermal conductance of metal-metal interfaces. *Phys. Rev. B* **72**, 245426 (2005).
- 196 Armelles, G. & Dmitriev, A. Focus on magnetoplasmonics. *New J. Phys.* **16**, 045012 (2014).